SYNTHETIC MOLECULAR PROBES OF ENDOCYTOSIS, ESCAPE FROM ENSOSOMES, AND PROTEIN-PROTEIN INTERACTIONS

By

David Hymel

Submitted to the graduate degree program in Medicinal Chemistry and the Graduate Faculty of the University of Kansas in partial fulfillment of the requirements for the degree of Doctor of Philosophy.

_____

Chairperson Dr. Blake R. Peterson

_____

Dr. Michael F. Rafferty

_____

Dr. Jane V. Aldrich

_____

Dr. Paul R. Hanson

_____

Dr. Jeffrey P. Krise

Date Defended: July 11, 2014

The dissertation committee for David Hymel

certifies that this is the approved version of the following dissertation:

SYNTHETIC MOLECULAR PROBES OF ENDOCYTOSIS, ESCAPE FROM ENDOSOMES, AND PROTEIN-PROTEIN INTERACTIONS

_____

Chairperson Dr. Blake R. Peterson

Date Approved: July 11, 2014

ABSTRACT

Over the past several years, the Peterson group has developed synthetic mimics of cholesterol that rapidly incorporate into the plasma membrane of mammalian cells. These *N*-alkyl-3β-cholesterylamines cycle between the plasma membrane and early/recycling endosomes similar to natural cell surface receptors. Because of this unique activity, cholesterylamines have been linked to protein-binding and other motifs to generate artificial cell surface receptors. More recently, they have been conjugated to membrane disruptive peptides to generate synthetic agents that selectively permeabilize early endosomes and deliver cell-impermeable small molecules to the cytosol. Although this pioneering work has significant potential as a system to deliver cell-impermeable small molecule drugs and/or therapeutic agents, additional research is needed to understand the mechanism of action and develop therapeutic applications.

To further evaluate this system, we first investigated the structure-activity relationships of cholesterylamines using fluorescent analogues designed to probe the mechanism of cellular uptake. This study produced probes with robust activity that suggests an unprecedented mechanism of cholesterol uptake on mammalian cell surfaces. Second, we investigated novel endosome disruptive peptides that provided insights into their mechanism of action. Additionally, we applied this knowledge to obtain proof-of-concept with antibody conjugates and endosome disruptive peptides as a new strategy to selectively deliver small molecules to tumor cells that overexpress specific cell surface receptors.

Another project involves the development of a fluorescence-based method to detect protein-protein interactions in complex biological systems. This method utilizes a novel fluorinated fluorophore that undergoes proximity-driven exchange between lysine residues at the interface of a protein complex. Transfer of this fluorophore from donor to acceptor lysine residues produces a fluorescent protein partner that can be detected by gel electrophoresis or proteomics methods. Since lysine is prevalent at the interface of numerous protein complexes, this method may be useful to identify novel protein-protein interactions and/or factors that affect these interactions.

ACKNOWLEDGEMENTS

First and foremost, I would like to thank my advisor, Prof. Blake R. Peterson, for his valuable advice and mentorship over the past several years. I have had a very rewarding experience working under his guidance on several diverse and interesting research projects. I thank the entire faculty of the Medicinal Chemistry department for their teaching and expertise throughout my graduate career. I would also like to thank the members of my defense committee, Dr. Mike Rafferty, Dr. Jane Aldrich, Dr. Paul Hanson, and Dr. Jeff Krise, for their time and advice.

I express my gratitude to the former members of the Peterson group involved with this research, specifically Dr. Qi Sun, Sutang Cai, Dr. Rebecca Henkhaus, Dr. Ze Li, Ning Yang, and Dr. Zachary Woydziak. I would like to thank all of my current and former colleagues in the Peterson group for their friendship and advice, especially Dr. Chamani Perera, Matt Meinig, and Molly Lee. I would also like to thank the countless friends and colleagues throughout KU for making my time in Lawrence memorable.

Finally, I would like to thank my parents, Lloyd and Deborah, my sister, Erin, and, my wife, Eva, for their constant support and motivation. Their encouragement has reinforced my desire to perform scientific research and achieve my professional goals.

TABLE OF CONTENTS

LIST OF FIGURES

LIST OF TABLES

Chapter 1

Synthetic Mimics of Cholesterol and their Application to the Delivery of Cell-Impermeable Molecules

1.1 Receptor-Mediated Endocytosis

The plasma membrane of mammalian cells is a highly complex structure of lipids and proteins that serves as a barrier to protect intracellular processes against toxins and other forms of environmental stress. The lipid portion of the membrane consists of a phospholipid bilayer that is only permeable to water or hydrophobic small molecules. Small polar nutrients, such as ions, carbohydrates and amino acids, are impermeable to the plasma membrane and require active transport by protein pumps and channels. Other small or macromolecular nutrients enter cells by a process called endocytosis, a term that describes several mechanisms in which a dynamic portion of the plasma membrane invaginates and pinches off to form a membrane bound vesicle.[1-3] These vesicles become part of an intricate network of intracellular compartments involved in sorting and metabolizing the encapsulated contents.

Receptor-mediated endocytosis (RME) represents one form of this mechanism that involves the internalization of receptor-ligand complexes.[4] Two examples of RME, low-density lipoprotein (LDL) and transferrin (TF), are shown in Figure 1.1. These macromolecules serve as carriers of cholesterol and iron, respectively.[5-8]

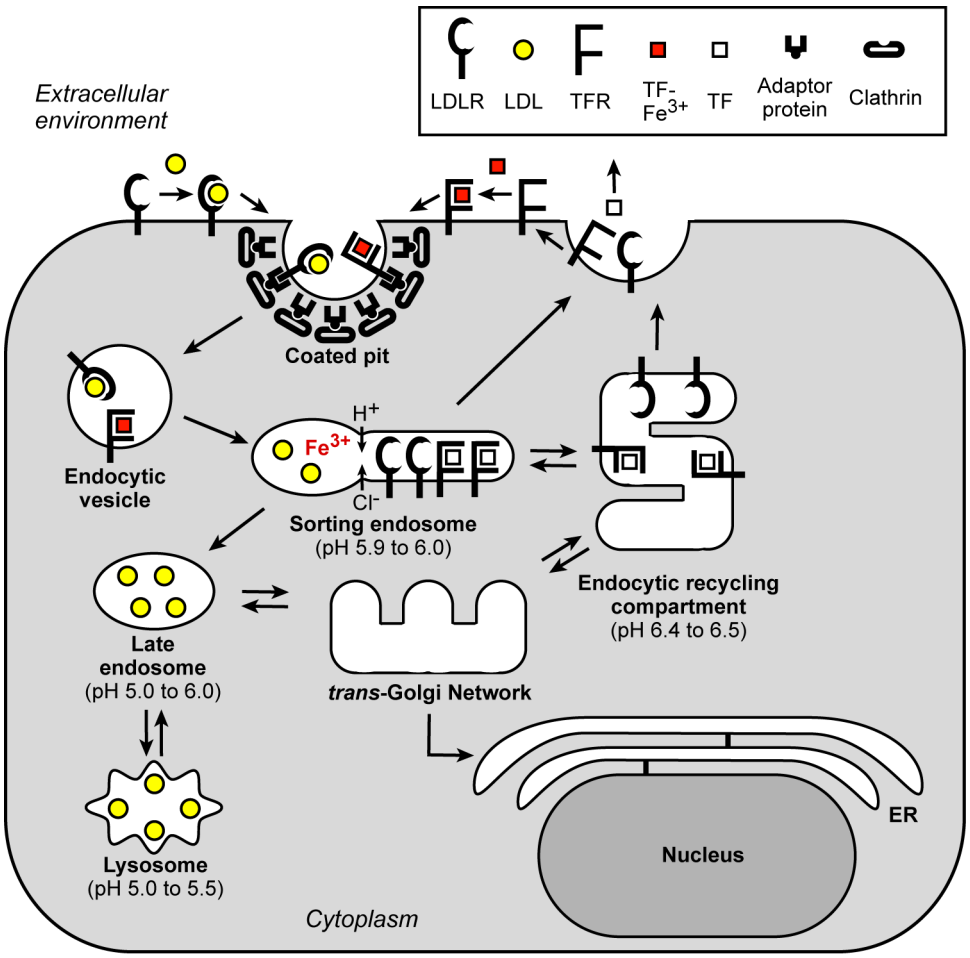

Figure 1.1. Receptor-mediated endocytosis of low-density lipoprotein (LDL) via the LDL receptor (LDLR) and transferrin (TF) via the transferrin receptor (TFR).

The LDL receptor (LDLR) and the transferrin receptor (TFR) are distributed throughout the plasma membrane. Upon binding their respective ligands, the receptor-ligand complexes are concentrated in dynamic regions of the plasma membrane that actively undergo endocytosis. The endocytic vesicle trafficks through the cytosol and fuses with early endosomes that are acidified to pH 6.0 by proton pumps and chloride channels. In the case of LDL, acidification causes the dissociation of the LDL particle from its receptor. The LDL particle is further sorted to late endosomes and lysosomes where metabolic enzymes

liberate cholesterol and amino acids for use by the cell. The LDLR is sorted through the endocytic recycling compartment and back to the plasma membrane to recapture LDL.[6, 7] The TF-TFR complex undergoes a similar mechanism, however iron is released upon acidification of sorting endosomes without dissociation of the ligand receptor complex. Receptor-bound *apo*-TF is cycled back to the plasma membrane and released into the extracellular environment.[8] For these reasons, fluorescent LDL and transferrin conjugates have been used extensively in microscopy as markers of lysosomes and early/recycling endosomes, respectively.[9, 10]

1.2 Synthetic Mimics of Cholesterol

Cholesterol is a critical constituent of membranes of animal cells. This sterol stabilizes lipid bilayers and decreases membrane permeability to small molecules.[11, 12] Its concentration needs to be tightly regulated in the plasma membrane and, as a result, mammalian cells have evolved multiple mechanisms for acquiring and transporting this sterol. A more detailed discussion of these mechanisms is provided in Chapter 2 of this dissertation. The lipid composition of the plasma membrane comprises ~30% cholesterol, and the plasma membrane and endocytic recycling compartment (ERC) contain the vast majority of total cellular cholesterol.[11]

Over the last decade, our lab has investigated the use of *N*-alkyl-cholesterylamines as synthetic cell surface receptors, and this work was recently reviewed.[13-16] More recently, we have focused on investigating fluorophore-linked

cholesterylamines as functional mimics of cholesterol to study uptake and trafficking properties in living cells. The localization and transport of cholesterol has been extensively studied by fluorescence microscopy using fluorescent analogues such as those shown in Figure 1.2.[17-21] However, the integration of a fluorophore onto the core sterol structure often greatly alters the ability of these compounds to stably incorporate into the lipid bilayer.[20] As a result, several of these compounds do not display cellular localization similar to cholesterol.

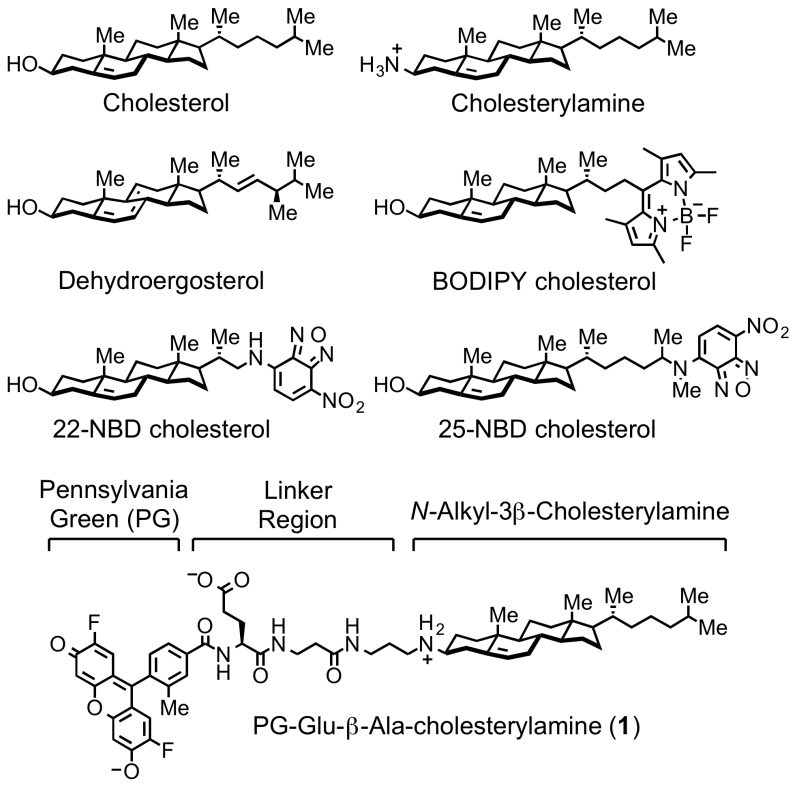

Figure 1.2. Structures of cholesterol, cholesterylamine, and fluorescent analogues of cholesterol. PG-Glu-β-Ala-cholesterylamine (**1**), synthesized in the Peterson group, comprises the Pennsylvania green fluorophore as a head group linked to cholesterylamine via a short peptide linker region.

As an example, 22-NBD cholesterol, a commonly used fluorescent cholesterol analogue, was added to Jurkat lymphocytes and analyzed by confocal laser scanning microscopy (Figure 1.3, Panels D-E). This compound

exhibits rapid trafficking into the Golgi apparatus and nuclear membrane due to its inability to stably incorporate into the plasma membrane. Structurally optimized *N*-alkyl-cholesterylamines, exemplified by compound **1** which includes the Pennsylvania Green fluorophore (Figure 1.2), are rapidly taken up by living mammalian cells, associate with the plasma membrane, and accumulate in transferrin-positive early/recycling endosomes (Figure 1.3, Panels A-C).[22, 23] In this way, fluorescent cholesterylamines demonstrate localization and trafficking properties that more meaningfully mimic the known properties of cholesterol.

Based on previous structural analogues of compound **1**, it was found that changes in the linker region greatly affected the efficacy of cellular uptake and partitioning between the plasma membrane and early/recycling endosomes.[14, 22] Compounds that contained hydrophobic uncharged linkers were found to show lower efficacy. Compounds that included one or two negatively charged amino acid residues showed higher efficacy and accumulate to a greater extent in early endosomes. These finding proved advantageous in that modifications of the linker region can be used to improve delivery of conjugated cargo into endosomes.

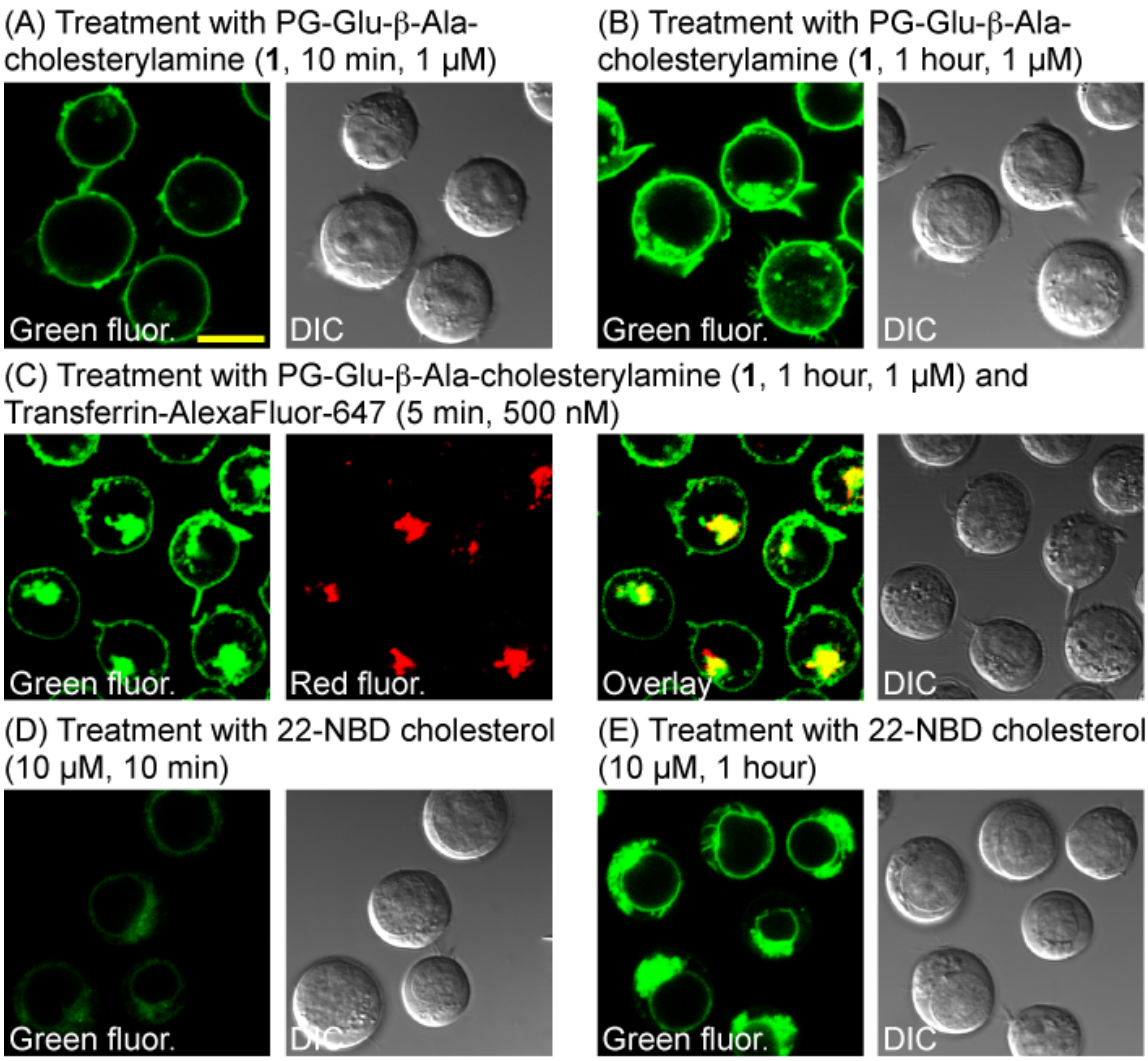

Figure 1.3. Confocal laser scanning microscopy and differential interference contrast (DIC) microscopy of Jurkat lymphocytes treated with fluorescent cholesterol analogues. These micrographs demonstrate the rapid binding of compound **1** and its accumulation on the plasma membrane and early/recycling endosomes (Panels A-B). Panel C illustrates the co-localization between green fluorescent **1** and red fluorescent transferrin-AlexaFluor 647, indicating accumulation of **1** in early/recycling endosomes. Panels D-E shows the non-specific binding activity of 22-NBD cholesterol, with fluorescence observed in the Golgi apparatus and nuclear membrane. Scale bar = 10 μm.

1.3 Disruption of Early Endosomes by Cholesterylamine-linked Peptides

Receptor-mediated endocytosis (RME) is an efficient mechanism of uptake for cell-impermeable molecules. However the majority of ligands

internalized by this process remain encapsulated until they are degraded in the lysosome. As a result, impermeable therapeutics or probe molecules that utilize RME for cellular internalization may show little efficacy since they cannot reach the cytosol in significant concentrations. To address this, encapsulation and/or modification of impermeable molecules with liposomes,[24, 25] polymers,[26, 27] or cell-penetrating peptides (CPPs)[28, 29] have been extensively studied, but these approaches have provided mixed success and are generally of limited applicability.

In order to deliver cell-impermeable molecules into the cytosol, our group developed a molecule that selectively disrupts early/recycling endosomes based on a derivative of a membrane-lytic dodecapeptide called PC-4.[30] This peptide was previously published by Weber *et al.* and demonstrated pH-dependent disruption of liposomes at acidic pH.[31] As shown in Figure 1.4, cholesterylamine-linked PC-4 (**2**) can be used to selectively disrupt early/recycling endosomes. This allows cleavage of a disulfide bond by reduced glutathione (GSH) and efficient release of the cholesterylamine-linked fluorophore into the cytosol and nucleus of living Jurkat lymphocytes.[30, 32] Because this release could be blocked by the proton pump inhibitor Bafilomycin A1, the pH-dependent nature of this activity was proposed to provide selectivity for early endosomes at pH 6.0 while preventing disruption of the plasma membrane at pH 7.4.

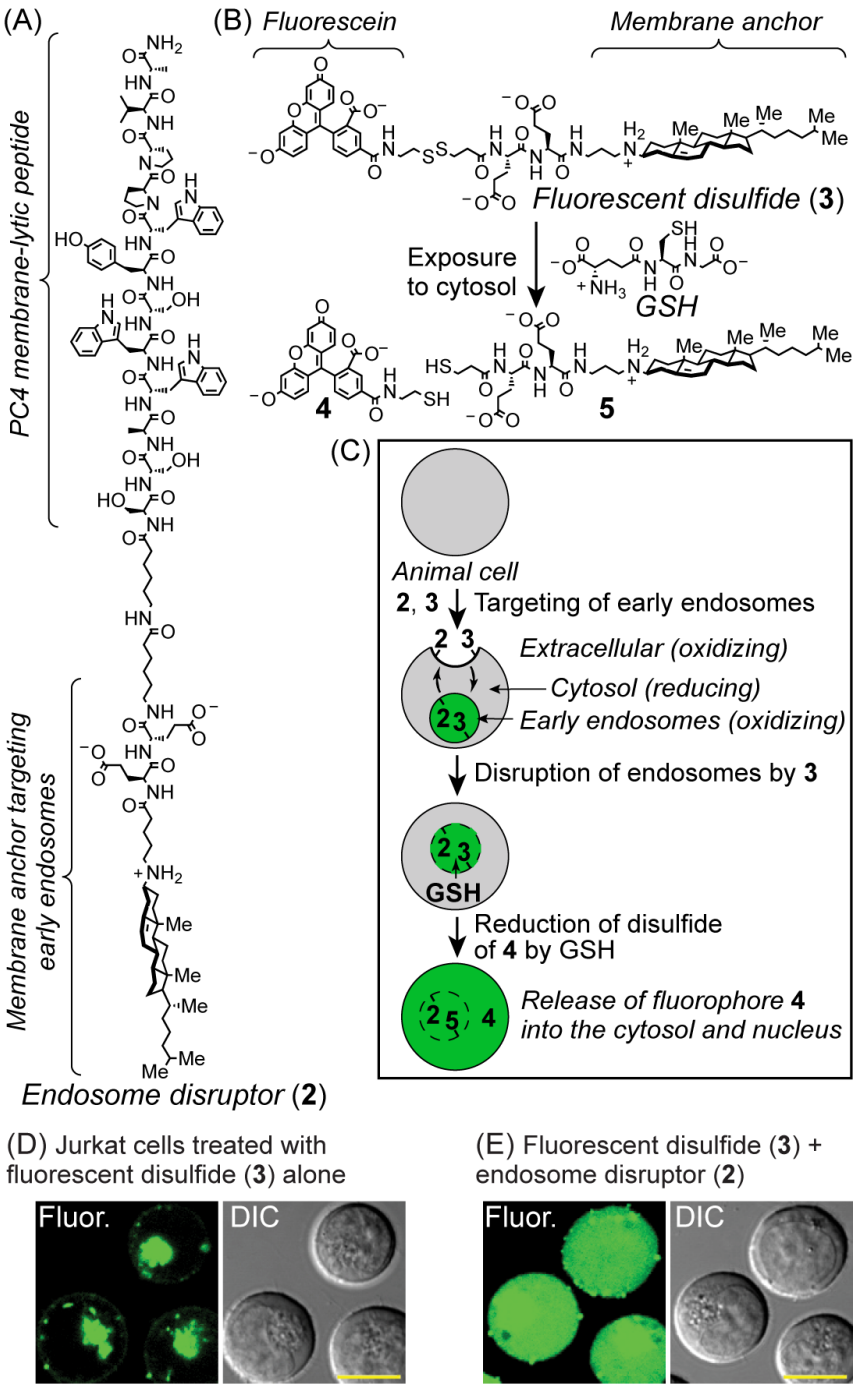

Figure 1.4. Structures of cholesterylamine-linked PC4 (**2**, Panel A), a fluorescent disulfide-linked cholesterylamine (**3**, Panel B), and products following cleavage of **3** by reduced glutathione (GSH). Panel C is a schematic representation of cellular release of **4** via endosome disruption. Panels D-E: Confocal fluorescence and DIC micrographs of Jurkat lymphocytes treated with **3** (2.5 μM, 12 h) in the absence and presence of endosome disruptor **2**. Scale bars = 10 μm.

1.4 Current Limitations in the Delivery of Cell-Impermeable Molecules

The use of cholesterylamines and endosome disruptive peptides for delivery applications faces a number of challenges. Previously designed fluorescent cholesterylamines have demonstrated that design of the head group and linker regions can greatly affect the uptake and trafficking properties of these compounds.[22] However, a thorough investigation into the structure-activity relationships that govern cellular binding has not been performed. Also, the mechanism by which these compounds associate with cells remains unclear. Addressing these questions could provide insight into the design of better delivery systems. More importantly, further investigating fluorescent cholesterylamines as functional analogues of cholesterol could provide new information regarding how mammalian cells acquire and transport cholesterol.

Another limitation of previous research on these agents is the toxicity of the cholesterylamine-PC4 derivative (**2**) to cultured cells. As shown in Figure 1.5, the potency of this compound can be measured by using flow cytometry to quantitate the increase in cellular fluorescence observed upon disruption of endosomes and release of the fluorophore. When compared to the toxicity observed at 48 hours, this compound exhibits a relatively narrow toxicity index.[30] New peptide compounds that show higher potency with reduced toxicity are needed. Also, the mechanism of membrane disruption by PC-4 has not been elucidated. Analogues designed to probe the structural requirements could provide insight into this mechanism and assist in improving the toxicity index.

Yet another obstacle to this research is its applicability to *in vivo* drug delivery applications. Conjugation to cholesterylamines provides highly efficient delivery of linked cargo to early/recycling endosomes, and endosome disruptive peptides provide a mechanism for releasing cargo to its desired target. However, cholesterylamines are rapidly taken up by nearly all mammalian cell types and would not provide adequate selectivity for drug delivery applications such as cancer chemotherapy. Examination of other early endosome targeting agents that provide selectivity for different cell types, such as tumor cells, could greatly expand the therapeutic potential of this approach.

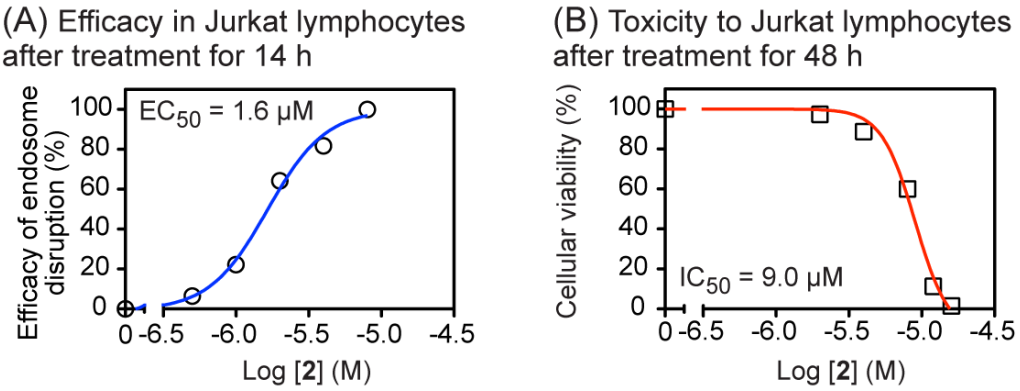

Figure 1.5. Panel A: Efficacy of compound **2** for the release of the fluorescent probe **3** in Jurkat lymphocytes. Panel B: Toxicity of compound **2** in Jurkat lymphocytes after 48 hours. Analyses performed by flow cytometry.

1.5 Outline of this Dissertation

Based on pioneering studies of synthetic mimics of cholesterol and endosome disruptive peptides by the Peterson group, my research has focused on addressing the limitations outlined in the previous section and investigating new methods to broaden the scope of this work. Chapter 2 describes the design, synthesis, and evaluation of fluorescent mimics of cholesterol to probe the

structure-activity relationships that dictate the cellular binding of cholesterylamines and related compounds. This chapter also reports the investigation into the mechanism of uptake of cholesterylamines and its relationship to cholesterol. Chapter 3 describes the development of endosome disruptive peptides with improved toxicity index and examination of the mechanism of their membrane disruptive properties. Chapter 4 describes the application of these peptides to cell-specific delivery of disulfide-linked cargo using antibodies and antibody-drug conjugates. Finally, Chapter 5 describes a novel method for fluorescence-based detection of protein-protein interactions in complex biological matrices. This system utilizes a proximity-driven nucleophilic aromatic substitution reaction (S_NAr) of lysine-linked fluorophores between two interacting proteins.

1.6 References

1. Doherty, G. J.; McMahon, H. T., Mechanisms of Endocytosis. In *Annu. Rev. Biochem.*, Annual Reviews: Palo Alto, 2009; Vol. 78, pp 857-902.

2. Hansen, C. G.; Nichols, B. J., Molecular mechanisms of clathrin-independent endocytosis. *J. Cell Sci.* **2009,** *122*, 1713-1721.

3. McMahon, H. T.; Boucrot, E., Molecular mechanism and physiological functions of clathrin-mediated endocytosis. *Nat. Rev. Mol. Cell Biol.* **2011,** *12*, 517-533.

4. Goldstein, J. L.; Anderson, R. G. W.; Brown, M. S., Coated Pits, Coated Vesicles, and Receptor-Mediated Endocytosis. *Nature* **1979,** *279*, 679-685.

5. Brown, M. S.; Goldstein, J. L., A Receptor-Mediated Pathway for Cholesterol Homeostasis (Nobel Lecture). *Angew. Chem.-Int. Edit. Engl.* **1986,** *25*, 583-602.

6. Goldstein, J. L.; Brown, M. S., The LDL Receptor. *Arterioscler. Thromb. Vasc. Biol.* **2009,** *29*, 431-438.

7. Goldstein, J. L.; Brown, M. S.; Anderson, R. G. W.; Russell, D. W.; Schneider, W. J., Receptor-Mediated Endocytosis - Concepts Emerging from the LDL Receptor System. *Annu. Rev. Cell Biol.* **1985,** *1*, 1-39.

8. Sheff, D.; Pelletier, L.; O'Connell, C. B.; Warren, G.; Mellman, I., Transferrin receptor recycling in the absence of perinuclear recycling endosomes. *J. Cell Biol.* **2002,** *156*, 797-804.

9. Bai, M.; Bornhop, D. J., Recent Advances in Receptor-Targeted Fluorescent Probes for In Vivo Cancer Imaging. *Curr. Med. Chem.* **2012,** *19*, 4742-4758.

10. Qian, Z. M.; Li, H. Y.; Sun, H. Z.; Ho, K., Targeted drug delivery via the transferrin receptor-mediated endocytosis pathway. *Pharmacol. Rev.* **2002,** *54*, 561-587.

11. Maxfield, F. R.; Mondal, M., Sterol and lipid trafficking in mammalian cells. *Biochem. Soc. Trans.* **2006,** *34*, 335-339.

12. Maxfield, F. R.; van Meer, G., Cholesterol, the central lipid of mammalian cells. *Curr. Opin. Cell Biol.* **2010,** *22*, 422-429.

13. Boonyarattanakalin, S.; Hu, J. F.; Dykstra-Rummel, S. A.; August, A.; Peterson, B. R., Endocytic delivery of vancomycin mediated by a synthetic cell

surface receptor: Rescue of bacterially infected mammalian cells and tissue targeting in vivo. *J. Am. Chem. Soc.* **2007,** *129*, 268-269.

14. Boonyarattanakalin, S.; Martin, S. E.; Sun, Q.; Peterson, B. R., A synthetic mimic of human Fc receptors: Defined chemical modification of cell surfaces enables efficient endocytic uptake of human immunoglobulin-G. *J. Am. Chem. Soc.* **2006,** *128*, 11463-11470.

15. Hymel, D.; Peterson, B. R., Synthetic cell surface receptors for delivery of therapeutics and probes. *Adv. Drug Deliv. Rev.* **2012,** *64*, 797-810.

16. Peterson, B. R., Synthetic mimics of mammalian cell surface receptors: prosthetic molecules that augment living cells. *Org. Biomol. Chem.* **2005,** *3*, 3607-3612.

17. Adams, M. R.; Konaniah, E.; Cash, J. G.; Hui, D. Y., Use of NBD-cholesterol to identify a minor but NPC1L1-independent cholesterol absorption pathway in mouse intestine. *Am. J. Physiol.-Gastroint. Liver Physiol.* **2011,** *300*, G164-G169.

18. Holtta-Vuori, M.; Uronen, R. L.; Repakova, J.; Salonen, E.; Vattulainen, I.; Panula, P.; Li, Z. G.; Bittman, R.; Ikonen, E., BODIPY-Cholesterol: A New Tool to Visualize Sterol Trafficking in Living Cells and Organisms. *Traffic* **2008,** *9*, 1839-1849.

19. Ishii, H.; Shimanouchi, T.; Umakoshi, H.; Walde, P.; Kuboi, R., Analysis of the 22-NBD-cholesterol transfer between liposome membranes and its relation to the intermembrane exchange of 25-hydroxycholesterol. *Colloid Surf. B-Biointerfaces* **2010,** *77*, 117-121.

20. Maxfield, F. R.; Wustner, D., Analysis of Cholesterol Trafficking with Fluorescent Probes. In *Lipids, Vol 108*, DiPaolo, G.; Wenk, M. R., Eds. Elsevier Academic Press Inc: San Diego, 2012; Vol. 108, pp 367-393.

21. Mukherjee, S.; Zha, X. H.; Tabas, I.; Maxfield, F. R., Cholesterol distribution in living cells: Fluorescence imaging using dehydroergosterol as a fluorescent cholesterol analog. *Biophys. J.* **1998,** *75*, 1915-1925.

22. Boonyarattanakalin, S.; Martin, S. E.; Dykstra, S. A.; Peterson, B. R., Synthetic mimics of small mammalian cell surface receptors. *J. Am. Chem. Soc.* **2004,** *126*, 16379-16386.

23. Mottram, L. F.; Boonyarattanakalin, S.; Kovel, R. E.; Peterson, B. R., The Pennsylvania green fluorophore: A hybrid of Oregon Green and Tokyo Green for the construction of hydrophobic and pH-insensitive molecular probes. *Org. Lett.* **2006,** *8*, 581-584.

24. Mallick, S.; Choi, J. S., Liposomes: Versatile and Biocompatible Nanovesicles for Efficient Biomolecules Delivery. *J. Nanosci. Nanotechnol.* **2014,** *14*, 755-765.

25. Torchilin, V. P., Recent advances with liposomes as pharmaceutical carriers. *Nat. Rev. Drug Discov.* **2005,** *4*, 145-160.

26. Schmaljohann, D., Thermo- and pH-responsive polymers in drug delivery. *Adv. Drug Deliv. Rev.* **2006,** *58*, 1655-1670.

27. Yoshida, T.; Lai, T. C.; Kwon, G. S.; Sako, K., pH- and ion-sensitive polymers for drug delivery. *Expert Opin. Drug Deliv.* **2013,** *10*, 1497-1513.

28. Gooding, M.; Browne, L. P.; Quinteiro, F. M.; Selwood, D. L., siRNA Delivery: From Lipids to Cell-penetrating Peptides and Their Mimics. *Chem. Biol. Drug Des.* **2012,** *80*, 787-809.

29. Nakase, I.; Akita, H.; Kogure, K.; Graslund, A.; Langel, U.; Harashima, H.; Futaki, S., Efficient Intracellular Delivery of Nucleic Acid Pharmaceuticals Using Cell-Penetrating Peptides. *Acc. Chem. Res.* **2012,** *45*, 1132-1139.

30. Sun, Q.; Cai, S.; Peterson, B. R., Selective disruption of early/recycling endosomes: Release of disulfide-linked cargo mediated by a *N*-alkyl-3β-cholesterylamine-capped peptide. *J. Am. Chem. Soc.* **2008,** *130*, 10064-10065.

31. Hirosue, S.; Weber, T., pH-dependent lytic peptides discovered by phage display. *Biochemistry* **2006,** *45*, 6476-6487.

32. Austin, C. D.; Wen, X. H.; Gazzard, L.; Nelson, C.; Scheller, R. H.; Scales, S. J., Oxidizing potential of endosomes and lysosomes limits intracellular cleavage of disulfide-based antibody-drug conjugates. *Proc. Natl. Acad. Sci. U. S. A.* **2005,** *102*, 17987-17992.

Chapter 2

Structure-Activity Relationships and Mechamism of Action Studies of Synthetic Mimics of Free Cholesterol

2.1 Introduction

Cholesterol plays a unique and critical role among the various lipids of mammalian cell membranes. It provides structural stability to a complex mixture of phospholipids containing both saturated and unsaturated fatty acids, while maintaining adequate fluidity to allow for biological processes such as endocytosis and mitosis to occur. As such, cells have evolved multiple mechanisms to acquire and transport cholesterol, as well as mechanisms to tightly regulate its concentration within membranes. Mammalian cells acquire the majority of their cholesterol through hydrolysis of cholesteryl esters. These esters are incorporated into lipoprotein particles such as low-density lipoprotein (LDL) that circulate through the bloodstream. The LDL receptor (LDLR) at the cell surface internalizes these particles via receptor-mediated endocytosis (RME) and the lipoproteins are delivered to the lysosome, where hydrolytic enzymes cleave the cholesteryl esters to release free cholesterol. The mechanism of LDL uptake via LDLR has been extensively studied and reviewed.[1] Free cholesterol is transported to and from the lysosomal membrane by the proteins Niemann-Pick C1 and C2 (NPC1/2).[2-5] From there, various cytosolic proteins are involved in

shuttling cholesterol to the plasma membrane and to various organelles, however these cellular processes are less understood.[6, 7]

Another mechanism by which cells acquire cholesterol involves the direct binding of free cholesterol by cell surface receptors such as Niemann-Pick C1 Like 1 protein (NPC1L1).[8-10] This receptor is mainly expressed in the liver and intestines and was shown to be the target for ezetimibe (**6**, Figure 2.2), an FDA-approved drug used to treat hypercholesterolemia.[11, 12] Ezetimibe, as well as its glucuronide metabolite, directly block the binding and uptake of dietary cholesterol in the intestinal epithelium. Figure 2.1 illustrates mechanisms by which cells can acquire exogenous cholesterol.

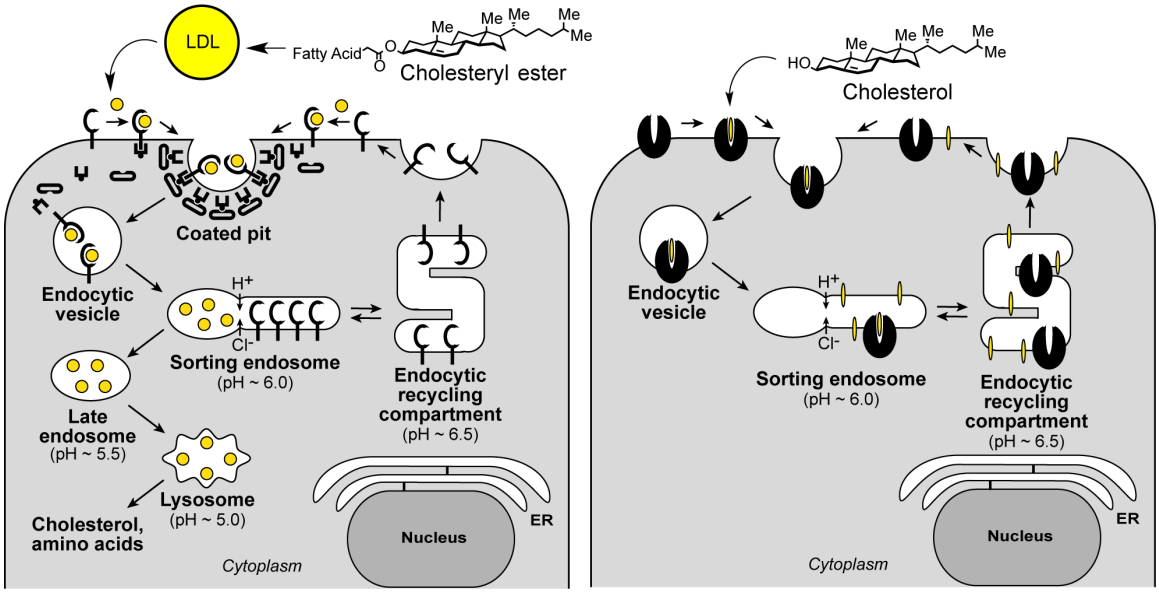

Figure 2.1. Schematic representation of two mechanisms of cellular cholesterol absorption. Cholesteryl esters are packaged into LDL and acquired via receptor-mediated endocytosis. Free cholesterol can directly bind cell surface receptors such as NPC1L1. This mechanism is inhibited in the intestine and liver by ezetimibe (**6**).

Derivatives of cholesterol have been used extensively as probes of cholesterol biology or as membrane targeting lipids for the delivery of macromolecules. Several fluorescent cholesterol analogues have been used to study cholesterol localization and trafficking, however their use has proven difficult since the addition of a fluorogenic moiety can dramatically change their biological properties.[13] The use of cholesterol conjugates, particularly cholesteryl carbamates, has shown success when applied to siRNA delivery[14], DNA transfection[15], and other cellular targeting applications.[16, 17] It has been shown that cellular uptake of these types of cholesterol conjugates is similar to cholesterol esters in that they require incorporation into lipoprotein particles for efficient delivery.[14] However, many of these conjugates fail to show appreciable activity under physiologically relevant conditions *in vivo*.

As mentioned in Chapter 1, previous research by the Peterson group on fluorescent *N*-alkyl-3β-cholesterylamines as synthetic mimics of cholesterol has shown that these compounds are avidly taken up by mammalian cells and engage in a trafficking pathway between the plasma membrane and early/recycling endosomes.[18-20] Several studies found that the design of the linker region between the cholesterylamine and fluorophore is critical to maintain high efficacy and trafficking properties. From these studies, it was shown that compounds containing one or two negatively charged glutamic acid residues in the linker region possessed high efficacy. Interestingly, subsequent experiments found that ezetimibe (**6**) inhibits the binding of cholesterylamines, exemplified by compound **1** (Figure 2.2), in living Jurkat lymphocytes. This finding that a non-

steroidal small molecule drug inhibits binding of these compounds provided strong evidence that the binding and uptake cholesterylamines is mediated by a cell-surface receptor.

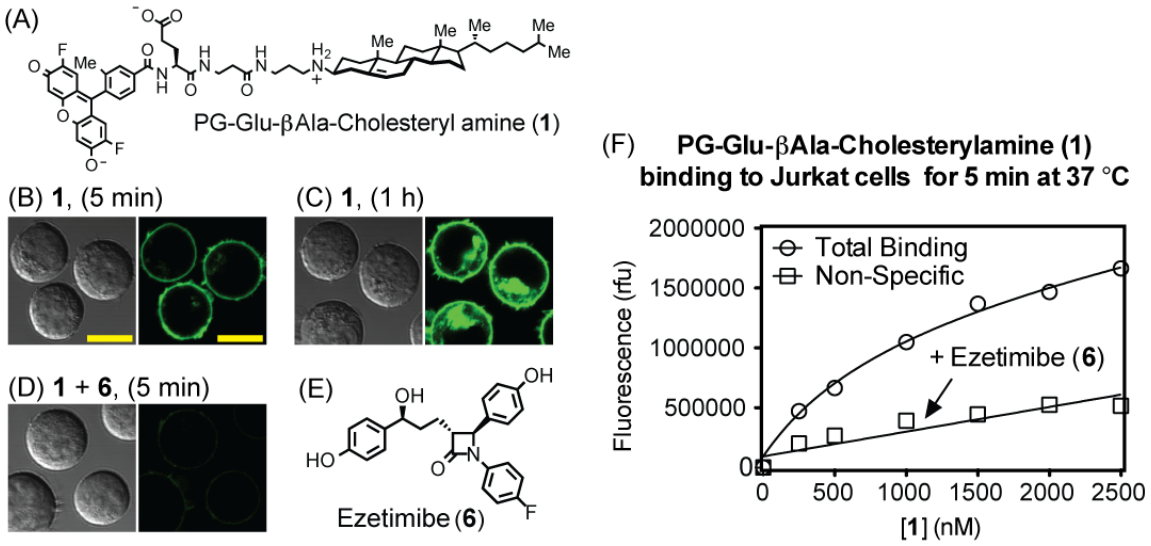

Figure 2.2. Cellular uptake of PG-Glu-βAla-cholesterylamine (**1**, Panel A) and inhibition by ezetimibe (**6**, Panel E). Panels B-D: Confocal fluorescence and DIC micrographs of Jurkat lymphocytes treated with **1** (2 μM) for 5 min (Panel B), 1 h (Panel C), and 5 min in the presence of **6** (200 μM, Panel D). Panel F: Saturation binding analysis of **1** in the presence and absence of **6** (200 μM). Scale bar = 10 μm.

I describe in this chapter the design and synthesis of novel fluorescent mimics of cholesterol to further probe the structure-activity relationships that dictate cellular binding. Furthermore, studies to further elucidate the mechanism of cellular uptake of fluorescent cholesterylamines, including efforts to identify the cell surface receptor responsible for the observed activity are reported.

2.2 Design and Synthesis of Fluorescent Mimics of Cholesterol

In order to probe the structure-activity relationships that govern the cellular uptake of fluorescent cholesterol mimics, we designed and synthesized a series of probes to systematically compare 1) the requirement of the negatively charged glutamic acid residue(s) in the linker region, 2) the requirement of the cationic *N*-alkyl-3β-cholesterylamine linkage, and 3) the specificity of the observed activity to cholesterol versus a structurally related sterol. Given that previous experiments suggested these compounds are bound by a cell-surface receptor, we hypothesized that the cationic secondary amino group of cholesterylamines might functionally mimic the 3β-hydroxyl group of cholesterol. In this way, cholesterylamines may demonstrate a cellular uptake mechanism similar to that of free cholesterol, whereas cholesteryl esters, carbamates and other related compounds undergo lipoprotein-mediated uptake. Figure 2.3 shows a series of fluorescent cholesterol analogues designed to probe this mechanism.

Since the majority of the compounds investigated contain a glutamic acid residue linked to the Pennsylvania green fluorophore, the syntheses of these compounds was simplified by precoupling amine-deprotected glutamic acid (**16**) to 4-carboxy Pennsylvania green NHS ester to produce compound **17** (Figure 2.4). Compound **17** could then be coupled to the deprotected amine of each precursor using EDC/HOBt peptide coupling conditions.

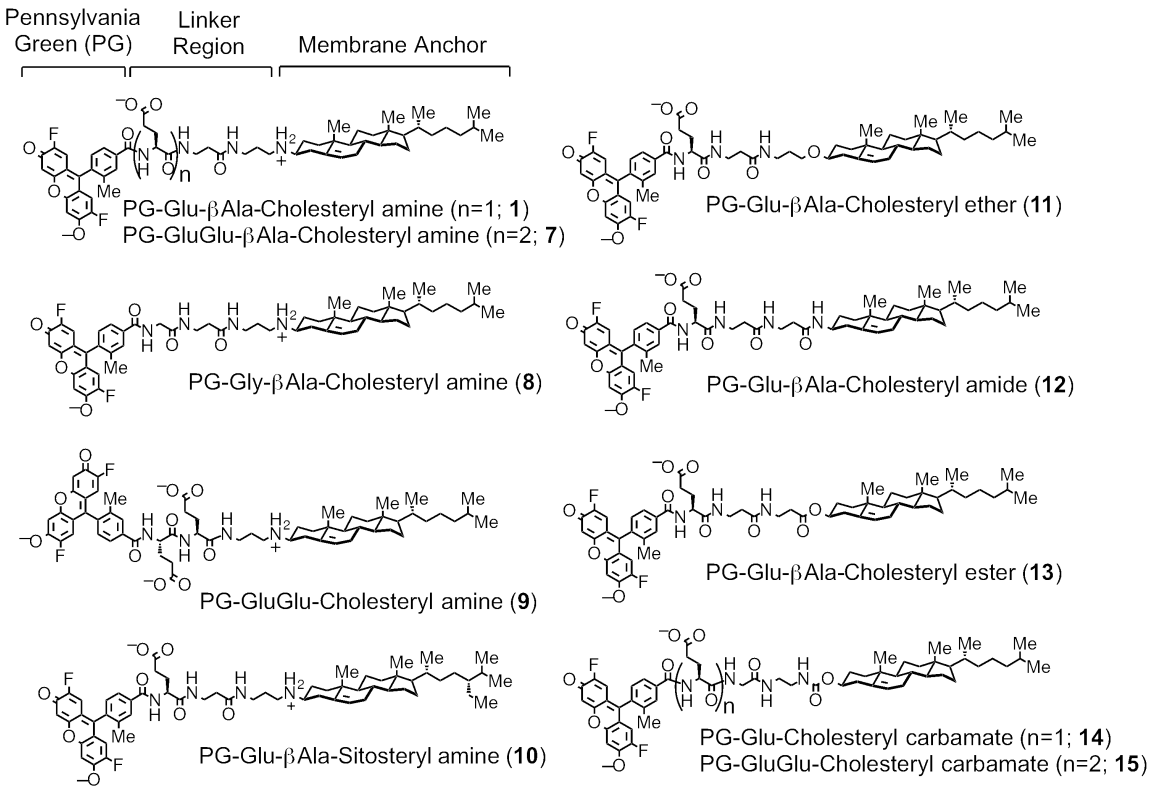

Figure 2.3. Structures of fluorescent *N*-alkyl-3β-cholesterylamines (**1**, **7** – **9**), *N*-alkyl-3β-sitosterylamine (**10**), cholesteryl ether (**11**), cholesteryl amide (**12**), cholesteryl ester (**13**), and cholesteryl carbamates (**14** – **15**).

To synthesize the *N*-alkyl-3β-cholesterylamine linked compounds **1** and **7** – **9**, the cholesterylamine precursor **18** was synthesized according to a previously described method.[21] Phthalimide deprotection with hydrazine afforded the primary amine in excellent yields. Standard Fmoc deprotection and EDC/HOBt peptide couplings with Fmoc protected glycine, β-alanine, or *tert*-butyl protected glutamic acid afforded the precursors **19** - **23**. Either the NHS ester of 4-carboxy-Pennsylvania green or compound **17** were coupled to the Fmoc deprotected precursors. The molecules were fully deprotected using TFA in dichloromethane

and purified by preparative reverse-phase HPLC (RP-HPLC). Compounds **1** and **7** – **9** were isolated as TFA salts.

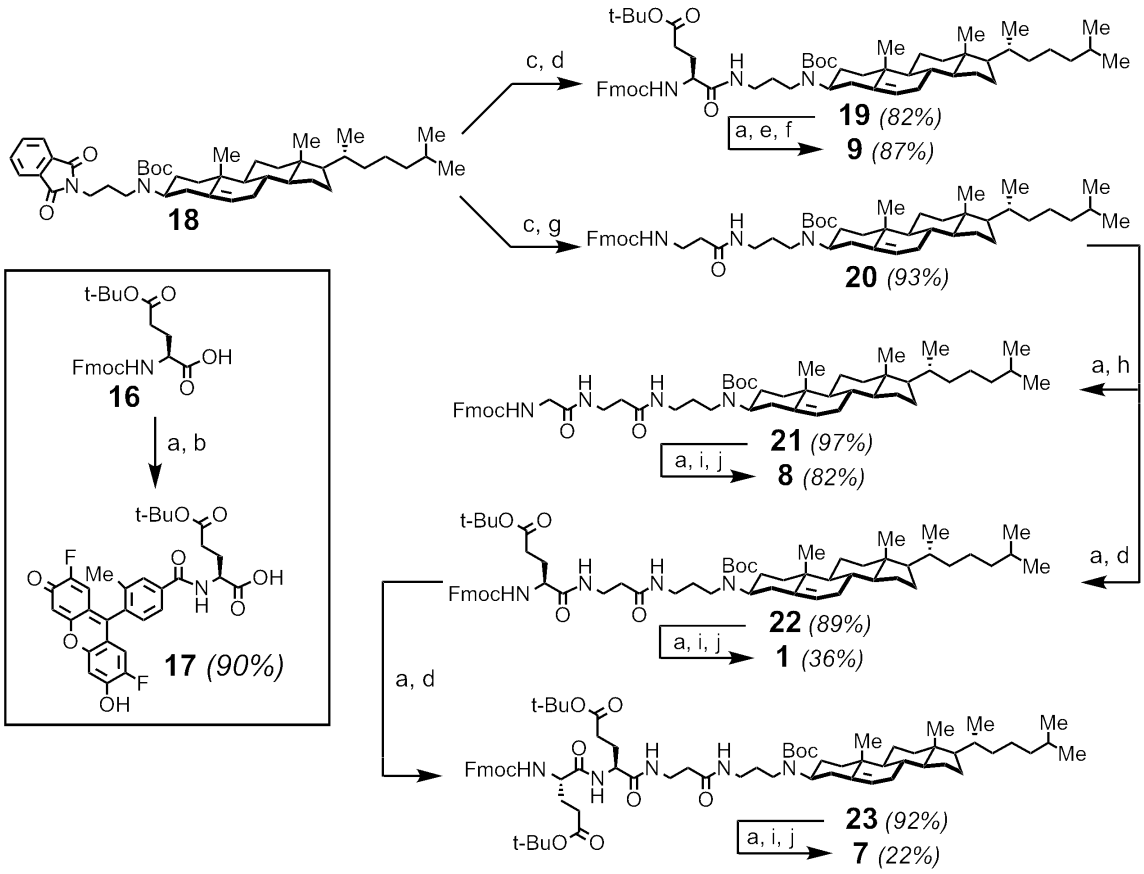

Figure 2.4. Synthesis of fluorescent *N*-alkyl-3β-cholesterylamines **1** and **7** – **9**. Reagents and conditions: (a) 20% piperidine, DMF, 30 min; (b) EDC, HOBt, 4 °C to 22 °C, 12 h; (c) H_2NNH_2, EtOH, 50°C, 4 h; (d) EDC, HOBt, Fmoc-Glu(O*t*-Bu)-OH, 4°C to 22°C, 12 h; (e) EDC, HOBt, **17**, DMF, 12 h; (f) 50% TFA, DCM, 2 h; (g) EDC, HOBt, Fmoc-β-Ala-OH, 4 °C to 22 °C, 12 h; (h) EDC, HOBt, Fmoc-Gly-OH, 4°C to 22°C, 12 h; (i) 4-carboxy Pennsylvania Green-NHS Ester, DIEA, DMF, 12 h; (j) 15% TFA, DCM, 12 h.

The *N*-alkyl-3β-sitosterylamine (**10**) was synthesized as shown in Figure 2.5 starting from β-sitosterol (**24**) using chemistry described for the synthesis of 3β-aminocholestene.[22] The 3β-hydroxyl group of sitosterol was converted to the mesylate (**25**) using mesyl chloride. Treatment with TMS-N_3 in the presence of BF_3•OEt_2 afforded 3β-sitostene (**26**) with retention of stereochemistry. Reduction

using LAH afforded the secondary amine **27**, followed by alkylation with 3-bromopropylphthalimide and Boc protection to afford the precursor **28**. Peptide coupling conditions using EDC/HOBt with Fmoc protected β-alanine provided compound **29**. Coupling to compound **17**, followed by deprotection with TFA and purification by preparative RP-HPLC afforded compound **10** as a TFA salt.

The cholesteryl ether **11** was synthesized from cholesterol as shown in Figure 2.5. The 3β-hydroxyl group of cholesterol was alkylated with acrylonitrile in the presence of KOH and 18-crown-6 followed by reduction to the primary amine **30** using $NaBH_4$ and $NiCl_2$ according to a literature procedure.[23] Peptide coupling conditions using EDC/HOBt with Fmoc-β-alanine gave compound **31**, followed by coupling to compound **17** to give the protected precursor to compound **11**. Deprotection of the *tert*-butyl ester protecting group with TFA and purification by preparative RP-HPLC provided compound **11**.

The cholesteryl amide (**12**) and ester (**13**) compounds were synthesized starting from 3β-aminocholestene (**32**) and cholesterol (**33**), respectively (Figure 2.5). In both cases, acylation was carried out using the acid chloride of Fmoc-β-alanine (**34**) to give compounds **35** and **36**. Peptide coupling conditions using EDC/HOBt with Fmoc-β-alanine afforded **37** and **38**, followed by coupling to compound **17** to provide the *tert*-butyl protected precursors. Deprotection with TFA and purification by preparative RP-HPLC afforded compounds **12** and **13**.

The cholesteryl carbamates **14** and **15** were synthesized from cholesteryl chloroformate (**39**). Treatment with excess ethylene diamine followed immediately by EDC/HOBt and Fmoc-glycine provided compound **40**.

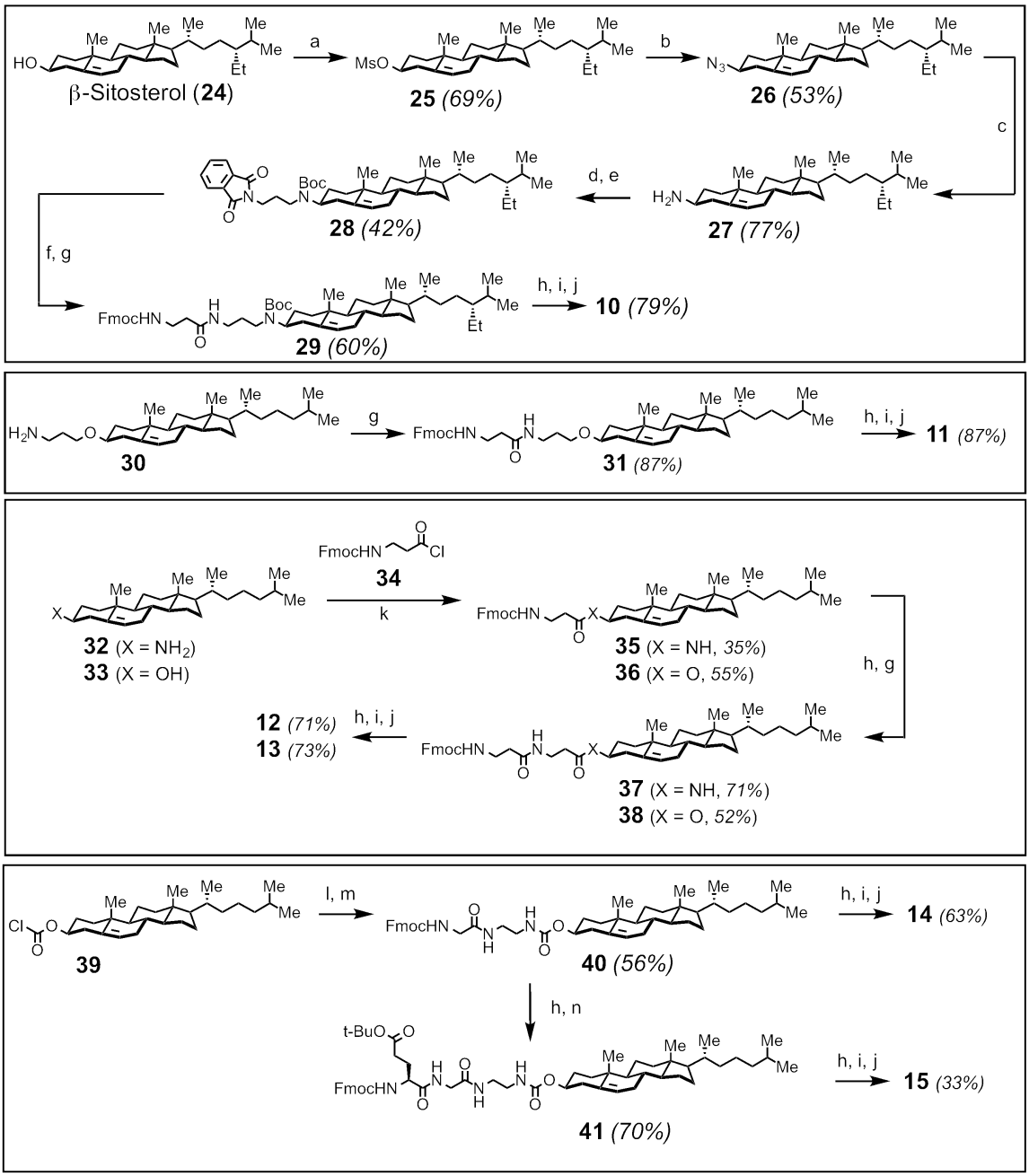

Figure 2.5. Synthesis of fluorescent cholesteryl conjugates **10** – **15**. Reagents and conditions: (a) MsCl, TEA, DCM, 4 °C to 22 °C, 16 h; (b) TMS-N_3, BF_3•OEt_2, DCM, 16 h; (c) $LiAlH_4$, Et_2O, DCM, 4 °C to 22 °C, 2h; (d) *N*-3-bromopropyl phthalimide, K_2CO_3, DMF, 60 °C, 24 h; (e) $(Boc)_2O$, DIEA, DCM, 4 h; (f) H_2NNH_2, EtOH, 50 °C, 4 h; (g) EDC, HOBt, Fmoc-β-Ala-OH, 4 °C to 22 °C, 12 h; (h) 20% piperidine, DMF, 30 min; (i) EDC, HOBt, **17**, DMF, 12 h; (j) 50% TFA, DCM, 2 h; (k) DMAP, DCM, 30 min; (l) Ethylene diamine, DCM, 2 h; (m) EDC, HOBt, Fmoc-Gly-OH, 4°C to 22°C, 12 h; (n) EDC, HOBt, Fmoc-Glu(O*t*-Bu)-OH.

Further coupling with compound **17** followed by deprotection of the *tert*-butyl ester with TFA and purification by RP-HPLC afforded compound **14**. Coupling of compound **40** with Fmoc-Glu(O*t*-Bu)-OH using EDC/HOBt gave compound **41**. Further coupling with compound **17** followed by deprotection with TFA and purification by RP-HPLC provided compound **15**.

2.3 Biological Evaluation of Fluorescent Cholesterol Mimics

To test the cellular uptake of fluorescent cholesterol mimics, confocal laser-scanning microscopy was used to analyze fluorescence intensity and cellular localization. In these experiments, Jurkat lymphocytes were treated for both 5 minutes and 1 hour with compounds **1** and **7** – **15** at 2 μM and 37 °C (Figure 2.6). Compounds containing the *N*-alkyl-cholesterylamine linkage showed significantly increased cellular uptake versus other linkages after only 5 minutes. At 1 hour, most of the probes showed visible uptake and similar cellular localization.

In order to generate quantitative data and accurately determine the structure-activity relationships, flow cytometry analysis was used to generate saturation binding data. In these experiments, Jurkat lymphocytes were treated with compounds **1** and **7** – **15** for 5 minutes at 37 °C in the absence and presence of excess of ezetimibe (200 μM) to block specific binding to the cell surface. The fluorescence values obtained from flow cytometry were normalized to fluorescent bead standards provided by Spherotech Inc. These beads provide a standard curve to convert raw fluorescence values to molecular equivalents of

fluorescein (MEFL). Given the similarities in structure and fluorescence properties between fluorescein and Pennsylvania green, this allows for the accurate measurement of the number of fluorescent probe molecules bound to each individual cell.

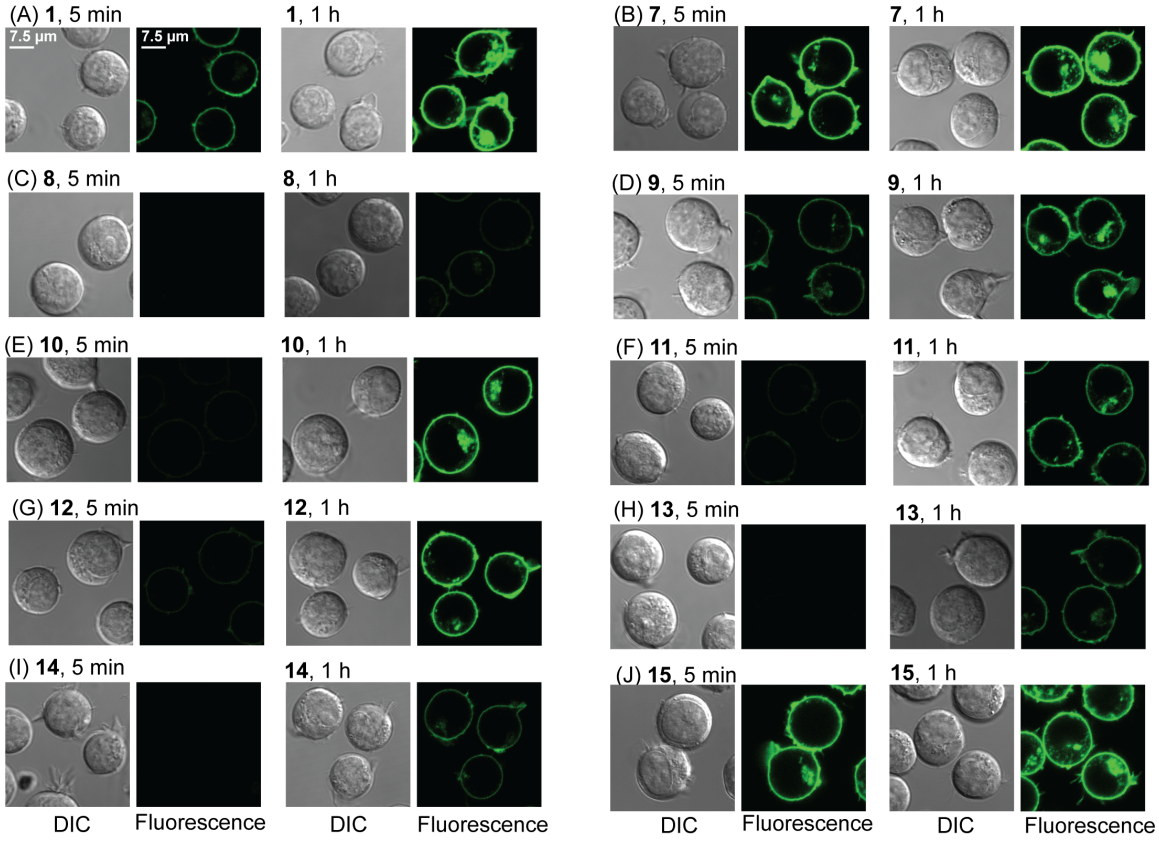

Figure 2.6. Confocal laser scanning and DIC micrographs of Jurkat lymphocytes treated with **1** and **7** – **15** (2 µM) for 5 min and 1 h at 37 °C.

Using both the total and non-specific binding data versus concentration (Figure 2.7), analysis for specific binding was performed using the 'one-site – specific binding' model in GraphPad Prism 5. This allows for the quantification of binding affinity (as an apparent dissociation constant, $K_{d,\ app}$) and efficacy (as maximum binding, B_{MAX}). The results of this analysis are shown in Figure 2.8 and Table 2.1.

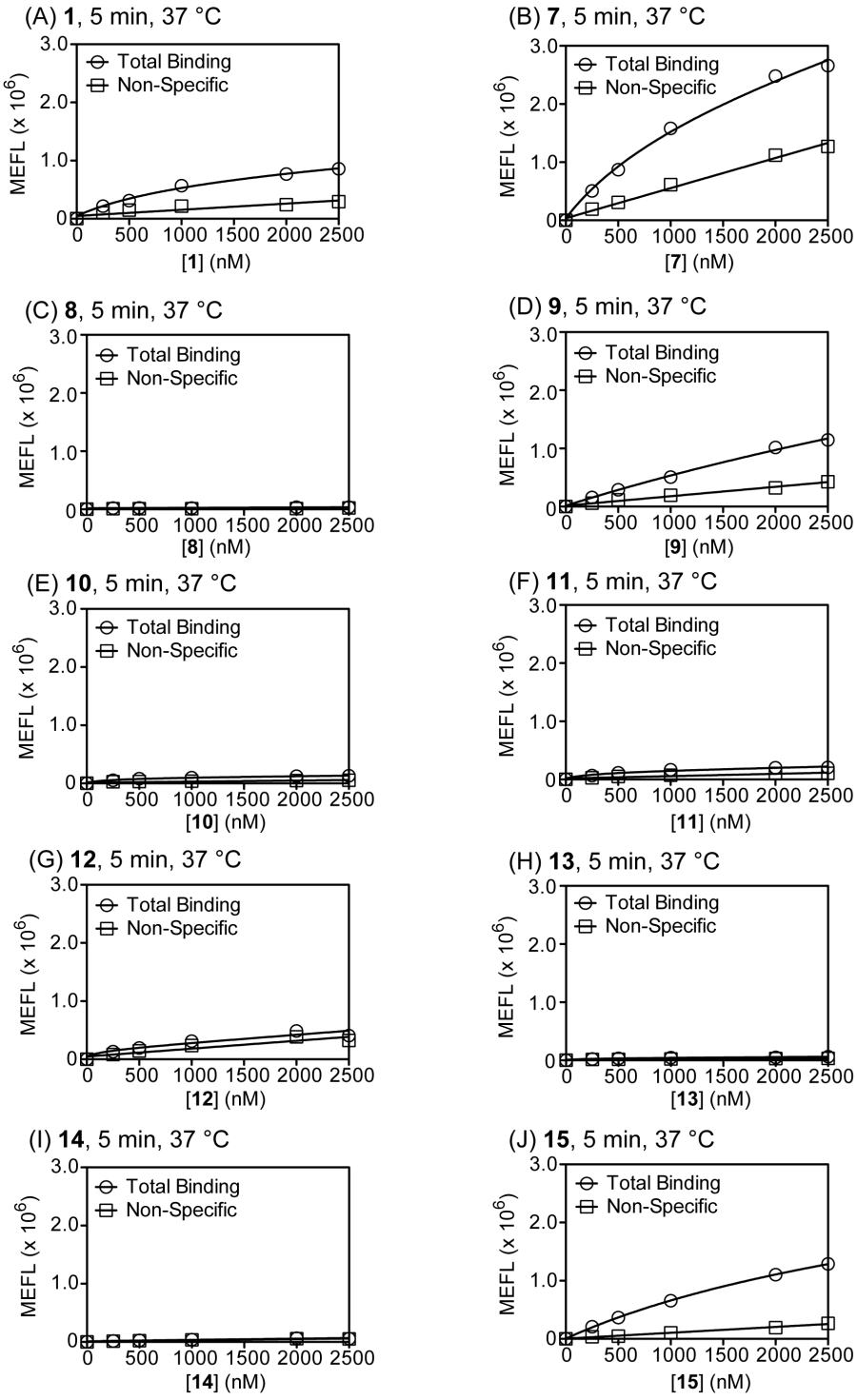

Figure 2.7. Saturation binding analysis of **1** and **7** – **15** in Jurkat lymphocytes. Cells were treated with each compound at 37 °C for 5 min in the absence and presence of ezetimibe (**6**, 200 μM) to determine non-specific binding, washed, and analyzed by flow cytometry. Fluorescence values expressed as molecular equivalents of fluorescein (MEFL).

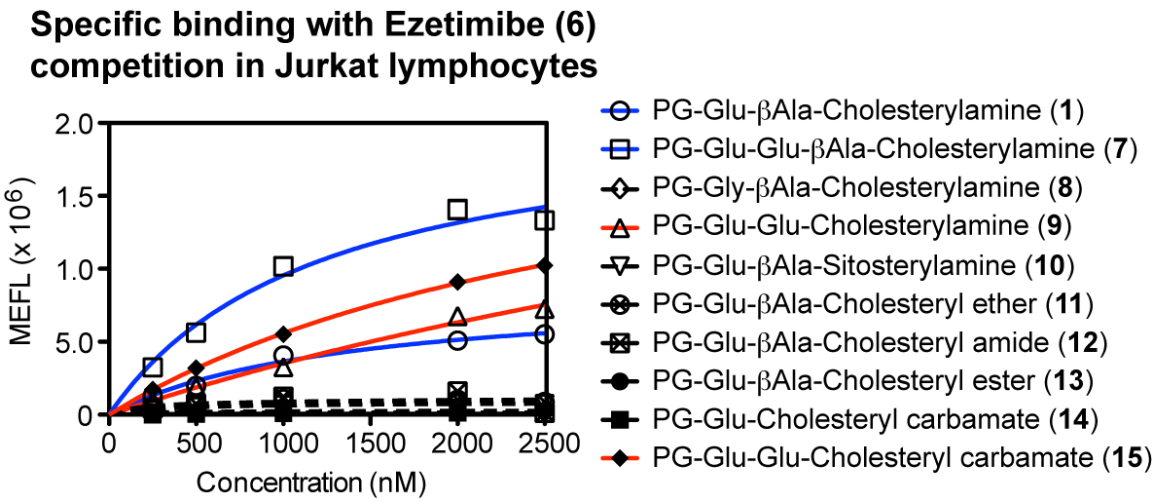

Figure 2.8. Specific binding of **1** and **7** – **15** to Jurkat lymphocytes treated for 5 min at 37 °C in the absence and presence of ezetimibe (**6**, 200 μM) and analyzed by flow cytometry. The linear non-specific binding component was subtracted from the total binding data and analyzed using the 'One site – specific binding' model in GraphPad Prism 5.

	Structure	K_d, app (μM)	B_{MAX} (MEFL x 10^6)
1	PG-Glu-βAla-Cholesterylamine	1.38 ± 0.45	0.86 ± 0.13
7	PG-Glu-Glu-βAla-Cholesterylamine	1.22 ± 0.24	2.12 ± 0.18
8	PG-Gly-βAla-Cholesterylamine	NC [a]	NC [a]
9	PG-Glu-Glu-Cholesterylamine	7.68 ± 4.09	3.12 ± 1.29
10	PG-Glu-βAla-Sitosterylamine	NC [a]	NC [a]
11	PG-Glu-βAla-Cholesteryl ether	NC [a]	NC [a]
12	PG-Glu-βAla-Cholesteryl amide	NC [a]	NC [a]
13	PG-Glu-βAla-Cholesteryl ester	NC [a]	NC [a]
14	PG-Glu-Gly-Cholesteryl carbamate	NC [a]	NC [a]
15	PG-Glu-Glu-Gly-Cholesteryl carbamate	3.18 ± 0.61	2.34 ± 0.28

Table 2.1. Affinity and efficacy of cellular binding for compounds **1** and **7** – **15** based on specific binding analysis in Jurkat lymphocytes with ezetimibe (**6**, 200 μM) competition. Affinity expressed as apparent K_d (μM) and efficacy expressed as maximum binding (B_{MAX}, in MEFL). [a] NC = Not calculated due to lack of efficacy and poor fit of the data to the one-site binding model.

Saturation binding analysis supported the original hypothesis that both the *N*-alkyl-3β-cholesterylamine linkage and one or two anionic glutamic acid residues in the linker region are critical for activity. Compounds **1** and **7** containing one and two glutamic acid residues respectively showed the highest affinity and efficacy of the series. Comparison of compound **1** with compound **8**, which substitutes glycine for glutamic acid, shows the dramatic loss of cellular binding that occurs when the anionic charge is removed from the linker region. Compounds **11** – **14**, which replace the *N*-alkyl-3β-cholesterylamine with various neutral linkages, showed very low activity, supporting the hypothesis that the cationic amine moiety is a functional mimic of free cholesterol that allows for rapid binding and cellular uptake at the cell surface. Linkages such as the cholesteryl amide, ether, and carbamate likely engage in a much slower lipoprotein-mediated cellular uptake mechanism. Interestingly, the addition of a second glutamic acid residue to the cholesteryl carbamate compound **15** was able to rescue the activity, further elaborating on the importance of anionic residues in the linker.

Compound **10** was used to probe the specificity of cellular binding and uptake. This compound utilizes sitosterol, a phytosterol bearing an ethyl substituent at the C-24 position, as its sterol membrane anchor. Remarkably, this compound shows a dramatic decrease in activity when compared to compound **1**. This illustrates a high degree of specificity that mammalian cells possess for incorporating cholesterol into their membranes versus other closely related sterols.

2.4 Kinetic Analysis of Uptake of Fluorescent Cholesterol Analogues

In order to further investigate the mechanism by which fluorescent cholesterol analogues are incorporated into the plasma membrane, more detailed flow cytometry analysis was conducted on a subset of the compounds from the previous series. It was unclear based on the previous data whether the observed activity was due to saturable binding at a cell surface receptor or kinetic uptake occurring via an active transport mechanism at the plasma membrane. Given the high efficacy and rapid binding activity, with 0.5 – 1.5 x 10^6 molecules bound per cell after 5 minutes, we hypothesized that an unknown protein at the cell surface may be actively transporting these cholesterol mimics into the plasma membrane. To test this, we performed time-dependent flow cytometry experiments to compare compounds **1**, **7**, **10**, and **15** (Figure 2.9). Analysis of the results using the Michaelis-Menten model of kinetics provided evidence that a catalytic process was occurring to actively insert these fluorescent probes into the plasma membrane.

Michaelis-Menten kinetic analysis allows for an alternative determination of binding affinity (as K_M) and also provides information about the rate of enzymatic turnover (as V_{MAX}, Table 2.2). This analysis reveals a highly efficient mechanism of cellular uptake of the most active molecules, with 1.8 – 5.0 x 10^5 molecules incorporated into the plasma membrane per minute per cell (Table 2.2). Comparison of compounds **1** and **7** further illustrates the importance of the negative charge in the linker, with an approximate 3-fold increase in V_{MAX} observed for compound **7**, which contains two glutamic acid residues.

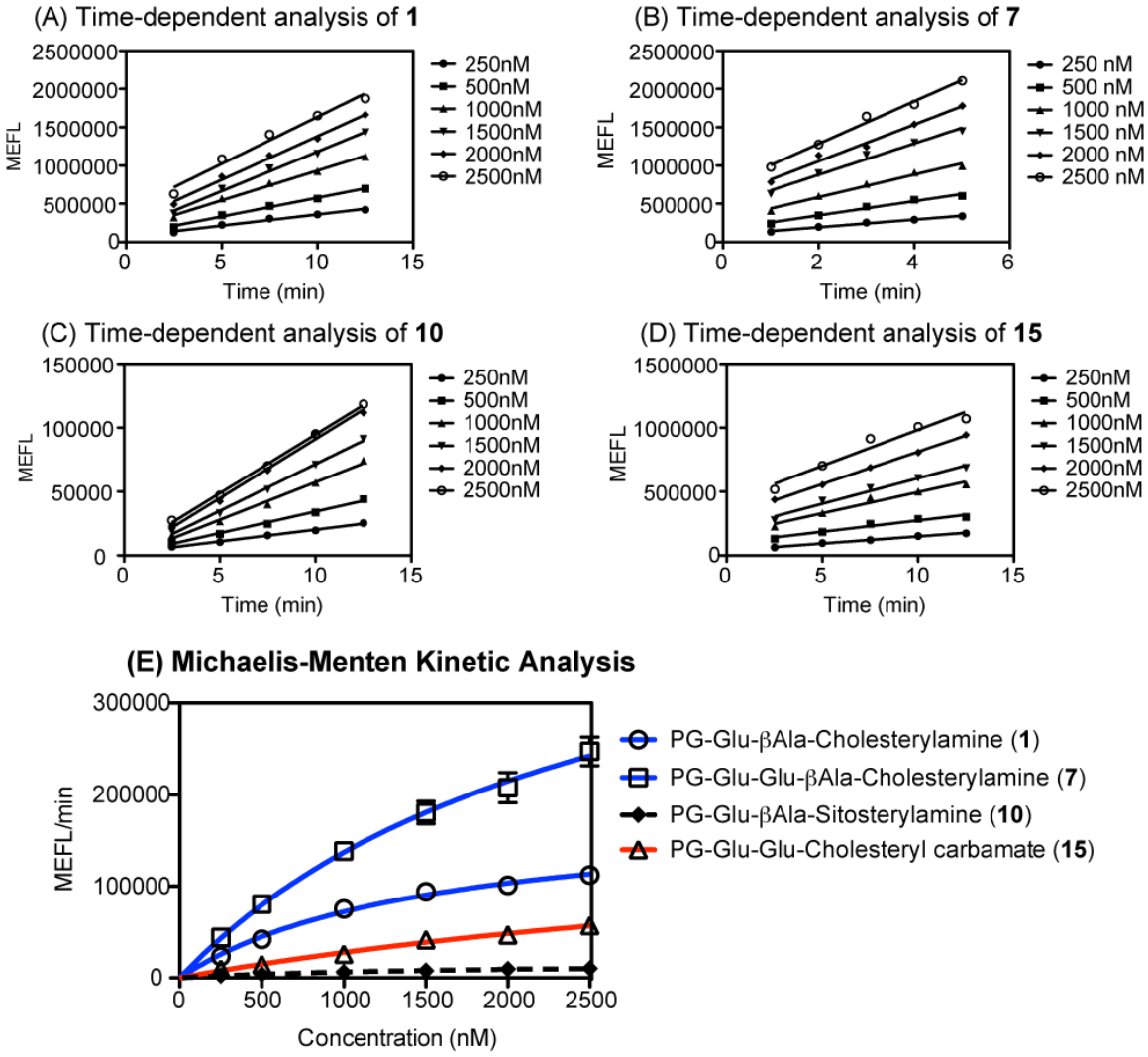

Figure 2.9. Kinetic analysis of cellular uptake of compounds **1**, **7**, **10**, and **15** in Jurkat lymphocytes by flow cytometry. Panels A – D: Representative data for the time-dependent analysis of each compound. Experiments were performed in triplicate at 22 °C in the presence of media containing 10% serum. Linear regression analysis provided the slope (MEFL/min) at each concentration. Panel E: Michaelis-Menton analysis of cellular uptake. MEFL/min at each concentration averaged from three independent experiments and plotted versus concentration. Analysis by non-linear regression using the 'Michaelis-Menten' model in GraphPad Prism 5 provided K_M and V_{MAX} values.

	Structure	K_M (μM)	V_{MAX} (MEFL/min x 10^5)
1	PG-Glu-βAla-Cholesterylamine	1.53 ± 0.34	1.83 ± 0.20
7	PG-Glu-Glu-βAla-Cholesterylamine	2.62 ± 0.70	4.97 ± 0.80
10	PG-Glu-βAla-Sitosterylamine	1.65 ± 0.52	0.17 ± 0.03
15	PG-Glu-Glu-Cholesteryl carbamate	5.75 ± 2.23	1.87 ± 0.54

Table 2.2. Binding affinity (K_M) and V_{MAX} of compounds **1**, **7**, **10**, and **15** based on Michaelis-Menten analysis of cellular uptake in Jurkat lymphocytes. Experiments were performed at 22 °C in the presence of media containing 10% serum. Values represent the mean and SEM from three independent experiments.

Once again, the experimental data shows the remarkable selectivity of this mechanism to cholesterol, with a 10- to 30-fold loss in V_{MAX} observed for the sitosterol analogue **10** versus **1** and **7**, respectively. The cholesteryl carbamate **15** illustrates the importance of the cationic amine linkage, with a >2-fold loss in both affinity and efficacy when compared to the cholesterylamine **10**. However, it is worth noting that the additional negative charge in the linker allows for efficient uptake of **15** to occur, with a V_{MAX} value similar to that of compound **1**. This result proved rather useful in the application of these cholesterol mimics to other ongoing projects in the Peterson lab, since cholesteryl carbamates can be prepared more easily than cholesterylamines.

2.5 Target Identification Studies

2.5.1 Niemann-Pick C1-Like 1 Protein (NPC1L1)

In order to identify the putative protein target responsible for binding of fluorescent cholesterylamines to the cell surface, we characterized the inhibition of cholesterylamine **1** by small molecules. Based on the inhibition of cellular

uptake by ezetimibe (**6**), we turned our attention to Niemann-Pick C1-Like 1 protein (NPC1L1) as a possible target. It is reported in the literature that the glucuronide metabolite of ezetimibe (**42**) shows greater potency compared with the parent drug toward blocking the intestinal uptake of free cholesterol by NPC1L1. Using a published route[24], ezetimibe glucuronide (**42**) was synthesized and tested for inhibition of uptake of compound **1**.

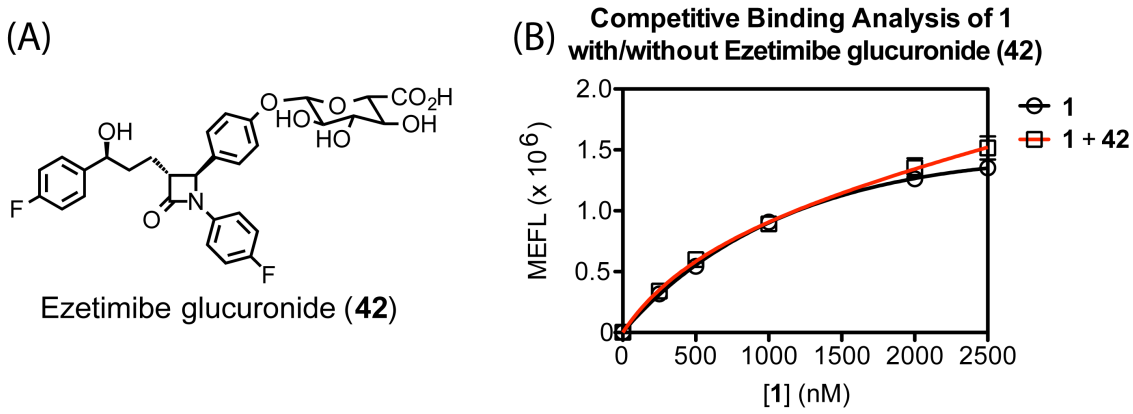

Figure 2.10. Panel A: Structure of ezetimibe glucuronide (**42**). Panel B: Competitive binding analysis of **1** in the absence and presence of **42** (200 μM). Jurkat lymphocytes were pre-incubated with **42** for 30 min at 37 °C, then treated with **1** for 5 min at 37 °C. Analysis performed by flow cytometry in triplicate and fit to the 'One site – total binding' model in GraphPad Prism 5.

Based on the competitive binding analysis, ezetimibe glucuronide (**42**) showed no inhibition of cellular uptake of **1**. This result was in agreement with a literature survey of NPC1L1, which suggested that expression of this protein was mainly restricted to the liver and intestines.[9, 25] Since the uptake of cholesterylamines is observed in nearly all mammalian cell types regardless of the tissue of origin, these results indicated that NPC1L1, the primary target of ezetimibe, is not responsible for the observed activity.

2.5.2 Scavenger Receptor B1 (SR-B1)

Ezetimibe has been reported to bind and inhibit other proteins including scavenger receptor B1 (SR-B1).[25-27] This protein is a cell surface receptor involved in transport of cholesteryl esters to and from high-density lipoprotein (HDL).[28] Previous work in the Peterson group found that BLT-4 (**43**, Figure 2.13), a small molecule inhibitor of SR-B1, also inhibited uptake of cholesterylamines. This napthylurea-based compound was identified in a high-throughput screen to inhibit uptake of cholesterol from HDL by SR-B1.[29] Several analogues of BLT-4 were synthesized by a former group member (Paul Munson) and showed inhibitory potencies similar to Ezetimibe. With this in mind, we began to investigate SR-B1 as a possible target. This cell surface protein is constitutively expressed in nearly all mammalian cell types and is relatively well studied as a cholesterol transport protein. Two experiments were performed to test this hypothesis using flow cytometry to measure uptake of cholesterylamine **1**. The first experiment involved transient overexpression of human SR-B1 (hSR-B1) in HEK-293 cells using expression vectors published by the Sahoo lab at the Medical College of Wisconsin.[30] Cells transfected with the plasmid expressing hSR-B1 were compared to non- transfected and empty vector controls, as well as two plasmids that express non-functional mutant forms of hSR-B1 (hSR-B1_S112F and hSR-B1_T175A).

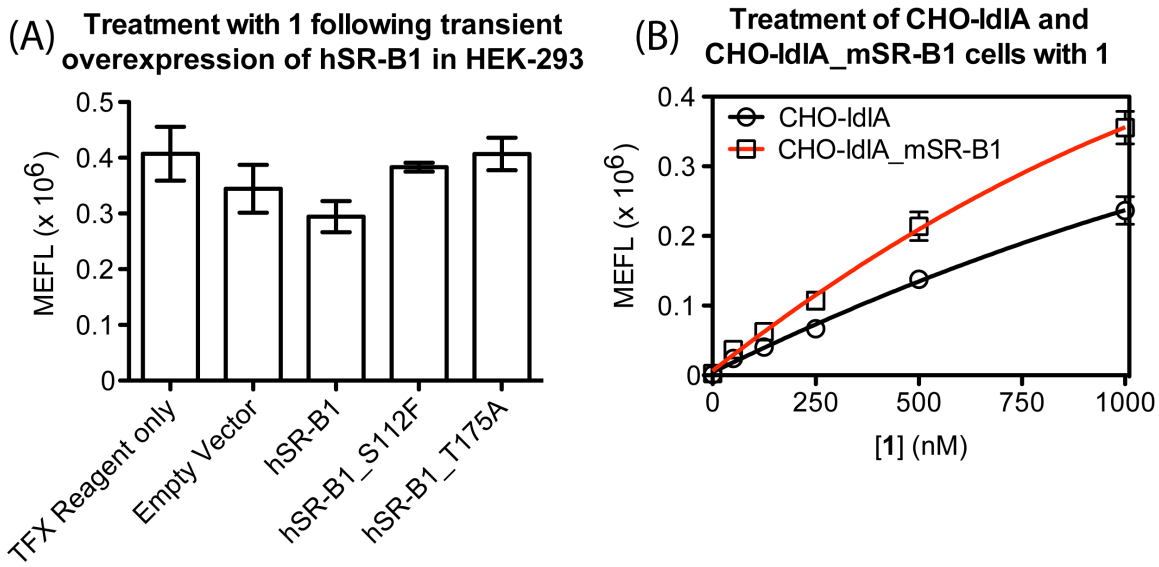

Figure 2.11. Investigation of SR-B1 as the cell surface target of cholesterylamines. Panel A: Cellular uptake of **1** following transient overexpression of HEK-293 cells with plasmids coding for human SR-B1 and two non-functional mutants. Transient expression was allowed to proceed for 48 h and cells were treated with **1** (100 nM) for 5 minutes at 37 °C. Analysis performed by flow cytometry in duplicate. Panel B: Cellular uptake of **1** by CHO-ldlA_mSR-B1 cells that stably overexpress mouse SR-B1. Cells were treated with **1** for 5 minutes at 37 °C. Analysis was performed by flow cytometry in duplicate and compared to the non-transfected control cell line. Data was fit to the 'One site – total binding' model of GraphPad Prism 5.

The second experiment involved CHO-ldlA cells that have been modified to knockdown expression of the LDL receptor. This cell line has been stably transfected with mouse SR-B1 (mSR-B1) to produce CHO-ldlA_mSR-B1 cells that overexpress mSR-B1.[28] The Krieger lab at MIT kindly provided these two cell lines for use in this experiment. Cellular uptake analysis with compound **1** was performed with CHO-ldlA_mSR-B1 cells and compared to non-transfected cells as a negative control.

As shown in Figure 2.11, HEK-293 cells transfected with hSR-B1 showed no increase in uptake of cholesterylamine **1** compared to empty vector and non-functional mutant controls. The CHO-ldlA_mSR-B1 cells showed a slight

increase in cellular uptake of ~30 – 40% compared to non-transfected CHO-ldlA cells. However this modest increase in activity does not correlate well with published results from the Krieger lab, in which cells overexpressing mSR-B1 demonstrated a >5-fold increase in HDL binding and a >10-fold increase in uptake of cholesteryl esters (measured by radioligand binding assays). Based on our results using experimental methods that are validated to upregulate SR-B1 activity, we concluded that SR-B1 was not likely to be responsible for the uptake of cholesterylamines.

2.5.3 Proteomics-Based Target Identification

Since two known targets of two small molecule inhibitors did not appear to be responsible for the uptake of cholesterylamines, we shifted to a proteomics-based screening approach to attempt to identify the target protein. In this approach, a small molecule photoaffinity probe containing a purification handle is used to bind the protein of interest. Irradiation with ultraviolet light generates a highly reactive intermediate, which forms a covalent bond with an active site residue of the target protein. Following cell lysis, the crosslinked protein is enriched using the purification handle and identified using MS/MS sequencing analysis of trypsin-digested peptides (Figure 2.12). Based on known structure-activity relationships of the BLT-4 scaffold, we designed and synthesized compounds **47** and **49** as photoaffinity labels. These compounds contain a phenylazide moiety as a photocrosslinker. Compound **47** contains a terminal alkyne, allowing target enrichment using click chemistry with azide-functionalized

biotin and immobilized streptavidin, whereas **49**, which lacks this purification handle, is used as a competitive binding control. The synthesis of these compounds is shown in Figure 2.13.

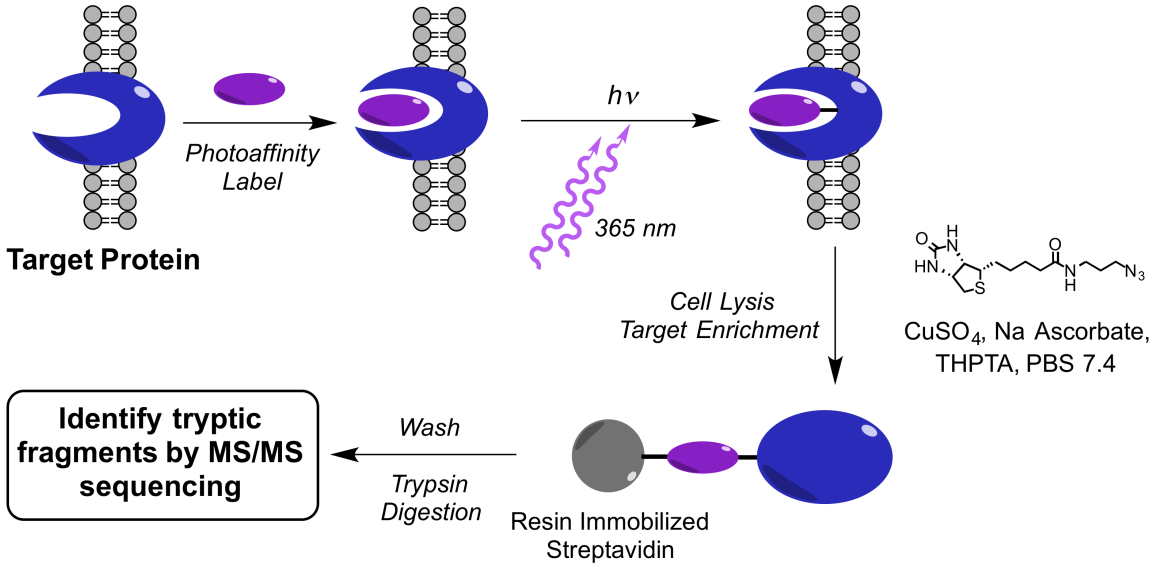

Figure 2.12. Schematic representation of a protein pull-down assay using a photoaffinity label for target identification.

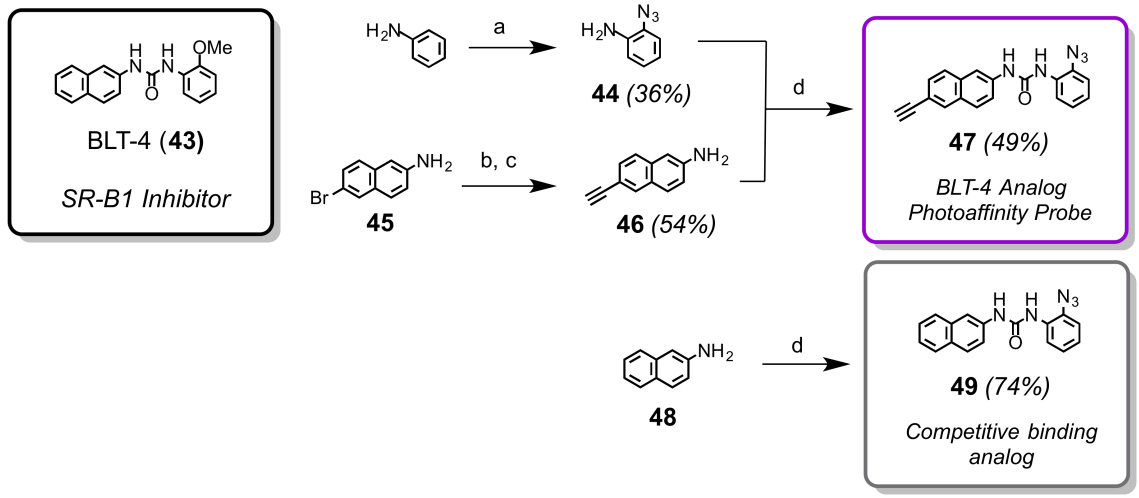

Figure 2.13. Synthesis of the BLT-4 analogue photoaffinity probe **47** and binding competitor **49**. Reagents and Conditions: (a) TMS-N_3, CuBr, TBHP, MeCN, 3 h; (b) TMS-Acetylene, $PdCl_2(PPh_3)_2$, CuI, TEA, 80 °C, 16 h; (c) 0.1 M aq. KOH, MeOH, 3 h; (d) **44**, Triphosgene, DCM, 3 h.

Compounds **47** and **49** were tested using flow cytometry with competitive binding analysis and found to be inhibitors of uptake of cholesterylamine **1** (Figure 2.14, Panel C). Interestingly, compound **47** (at 25 μM) showed better inhibition than Ezetimibe (at 200 μM), indicating that it is a relatively good inhibitor of the target protein. Based on this result, target identification experiments were performed using the protein pull-down assay described in Figure 2.12.

As a preliminary experiment, Jurkat lymphocytes were treated with photoaffinity probe **47** (10 μM, 1 h) in the presence and absence of compound **49** (100 μM) as a competitive inhibitor, then irradiated with 365 nm light for 5 minutes. The cells were washed and lysed using brief ultra-sonication and the membrane protein fraction was separated from the cytosolic fraction using centrifugation. The crosslinked membrane proteins were enriched from the resulting cell lysates and analyzed by SDS-PAGE with silver staining. As shown in Figure 2.14 (Panel D), a protein band was observed at ~80 kDa that did not appear in either the untreated or competitive knockdown conditions, indicating a specific interaction and possible protein target.

The experiment was repeated and the resulting enriched protein samples were subjected to on-bead trypsin digestion and submitted to the KU Analytical Proteomics Laboratory (APL) for sequencing analysis. Unfortunately, despite several attempts, the experimental procedure did not provide a strong enough signal-to-noise ratio to observe any specific proteins compared to untreated and competitive-binding controls. Furthermore, the protein band at ~80 kDa observed

in the SDS-PAGE analysis is consistent with the molecular weight of glycosylated human SR-B1 (~82 kDa).[30] Since human SR-B1 is a known target of the naphthylurea-based BLT analogues, we would expect to observe this protein in a pulldown experiment using a BLT-based photoaffinity probe. However, since SR-B1 was previously determined to be an unlikely target and no other proteins were observed by SDS-PAGE or MS/MS analyses, we are currently focused on new approaches to identify the protein responsible for uptake of cholesterylamines.

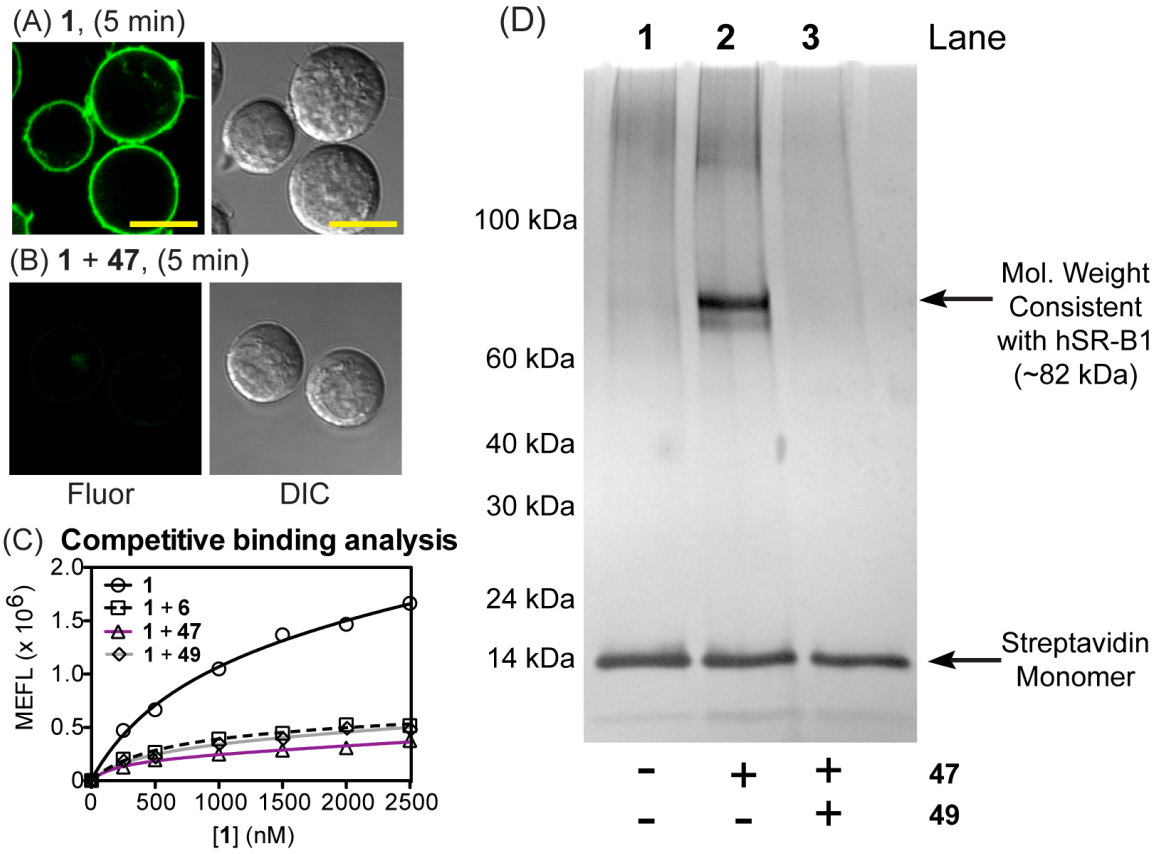

Figure 2.14. Panels A – B: Confocal laser scanning and DIC micrographs of Jurkat lymphocytes treated with **1** (2 μM) in the absence and presence of **47** (25 μM). Scale bar = 10 μm. Panel C: Competitive binding analysis of **1** in Jurkat lymphocytes in the absence and presence of ezetimibe (**6**, 200 μM), **47** (25 μM), or **49** (100 μM). Analysis by flow cytometry and fit to a non-linear regression. Panel D: Protein pulldown assay using Jurkat lymphocytes and SDS-PAGE analysis with silver staining. Lane 1: untreated control; Lane 2: **47** (10 μM); Lane 3: co-treatment of **47** (10 μM) with **49** (100 μM) as a binding competitor.

2.6 Conclusions

We designed and synthesized a series of fluorescent cholesterol mimics to probe structure-activity relationships that govern uptake by mammalian cells. Compounds possessing an *N*-alkyl-3β-cholesterylamine and a cholesteryl carbamate bearing a negatively charged linker showed highly efficient cellular uptake. Evidence from competitive binding and kinetic experiments suggests that uptake occurs via a receptor-mediated process at the plasma membrane. In this way, these compounds appear to function as mimics of free cholesterol since their uptake does not require lipoprotein or receptor-mediated endocytosis. Target identification studies were performed, but have not identified a cell surface protein responsible for the observed activity. Other target identification approaches are still being actively pursued in the Peterson lab. Because of the structural and functional similarities between cholesterylamines and free cholesterol, this unknown cell surface receptor may play a key role in the cellular uptake of cholesterol and/or charged cholesterol metabolites.

2.7 Experimental Section

2.7.1 General

Chemical reagents were purchased from Apptec, Acros, Aldrich, Alfa Aesar, EMD Biosciences, or TCI America, and were used without further purification. Solvents were from Aldrich or Fisher Scientific. Ezetimibe (Zetia®), obtained from a local pharmacy, was isolated in pure form by extraction of crushed tablets from ddH_2O with DCM, drying the organic layer over anhydrous

Na_2SO_4, and removal of solvent under vacuum. Biotin-azide was commercially available from TCI America. 3β-Amino-5-cholestene (**32**)[22], cholesteryl-oxypropan-1-amine (**30**)[23], 4-carboxy-Pennsylvania green NHS ester[31, 32], **18**[21], **19**[21], ezetimibe glucuronide (**42**)[24], and **44**[33] were synthesized by previously reported methods. Anhydrous solvents were obtained after passage through a drying column of a solvent purification system from GlassContour/SG Waters (Nashua, NH). All reactions were performed under an atmosphere of dry argon or nitrogen. Reactions were monitored by analytical thin-layer chromatography on plates coated with 0.25 mm silica gel 60 F254 (EMD Biosciences). TLC plates were visualized by UV irradiation (254 nm) or stained with either phosphomolybdic acid (20%) in ethanol or ninhydrin in ethanol. Column chromatography employed Silica Gel (SiliCycle, 40-63 μm). Preparative HPLC employed an Agilent 1200 Series preparative pump / gradient extension with a Hamilton PRP-1 (polystyrene-divinylbenzene) reverse-phase preparative column (10-12 μm particle size, 21.5 mm x 25 cm) with a flow rate of 25.0 mL/min. Melting points were measured with a Thomas Hoover capillary melting point apparatus and are uncorrected. Infrared spectra were obtained with a Perkin Elmer Spectrum 100 FTIR. NMR spectra were obtained with a Bruker Avance-400 or DRX-500 instrument with chemical shifts reported in parts per million (ppm, δ) referenced to either $CDCl_3$ (^1H, 7.26 ppm; ^{13}C, 77.16 ppm), CD_3OD (^1H, 3.34 ppm; ^{13}C, 49.00 ppm), or $(CD_3)_2SO$ (^1H, 2.50 ppm; ^{13}C, 128.06 ppm). High-resolution mass spectra were obtained at the University of Kansas Mass

Spectrometry Facility (ESI and EI). Peaks are reported as *m/z*. Basic compounds purified by reverse-phase HPLC were isolated as trifluoroacetic acid salts.

2.7.2 Synthetic Procedures and Compound Characterization Data

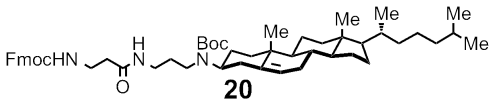

20

9*H*-Fluoren-9-ylmethyl(3-((3-((*tert*-butoxycarbonyl)(3β-cholest-5-en-3-yl)amino)propyl)amino)-3-oxopropyl) carbamate (**20**). To a solution of **18** (1.41 g, 2.1 mmol) in absolute ethanol (50 mL) was added anhydrous hydrazine (350 µL, 11 mmol). The solution was heated to 50 °C and stirred for 4 h. The reaction was cooled to 22 °C, and a white precipitate was removed by filtration. The filtrate was concentrated under vacuum, and the residue was dissolved in chloroform (100 mL). After insoluble material was removed by filtration, concentration of the filtrate under vacuum afforded the phthalimide-deprotected primary amine (1.13 g, 99%), a white solid that was carried forward without further purification. To Fmoc-β-Ala-OH (715 mg, 2.3 mmol) in anhydrous DCM (50 mL) at 4 °C was added hydroxybenzotriazole (HOBt, 340 mg, 2.5 mmol) and 1-ethyl-3-(3-dimethylaminopropyl) carbodiimide (EDC, 480 mg, 2.5 mmol). This mixture was stirred at 4 °C for 30 min. The phthalimide-deprotected primary amine in anhydrous DCM (25 mL) was added dropwise, the reaction was allowed to warm to 22 °C and was further stirred for 12 h. The solution was diluted with DCM (100 mL) and washed with aqueous NaOH (0.1 M, 100 mL) followed by saturated aqueous NaCl (100 mL). The organic layer was dried over anhydrous

Na_2SO_4 and concentrated under vacuum. Flash column chromatography (hexanes/ethyl acetate, 2:1) afforded **20** (1.62 g, 93%) as a glassy solid, mp 84-86 °C; ^{1}H NMR (400 MHz, $CDCl_3$) δ 7.76 (d, *J* = 7.3 Hz, 2H), 7.58 (d, *J* = 7.4 Hz, 2H), 7.39 (m, 2H), 7.30 (m, 2H), 7.05 (br, 1H), 5.82 (br, 1H), 5.33 (s, 1H), 4.34 (d, *J* = 7.2 Hz, 2H), 4.22 (t, *J* = 6.8 Hz, 1H), 3.51-3.24 (m, 6H), 2.60-0.86 (m, 54H), 0.67 (s, 3H); ^{13}C NMR (100 MHz, $CDCl_3$) δ 172.0, 156.5, 144.0, 143.9, 141.2, 127.6, 127.6, 127.0, 125.1, 125.0, 121.4, 119.9, 77.1, 66.7, 56.7, 56.1, 50.0, 47.2, 42.3, 39.7, 39.5, 37.2, 36.8, 36.5, 36.1, 35.9, 35.7, 31.8, 28.5, 28.2, 27.9, 26.8, 24.2, 23.8, 22.8, 22.5, 20.9, 19.4, 18.7, 11.8 ; IR (film) ν_{max} 3323, 2949, 1717, 1668, 1539, 1449, 1412, 1366, 1251, 1169, 1081, 908, 737 cm^{-1}; HRMS (ESI+) m/z 836.5831 (M+Na$^+$, $C_{53}H_{77}N_3O_5Na$ requires 836.5755).

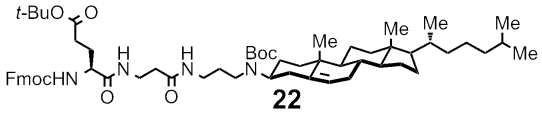

22

***tert*-Butyl-(15*S*)-5-(3β-cholest-5-en-3-yl)-15-(((9*H*-fluoren-9-ylmethoxy)carbonyl)amino)-2,2-dimethyl-4,10,14-trioxo-3-oxa-5,9,13-triazaoctadecan-18-oate**(**22**). Compound **20** (303 mg, 0.36 mmol) was added to DMF (2 mL) containing piperidine (20%) and stirred for 30 min at 22 °C. The solvent was removed under vacuum to afford the crude primary amine. To a solution of Fmoc-Glu(O*t*-Bu)-OH (157 mg, 0.37 mmol) in anhydrous DCM (10 mL) at 4 °C were added HOBt (55 mg, 0.41 mmol) and EDC (79 mg, 0.41 mmol) and the solution was stirred for 30 min. To this solution was added the crude primary amine derived from **20** dissolved in anhydrous DCM (5 mL). The reaction

was allowed to warm to 22 °C and stirred for 12 h. This solution was diluted with DCM (30 mL) and washed with aqueous NaOH (0.1 M, 30 mL) followed by saturated aqueous NaCl (30 mL). The organic layer was dried over anhydrous Na_2SO_4 and concentrated under vacuum. Flash column chromatography (DCM/MeOH, 50:1) afforded **22** (361 mg, 98%) as a white solid, mp 120-122 °C; ^{1}H NMR (400 MHz, $CDCl_3$) δ7.76 (d, *J* = 7.5 Hz, 2H), 7.60 (d, *J* = 7.5 Hz, 2H), 7.51 (br, 1H), 7.39 (t, *J* = 7.5 Hz, 2H), 7.31 (t, *J* = 7.5 Hz, 2H), 7.09 (br, 1H), 5.88 (d, *J* = 8.0 Hz, 1H), 5.31 (d, *J* = 4.0 Hz, 1H), 4.34 (t, *J* = 7.1 Hz, 2H), 4.21 (t, *J* = 7.1 Hz, 2H), 3.57-3.16 (m, 6H), 2.60-0.85 (m, 67H), 0.66 (s, 3H); ^{13}C NMR (100 MHz, $CDCl_3$) δ 172.7, 171.4, 171.4, 156.2, 143.9, 143.8, 141.3, 127.7, 127.9, 125.2, 121.4, 119.9, 80.9, 79.9, 67.1, 56.7, 56.1, 54.6, 50.1, 47.2, 42.3, 39.7, 39.8, 39.6, 38.4, 37.1, 36.7, 36.2, 36.0, 35.8, 31.9, 31.5, 28.6, 28.2, 28.1, 28.0, 27.9, 27.0, 24.3, 23.8, 22.8, 22.6, 21.0, 19.5, 18.7, 11.8 ; IR (film) ν_{max} 3295, 3066, 3005, 2935, 2863, 1726, 1652, 1540, 1465, 1451, 1415, 1366, 12523, 1163, 1046, 849, 757, 666 cm^{-1}; HRMS (ESI+) m/z 1043.6853 (M+Na$^+$, $C_{62}H_{92}N_4O_8Na$ requires 1043.6813).

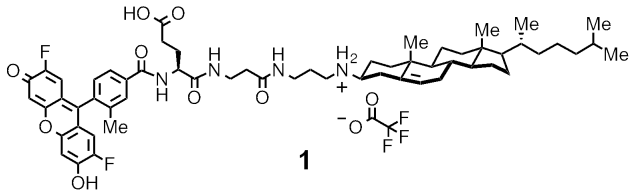

1

(4*S*)-5-((3-((3-(3β-Cholest-5-en-3-ylamino)propyl)amino)-3-oxopropyl)amino)-4-((4-(2,7-difluoro-6-hydroxy-3-oxo-3*H*-xanthen-9-yl)-3-methylbenzoyl)amino)-5-oxopentanoic acid (**1**). Compound **22** (75 mg, 0.074

mmol) was added to DMF (1 mL) containing piperidine (20%) and stirred for 30 min at 22 °C. The solvent was removed under vacuum to afford the crude primary amine. The resulting residue was dissolved in anhydrous DMF (5 mL), 4-carboxy-Pennsylvania Green succinimidyl ester (30 mg, 0.062 mmol) was added, followed by diisopropylethylamine (DIEA, 50 µL, 0.24 mmol). The reaction was stirred at 22 °C for 12 h and concentrated under vacuum. To the resulting orange residue was added DCM (5 mL) containing TFA (30%) and the solution was stirred at 22 °C for 12 h. The reaction was concentrated under vacuum, the crude product was dissolved in DMSO (2 mL), and the product was purified by preparative reverse-phase HPLC (gradient: 90/10 H_2O/MeCN to 100% MeCN over 20 min with 0.1% TFA added; retention time = 15 min (495 nm)) to afford **1** (23 mg, 36.4%) as an orange solid, mp 196-198 °C; ^{1}H NMR (300 MHz, DMSO-*d*$_6$) δ 8.76-8.72 (m, 3H), 8.19 (s, 2H), 8.14 (s, 1H), 8.05 (d, *J* = 5.4 Hz, 1H), 7.49 (d, *J* = 5.7 Hz, 1H), 6.98 (s, 2H), 6.72 (d, *J* = 8.2 Hz, 2H), 5.45 (s, 1H), 4.53 (d, *J* = 2.7 Hz, 1H), 3.23 (m, 2H), 3.14 (m, 2H), 3.01 (m, 3H), 2.46-0.92(m, 51H), 0.72 (s, 3H); ^{13}C NMR (75 MHz, DMSO-*d*$_6$) δ 174.0, 172.7, 171.2, 170.8, 165.9, 158.0, 149.3, 138.6, 135.9, 135.2, 134.5, 129.8, 129.0, 125.5, 122.4, 105.2, 56.6, 56.1, 55.5, 53.1, 49.3, 41.8, 41.6, 36.4, 36.2, 35.6, 35.3, 35.2, 34.3, 31.2, 30.5, 27.7, 27.4, 26.9, 26.2, 24.3, 23.8, 23.2, 22.6, 22.4, 20.5, 19.2, 18.7, 18.5, 11.6 ; IR (film) ν_{max} 3324, 3071, 2950, 2863, 1671, 1646, 1610, 1539, 1503, 1465, 1373, 1310, 1193, 1136, 836, 759 cm^{-1}; HRMS (ESI+) m/z 1007.5679 (M+H$^+$, $C_{59}H_{77}F_2N_4O_8Na$ requires 1007.5704).

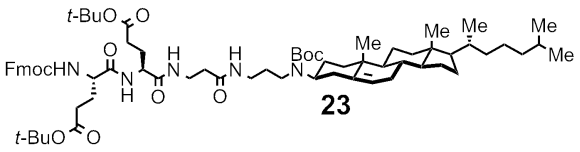

23

***tert*-Butyl (15*S*,18*S*)-15-(3-*tert*-butoxy-3-oxopropyl)-5-(3β-cholest-5-en-3-yl)-18-(((9*H*-fluoren-9-ylmethoxy)carbonyl) amino)-2,2-dimethyl-4,10,14,17-tetraoxo-3-oxa-5,9,13,16-tetraazahenicosan-21-oate** (**23**). Compound **22** (150 mg, 0.15 mmol) was added to DMF (2 mL) containing piperidine (20%) and stirred for 30 min at 22 °C. The solvent was removed under vacuum to afford the crude primary amine. To Fmoc-Glu(O*t*-Bu)-OH (70 mg, 0.16 mmol) in anhydrous DCM (10 mL) at 4 °C was added HOBt (24 mg, 0.18 mmol) and EDC (35 mg, 0.18 mmol) and the solution was stirred for 30 min. The crude primary amine derived from **22** in anhydrous DCM (5 mL) was added. The reaction was allowed to warm to 22 °C and stirred for 12 h. This solution was diluted with DCM (30 mL) and washed with aqueous NaOH (0.1 M, 30 mL) followed by saturated aqueous NaCl (30 mL). The organic layer was dried over anhydrous Na_2SO_4 and concentrated under vacuum. Flash column chromatography (DCM/MeOH, 30:1) afforded **23** (162 mg, 92%) as a white solid, mp 138-144 °C; ^{1}H NMR (400 MHz, $CDCl_3$) δ7.78 (d, *J* = 7.5 Hz, 2H), 7.63 (d, *J* = 7.2 Hz, 2H), 7.59 (br, 1H), 7.41 (t, *J* = 7.4 Hz, 2H), 7.36 (br, 1H), 7.33 (t, *J* = 7.4 Hz, 2H), 7.19 (br, 1H), 5.92 (br, 1H), 5.32 (d, J = 6.4 Hz, 1H), 4.36 (d, *J* = 7.2 Hz, 3H), 4.24 (t, *J* = 7.0 Hz, 2H), 3.58-3.20 (br, 7H), 2.60-0.86 (m, 79H), 0.67 (s, 3H); ^{13}C NMR (100 MHz, $CDCl_3$) δ 172.9, 172.8, 171.4, 171.1, 156.3, 156.3, 143.9, 143.7, 141.2, 127.7, 127.1, 125.2, 121.3, 120.0, 81.0, 80.9, 77.2, 67.2, 56.7, 56.2, 53.1, 50.1, 47.1, 42.3, 39.8, 39.5, 38.4, 36.7, 36.2, 35.8, 31.9, 28.6, 28.2, 28.0, 27.9, 24.3, 23.8, 22.8,

22.6, 21.0, 19.5, 18.7, 11.8 ; IR (film) ν_{max} 3289, 3066, 3005, 2934, 2868, 1729, 1693, 1679, 1636, 1539, 1450, 1413, 1388, 1367, 1281, 1254, 1158, 1044, 757, 667 cm^{-1}; HRMS (ESI+) m/z 1206.8032 (M+H+, $C_{71}H_{108}N_5O_{11}$ requires 1206.8040).

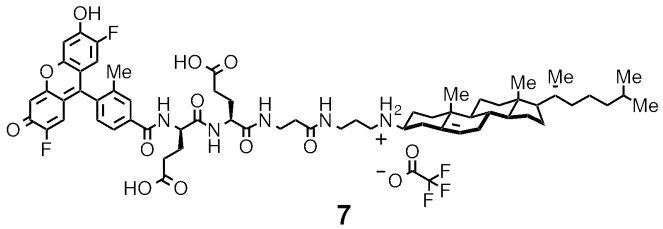

7

(4*S*)-5-(((1*S*)-3-Carboxy-1-(((3-((3-(3β-cholest-5-en-3-ylamino)propyl)amino)-3-oxopropyl)amino)carbonyl)propyl)amino)-4-((4-(2,7-difluoro-6-hydroxy-3-oxo-3H-xanthen-9-yl)-3-methylbenzoyl)amino)-5-oxopentanoic acid (**7**). Compound **23** (30 mg, 0.025 mmol) was added to DMF (1 mL) containing piperidine (20%) and stirred for 30 min at 22°C. The solvent was removed under vacuum to afford the crude primary amine. To the resulting residue in dry DMF (2 mL) was added 4-carboxy-Pennsylvania Green succinimidyl ester (13 mg, 0.027 mmol) followed by DIEA (50 µL, 0.24 mmol). The reaction was stirred at 22 °C for 12 h and concentrated under vacuum. The orange residue was treated with DCM (5 mL) containing TFA (30%) and stirred at 22 °C for 12 h. The reaction was concentrated under vacuum, and the crude product was dissolved in DMSO (2 mL) and purified by preparative reverse-phase HPLC (gradient: 90/10 H_2O/MeCN to 100% MeCN over 20 min with 0.1% TFA added; retention time = 14 min (495 nm)) to afford **7** (6.2 mg, 22%) as an orange solid, mp 145-148 °C; ^{1}H NMR (400 MHz, DMSO-d_6) δ 8.65 (d, J = 7.8 Hz, 1H), 8.37 (s, 2H), 8.07-7.92

(m, 4H), 7.39 (d, J = 8.0 Hz, 1H), 6.85 (s, 1H), 6.62 (d, J = 10.9 Hz, 1H), 5.37 (s, 1H), 4.46 (m, 1H), 4.21 (m, 1H), 3.29-3.20 (m, 4H), 2.90 (m, 3H), 2.46-0.92 (m, 55H), 0.63 (s, 3H); ^{13}C NMR (100 MHz, DMSO-d_6) δ 174.4, 172.6, 171.8, 171.7, 129.8, 129.0, 125.5, 122.4, 105.2, 57.0, 56.5, 56.0, 49.8, 42.3, 42.1, 39.3, 39.2, 39.1, 36.8, 36.6, 36.1, 36.0, 35.8, 35.6, 33.8, 31.7, 31.0, 30.6, 27.9, 25.8, 24.9, 24.8, 24.3, 23.6, 23.1, 22.8, 19.5, 19.2, 19.0, 12.1 ; IR (film) ν_{max} 3419, 2951, 1682, 1643, 1540, 1438, 1375, 1310, 1205, 1142, 1015, 801, 721.6 cm^{-1}; HRMS (ESI+) m/z 1136.6179 (M+H+, $C_{64}H_{84}F_2N_5O_{11}$ requires 1136.6130).

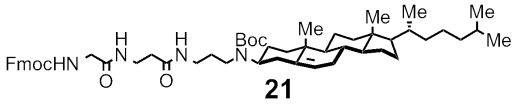

21

***tert*-Butyl-3β-cholest-5-en-3-yl(14-(9*H*-fluoren-9-yl)-5,9,12-trioxo-13-oxa-4,8,11-triazatetradec-1-yl)carbamate** (**21**). Compound **20** (150 mg, 0.18 mmol) was added to DMF (2 mL) containing piperidine (20%) and stirred for 30 min at 22 °C. The solvent was removed under vacuum to afford the crude primary amine. To a solution of Fmoc-Gly-OH (60 mg, 0.20 mmol) in anhydrous DCM (10 mL) at 4 °C was added HOBt (30 mg, 0.22 mmol) and EDC (42 mg, 0.22 mmol) and the solution was stirred for 30 min. The primary amine derived from **20** in anhydrous DCM (5 mL) was added. The reaction was allowed to warm to 22 °C and stirred for 12 h. This solution was diluted with DCM (30 mL) and washed with aqueous NaOH (0.1 M, 30 mL) followed by saturated aqueous NaCl (30 mL). The organic layer was dried over anhydrous Na_2SO_4 and concentrated under vacuum. Flash column chromatography (DCM/MeOH, 20:1) afforded **21** (153 mg,

97%) as a white solid, mp 112-114 °C; ^{1}H NMR (400 MHz, $CDCl_3$) δ 7.75 (d, *J* = 7.4 Hz, 2H), 7.60 (d, *J* = 7.0 Hz, 2H), 7.39 (t, *J* = 7.3 Hz, 2H), 7.30 (t, *J* = 7.3 Hz, 2H), 6.99 (br, 1H), 5.78 (br, 1H), 5.31 (s, 1H), 4.38 (d, *J* = 6.9 Hz, 2H), 4.22 (t, *J* = 7.0 Hz, 1H), 3.86 (d, *J* = 4.5 Hz, 2H), 3.56 (d, *J* = 5.0 Hz, 2H), 3.22 (m, 2H), 2.52-0.86 (m, 56H), 0.67 (s, 3H); ^{13}C NMR (100 MHz, $CDCl_3$) δ 171.5, 169.0, 156.5, 148.3, 143.8, 141.2, 127.7, 127.0, 125.1, 121.4, 119.9, 80.0, 67.1, 56.7, 56.1, 50.0, 47.1, 44.3, 42.3, 41.5, 39.7, 39.5, 38.4, 37.1, 36.7, 36.1, 35.9, 35.7, 31.8, 28.5, 28.2, 27.9, 26.8, 24.2, 23.8, 22.8, 22.5, 20.9, 19.4, 18.7, 11.8 ; IR (film) v max 3311, 2936, 2868, 1717, 1667, 1543, 1465, 1450, 1413, 1365, 1249, 1168, 1048, 758 cm^{-1}; HRMS (ESI+) m/z 893.6122 (M+H+, $C_{55}H_{81}N_4O_6$ requires 893.6151).

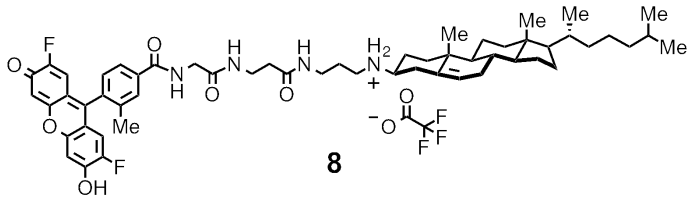

8

***N*-(2-((3-((3-(3β-Cholest-5-en-3-ylamino)propyl)amino)-3-oxopropyl)amino)-2-oxoethyl)-4-(2,7-difluoro-6-hydroxy-3-oxo-3H-xanthen-9-yl)-3-methylbenzamide** (**8**). Compound **21** (25 mg, 0.028 mmol) was added to DMF (1 mL) containing piperidine (20%) and stirred for 30 min at 22 °C. The solvent was removed under vacuum to afford the crude primary amine. To the resulting residue in dry DMF (2 mL) was added 4-carboxy-Pennsylvania Green succinimidyl ester (11 mg, 0.023 mmol) followed by DIEA (50 µL, 0.24 mmol). The reaction was stirred at 22 °C for 12 h and concentrated under vacuum. The

orange residue was treated with DCM (5 mL) containing TFA (30%) and stirred at 22 °C for 12 h. The reaction was concentrated under vacuum, and the crude product was dissolved in DMSO (2 mL) and purified by preparative reverse-phase HPLC (gradient: 90/10 H_2O/MeCN to 100% MeCN over 20 min with 0.1% TFA added; retention time = 13 min (495 nm)) to afford **8** (18 mg, 82%) as an orange solid, mp 200-203 °C; ^{1}H NMR (300 MHz, DMSO-d_6) δ 8.91 (s, 1H), 8.56 (s, 2H), 8.0-7.91 (m, 4H), 7.40 (d, *J* = 7.6 Hz, 1H), 6.86 (s, 2H), 6.60 (d, *J* = 11.1 Hz, 2H), 5.38 (s, 1H), 3.87 (m, 2H), 3.14 (m, 4H), 2.93 (m, 3H), 2.30-0.85 (m, 47H), 0.61 (s, 3H); ^{13}C NMR (75 MHz, DMSO-d_6) δ 170.9, 168.8, 166.0, 149.0, 138.5, 136.0, 135.2, 134.8, 129.9, 129.0, 125.3, 122.6, 105.0, 56.5, 56.1, 55.5, 49.3, 42.7, 41.7, 41.5, 36.1, 35.9, 35.6, 35.4, 35.2, 34.2, 31.2, 27.7, 27.4, 26.2, 26.1, 24.4, 23.2, 22.7, 22.4, 20.5, 19.2, 18.7, 18.5, 11.6; IR (film) ν_{max} 3419, 2950, 2115, 1646, 1540, 1465, 1374, 1310, 1194, 1147, 1016, 875 cm^{-1}; HRMS (ESI+) m/z 957.5350 (M+Na+, $C_{56}H_{72}F_2N_4O_6Na$ requires 957.5350).

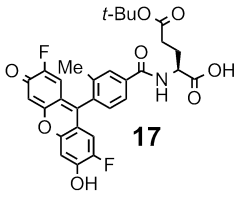

17

5-(tert-butoxy)-2-(4-(2,7-difluoro-6-hydroxy-3-oxo-3H-xanthen-9-yl)-3-methylbenzamido)-5-oxopentanoic acid (17) Fmoc-Glu(O-*t*-Bu)-OH (**16**, 67mg, 0.156 mmol) was treated with piperidine (20%) in DMF (1 mL) for 30 min. The solvent was removed under vacuum to afford the crude primary amine. A solution of 4-carboxy-Pennsylvania Green succinimidyl ester (25 mg, 0.052

mmol) in DMF (1 mL) was added to the crude primary amine in DMF (1 mL) followed by DIEA (0.25 mL). The reaction was allowed to stir at 22 °C for 16 h, dried under vacuum, and purified by flash column chromatography (MeOH/DCM/ AcOH, 5:94.9:0.1) to afford **17** (27 mg, 90%) as an orange residue, mp 134-138 °C; ^{1}H NMR (400 MHz, CD_3OD) δ 8.00 (s, 1H), 7.94 (d, *J* = 7.9 Hz, 1H), 7.40 (d, *J* = 7.9 Hz, 1H), 6.98 – 6.89 (m, 2H), 6.81 – 6.77 (m, 2H), 4.70 (d, *J* = 9.6 Hz, 1H), 2.47 (t, *J* = 7.0 Hz, 2H), 2.39 – 2.27 (m, 1H), 2.14 – 2.08 (m, 1H), 2.12 (s, 3H), 1.46 (s, 9H); ^{13}C NMR (101 MHz, CD_3OD) δ 174.95, 173.97, 169.66, 156.19, 138.02, 137.15, 136.55, 131.01, 130.47, 126.62, 112.98, 112.76, 106.32, 81.94, 53.70, 32.95, 28.35, 27.66, 19.60 ; IR (film) ν_{max} 2929, 1678, 1607, 1536, 1371, 1302, 1190, 1139, 953, 842, 801, 750, 724 cm^{-1}; HRMS (ESI+) m/z 568.1779 ($M+H^+$, $C_{30}H_{28}F_2NO_8$, requires 568.1777).

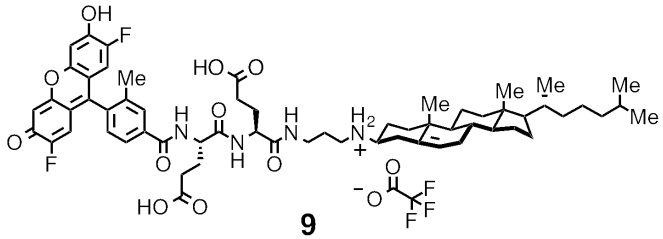

9

(4S)-5-(((2S)-4-carboxy-1-((3-(3β-cholest-5-en-3-ylamino)propyl)amino)-1-oxobutan-2-yl)amino)-4-(4-(2,7-difluoro-6-hydroxy-3-oxo-3H-xanthen-9-yl)-3-methylbenzamido)-5-oxopentanoic acid (**9**). Compound **19** (26.8 mg, 0.028 mmol), synthesized by a previously reported method[21], was added to DMF (0.5 mL) containing piperidine (20%) and stirred for 30 min at 22 °C. The solvent was removed under vacuum to afford the crude primary amine. To a solution of **17** (8.0 mg, 0.014 mmol) in anhydrous DMF (2 mL) at 4 °C was added HOBt (4.0

mg, 0.028 mmol) and EDC (5.4 mg, 0.028 mmol) and the solution was stirred at 22 °C for 30 min. The primary amine derived from **19** in anhydrous DMF (1 mL) was added at 4 °C, then the reaction was allowed to warm to 22 °C and stirred for 12 h. The reaction was concentrated under vacuum and the resulting residue was re-dissolved in DCM containing TFA (30%) and stirred at 22 °C for 2 h. The solvent was removed under vacuum, the crude product was dissolved in DMSO (2 mL), and purified by preparative reverse-phase HPLC (gradient: 90/10 H_2O/MeCN to 100% MeCN over 20 min with 0.1% TFA added; retention time = 16 min (495 nm)) to afford **9** (13.1 mg, 87%) as a orange solid, mp 175-178 °C; ^{1}H NMR (500 MHz, CD_3OD) δ 7.93 (s, 1H), 7.87 – 7.84 (m, 1H), 7.45 (t, *J* = 7.5 Hz, 1H), 6.87 – 6.75 (m, 2H), 6.72 – 6.58 (m, 2H), 5.39 (d, *J* = 4.9 Hz, 1H), 4.45 (m, 1H), 4.19 (m, 1H), 3.37 – 3.28 (m, 2H), 3.28 – 3.23 (m, 2H), 3.03 – 2.94 (m, 2H), 2.88 (m, 1H), 2.54 – 0.69 (m, 52H), 0.59 (s, 3H); ^{13}C NMR (126 MHz, CD_3OD) δ 176.85, 176.47, 174.94, 174.34, 169.92, 156.15, 146.38, 140.74, 139.53, 138.09, 136.70, 131.60, 131.47, 131.15, 130.50, 130.09, 127.07, 125.93, 125.15, 124.55, 122.22, 115.64, 113.74, 106.42, 59.41, 58.03, 57.51, 55.76, 55.01, 51.42, 44.75, 41.95, 40.99, 40.69, 38.22, 37.82, 37.35, 37.10, 36.92, 36.38, 33.77, 32.11, 31.55, 31.23, 30.01, 28.44, 27.82, 27.67, 27.58, 26.27, 25.98, 25.24, 24.96, 24.09, 22.10, 22.06, 19.64 19.43, 19.22, 12.27; IR (film) ν_{max} 3387, 2323, 1675, 1541, 1439, 1202, 1135, 842, 802, 724 cm^{-1}; HRMS (ESI-) m/z 1063.5757 (M-H$^+$, $C_{61}H_{77}F_2N_4O_{10}$ requires 1063.5613).

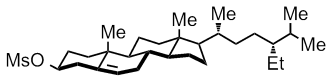

25

Sitost-5-en-3β-ol methanesulfonate (25). To a solution of β-sitosterol (**24**, 5.0 g, 12.0 mmol) in anhydrous DCM (100 mL) at 4 °C was added freshly distilled triethylamine (2.7 mL, 18.1 mmol) followed by a dropwise solution of methanesulfonyl chloride (1.03 mL, 13.25 mmol) in anhydrous DCM (10 mL). The reaction was maintained at 4 °C for 30 min, warmed to 22 °C, and stirred for 16 h. The reaction was concentrated under vacuum and the resulting residue was purified by flash chromatography (ethyl acetate/hexane, 1:4) to give **25** (4.1 g, 69%) as a white solid, mp 97-100 °C; ^{1}H NMR (400 MHz, $CDCl_3$) δ 5.45 – 5.38 (m, 1H), 4.52 (dt, *J* = 11.9, 3.7 Hz, 1H), 2.99 (s, 3H), 2.51 (d, *J* = 7.2 Hz, 2H), 2.09 – 0.75 (m, 42H), 0.68 (s, 3H). ^{13}C NMR (101 MHz, $CDCl_3$) δ 138.57, 123.61, 81.82, 56.52, 55.96, 49.86, 45.76, 42.19, 39.55, 39.04, 38.62, 36.79, 36.25, 35.97, 33.84, 31.71, 31.52, 29.12, 28.85, 28.04, 26.09, 24.11, 22.98, 20.89, 19.62, 19.12, 18.96, 18.63, 11.75, 11.43; IR (film) ν_{max} 2958, 2931, 2867, 1465, 1350, 1326, 1168, 946, 865, 802 cm^{-1}; HRMS (EI+) m/z 492.3637 (M+, $C_{30}H_{52}O_3S$ requires 492.3632).

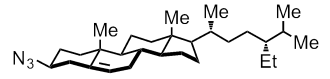

26

3β-Azido-5-sitostene (26). To a solution of **25** (1.7 g, 3.45 mmol) in anhydrous DCM (30 mL) was added TMS-N_3 (0.68 mL, 5.20 mmol), followed by $BF_3{\cdot}Et_2O$ (0.86 mL, 6.90 mmol). The reaction was stirred at 22 °C for 16 h. The reaction

was slowly poured into aqueous NaOH (1.0 M, 30 mL) and stirred for 5 min. The organic phase was separated and the aqueous layer was extracted with DCM (30 mL). The combined organic extracts were washed with saturated NaCl solution (500 mL), dried over anhydrous Na_2SO_4, and concentrated under vacuum to give the crude product as light yellow oil. The crude product was purified by flash column chromatography (ethyl acetate/hexane, 2:98) to afford **26** (800 mg, 53%) as a white solid, mp 74-78 °C; ^{1}H NMR (400 MHz, $CDCl_3$) δ 5.42 – 5.35 (m, 1H), 3.20 (t, *J* = 11.5 Hz, 1H), 2.29 (d, *J* = 7.9 Hz, 2H), 2.05 – 0.75 (m, 42H), 0.68 (s, 3H). ^{13}C NMR (101 MHz, $CDCl_3$) δ 139.84, 122.55, 61.17, 56.73, 56.07, 50.11, 45.84, 42.32, 39.72, 38.17, 37.59, 36.62, 36.16, 33.95, 31.85, 31.73, 29.16, 28.25, 27.96, 26.08, 24.29, 23.08, 21.01, 19.84, 19.29, 19.05, 18.80, 11.93, 11.65; IR (film) ν_{max} 2935, 2867, 2090, 1463, 1377, 1259, 750 cm^{-1}; HRMS (EI+) m/z 411.3872 (M-N_2, $C_{29}H_{49}N$ requires 411.3865).

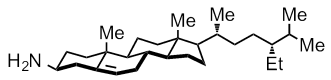

27

3β-Amino-5-sitostene (27). To a solution of **26** (180 mg, 0.44 mmol) in anhydrous diethyl ether (5 mL) at 4 °C was added $LiAlH_4$ powder (25 mg, 0.66 mol) in two equal portions. The reaction was maintained at 4 °C for 30 min, warmed to 22 °C, and stirred for 2 h. The reaction was cooled to 4 °C and carefully quenched by slow dropwise addition of ice-cold water. When evolution of H_2 gas ceased, the solution was poured into water (10 mL). The organic phase was separated, and the aqueous phase was extracted with ethyl acetate (10 mL

× 2). The combined organic extracts were washed with saturated NaCl solution (10 mL), dried over anhydrous Na_2SO_4, and concentrated under vacuum. The resulting solid was dissolved in chloroform (10 mL) and residual inorganic salts were removed by filtration. Concentration of the filtrate afforded **27** (140 mg, 77%) as a white solid, mp 122-125 °C; ^{1}H NMR (400 MHz, $CDCl_3$) δ 5.39 – 5.27 (m, 1H), 2.78 – 2.72 (m, 1H), 2.49 (d, *J* = 13.0 Hz, 2H), 2.21 – 0.74 (m, 42H), 0.67 (s, 3H); ^{13}C NMR (101 MHz, $CDCl_3$) δ 141.54, 120.89, 56.80, 56.06, 51.90, 50.23, 45.74, 45.56, 42.74, 42.32, 39.80, 38.11, 36.56, 36.16, 33.95, 32.14, 31.90, 29.15, 28.26, 26.07, 24.31, 23.07, 21.02, 19.83, 19.45, 19.04, 18.79, 11.93, 11.68; IR (film) ν_{max} 3360, 3280, 3160, 2926, 2852, 1587, 1462, 1381, 1022, 957, 836, 799, 738 cm^{-1}; HRMS (ESI+) m/z 414.4074 (M+H+, $C_{29}H_{52}N$ requires 414.4094).

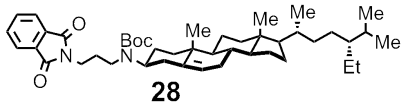

28

***tert*-Butyl-3β-sitost-5-en-3-yl(3-(1,3-dioxo-1,3-dihydro-2*H*-isoindol-2-yl) propyl)carbamate** (**28**). Compound **27** (130 mg, 0.31 mmol), *N*-(3-bromopropyl)phthalimide (103 mg, 0.38 mmol), and K_2CO_3 (108 mg, 0.78 mmol) were added to DMF (8 mL) and the solution was heated to 60 °C and stirred for 24 h. The reaction was cooled to 22 °C, and the solvent removed under vacuum. To the resulting residue was added DCM (10 mL). The insoluble material was removed by filtration and washed with DCM (2 × 5 mL). To the combined filtrate and wash solutions containing the crude secondary amine product was added

$(Boc)_2O$ (135 mg, 0.62 mmol) and DIEA (0.17 mL, 1.24 mmol). The reaction was stirred for 4 h at 22 °C, then concentrated under vacuum. Flash column chromatography (hexane/ethyl acetate, 85:15) afforded **28** (90 mg, 42% over 2 steps) as a white solid, mp 122-124 °C; ^{1}H NMR (400 MHz, $CDCl_3$) δ 7.88 – 7.79 (m, 2H), 7.72 (m, 2H), 5.37 – 5.25 (m, 1H), 3.85 (t, *J* = 6.9 Hz, 1H), 3.70 (t, *J* = 7.1 Hz, 2H), 3.15 (br, 2H), 2.06 – 0.73 (m, 56H), 0.66 (s, 3H); ^{13}C NMR (101 MHz, $CDCl_3$) δ 168.34, 134.07, 133.94, 132.11, 123.35, 123.21, 79.42, 56.71, 56.04, 50.12, 45.83, 42.31, 39.75, 36.17, 35.96, 33.94, 31.88, 29.14, 28.47, 28.26, 26.07, 24.29, 23.06, 20.99, 19.83, 19.41, 19.04, 18.78, 11.93, 11.64; IR (film) ν_{max} 3340, 2935, 2869, 1713, 1676, 1466, 1365, 1249, 1169, 1143, 907, 730 cm^{-1}; HRMS (ESI+) m/z 723.4980 ($M+Na^+$, $C_{45}H_{68}N_2O_4Na$, requires 723.5071).

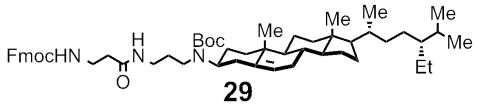

29

9*H*-Fluoren-9-ylmethyl (3-((3-((*tert*-butoxycarbonyl)(3β-sitost-5-en-3-yl) amino)propyl)amino)-3-oxopropyl) carbamate (**29**). To a solution of **28** (80 mg, 0.11 mmol) in absolute ethanol (3 mL) was added anhydrous hydrazine (17 μL, 0.55 mmol). The solution was heated to 50 °C and stirred for 4 h. The reaction was cooled to 22 °C, and a white precipitate was removed by filtration. The filtrate was concentrated under vacuum, and the residue was dissolved in chloroform (6 mL). After insoluble material was removed by filtration, concentration of the filtrate under vacuum afforded the phthalimide-deprotected

primary amine, a white solid that was carried forward without further purification. To Fmoc-β-Ala-OH (69 mg, 0.22 mmol) in anhydrous DCM (2 mL) at 4 °C were added HOBt (30 mg, 0.22 mmol) and EDC (42 mg, 0.22 mmol) followed by stirring at 4 °C for 30 min. The phthalimide-deprotected primary amine in anhydrous DCM (2 mL) was slowly added, and the reaction was allowed to warm to 22 °C and stirred for 12 h. The solution was concentrated under vacuum, and flash column chromatography (DCM/MeOH, 99:1) afforded **29** (56 mg, 60% over two steps) as a white solid, mp 86-90 °C; ^{1}H NMR (400 MHz, $CDCl_3$) δ 7.76 (d, *J* = 7.5 Hz, 2H), 7.60 (d, *J* = 7.5 Hz, 2H), 7.39 (t, *J* = 7.4 Hz, 2H), 7.30 (t, *J* = 7.4 Hz, 2H), 6.99 (br, 1H), 5.79 (br, 1H), 5.33 (d, *J* = 4.6 Hz, 1H), 4.35 (d, *J* = 7.2 Hz, 2H), 4.20 (t, *J* = 7.1 Hz, 1H), 3.56 – 3.46 (m, 2H), 3.25 (m, 4H), 2.44 (m, 2H), 2.07 – 0.73 (m, 56H), 0.67 (s, 3H); ^{13}C NMR (101 MHz, $CDCl_3$) δ 156.50, 144.04, 141.29, 127.64, 127.03, 125.19, 121.47, 119.94, 66.71, 56.75, 56.06, 50.10, 47.27, 45.84, 42.32, 39.75, 38.45, 36.74, 36.16, 35.98, 33.95, 31.88, 29.15, 28.55, 28.26, 26.08, 24.30, 23.07, 21.01, 19.84, 19.47, 19.04, 18.79, 11.93, 11.66; IR (film) ν_{max} 3320, 2934, 2869, 1665, 1541, 1450, 1365, 1249, 1167, 1141, 908, 732 cm^{-1}; HRMS (ESI+) m/z 886.5963 (M+Na^{+}, $C_{55}H_{81}N_3O_5Na$, requires 668.6068).

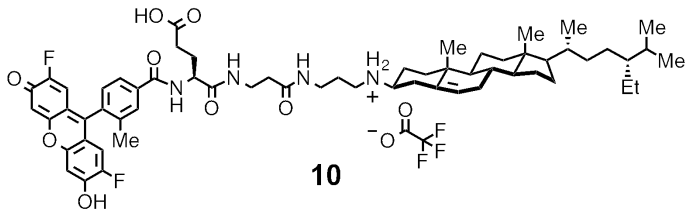

10

(4*S*)-5-((3-((3-(3β-Sitost-5-en-3-ylamino)propyl)amino)-3-oxopropyl)amino)-4-((4-(2,7-difluoro-6-hydroxy-3-oxo-3*H*-xanthen-9-yl)-3-methylbenzoyl)

amino)-5-oxopentanoic acid (**10**). Compound **29** (24.4 mg, 0.028 mmol) was added to DMF (0.5 mL) containing piperidine (20%) and stirred for 30 min at 22 °C. The solvent was removed under vacuum to afford the crude primary amine. To a solution of **17** (8.0 mg, 0.014 mmol) in anhydrous DMF (2 mL) at 4 °C was added HOBt (4.0 mg, 0.028 mmol) and EDC (5.4 mg, 0.028 mmol), and the solution was stirred for 30 min. The primary amine derived from **29** was added in anhydrous DMF (1 mL). The reaction was allowed to warm to 22 °C and stirred for 12 h. The reaction was concentrated under vacuum, DCM (2 mL) containing TFA (30%) was added, and the mixture was stirred for 2 h. The solvent was removed under vacuum and the crude product was dissolved in DMSO (2 mL). Purification by preparative reverse-phase HPLC (gradient: 90/10 H_2O/MeCN to 100% MeCN over 20 min with 0.1% TFA added; retention time = 18 min (495 nm)) afforded **10** (11.4 mg, 79%) as an orange solid, mp 192-195 °C; ^{1}H NMR (500 MHz, CD_3OD) δ 7.93 (s, 1H), 7.85 (d, *J* = 7.4 Hz, 1H), 7.30 (d, *J* = 7.9 Hz, 1H), 6.86 – 6.75 (m, 2H), 6.73 – 6.57 (m, 2H), 5.37 (d, *J* = 4.5 Hz, 1H), 4.44 (d, *J* = 9.1, 1H), 3.43 (t, *J* = 6.3 Hz, 2H), 2.98 (t, *J* = 7.2 Hz, 2H), 2.89 (d, *J* = 12.1 Hz, 1H), 2.48 – 0.66 (m, 57H), 0.60 (s, 3H); ^{13}C NMR (126 MHz, CD_3OD) δ 176.70, 175.01, 174.05, 169.61, 156.14, 139.52, 138.29, 138.09, 137.87, 136.96, 136.67, 131.10, 130.51, 126.76, 124.79, 112.74, 111.92, 106.43, 59.30, 58.05, 57.41, 55.45, 51.45, 49.52, 49.35, 49.18, 49.07, 48.88, 48.84, 48.58, 48.42, 47.26, 43.40, 43.24, 40.99, 38.24, 37.81, 37.41, 37.19, 36.91 36.60, 36.34, 35.07, 32.98, 31.77, 31.52, 30.37, 29.32, 27.97, 27.88, 27.15, 26.33, 25.24, 24.14, 22.05, 20.21, 19.69, 19.62, 19.17, 12.32, 11.94; IR (film) v max 3306, 2956,

2869, 1671, 1541, 1302, 1201, 1135, 841, 801, 724 cm^{-1}; HRMS (ESI-) m/z 1033.5874 ($M\text{-}H^+$, $C_{61}H_{79}F_2N_4O_8$ requires 1033.5871).

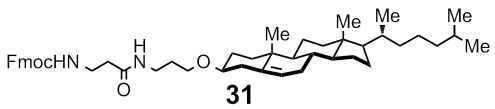

31

9H-fluoren-9-ylmethyl (3-((3-((3β-cholest-5-en-3-yl)oxy)propyl)amino)-3-oxopropyl)carbamate (31). To Fmoc-β-Ala-OH (380 mg, 1.22 mmol) in anhydrous DCM (5 mL) at 4 °C was added HOBt (165 mg, 1.22 mmol) and EDC (234 mg, 1.22 mmol), and the mixture was stirred at 4 °C for 30 min. Compound **30**, synthesized as previously reported, (350 mg, 0.81 mmol) was added in anhydrous DCM (5 mL). The reaction was allowed to warm to 22 °C and was stirred for 12 h. The solution was diluted with DCM (10 mL) and washed with saturated aqueous $NaHCO_3$ (10 mL) and saturated aqueous NaCl (10 mL). The organic layer was dried over anhydrous Na_2SO_4 and concentrated under vacuum. Flash column chromatography (DCM/MeOH, 99:1) afforded **31** (515 mg, 87%) as a glassy solid, mp 148-150 °C; ^{1}H NMR (400 MHz, $CDCl_3$) δ 7.76 (d, *J* = 7.5 Hz, 2H), 7.59 (d, *J* = 7.5 Hz, 2H), 7.39 (t, *J* = 7.4 Hz, 2H), 7.30 (t, *J* = 7.4 Hz, 2H), 6.34 (br, 1H), 5.58 (br, 1H), 5.34 – 5.26 (m, 1H), 4.35 (d, *J* = 7.2 Hz, 2H), 4.20 (t, *J* = 7.1 Hz, 1H), 3.61 – 3.44 (m, 4H), 3.38 (d, *J* = 11.4 Hz, 2H), 3.16 – 3.04 (m, 1H), 2.46 – 0.79 (m, 44H), 0.69 – 0.63 (m, 3H); ^{13}C NMR (101 MHz, $CDCl_3$) δ 171.19, 156.62, 144.12, 141.42, 140.64, 127.79, 127.17, 125.29, 122.02, 120.09, 79.46, 67.37, 66.90, 56.87, 56.29, 50.27, 47.35, 42.44, 39.89, 39.65, 39.23, 38.86, 37.24, 36.96, 36.33, 35.99, 35.86, 32.00, 31.64, 29.24,

28.61, 28.36, 28.15, 24.40, 23.96, 22.96, 22.70, 21.17, 19.49, 18.86, 11.99 ; IR (film) ν_{max} 3306, 2934, 2867, 1682, 1639, 1537, 1448, 1376, 1342, 1268, 1240, 1103, 1018, 908, 735 cm^{-1}; HRMS (ESI+) m/z 775.4972 ($M+K^+$, $C_{48}H_{68}N_2O_4K$ requires 775.4811).

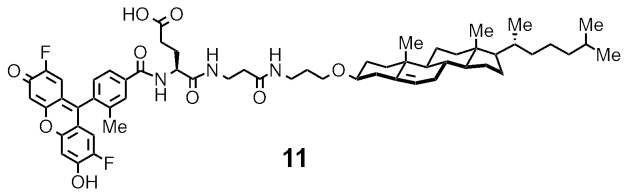

11

(4S)- 5-((3-((3-(3β-Cholest-5-en-3-yloxy)propyl)amino)-3-oxopropyl)amino)-4-((4-(2,7-difluoro-6-hydroxy-3-oxo-3*H*-xanthen-9-yl)-3-methylbenzoyl) amino)-5-oxopentanoic acid (11). Compound **31** (15.0 mg, 0.020 mmol) was added to DMF (0.5 mL) containing piperidine (20%) and stirred for 30 min at 22 °C. The solvent was removed under vacuum to afford the crude primary amine. To a solution of **17** (11.3 mg, 0.020 mmol) in anhydrous DMF (2 mL) at 4 °C was added HOBt (5.5 mg, 0.040 mmol) and EDC (8.0 mg, 0.040 mmol) and the solution was stirred for 30 min. The primary amine derived from **31** was added in anhydrous DMF (1 mL), and the reaction was allowed to warm to 22 °C and stirred for 12 h. The reaction was concentrated under vacuum, DCM (2 mL) containing TFA (30%) was added, and the solution was stirred at 22 °C for 2 h. The solvent was removed under vacuum and the crude product was dissolved in DMSO (2 mL). Purification by preparative reverse-phase HPLC (gradient: 90/10 H_2O/MeCN to 100% MeCN over 20 min with 0.1% TFA added; retention time = 17 min (495 nm)) afforded **11** (13.1 mg, 87%) as an orange solid, mp 192-194

°C; ^{1}H NMR (400 MHz, CD_3OD) δ 8.01 (s, 1H), 7.94 (d, *J* = 7.9 Hz, 1H), 7.28 – 7.36 (m, 1H), 7.04 – 6.85 (m, 2H), 6.82 – 6.70 (m, 2H), 5.32 – 5.26 (m, 1H), 4.60 – 4.54 (m, 1H), 3.56 – 3.45 (m, 4H), 3.45 – 3.36 (m, 2H), 3.28 – 3.22 (m, 4H), 3.17 – 3.04 (m, 2H), 2.62 – 0.81 (m, 46H), 0.67 (s, 3H); ^{13}C NMR (101 MHz, CD_3OD) δ 190.52, 183.25, 180.16, 173.46, 171.19, 161.26, 155.36, 150.34, 141.55, 136.58, 133.73, 130.91, 126.48, 122.52, 106.27, 80.31, 67.05, 66.56, 57.81, 57.19, 51.31, 43.21, 40.79, 40.41, 39.93, 38.54, 38.11, 37.76, 37.62, 37.08, 36.94, 36.78, 36.34, 32.82, 32.77, 31.33, 30.49, 29.14, 28.87, 27.88, 25.06, 24.68, 23.15, 22.89, 21.91, 19.81, 19.17, 12.28. IR (film) v_{max} 3369, 2925, 2853, 2076, 1646, 1543, 1464, 1375, 1314, 1193, 1117, 971, 735 cm^{-1}; HRMS (ESI-) m/z 1006.5441 (M-H^{+}, $C_{59}H_{74}F_2N_3O_9$ requires 1006.5399).

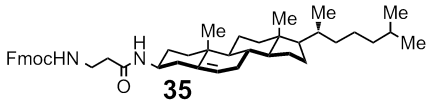

35

(9H-fluoren-9-yl)methyl (3-((3β-cholest-5-en-3-yl)amino)-3-oxopropyl) carbamate (35). Fmoc-β-Ala-Cl (**34**, 170 mg, 0.54 mmol, prepared by treatment of Fmoc-β-Ala-OH with excess $SOCl_2$ for 1 h followed by removal of $SOCl_2$ under vacuum) was dissolved in anhydrous DCM (5 mL). A solution of 3β-amino-5-cholestene (**32**, 250 mg, 0.65 mmol) and 4-dimethylaminopyridine (DMAP, 15 mg, 0.10 mmol) in anhydrous DCM was slowly added and the solution was stirred at 22 °C for 30 min. The reaction was diluted with DCM (25 mL) and filtered to remove precipitated solids. The resulting filtrate was concentrated under vacuum and purified via flash column chromatography (DCM, MeOH, 99:1)

to afford **35** (128 mg, 35%) as a white solid, mp 124-128 °C; ^{1}H NMR (400 MHz, $CDCl_3$) δ 7.75 (d, *J* = 7.5 Hz, 2H), 7.58 (d, *J* = 7.5 Hz, 2H), 7.39 (t, *J* = 7.4 Hz, 2H), 7.30 (t, *J* = 7.3 Hz, 2H), 5.54 (br, 1H), 5.41 – 5.32 (m, 2H), 4.36 (m, 2H), 4.20 (t, *J* = 6.9 Hz, 1H), 3.69 (m, 1H), 3.48 (m, 2H), 2.39 (m, 2H), 2.29 (d, *J* = 13.2 Hz, 1H), 2.14 – 0.82 (m, 39H), 0.69 (s, 3H); ^{13}C NMR (101 MHz, $CDCl_3$) δ 170.28, 156.57, 144.00, 141.33, 140.12, 127.65, 127.04, 125.07, 122.07, 119.93, 77.32, 77.00, 76.68, 66.78, 56.74, 56.23, 50.16, 49.86, 47.30, 42.34, 39.78, 39.54, 39.31, 37.86, 37.22, 36.57, 36.22, 35.79, 31.87, 31.66, 29.18, 28.20, 27.99, 24.27, 23.86, 22.77, 22.53, 20.99, 19.31, 18.73, 11.86; IR (film) ν_{max} 3313, 2933, 2867, 1686, 1636, 1534, 1449, 1267, 1148, 1023, 992, 735 cm^{-1}; HRMS (ESI+) m/z 701.4615 ($M+Na^+$, $C_{45}H_{62}N_2O_3Na$, requires 701.4658).

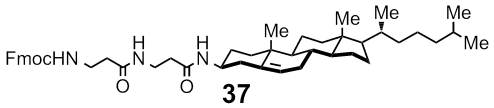

37

(9H-fluoren-9-yl)methyl (3-((3-((3β-cholest-5-en-3-yl)amino)-3-oxopropyl)amino)-3-oxopropyl) carbamate (**37**). Compound **35** (30.0 mg, 0.045 mmol) was added to DMF (0.5 mL) containing piperidine (20%) and stirred for 30 min at 22 °C. The solvent was removed under vacuum to afford the crude primary amine. To a solution of Fmoc-β-Ala-OH (27.5 mg, 0.090 mmol) in anhydrous DMF (2 mL) at 4 °C were added HOBt (12.0 mg, 0.090 mmol) and EDC (17.0 mg, 0.090 mmol) and the solution was stirred for 30 min. The primary amine derived from **35** was added in anhydrous DMF (1 mL), and the reaction was warmed to 22 °C and stirred for 12 h. The reaction was concentrated under

vacuum, and flash column chromatography (DCM/MeOH, 98/2) afforded **37** (23.8 mg, 71%) as a white solid, mp 178-180 °C; ^{1}H NMR (400 MHz, $CDCl_3$) δ 7.76 (d, *J* = 7.5 Hz, 2H), 7.59 (d, *J* = 7.4 Hz, 2H), 7.39 (t, *J* = 7.4 Hz, 2H), 7.30 (t, *J* = 7.4 Hz, 2H), 6.52 (br, 1H), 5.66 – 5.49 (m, 2H), 5.31 (d, *J* = 11.0 Hz, 1H), 4.35 (d, *J* = 7.0 Hz, 2H), 4.20 (t, *J* = 7.1 Hz, 1H), 3.65 (m, 1H), 3.58 – 3.42 (m, 4H), 2.39 (m, 4H), 2.24 (m, 1H), 2.12 – 0.78 (m, 39H), 0.66 (s, 3H); ^{13}C NMR (101 MHz, $CDCl_3$) δ 170.64, 156.46, 143.99, 141.30, 139.96, 127.68, 127.05, 125.17, 122.18, 119.97, 66.76, 56.67, 56.13, 49.97, 49.89, 47.25, 42.29, 39.62, 39.21, 37.77, 36.51, 36.19, 35.98, 35.80, 35.54, 35.44, 31.80, 29.08, 28.13, 28.01, 27.92, 24.27, 23.84, 22.83, 22.57, 20.94, 19.30, 18.72, 11.86; IR (film) ν_{max} 3310, 2932, 2867, 1687, 1637, 1536, 1450, 1367, 1273, 1148, 1105, 1025, 739 cm^{-1}; HRMS (ESI+) m/z 772.4980 (M+Na^{+}, $C_{48}H_{67}N_3O_4Na$, requires 772.5024).

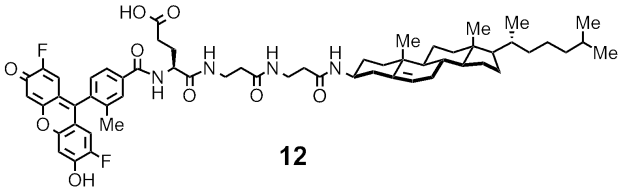

12

(4S)-4-(4-(2,7-difluoro-6-hydroxy-3-oxo-3H-xanthen-9-yl)-3-methylbenzamido)-5-((3-((3-((3β-cholest-5-en-3-yl)amino)-3-oxopropyl)amino)-3-oxopropyl)amino)-5-oxopentanoic acid (12). Compound **37** (21.0 mg, 0.028 mmol) was added to DMF (0.5 mL) containing piperidine (20%) and stirred for 30 min at 22 °C. The solvent was removed under vacuum to afford the crude primary amine. To a solution of **17** (8.0 mg, 0.014 mmol) in

anhydrous DMF (2 mL) at 4 °C was added HOBt (4.0 mg, 0.028 mmol) and EDC (5.4 mg, 0.028 mmol) and the solution was stirred for 30 min. The primary amine derived from **37** was added in anhydrous DMF (1 mL), and the reaction was warmed to 22 °C and stirred for 12 h. The reaction was concentrated under vacuum. DCM (2 mL) containing TFA (30%) was added and the solution was stirred for 2 h at 22 °C. The solvent was removed under vacuum, and the crude product was dissolved in DMSO (2 mL). Purification by preparative reverse-phase HPLC (gradient: 90/10 H_2O/MeCN to 100% MeCN over 20 min with 0.1% TFA added; retention time = 19 min (495 nm)) afforded **12** (10.2 mg, 71%) as a orange solid, mp 192-194 °C; ^{1}H NMR (500 MHz, CD_3OD) δ 8.01 (s, 1H), 7.96 (d, *J* = 6.8 Hz, 1H), 7.33 (d, *J* = 7.7 Hz, 1H), 6.85 (m, 2H), 6.66 (m, 2H), 5.32 (m, 1H), 3.64 – 3.52 (m, 2H), 3.52-3.44 (m, 2H), 2.58 – 0.81 (m, 53H), 0.69 (s, 3H); ^{13}C NMR (126 MHz, CD_3OD) δ 175.61, 173.36, 168.58, 163.08, 155.99, 141.21, 137.35, 136.58, 135.94, 130.61, 130.43, 129.83, 126.05, 122.33, 113.29, 111.80, 106.20, 57.46, 56.87, 50.95, 50.55, 43.30, 42.94, 40.46, 40.17, 39.35, 38.62, 37.24, 36.83, 36.51, 32.51, 29.19, 28.85, 28.63, 24.84, 24.45, 23.09, 22.83, 21.59, 19.83, 19.64, 19.07, 12.21; IR (film) ν_{max} 3305, 2932, 2871, 1646, 1541, 1371, 1306, 1188, 952, 750 cm^{-1}; HRMS (ESI-) m/z 1019.5361 (M-H$^+$, $C_{59}H_{73}F_2N_4O_9$ requires 1019.5351).

36

Cholesteryl 3-((((9H-fluoren-9-yl)methoxy)carbonyl)amino)propanoate (36). A solution of cholesterol (**33**, 681 mg, 1.76 mmol) and 4-dimethylaminopyridine (60 mg, 0.50 mmol) in anhydrous DCM (5 mL) was slowly added to Fmoc-β-Ala-Cl (**34**, 500 mg, 1.60 mmol) in anhydrous DCM (5 mL) and the reaction was stirred at 22 °C for 12 h. The reaction was diluted with DCM (25 mL) and filtered to remove precipitated solids. The resulting filtrate was concentrated under vacuum and purified via flash column chromatography (hexane/ethyl acetate, 7:3) to provide **36** (590 mg, 55%) as a white foam, mp 102-104 °C; ^{1}H NMR (400 MHz, $CDCl_3$) δ 7.76 (d, *J* = 7.5 Hz, 2H), 7.59 (d, *J* = 6.9 Hz, 2H), 7.40 (t, *J* = 7.4 Hz, 2H), 7.31 (t, *J* = 7.4 Hz, 2H), 5.39 (d, *J* = 3.8 Hz, 1H), 5.39-5.33 (m, 1H), 4.66 (d, *J* = 8.4 Hz, 1H), 4.38 (d, *J* = 7.1 Hz, 2H), 4.21 (t, *J* = 7.0 Hz, 1H), 3.50 – 3.45 (m, 2H), 2.54 (t, *J* = 5.7 Hz, 2H), 2.33 (d, *J* = 7.8 Hz, 2H), 2.07 – 0.80 (m, 38H), 0.69 (s, 3H); ^{13}C NMR (101 MHz, $CDCl_3$) δ 171.86, 156.32, 143.95, 141.32, 139.48, 127.70, 127.05, 125.09, 122.87, 119.99, 74.52, 66.76, 56.70, 56.15, 50.03, 47.25, 42.33, 39.64, 39.22, 38.14, 36.97, 36.60, 36.20, 35.81, 34.72, 31.89, 28.25, 28.04, 27.82, 24.30, 23.85, 22.85, 22.59, 21.05, 19.33, 18.74, 11.88 ; IR (film) ν_{max} 3356, 2946, 2868, 1721, 1512, 1450, 1376, 1263, 1189, 1006, 735 cm^{-1}; HRMS (ESI+) m/z 702.4473 ($M+Na^+$, $C_{45}H_{61}NO_4Na$, requires 702.4493).

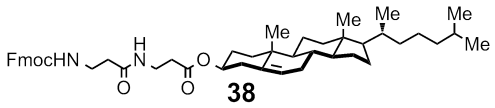

38

Cholesteryl 3-(3-((((9H-fluoren-9-yl)methoxy)carbonyl)amino)propanamido) propanoate (38). Compound **36** (200 mg, 0.30 mmol) was added to DMF (1.0 mL) containing piperidine (20%) and stirred for 30 min at 22 °C. The solvent was removed under vacuum to afford the crude primary amine. To a solution of Fmoc-β-Ala-OH (102 mg, 0.33 mmol) in anhydrous DMF (3 mL) at 4 °C was added HOBt (45 mg, 0.33 mmol) and EDC (64 mg, 0.33 mmol) and the solution was stirred for 30 min. The primary amine derived from **36** was added in anhydrous DMF (3 mL), and the reaction was warmed to 22 °C and stirred for 12 h. The reaction was concentrated under vacuum, and flash column chromatography (DCM/MeOH, 98/2) afforded **38** (150 mg, 52%) as a white foam, mp 158-160 °C; ^{1}H NMR (400 MHz, $CDCl_3$) δ 7.75 (d, *J* = 7.3 Hz, 2H), 7.59 (d, *J* = 7.3 Hz, 2H), 7.39 (t, *J* = 7.2 Hz, 2H), 7.30 (t, *J* = 7.1 Hz, 2H), 6.24 (br, 1H), 5.60 (br, 1H), 5.35 (m, 1H), 4.62 (m, 1H), 4.35 (d, *J* = 6.5 Hz, 2H), 4.20 (t, *J* = 6.6 Hz, 1H), 3.61 – 3.45 (m, 4H), 2.50 (t, *J* = 6.1 Hz, 2H), 2.45 – 2.35 (m, 1H), 2.29 (d, *J* = 7.3 Hz, 2H), 2.04 – 0.78 (m, 39H), 0.67 (s, 3H); ^{13}C NMR (101 MHz, $CDCl_3$) δ 172.09, 171.42, 156.61, 144.07, 141.39, 139.49, 127.77, 127.15, 125.25, 122.98, 120.05, 74.71, 66.83, 56.76, 56.23, 50.07, 47.34, 42.39, 39.71, 38.19, 37.19, 37.00, 36.64, 36.29, 35.97, 35.86, 35.03, 34.37, 31.93, 31.81, 28.33, 28.12, 27.87, 24.37, 23.94, 22.94, 22.68, 21.11, 19.38, 18.82, 11.95 ; IR (film) ν_{max} 3314, 2937, 1729, 1687, 1640, 1544, 1449, 1377, 1269, 1186, 1027, 739 cm^{-1}; HRMS (ESI+) m/z 773.4793 ($M+Na^+$, $C_{48}H_{66}N_3O_4Na$, requires 773.4864).

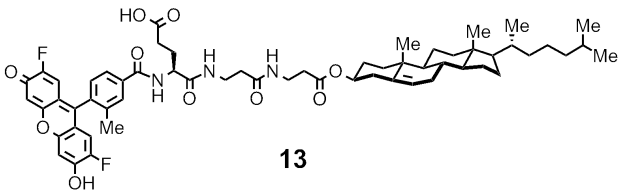

13

(4S)-4-(4-(2,7-difluoro-6-hydroxy-3-oxo-3H-xanthen-9-yl)-3-methylbenzamido)-5-((3-((3-((3-cholester -3-yl)oxy) 3-oxopropyl)amino)-3-oxopropyl)amino)-5-oxopentanoic acid (13). Compound **38** (21.0 mg, 0.028 mmol) was added to DMF (0.5 mL) containing piperidine (20%) and stirred for 30 min at 22 °C. The solvent was removed under vacuum to afford the crude primary amine. To a solution of **17** (8.0 mg, 0.014 mmol) in anhydrous DMF (2 mL) at 4 °C was added HOBt (4.0 mg, 0.028 mmol) and EDC (5.4 mg, 0.028 mmol) and the solution was stirred for 30 min. The primary amine derived from **38** was added in anhydrous DMF (1 mL), and the reaction was warmed to 22 °C and stirred for 12 h. The reaction was concentrated under vacuum. DCM (2 mL) containing TFA (30%) was added and the solution stirred at 22 °C for 2 h. The solvent was removed under vacuum and the crude product was dissolved in DMSO (2 mL). Purification by preparative reverse-phase HPLC (gradient: 90/10 H_2O/MeCN to 100% MeCN over 20 min with 0.1% TFA added; retention time = 17 min (495 nm)) afforded **13** (10.5 mg, 73%) as an orange solid, mp 180-184 °C; ^{1}H NMR (500 MHz, CD_3OD) δ 8.03 (s, 1H), 7.97 (d, *J* = 7.7 Hz, 1H), 7.36 (d, *J* = 7.9 Hz, 1H), 6.84 (m, 2H), 6.76 (m, 2H), 5.32 (d, *J* = 4.2 Hz, 1H), 4.59 (m, 2H), 3.59 – 3.39 (m, 4H), 2.58 – 2.48 (m, 4H), 2.43 (d, *J* = 10.6 Hz, 2H), 2.29 (d, *J* = 7.7 Hz, 2H), 2.16 (s, 3H), 2.06 – 0.78 (m, 40H), 0.69 (s, 3H); ^{13}C NMR (126 MHz, CD_3OD) δ 174.83, 171.84, 171.03, 167.27, 148.36, 141.22, 139.66, 138.91

(d, *J* = 9.8 Hz), 135.96, 134.86, 134.59, 131.93, 129.58 – 129.33, 129.20, 128.73, 128.43, 126.53, 125.57, 124.73, 123.97, 122.66, 121.83, 119.23, 118.47, 113.50, 112.21, 104.60, 73.79, 56.06, 55.49, 53.34, 49.49, 46.96, 43.56, 41.51, 39.05, 38.74, 37.21, 36.23, 35.77, 35.40, 35.11, 34.63, 33.33, 31.09, 29.65, 29.06, 27.39, 27.20, 26.85, 26.11, 23.37, 23.00, 21.47, 21.21, 20.19, 18.07, 17.48, 10.58 ; IR (film) v_{max} 3298, 2930, 2868, 1725, 1643, 1610, 1534, 1456, 1374, 1295, 1188, 1024, 952, 838, 732 cm^{-1}; HRMS (ESI-) m/z 1020.5208 ($M-H^+$, $C_{59}H_{73}F_2N_3O_{10}$ requires 1020.5191).

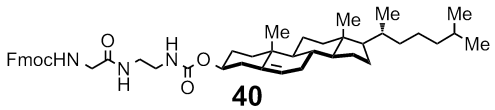

40

9H-fluoren-9-ylmethyl (3-((3-(((((cholester-3-yl)oxy) carbonyl)amino)ethyl) amino)-2-oxoethyl)amino)carbamate (40). A solution of cholesteryl chloroformate (**39**, 500 mg, 1.11 mmol) in DCM (5 mL) was very slowly added to a solution of ethylene diamine (1.50 mL, 22.26 mmol) in DCM (10 mL). The reaction was allowed to stir at 22 °C for 2 h. The excess diamine was removed under vacuum, the resulting solid was dissolved in DCM (10 mL), and the organic layer was washed with aqueous NaOH (1 M, 10 mL). The organic phase was dried over anhydrous Na_2SO_4, and concentrated under vacuum to provide the primary amine product, which was used without further purification. To a solution of Fmoc-Gly-OH (104 mg, 0.35 mmol) in anhydrous DCM (5 mL) at 4 °C was added HOBt (47 mg, 0.35 mmol) and EDC (67 mg, 0.35 mmol) and the solution was stirred for 30 min. The primary amine derived from **39** (150 mg, 0.32 mmol)

was added in anhydrous DCM (3 mL), and the reaction was warmed to 22 °C and stirred for 12 h. The reaction was concentrated under vacuum, and purified by flash column chromatography (DCM/MeOH, 98/2) to afford **40** (130 mg, 56%) as a white foam, mp 82-84 °C; ^{1}H NMR (400 MHz, $CDCl_3$) δ 7.76 (d, *J* = 7.5 Hz, 2H), 7.60 (d, *J* = 7.2 Hz, 2H), 7.40 (t, *J* = 7.3 Hz, 2H), 7.31 (t, *J* = 7.5 Hz, 2H), 6.74 (br, 1H), 5.46 (br, 1H), 5.35 – 5.26 (m, 1H), 5.04 (br, 1H), 4.43 (d, *J* = 7.2 Hz, 2H), 4.22 (t, *J* = 6.9 Hz, 1H), 3.87 (s, 2H), 3.42 – 3.38 (m, 2H), 3.38 – 3.28 (m, 2H), 2.92 (d, *J* = 32.0 Hz, 2H), 2.38 – 0.73 (m, 40H), 0.65 (s, 3H); ^{13}C NMR (101 MHz, $CDCl_3$) δ 170.08, 162.84, 156.80, 143.88, 141.40, 139.71, 127.87, 127.22, 125.23, 122.75, 120.12, 74.93, 67.38, 56.72, 56.27, 49.99, 47.24, 44.59, 42.39, 39.72, 38.59, 36.98, 36.66, 36.31, 35.91, 31.78, 28.53, 28.02, 24.35, 23.97, 22.94, 22.68, 21.11, 19.39, 18.83, 11.95 ; IR (film) v_{max} 3319, 2937, 2867, 1665, 1527, 1450, 1382, 1252, 1153, 1031, 1009, 737 cm^{-1}; HRMS (ESI-) m/z 786.4638 ($M+Cl^-$, $C_{47}H_{65}N_3O_5Cl$ requires 786.4618).

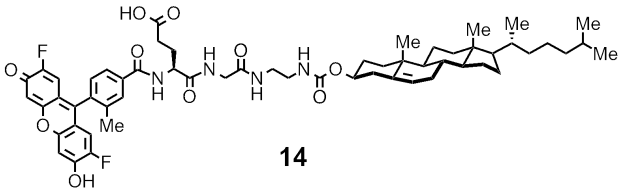

14

(4S)-4-(4-(2,7-difluoro-6-hydroxy-3-oxo-3H-xanthen-9-yl)-3-methylbenzamido)-5-(3-((3-(((((3-cholester-3-y)oxy)carbonyl)amino)ethyl)amino)-2-oxoethyl)amino)-5-oxopentanoic acid (14). Compound **40** (21.0 mg, 0.028 mmol) was added to DMF (0.5 mL)

containing piperidine (20%) and stirred for 30 min at 22 °C. The solvent was removed under vacuum to afford the crude primary amine. To a solution of **17** (8.0 mg, 0.014 mmol) in anhydrous DMF (2 mL) at 4 °C was added HOBt (4.0 mg, 0.028 mmol) and EDC (5.4 mg, 0.028 mmol) and the solution was stirred for 30 min. The primary amine derived from **40** in anhydrous DMF (1 mL) was added. The reaction was allowed to warm to 22 °C and stirred for 12 h. The reaction was concentrated under vacuum. DCM (2 mL) containing TFA (30%) was added and the solution was stirred at 22 °C for 2 h. The solvent was removed under vacuum and the crude product was dissolved in DMSO (2 mL). Purification by preparative reverse-phase HPLC (gradient: 90/10 H_2O/MeCN to 100% MeCN over 20 min with 0.1% TFA added; retention time = 19 min (495 nm)) afforded **14** (9.0 mg, 63%) as an orange solid, mp 186-190 °C; ^{1}H NMR (500 MHz, CD_3OD) δ 8.06 (s, 1H), 8.01 (d, *J* = 7.0 Hz, 1H), 7.35 (d, *J* = 7.8 Hz, 1H), 7.05 – 6.90 (m, 2H), 6.90 – 6.69 (m, 2H), 5.30 – 5.24 (m, 1H), 4.57 – 4.48 (m, 1H), 4.42 – 4.32 (m, 2H), 4.18 (s, 1H), 3.95 – 3.87 (m, 2H), 3.41 – 3.33 (m, 2H), 3.31 – 3.25 (m, 2H), 2.62 – 2.51 (m, 2H), 2.40 – 0.78 (m, 43H), 0.68 (s, 3H); ^{13}C NMR (126 MHz, CD_3OD) δ 176.93, 174.60, 171.87, 169.77, 158.73, 150.37, 141.11, 130.75, 128.54, 127.59, 125.98, 124.67, 123.60, 121.25, 120.48, 114.22, 106.58, 75.79, 58.06, 57.50, 51.48, 43.90, 43.52, 41.54, 41.39, 41.54, 41.34, 40.98, 39.75, 38.26, 37.75, 37.42, 37.13, 33.10, 31.59, 29.56, 29.12, 27.36, 25.38, 25.01, 23.47, 23.22, 22.20, 20.09, 19.48, 12.59; IR (film) ν_{max} 3312, 2931, 2867, 1644, 1610, 1526, 1463, 1373, 1266, 1188, 1026, 952, 874, 733 cm^{-1}; HRMS (ESI-) m/z 1021.5169 ($M\text{-}H^+$, $C_{58}H_{71}F_2N_3O_{10}$ requires 1021.5144).

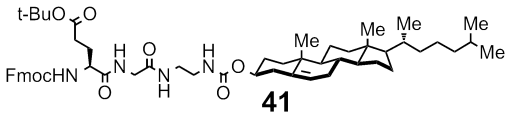

41

***tert*-butyl (*S*)-4-((((9*H*-fluoren-9-yl)methoxy)carbonyl)amino)-5-((2-((2-((((Cholester-3-yl)oxy)carbonyl)amino)ethyl)amino)-2-oxoethyl)amino)-5-oxopentanoate (41).** Compound **40** (100 mg, 0.136 mmol) was added to DMF (2 mL) containing piperidine (20%) and stirred for 30 min at 22 °C. The solvent was removed under vacuum to afford the crude primary amine. To a solution of Fmoc-Glu(O*t*-Bu)-OH (115 mg, 0.272 mmol) in anhydrous DCM (10 mL) at 4 °C was added HOBt (37 mg, 0.272 mmol) and EDC (52 mg, 0.272 mmol) and the solution was stirred for 30 min. The crude primary amine derived from **40** was added in anhydrous DCM (5 mL), and the reaction was warmed to 22 °C and stirred for 12 h. This solution was diluted with DCM (30 mL) and washed with aqueous NaOH (0.1 M, 30 mL) followed by saturated aqueous NaCl (30 mL). The organic layer was dried over anhydrous Na_2SO_4 and concentrated under vacuum. Flash column chromatography (DCM/MeOH, 50:1) afforded **41** (87 mg, 70%) as a white solid, mp 88-92 °C; ^{1}H NMR (400 MHz, $CDCl_3$) δ 7.74 (d, *J* = 7.5 Hz, 2H), 7.58 (d, *J* = 7.0 Hz, 2H), 7.38 (t, *J* = 7.5 Hz, 2H), 7.28 (t, *J* = 7.5 Hz, 2H), 7.09 (br, 2H), 6.26 (br, 1H), 5.49 (br, 1H), 5.35 – 5.28 (m, 1H), 4.39 (d, *J* = 6.6 Hz, 2H), 4.20 (t, *J* = 7.0 Hz, 1H), 4.19 – 4.11 (m, 1H), 3.93 (s, 2H), 3.70 – 3.64 (m, 1H), 3.37 – 3.30 (m, 2H), 3.28 – 3.21 (m, 2H), 2.60 – 0.77 (m, 53H), 0.65 (s, 3H); ^{13}C NMR (101 MHz, $CDCl_3$) δ 172.96, 172.01, 169.39, 156.84, 143.70, 141.29, 139.74, 127.77, 127.13, 125.08, 122.48, 120.00, 81.29, 74.57, 67.24,

56.66, 56.15, 55.35, 49.98, 47.12, 43.16, 42.30, 39.72, 39.52, 38.51, 36.94, 36.50, 36.20, 35.79, 31.83, 28.22, 28.08, 28.01, 24.26, 23.85, 22.82, 22.57, 21.02, 19.30, 18.72, 11.85; IR (film) ν_{max} 3319, 2942, 1681, 1525, 1450, 1367, 1250, 1152, 1032, 843, 735, 702 cm^{-1}; HRMS (ESI+) m/z 959.5876 ($M+Na^+$, $C_{56}H_{80}N_4O_8Na^+$ requires 959.5868).

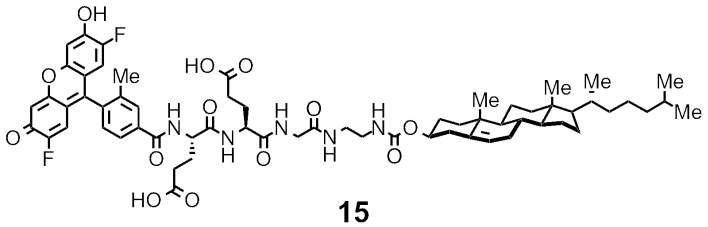

15

(10*S*,13*S*)-10-(2-carboxylatoethyl)-13-(4-(2,7-difluoro-6-oxido-3-oxo-3*H*-xanthen-9-yl)-3-methylbenzamido)-1-((Cholester-3-yl)oxy)-1,6,9,12-tetraoxo-2,5,8,11-tetraazahexadecan-16-oate (15). Compound **41** (30 mg, 0.027 mmol) was added to DMF (0.5 mL) containing piperidine (20%) and stirred for 30 min at 22 °C. The solvent was removed under vacuum to afford the crude primary amine. To a solution of **17** (23 mg, 0.040 mmol) in anhydrous DMF (2 mL) at 4 °C was added HOBt (5 mg, 0.040 mmol) and EDC (8 mg, 0.040 mmol) and the solution was stirred for 30 min. The primary amine derived from **41** was added in anhydrous DMF (1 mL), and the reaction was warmed to 22 °C and stirred for 12 h. The reaction was concentrated under vacuum, DCM (2 mL) containing TFA (30%) was added, and the solution was stirred at 22 °C for 2 h. The solvent was removed under vacuum and the crude product was dissolved in DMSO (2 mL). Purification by preparative reverse-phase HPLC (gradient: 90/10 H_2O/MeCN to 100% MeCN over 20 min with 0.1% TFA added; retention time = 19 min (495

nm)) afforded **15** (10 mg, 33%) as an orange solid, mp 182-186 °C; ^{1}H NMR (500 MHz, CD_3OD) δ 8.02 (s, 1H), 7.99 (d, *J* = 8.1 Hz, 1H), 7.40 (d, *J* = 7.9 Hz, 1H), 6.97 – 6.91 (m, 2H), 6.81 – 6.63 (m, 2H), 5.35 – 5.29 (m, 1H), 4.65 – 4.57 (m, 1H), 4.40 - 4.34 (m, 1H), 4.31 – 4.24 (m, 1H), 4.10 – 3.73 (m, 2H), 3.33 – 3.18 (m, 4H), 2.58 (t, *J* = 8.1 Hz, 4H), 2.53 – 0.80 (m, 48H), 0.68 (s, 3H); ^{13}C NMR (126 MHz, CD_3OD) δ 176.76, 176.34, 174.80, 174.43, 171.80, 169.87, 158.62, 156.09, 153.56, 141.21, 138.02, 136.81, 136.61, 131.33, 130.56, 126.75, 123.53, 115.90, 112.90, 112.74, 106.49, 75.58, 58.05, 57.53, 55.42, 55.23, 51.66, 43.70, 43.43, 41.04, 40.70, 40.50, 39.70, 38.19, 37.64, 37.37, 37.13, 33.06, 32.92, 31.49, 31.13, 30.77, 29.29, 29.18, 28.02, 27.13, 25.24, 24.99, 23.21, 22.96, 22.07, 19.75, 19.69, 19.25, 12.26; IR (film) ν_{max} 3317, 2941, 1644, 1611, 1536, 1465, 1372, 1336, 1307, 1191, 1032, 952, 875, 833 cm^{-1}; HRMS (ESI+) m/z 1174.5601 ($M+Na^+$, $C_{63}H_{79}F_2N_5O_{13}Na^+$ requires 1174.5535).

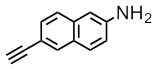

46

6-ethynylnaphthalen-2-amine (46). 6-Bromonaphthyl-2-amine **45** (100 mg, 0.450 mmol) was added to dry, argon-flushed triethylamine (3 mL). Ethynyl trimethylsilane (100 µL, 0.675 mmol), palladium dichloride bis-triphenylphosphine (15 mg, 0.025 mmol), and copper (I) iodide (7 mg, 0.037 mmol) were added, and the reaction was heated to 80 °C and stirred for 16 h. The reaction mixture was dried under vacuum, re-dissolved in DCM (3 mL), loaded onto a short plug of silica, and eluted with DCM/MeOH (95/5). The eluted product was dried under vacuum, re-dissolved in methanol (3 mL), and 1 M aqueous potassium hydroxide

(0.3 mL) was added and allowed to stir at 22 °C for 3 h. The reaction mixture was diluted with chloroform (20 mL) and extracted with saturated $NaHCO_3$ (2 x 10 mL). The organic layer was washed with brine, dried over Na_2SO_4, and concentrated under vacuum. Flash chromatography (hexames/ethyl acetate, 5:1) afforded compound **46** (41 mg, 54%) as a white solid, mp 82 – 86 °C; ^1H NMR (500 MHz, $CDCl_3$) δ 7.87 (s, 1H), 7.61 (d, *J* = 8.3 Hz, 1H), 7.52 (d, *J* = 8.5 Hz, 1H), 7.41 (d, *J* = 8.5 Hz, 1H), 6.96 (d, *J* = 2.4 Hz, 1H), 6.94 (s, 1H), 3.94 (br, 2H), 3.08 (s, 1H); ^{13}C NMR (126 MHz, $CDCl_3$) δ 145.30, 134.85, 132.39, 129.39, 129.26, 127.29, 125.96, 118.88, 115.65, 108.39, 84.67, 76.37; IR (film) v_{max} 3215, 2925, 2854, 1630, 1503, 1390, 1286, 1176, 905, 866, 811, 727 cm^{-1}; HRMS (ESI+) m/z 168.0822 ($M+H^+$, $C_{12}H_{10}N^+$ requires 168.0808).

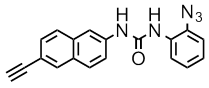

47

1-(2-azidophenyl)-3-(6-ethynylnaphthalen-2-yl)urea (47). Compound **44** (20 mg, 0.150 mmol) was dissolved in DCM (4 mL). Triphosgene (130 mg, 0.450 mmol) was added and allowed to stir at 22 °C for 30 minutes. The solution was then added directly to a short plug of silica and eluted using DCM/MeOH (95/5, 30 mL). The eluent was immediately dried under vacuum. The crude chloroformate of **44** was dissolved in DCM (3 mL), and then *N,N*-dimethylaminopyridine (DMAP, 12 mg, 0.100 mmol) and compound **46** (25 mg, 0.150 mmol) were added. The reaction was allowed to stir for 3 h at 22 °C. The reaction mixture was added directly to a column of silica and subjected to flash

chromatography (eluted with a gradient of DCM to 95/5 DCM/MeOH) to yield 24 mg (0.074 mmol, 49%) as an off-white solid. The final product was protected form light until use. mp 204 – 208 °C; ^{1}H NMR (500 MHz, $(CD_3)_2SO$) δ 9.61 (s, 1H), 8.34 (s, 1H), 8.20 – 8.12 (m, 2H), 8.05 – 7.98 (m, 1H), 7.87 (d, *J* = 8.9 Hz, 1H), 7.80 (d, *J* = 8.5 Hz, 1H), 7.50 (dd, *J* = 8.9, 2.2 Hz, 1H), 7.45 (dd, *J* = 8.5, 1.7 Hz, 1H), 7.31 (dd, *J* = 7.9, 1.5 Hz, 1H), 7.16 (dd, *J* = 8.1, 1.5 Hz, 1H), 7.11 (dd, *J* = 7.7, 1.6 Hz, 1H), 4.21 (s, 1H); ^{13}C NMR (126 MHz, DMSO) δ 152.14, 138.29, 133.38, 131.39, 130.43, 128.61, 128.57, 128.44, 127.44, 127.40, 125.33, 122.98, 120.12, 120.00, 118.77, 116.83, 112.94, 83.99, 80.49; IR (film) v_{max} 3287, 2137, 1643, 1577, 1485, 1453, 1300, 1237, 890, 813, 741 cm^{-1}; HRMS (ESI+) m/z 328.1202 ($M+H^+$, $C_{19}H_{14}N_5O^+$ requires 328.1193).

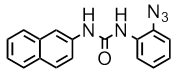

49

1-(2-azidophenyl)-3-(naphthalen-2-yl)urea (49). Compound **44** (40 mg, 0.30 mmol) was dissolved in DCM (3 mL). Triphosgene (130 mg, 0.450 mmol) was added and allowed to stir at 22 °C for 30 minutes. The solution was then added directly to a short plug of silica and eluted using DCM/MeOH (95/5, 30 mL). The eluent was immediately dried under vacuum. The crude chloroformate of **44** was dissolved in DCM (3 mL), and then *N,N*-dimethylaminopyridine (DMAP, 24 mg, 0.20 mmol) and naphthylamine (**48**, 40 mg, 0.28 mmol) were added. The reaction was allowed to stir for 3 h at 22 °C. The reaction mixture was added

directly to a column of silica and subjected to flash chromatography (eluted with a gradient of DCM to 95/5 DCM/MeOH) to yield 64 mg (0.21 mmol, 74%) as an off-white solid. The final product was kept protected form light until use. mp 180 – 184 °C; ^{1}H NMR (500 MHz, $(CD_3)_2SO$) δ 9.52 (s, 1H), 8.31 (s, 1H), 8.19 (d, *J* = 8.2 Hz, 1H), 8.14 (s, 1H), 7.89 – 7.77 (m, 3H), 7.45 (t, *J* = 8.8 Hz, 2H), 7.36 (t, *J* = 7.4 Hz, 1H), 7.31 (d, *J* = 6.5 Hz, 1H), 7.20 – 7.13 (m, 1H), 7.13 – 7.06 (m, 1H); ^{13}C NMR (126 MHz, $(CD_3)_2SO$) δ 152.30, 137.21, 133.73, 130.62, 129.14, 128.54, 127.47, 127.36, 127.03, 126.41, 125.38, 124.03, 122.91, 120.02, 119.45, 118.80, 113.30; IR (film) ν_{max} 3285, 2128, 1644, 1584, 1560, 1485, 1451, 1297, 1232, 891, 856, 814, 740 cm^{-1}; HRMS (ESI+) m/z 304.1191 ($M+H^+$, $C_{17}H_{14}N_5O^+$ requires 304.1193).

2.7.3 Biological Assays and Protocols

General. All cell culture reagents were purchased from Sigma, Fisher, USA Scientific, Santa Cruz Biotechnology, or ATCC. The XTremeGene HP transfection reagent was purchased from Roche. The human SR-B1 and mutant plasmids were kindly provided by Prof. Daisy Sahoo at the Medical College of Wisconsin. The CHO-ldlA and CHO-ldlA_mSR-B1 cell lines were kindly provided by Prof. Monty Krieger at MIT. NeutrAvidin resin (immobilized streptavidin) was purchased from Pierce Biotechnology. SDS-PAGE analysis was performed on an Invitrogen XCell II module with Invitrogen pre-cast 4-20% polyacrylamide gradient, Bis-Tris gels. Silver staining was done using a kit from Pierce

Biotechnology. UV irradiation for photocrosslinking was performed with an 8-watt lamp from UltraViolet Products at 365 nm.

Cell culture. Jurkat lymphocytes (human acute leukemia, ATCC #TIB-152) were cultivated in Roswell Park Memorial Institute (RPMI) 1640 medium. HEK-293 (human embryonic kidney) cells were cultivated in DMEM. CHO-ldlA cells were cultivated in Ham's F12K media. CHO-ldlA_mSR-B1 cells were cultivated under the same conditions with the addition of 0.25 mg/mL of G418 added to the media to maintain stable selection of mSR-B1 expressing cells. All media types were supplemented with fetal bovine serum (FBS, 10%), penicillin (100 U/mL), and streptomycin (100 µg/mL). All cell lines were incubated in a humidified 5% CO_2 incubator at 37 °C. Media used for cell culture and all wash steps contained antibiotics and 10% FBS unless otherwise noted.

Microscopy. An inverted Leica TCS SPE confocal laser-scanning microscope fitted with a Leica 63X oil-immersion objective was employed for imaging. Fluorescent probes were excited with a 488 nm solid-state laser and emitted photons were collected from 495-600 nm. Propidium iodide, used to counterstain dead cells red fluorescent, was excited with a 532 nm solid-state laser and emitted photons were collected from 650-800 nm. To image living Jurkat cells, 50 µL of cells in media was pipetted to form a small droplet in the center of a coverslip fitted with a press-to-seal silicone isolator (Invitrogen). A microscope slide was added to the top of the coverslip to create a column of media

containing living cells. To allow accurate comparisons of differences in cellular fluorescence, laser power and PMT gain settings were identical for all samples shown in a given figure.

Flow Cytometry. Populations of 10,000 Jurkat cells were analyzed for each sample using an Accuri C6 flow cytometer equipped with 488 nm and 640 nm solid-state lasers. Live cells were gated using both forward scattering (FSC) and side scattering (SSC) dot plots to identify physical cellular properties of size and granularity. In some cases, propidium iodide (3 μM, excitation: 488 nm; emission: 670 nm LP) was used to identify cells with compromised membranes. When applicable, the average cellular fluorescence from excitation at 488 nm was converted to molecular equivalents of fluorescein (MEFL) using a normalization factor obtained from analysis of bead standards from Spherotech Inc. These beads contained known fluorescein concentrations and provided a standard curve to convert raw fluorescence values into MEFL.

Confocal microscopy of fluorescent probes. Cells were suspended at 300,000 cells/mL in RPMI-1640 media containing 10% FBS. Fluorescent probes were added at 2 μM (diluted 1:1000 into media from DMSO stocks) and incubated at 37 °C for 5 minutes or 1 hour. After this incubation, the samples were washed once with RPMI-1640 containing 0.5% FBS and immediately imaged by confocal microscopy as described above.

Saturation binding studies of fluorescent probes. Cells were suspended at 300,000 cells/mL in RPMI-1640 media containing 10% FBS. Ezetimibe (200 μM; diluted 1:1000 from a 200 mM DMSO stock), Ezetimibe glucuronide (200 μM; diluted 1:1000 from a 200 mM DMSO stock), compound **47** (25 μM; diluted 1:1000 from a DMSO stock), or vehicle control (DMSO) was added in competitive binding experiments. Cell suspensions containing the competitor or vehicle control were prepared as 1 mL aliquots in 1.5 mL Eppendorf tubes. Fluorescent probes were added at concentrations ranging from 0 nM to 2500 nM (diluted 1:1000 into media from stocks in DMSO). Once the probe was added and mixed well, the samples were split into three tubes each containing 330 μL. Cells were incubated at 37 °C for 5 minutes. After this incubation, the samples were washed once with RPMI-1640 containing 0.5% FBS (to minimize efflux of the probe from the cell surface) and propidium iodide (3 μM). Samples were immediately analyzed by flow cytometry. Fluorescence values in MEFL were analyzed as total binding (no competitor added) and a linear non-specific binding component (with added competitor) to calculate specific binding curves. Using GraphPad Prism 5.0 software, these curves were analyzed with a 'One site with hill slope' saturation binding model to determine the relative apparent K_d and B_{max} values listed in Table 2.1.

Kinetic analysis of cellular uptake of fluorescent probes. Cells were suspended at 300,000 cells/mL in RPMI-1640 media containing 10% FBS. Fluorescent probes were added at concentrations ranging from 0 nM to 2500 nM

(diluted 1:1000 into media from DMSO stocks). Cells were incubated at 22 °C for timepoints ranging from 1 – 12.5 minutes. After this incubation, the samples were washed once with RPMI-1640 containing 0.5% FBS (to minimize efflux of the probe from the cell surface). Samples were immediately analyzed by flow cytometry. Each probe was analyzed at 6 concentrations over 5 time points. Fluorescence values were converted to MEFL and plotted versus time for each of the 6 concentrations. The data was fit to a linear regression and the slope of each line (MEFL/min) was plotted versus concentration. Each assay was performed three times to give average MEFL/min values and SEM for each concentration. These plots were analyzed by non-linear regression using the 'Michaelis-Menton' kinetic model in GraphPad Prism 5 to generate the K_M and V_{MAX} data shown in Table 2.2.

Transient expression of hSR-B1 plasmids in HEK-293 cells. HEK-293 cells were plated on 24-well plates at 50,000 cells per well and allowed to attach overnight. Transfection of plasmids encoding human SR-B1, non-functional mutant hSR-B1 (2), and empty vector control was done using the XTremeGene HP transfection reagent (Roche) according to the commercial protocol at ratio of 2 µL of transfection reagent per microgram DNA. Expression was allowed to proceed for 48 h. Following this period, cells were treated with 100 nM of compound **1** at 37 °C for 5 minutes. After treatment the cells were washed twice with DMEM, once with PBS 7.4, and trypsinized using 150 µL of 0.25% trypsin at 37 °C for 5 minutes. Once the cells were detached, the trypsin was neutralized

with 300 µL of DMEM and immediately analyzed by flow cytometry. Each condition was performed in duplicate and reported as average fluorescence and SEM in MEFL.

Saturation binding analysis in CHO-ldlA_mSR-B1 cells. CHO-ldlA and CHO-ldlA_mSR-B1 cells were plated on 24-well at 150,000 cells per well and allowed to attach overnight. Compound **1** was added at concentrations ranging from 0 nM to 1000 nM (diluted 1:1000 into media from DMSO stocks). The cells were incubated at 37 °C for 5 minutes to allow uptake. After incubation, the cells were washed twice with Ham's F12K media, once with PBS 7.4, and trypsinized with 150 µL of 0.25% trypsin at 37 °C for 5 miuntes. After the cells were detached, the trypsin was neutralized with 300 µL of Ham's F12K media and immediately analyzed by flow cytometry. Each condition was performed in duplicate and plotted as averaged fluorescence and SEM in MEFL. The data was analyzed by non-linear regression using the 'One site – total binding' model in GraphPad Prism 5.

Photoaffinity labeling and protein pulldown protocol for target identification. Approximately 6 x 10^7 Jurkat lymphocytes were suspended in 15 mL of RPMI 1640 media and aliquoted into 5 mL samples (~2 x 10^7 each). Sample 1 remained untreated and was incubated at 37 °C in RPMI 1640 prior to washing and cell lysis. Sample 2 was incubated in RPMI 1640 containing photoaffinity probe **47** at 10 µM for 1 hour at 37 °C. Sample 3 was co-treated

with **47** at 10 μM and **49** at 200 μM for 1 hour at 37 °C. After 1 hour, samples 2 and 3 containing the photoaffinity label were irradiated with UV light (365 nm) for 5 minutes in 10 cm culture dishes. Following irradiation, all samples were washed once with RPMI-1640, once with PBS 7.4, re-suspended in 500 μL of PBS 7.4 containing 1 mM DTT and 1 mM PMSF, and placed on ice. The cells were lysed using brief ultrasonication (one 3 second pulse) and the lysate was centrifuged at 10,000 x g and 4 °C for 10 minutes. The supernatants containing the cytosolic fractions were removed, added to separate tubes, and placed on ice. The pellets were re-suspended in 500 μL PBS 7.4 containing 1 mM DTT, 1 mM PMSF, and 1% Triton X-100. The samples were centrifuged 18,000 x g and 4 °C for 10 minutes. The supernatants containing the membrane fractions were removed and added to separate tubes. Each of the 6 samples (3 cytosolic fractions and 3 membrane fractions) received 1 mM $CuSO_4$, 2 mM Tris(3-hydroxypropyltriazolylmethyl)amine (THPTA), and 1 mM sodium ascorbate diluted from 100X stocks in ddH_2O. Each tube also received 50 μM biotin-azide diluted from a 100X stock in DMSO. The click reaction was allowed to proceed overnight at 37 °C. Following incubation, each tube received 50 μL of NeutrAvidin resin (provided as a 50% w/v suspension in PBS) and was incubated at 22 °C for 4 h with agitation. The resin was washed three times by brief centrifugation and re-suspension in 1 mL PBS 7.4 containing 0.5% Triton X-100. The resin was then loaded into empty mini-spin columns (USA Scientific) and washed an additional five times with 500 μL of PBS 7.4. Following washing, the resin was prepared for either SDS-PAGE or MS/MS sequencing analysis.

For SDS-PAGE Analysis. The resin was suspended in 40 µL 4X SDS-PAGE loading buffer containing 1 mM biotin and heated to 70 °C for 5 minutes. The samples were briefly centrifuged to pellet the resin and 25 µL of the supernatant was loaded onto a pre-cast polyacrylamide gel and subjected to SDS-PAGE analysis. The gel was visualized using silver staining following the commercial kit protocol (Pierce Biotechnology).

For MS/MS Sequencing Analysis. The resin was further washed with 0.2 M ammonium bicarbonate buffer. On-resin trypsin digestion was performed following protocols provided by the KU Analytical Proteomics Laboratory (KU APL). The resulting samples were submitted to the KU APL for sequencing analysis.

2.8 References

1. Goldstein, J. L.; Brown, M. S., The LDL Receptor. *Arterioscler. Thromb. Vasc. Biol.* **2009,** *29*, 431-438.

2. Kwon, H. J.; Abi-Mosleh, L.; Wang, M. L.; Deisenhofer, J.; Goldstein, J. L.; Brown, M. S.; Infante, R. E., Structure of N-Terminal Domain of NPC1 Reveals Distinct Subdomains for Binding and Transfer of Cholesterol. *Cell* **2009,** *137*, 1213-1224.

3. Infante, R. E.; Wang, M. L.; Radhakrishnan, A.; Kwon, H. J.; Brown, M. S.; Goldstein, J. L., NPC2 facilitates bidirectional transfer of cholesterol between

NPC1 and lipid bilayers, a step in cholesterol egress from lysosomes. *Proc. Natl. Acad. Sci. U. S. A.* **2008,** *105*, 15287-15292.

4. Xie, X. F.; Brown, M. S.; Shelton, J. M.; Richardson, J. A.; Goldstein, J. L.; Liang, G. S., Amino acid substitution in NPC1 that abolishes cholesterol binding reproduces phenotype of complete NPC1 deficiency in mice. *Proc. Natl. Acad. Sci. U. S. A.* **2011,** *108*, 15330-15335.

5. Wang, M. L.; Motamed, M.; Infante, R. E.; Abi-Mosleh, L.; Kwon, H. J.; Brown, M. S.; Goldstein, J. L., Identification of Surface Residues on Niemann-Pick C2 Essential for Hydrophobic Handoff of Cholesterol to NPC1 in Lysosomes. *Cell Metab.* **2010,** *12*, 166-173.

6. Mesmin, B.; Maxfield, F. R., Intracellular sterol dynamics. *Biochim. Biophys. Acta Mol. Cell Biol. Lipids* **2009,** *1791*, 636-645.

7. Chang, T. Y.; Reid, P. C.; Sugii, S.; Ohgami, N.; Cruz, J. C.; Chang, C. C. Y., Niemann-Pick type C disease and intracellular cholesterol trafficking. *J. Biol. Chem.* **2005,** *280*, 20917-20920.

8. Altmann, S. W.; Davis, H. R.; Zhu, L. J.; Yao, X. R.; Hoos, L. M.; Tetzloff, G.; Iyer, S. P. N.; Maguire, M.; Golovko, A.; Zeng, M.; Wang, L. Q.; Murgolo, N.; Graziano, M. P., Niemann-Pick C1 like 1 protein is critical for intestinal cholesterol absorption. *Science* **2004,** *303*, 1201-1204.

9. Davis, H. R.; Altmann, S. W., Niemann-Pick C1 Like 1 (NPC1L1) an intestinal sterol transporter. *Biochim. Biophys. Acta Mol. Cell Biol. Lipids* **2009,** *1791*, 679-683.

10. Ioannou, Y. A., The structure and function of the Niemann-Pick C1 protein. *Mol. Genet. Metab.* **2000,** *71*, 175-181.

11. Garcia-Calvo, M.; Lisnock, J. M.; Bull, H. G.; Hawes, B. E.; Burnett, D. A.; Braun, M. P.; Crona, J. H.; Davis, H. R.; Dean, D. C.; Detmers, P. A.; Graziano, M. P.; Hughes, M.; MacIntyre, D. E.; Ogawa, A.; O'Neill, K. A.; Iyer, S. P. N.; Shevell, D. E.; Smith, M. M.; Tang, Y. S.; Makarewicz, A. M.; Ujjainwalla, F.; Altmann, S. W.; Chapman, K. T.; Thornberry, N. A., The target of ezetimibe is Niemann-Pick Cl-Like 1 (NPC1L1). *Proc. Natl. Acad. Sci. U. S. A.* **2005,** *102*, 8132-8137.

12. Davis, H. R.; Veltri, E. R., Zetia: Inhibition of Niemann-Pick C1 like 1 (NPC1L1) to reduce intestinal cholesterol absorption and treat hyperlipidemia. *J. Atheroscler. Thromb.* **2007,** *14*, 99-108.

13. Maxfield, F. R.; Wustner, D., Analysis of Cholesterol Trafficking with Fluorescent Probes. In *Lipids, Vol 108*, DiPaolo, G.; Wenk, M. R., Eds. Elsevier Academic Press Inc: San Diego, 2012; Vol. 108, pp 367-393.

14. Wolfrum, C.; Shi, S.; Jayaprakash, K. N.; Jayaraman, M.; Wang, G.; Pandey, R. K.; Rajeev, K. G.; Nakayama, T.; Charrise, K.; Ndungo, E. M.; Zimmermann, T.; Koteliansky, V.; Manoharan, M.; Stoffel, M., Mechanisms and optimization of in vivo delivery of lipophilic siRNAs. *Nat. Biotechnol.* **2007,** *25*, 1149-1157.

15. Pitard, B.; Oudrhiri, N.; Vigneron, J. P.; Hauchecorne, M.; Aguerre, O.; Toury, R.; Airiau, M.; Ramasawmy, R.; Scherman, D.; Crouzet, J.; Lehn, J. M.; Lehn, P., Structural characteristics of supramolecular assemblies formed by

guanidinium-cholesterol reagents for gene transfection. *Proc. Natl. Acad. Sci. U. S. A.* **1999,** *96*, 2621-2626.

16. Sato, S. B.; Ishii, K.; Makino, A.; Iwabuchi, K.; Yamaji-Hasegawa, A.; Senoh, Y.; Nagaoka, I.; Sakuraba, H.; Kobayashi, T., Distribution and transport of cholesterol-rich membrane domains monitored by a membrane-impermeant fluorescent polyethylene glycol-derivatized cholesterol. *J. Biol. Chem.* **2004,** *279*, 23790-23796.

17. Firestone, R. A., Low-density-lipoprotein as a vehicle for targeting antitumor compounds to cancer-cells. *Bioconjugate Chem.* **1994,** *5*, 105-113.

18. Boonyarattanakalin, S.; Martin, S. E.; Dykstra, S. A.; Peterson, B. R., Synthetic mimics of small mammalian cell surface receptors. *J. Am. Chem. Soc.* **2004,** *126*, 16379-16386.

19. Peterson, B. R., Synthetic mimics of mammalian cell surface receptors: prosthetic molecules that augment living cells. *Org. Biomol. Chem.* **2005,** *3*, 3607-3612.

20. Hymel, D.; Peterson, B. R., Synthetic cell surface receptors for delivery of therapeutics and probes. *Adv. Drug Deliv. Rev.* **2012,** *64*, 797-810.

21. Sun, Q.; Cai, S.; Peterson, B. R., Selective disruption of early/recycling endosomes: Release of disulfide-linked cargo mediated by a N-alkyl-3 beta-cholesterylamine-capped peptide. *J. Am. Chem. Soc.* **2008,** *130*, 10064-+.

22. Sun, Q.; Cai, S.; Peterson, B. R., Practical Synthesis of 3 beta-Amino-5-cholestene and Related 3 beta-Halides Involving i-Steroid and Retro-i-Steroid Rearrangements. *Org. Lett.* **2009,** *11*, 567-570.

23. Kim, B.-K.; Doh, K.-O.; Nam, J. H.; Kang, H.; Park, J.-G.; Moon, I.-J.; Seu, Y.-B., Synthesis of novel cholesterol-based cationic lipids for gene delivery. *Bioorganic & Medicinal Chemistry Letters* **2009,** *19*, 2986-2989.

24. Kvaerno, L.; Ritter, T.; Werder, M.; Hauser, H.; Carreira, E. M., An in vitro assay for evaluation of small-molecule inhibitors of cholesterol absorption. *Angew. Chem.-Int. Edit.* **2004,** *43*, 4653-4656.

25. Altmann, S. W.; Davis, H. R.; Yao, X. R.; Laverty, M.; Compton, D. S.; Zhu, L. J.; Crona, J. H.; Caplen, M. A.; Hoos, L. M.; Tetzloff, G.; Priestley, T.; Burnett, D. A.; Strader, C. D.; Graziano, M. P., The identification of intestinal scavenger receptor class B, type I (SR-BI) by expression cloning and its role in cholesterol absorption. *Biochim. Biophys. Acta Mol. Cell Biol. Lipids* **2002,** *1580*, 77-93.

26. Labonte, E. D.; Howles, P. N.; Granholm, N. A.; Rojas, J. C.; Davies, J. P.; Ioannou, Y. A.; Hui, D. Y., Class B type I scavenger receptor is responsible for the high affinity cholesterol binding activity of intestinal brush border membrane vesicles. *Biochim. Biophys. Acta Mol. Cell Biol. Lipids* **2007,** *1771*, 1132-1139.

27. Knoepfel, M.; Davies, J. P.; Duong, P. T.; Kvaerno, L.; Carreira, E. M.; Phillips, M. C.; Ioannou, Y. A.; Hauser, H., Multiple plasma membrane receptors but not NPC1L1 mediate high-affinity, ezetimibe-sensitive cholesterol uptake into the intestinal brush border membrane. *Biochim. Biophys. Acta Mol. Cell Biol. Lipids* **2007,** *1771*, 1140-1147.

28. Acton, S.; Rigotti, A.; Landschulz, K. T.; Xu, S. Z.; Hobbs, H. H.; Krieger, M., Identification of scavenger receptor SR-BI as a high density lipoprotein receptor. *Science* **1996,** *271*, 518-520.

29. Nieland, T. J. F.; Penman, M.; Dori, L.; Krieger, M.; Kirchhausen, T., Discovery of chemical inhibitors of the selective transfer of lipids mediated by the HDL receptor SR-BI. *Proc. Natl. Acad. Sci. U. S. A.* **2002,** *99*, 15422-15427.

30. Chadwick, A. C.; Sahoo, D., Functional Characterization of Newly-Discovered Mutations in Human SR-BI. *PLoS One* **2012,** *7*, 7.

31. Mottram, L. F.; Boonyarattanakalin, S.; Kovel, R. E.; Peterson, B. R., The Pennsylvania green fluorophore: A hybrid of Oregon Green and Tokyo Green for the construction of hydrophobic and pH-insensitive molecular probes. *Org. Lett.* **2006,** *8*, 581-584.

32. Woydziak, Z. R.; Fu, L.; Peterson, B. R., Efficient and Scalable Synthesis of 4-Carboxy-Pennsylvania Green Methyl Ester: A Hydrophobic Building Block for Fluorescent Molecular Probes. *Synthesis* **2014,** *46*, 158-164.

33. Tang, C. H.; Jiao, N., Copper-Catalyzed C-H Azidation of Anilines under Mild Conditions. *J. Am. Chem. Soc.* **2012,** *134*, 18924-18927.

Chapter 3

Biological Evaluation of Endosome Disruptive Peptides with Improved Biological Properties

3.1 Introduction

As described in Chapter 2, cholesterylamines and other cholesterol-mimetic membrane anchors provide a highly efficient mechanism to deliver conjugated cargo into early/recycling endosomes. Previous work from the Peterson group has utilized these molecules as synthetic cell surface receptors capable of binding non-covalently and internalizing a variety of extracellular ligands via endocytosis.[1, 2] Over the last several years we have focused on utilizing these membrane anchors as a delivery mechanism for covalently-linked cell-impermeable molecules.[3] To accomplish this, one must employ a mechanism to allow entrapped endosomal cargo to be released into the cytosol to reach its molecular target.[4, 5]

There are numerous examples in nature of pathogens that disrupt endosomal membranes as a mechanism of virulence and/or protection. Several enveloped viruses, such as the influenza virus, infect host cells using viral fusion peptides[6] that induce mixing of host cell and viral membranes at acidic pH to release viral components.[7, 8] Other non-enveloped viruses release membrane-lytic peptides that enable escape of viral components into the cytosol. Several of these natural peptides have been characterized and often consist of a

hydrophobic or amphipathic helix that is kinked by internal proline or glycine residues.[9-11] Bacteria also utilize membrane disruptive agents as a virulence factor. For example, *Listeria monocytogenes* produces listerolysin O (LLO), a protein toxin that forms pores in cholesterol-containing membranes at acidic pH.[12, 13] Other organisms produce membrane-active antimicrobial peptides that adopt kinked helical structures similar to viral peptides.[14-17]

A number of synthetic peptides have been generated to mimic the pore forming activity of natural endosome disruptive peptides.[5, 18, 19] One example is the GALA peptide consisting of 30-amino acids with a repeating Glu-Ala-Leu-Ala sequence. This peptide forms hydrophobic alpha helices at acidic pH that insert into lipid bilayers. These membrane-spanning helices aggregate to form a pore structure capable of releasing endosomal contents.[18, 20]

In 2006, Weber and co-workers identified the PC-4 peptide using a phage display library.[21] This 12-amino acid peptide demonstrated pH-dependent leakage of lipid vesicles with activity similar to known viral peptides. The Peterson group hypothesized that targeting this peptide to early endosomes using cholesterylamine might disrupt these endosomes and allow release of entrapped cargo. In 2008, our group reported the synthesis of cholesterylamine-linked PC-4 and its ability to selectively disrupt early endosomes to release a disulfide-linked fluorophore into the cytosol of living mammalian cells (Figure 1.4).[3] Because early endosomes are oxidizing, the disulfide bond linking cholesterylamine to its fluorescent cargo remains stable and membrane bound.[22] However disruption of endosomes by cholesterylamine-PC-4 (**2**) exposes the

endosomal contents to reduced glutathione in the cytosol, cleaving the disulfide bond and enabling release of the free fluorophore.

As mentioned in Chapter 1, therapeutic applications of cholesterylamine-PC-4 are limited by the toxicity index, a ratio of the observed toxicity and potency in cultured cells. Moreover, its mechanism of endosome disruption was unclear. This chapter describes the evaluation of novel endosome disruptors with improved biological properties and studies to elucidate their mechanism of action. Building on the work of Dr. Qi Sun and Sutang Cai, these new endosome disruptors, synthesized by Drs. Chamani Perera and Ze Li, may serve as useful agents for the delivery of cell-impermeable therapeutic molecules.

3.2 Description of Biological Screening Assays

In order to accurately assess the potency and efficacy of new endosome disruptors, we used a biological screening assay similar to the assay used to quantify the activity of cholesterylamine-linked PC-4 (**2**).[3] In this assay, carboxyfluorescein is conjugated to cholesterylamine through a disulfide-containing linker and serves as the releasable cargo (**3**, Figure 3.1). This probe contains two anionic glutamic acid residues that increase its propensity to accumulate in early endosomes versus the plasma membrane. The pKa of carboxyfluorescein is 6.5.[23] Therefore in early endosomes at pH 6.0, the fluorescence of the probe is approximately 60 – 70% quenched. Upon endosome disruption, accumulation of the free fluorophore in the cytosol at pH 7.4 produces a 4- to 5-fold increase in cellular fluorescence that can be

measured by flow cytometry (Figure 3.1). Using Jurkat lymphocytes, the concentration of the fluorescent probe is held constant at 2.5 μM and the endosome disruptor is added at increasing concentrations. The cells are allowed to incubate for 14 hours, then washed with complete media and incubated for another 30 minutes to allow the excess intact fluorescent probe to efflux from the cell surface. This step was found to significantly increase the signal-to-noise ratio of the assay. The cellular fluorescence with no endosome disruptor is taken as the background signal and subtracted from subsequent concentrations for each compound. Cellular fluorescence is plotted versus disruptor concentration and fit using non-linear regression to generate potency data as EC_{50} values.

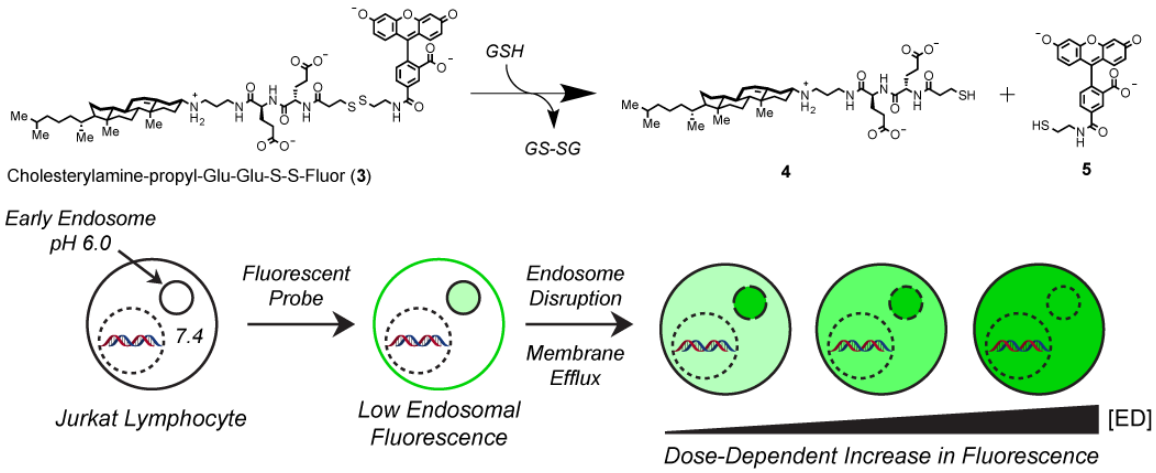

Figure 3.1. Schematic representation of the fluorescence assay used to obtain structure-activity relationships for endosome disruptors.

The efficacy of each endosome disruptor is determined by the amount of cellular fluorescence observed at concentrations where the activity is saturated. In order to accurately compare efficacy values and decrease interassay variability, each round of testing included one previously tested compound as a

control to which the efficacy is normalized. All values were normalized as percent efficacy as compared to the published cholesterylamine-PC-4 (**2**) at 100%.

The toxicity of each endosome disruptor was measured after incubating Jurkat lymphocytes at concentrations up to 32 μM for 48 hours. Analysis was performed by flow cytometry using forward and side light scattering to measure cell morphology. The percent viability was represented by the percent of cells that fall within a live cell gate.

Given that the majority of the endosome disruptors in this project are relatively hydrophobic peptides, we included thermodynamic solubility testing into our biological screening to aid in compound design. The vast majority of analogues contain a combination of tryptophan and tyrosine residues that allow for easy quantitation of concentration by UV absorbance at 280 nm. Using the calculated extinction coefficient for each peptide sequence, thermodynamic solubility was measured in PBS at pH 7.4.

3.3 Structure-Activity Relationships of Endosome Disruptor Analogues

Based on cholesterylamine-PC-4 (**2**), we designed several cholesterylamine-linked endosome disruptors to probe the structure-activity relationships (SAR) of the peptide sequence, linker, and membrane anchor regions of the molecule (Figure 3.2). The first structural analogues probed the SAR of the membrane anchor and linker regions. Inclusion of a β-alanine residue in the anchor and removal of aminohexanoic acid in the linker provided endosome disruptor **50** with similar activity to **2** (Figure 3.3, Table 3.1). The

membrane anchor of compounds **50** – **52**, containing β-alanine, was chosen based on the SAR provided by the fluorescent probes described in Chapter 2.

We then turned our attention to the PC-4 sequence. An initial screen was performed using an alanine scan in which each analogue systematically substituted each amino acid with alanine along the complete sequence. We found that substitution of each serine residue with alanine slightly enhanced potency (data not shown). The combined substitution of all serine residues produced compound **51**, which demonstrated an improved toxicity index.

We hypothesized that these peptides were helical in nature, and that this conformation influenced the observed activity. We systematically substituted the N-terminal alanine residues of **51** with aminoisobutyric acid (Aib, U), a residue known to increase the propensity of peptides to form alpha- and 3_{10}-helices.[24, 25] Compound **52** showed a 4-fold increase in potency compared to the parent PC-4 sequence with no increase in toxicity. Moreover, it provided evidence for our hypothesis that helix formation could be responsible for the observed activity.

It was known from the literature that lipid-conjugated molecules often possess poor pharmacokinetic (PK) properties, mostly due to high serum binding and/or high clearance by the liver.[26-28] In order to increase the therapeutic applicability of endosome disruptive compounds, we also studied compounds **53** – **55** that do not contain the membrane anchor. It was observed that compound **55** containing Aib residues demonstrated modest potency despite lacking the endosome targeting cholesterylamine moiety. This activity was beneficial for several reasons: 1) it increased the therapeutic potential of endosome disruptors

by eliminating the potential PK limitations of the lipid moiety, 2) it significantly decreased the time and cost of synthesis to produce analogues, and 3) it simplified the study by limiting the SAR to only the peptide sequence. We moved forward using the peptide sequence alone to study SAR of the peptide sequence and guide the design of new endosome disruptors. The optimal sequence from each round of analogues was also studied in conjugation with the membrane anchor to generate highly potent endosome disruptors for *in vitro* probe applications.

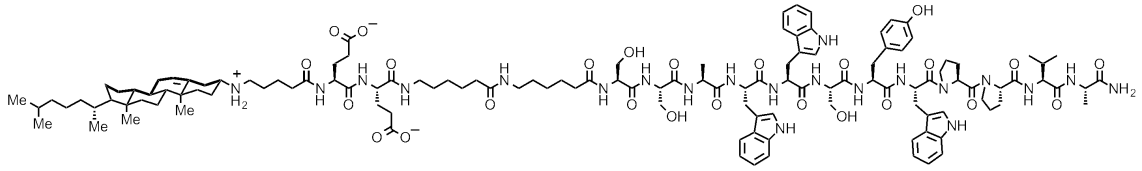

Cholesterylamine-Glu-Glu-Ahx-Ahx-SSAWWSYWPPVA-NH_2 (**2**, Cholesterylamine-PC-4 peptide)

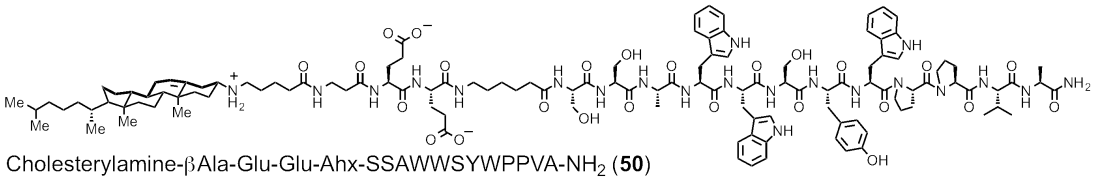

Cholesterylamine-βAla-Glu-Glu-Ahx-SSAWWSYWPPVA-NH_2 (**50**)

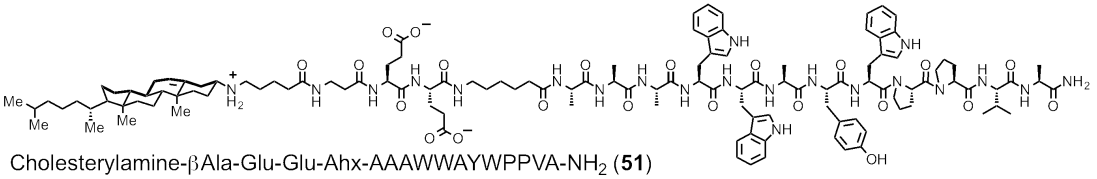

Cholesterylamine-βAla-Glu-Glu-Ahx-AAAWWAYWPPVA-NH_2 (**51**)

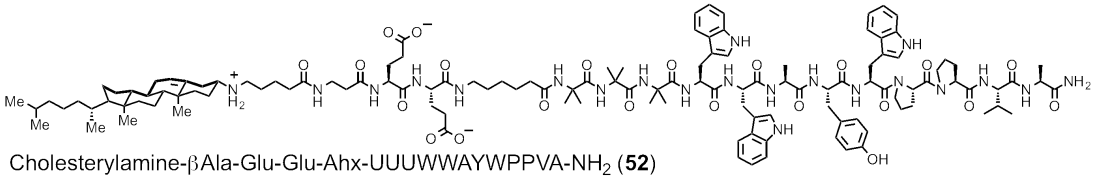

Cholesterylamine-βAla-Glu-Glu-Ahx-UUUWWAYWPPVA-NH_2 (**52**)

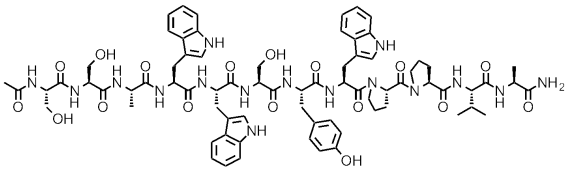

Ac-SSAWWSYWPPVA-NH_2 (**53**)

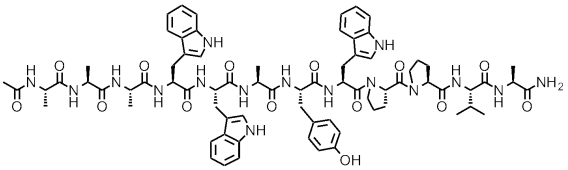

Ac-AAAWWAYWPPVA-NH_2 (**54**)

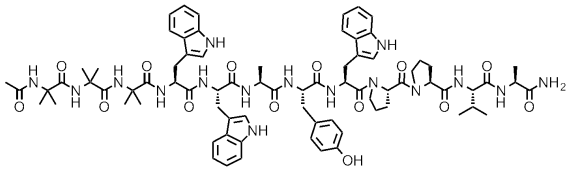

Ac-UUUWWAYWPPVA-NH_2 (**55**)

Figure 3.2. Structures of the previously published PC-4 peptide derivative (**2**) and endosome disruptor analogues **50** – **55**.

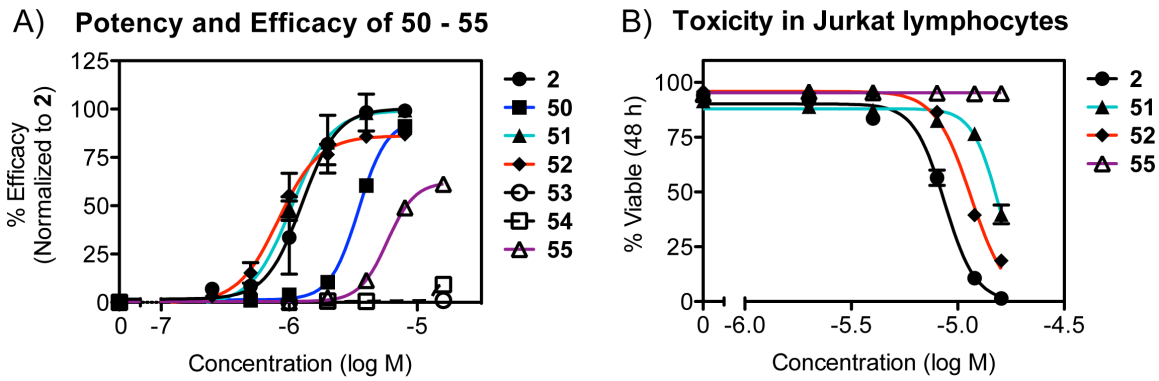

Figure 3.3. SAR of compounds **50** – **55** in Jurkat lymphocytes. A) Potency and efficacy based on the release of **3** after 14 h. B) Toxicity of select analogues in Jurkat lymphocytes after 48 h.

Cpd.	Sequence	Potency (EC_{50}, μM)	Efficacy (% of 2)	Toxicity (IC_{50}, μM)	Sol. (μM)
2	*MA*-SSAWWSYWPPVA-NH_2	1.3 ± 0.3	99 ± 2	9 ± 0.3	112
50	*MA*-SSAWWSYWPPVA-NH_2	3.5 ± 1.0	93 ± 2	*ND*	*ND*
51	*MA*-AAAWWAYWPPVA-NH_2	1.0 ± 0.3	101 ± 2	16 ± 0.6	*ND*
52	*MA*-UUUWWAYWPPVA-NH_2	0.4 ± 0.1	86 ± 1	12 ± 1.3	*ND*
53	Ac-SSAWWSYWPPVA-NH_2	*ND*	*ND*	*ND*	173
54	Ac-AAAWWAYWPPVA-NH_2	>15	<10	*ND*	41
55	Ac-UUUWWAYWPPVA-NH_2	5.9 ± 1.8	61 ± 2	>16	*ND*

Table 3.1. SAR data for endosome disruptors **50** – **55** compared to the published PC-4 peptide (**2**). Potency and efficacy (± standard deviation) were calculated based on non-linear regression of fluorescence (as a percentage of **2**) plotted versus concentration. *MA* = Membrane anchor. *ND* = Not Determined.

Using the Aib containing peptide **55** as a lead compound, we designed and tested new analogues highlighted by compounds **56** – **62** (Figure 3.4). Peptides **56** and **57** contained four and five N-terminal Aib residues, respectively, to further induce a helical confirmation. Both peptides showed improved potency compared to **55**, however it was found that addition of a fifth residue did not significantly improve activity versus four Aib residues.

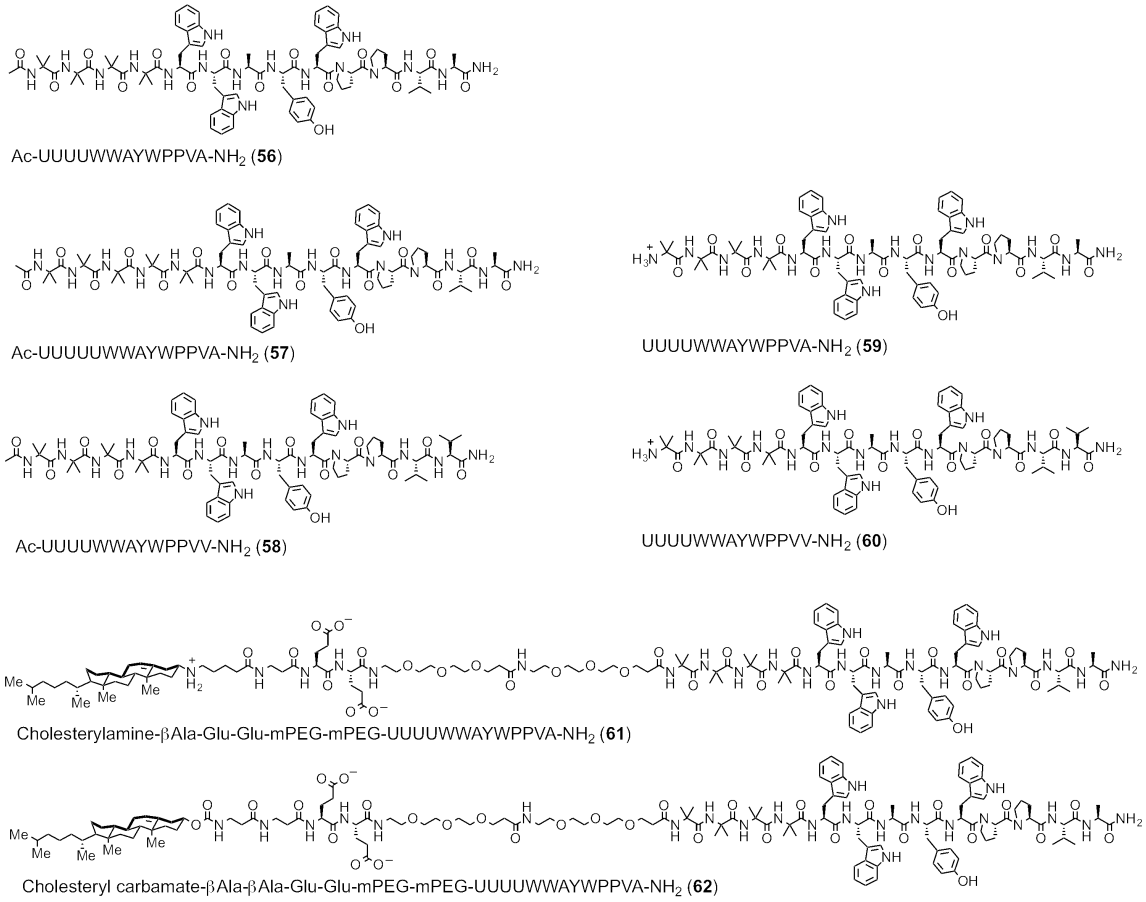

Figure 3.4. Structures of endosome disruptor analogues **56** – **62**.

Substitution of the C-terminal alanine with valine in peptide **58** was also shown to improve potency compared to **56**. To improve solubility, we evaluated peptides **59** and **60**, which eliminated the N-terminal acetyl group to provide a cationic amine. Peptide **59** showed a slight loss in activity compared to its acetylated analogue **56**. Peptide **60** containing the alanine to valine substitution showed similar properties to peptide **58**, indicating the cationic charge at the N-terminus was tolerated. Compounds **61** and **62** utilized the peptide sequence of **56** conjugated to cholesterylamine and cholesteryl carbamate containing membrane anchors, respectively. Both compounds included a miniature

polyethylene glycol amino acid (mPEG) linker to improve their solubility. These membrane anchored compounds showed 50- to 100-fold improvement in potency versus the parent peptide **56** and ~20-fold improvement versus the published cholesterylamine-PC-4 derivative (**2**).

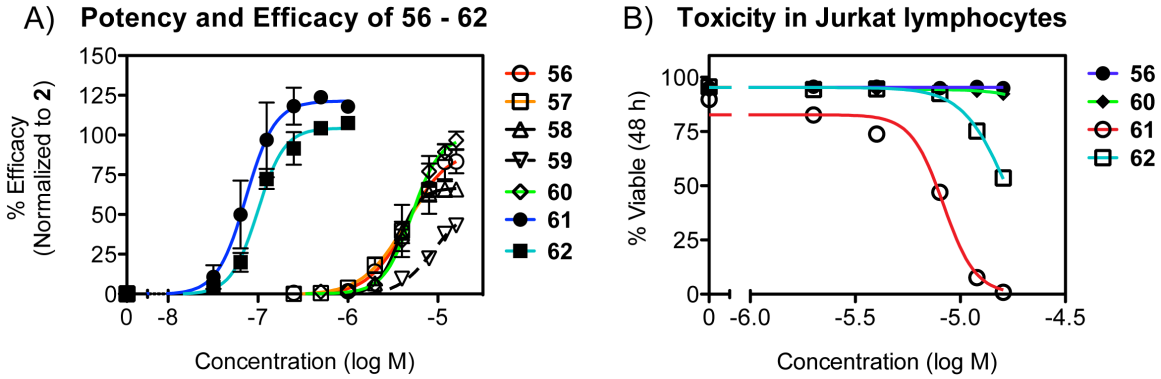

Figure 3.5. SAR of compounds **56** – **62** in Jurkat lymphocytes. A) Potency and efficacy based on the release of **3** after 14 h. B) Toxicity of select analogues in Jurkat lymphocytes after 48 h.

Cpd.	Sequence	Potency (EC_{50}, μM)	Efficacy (% of 2)	Toxicity (IC_{50}, μM)	Sol. (μM)
56	Ac-UUUUWWAYWPPVA-NH_2	4.9 ± 1.9	89 ± 13	>16	*ND*
57	Ac-UUUUUWWAYWPPVA-NH_2	4.2 ± 1.3	86 ± 7	*ND*	*ND*
58	Ac-UUUUWWAYWPPVV-NH_2	3.8 ± 1.1	68 ± 3	*ND*	*ND*
59	UUUUWWAYWPPVA-NH_2	8.8 ± 2.6	57 ± 7	*ND*	40
60	UUUUWWAYWPPVV-NH_2	5.1 ± 0.6	98 ± 2	>16	22
61	*MA*-UUUUWWAYWPPVA-NH_2	0.08 ± 0.02	123 ± 6	8 ± 0.2	*ND*
62	*MA*-UUUUWWAYWPPVA-NH_2	0.1 ± 0.03	106 ± 10	17 ± 0.4	*ND*

Table 3.2. SAR data for endosome disruptors **56** – **62**. Potency and efficacy (± standard deviation) were calculated based on non-linear regression of fluorescence (as a percentage of **2**) plotted versus concentration. *MA* = Membrane anchor. *ND* = Not Determined.

Based on the sequence of peptide **60**, we performed a second alanine scan to determine the importance of the aromatic and proline residues for

endosome disruptive activity. Our previous alanine scan proved fruitful in providing more potent analogues, however the activity of these compounds may have been driven by the high endosomal accumulation provided by the membrane anchor. Compounds **63** – **69** systematically replaced each residue with alanine to provide SAR for each amino acid in the peptide sequence alone (Figure 3.6).

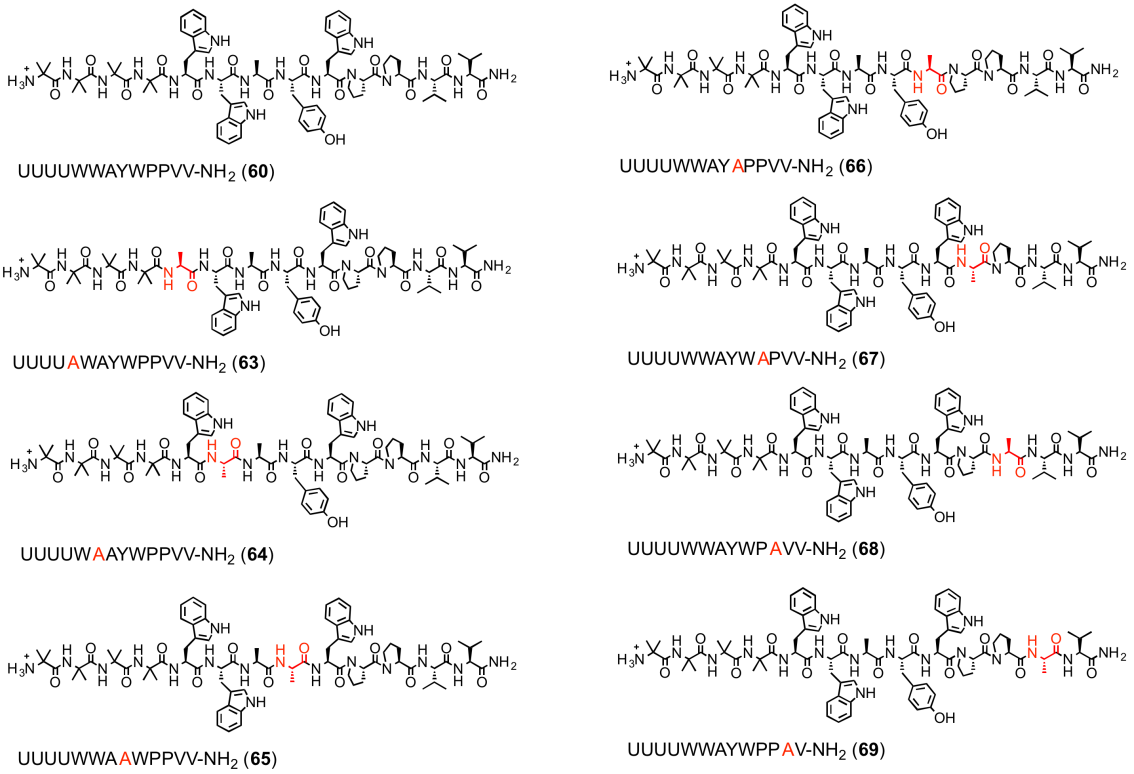

Figure 3.6. Structures of the alanine scan endosome disruptor analogues **63** – **69**. The alanine substitution for each compound is illustrated in red.

As shown in Table 3.3, compounds **63** – **66** containing substitutions of the aromatic residues showed a dramatic decrease in potency, with little to no observed activity at concentrations up to 16 μM. Compounds **67** and **68**, which substituted each proline residue, showed significant decreases in efficacy, but

still demonstrated some activity at high concentration. Compound **69**, substituting a valine in the C-terminal region, also showed some activity.

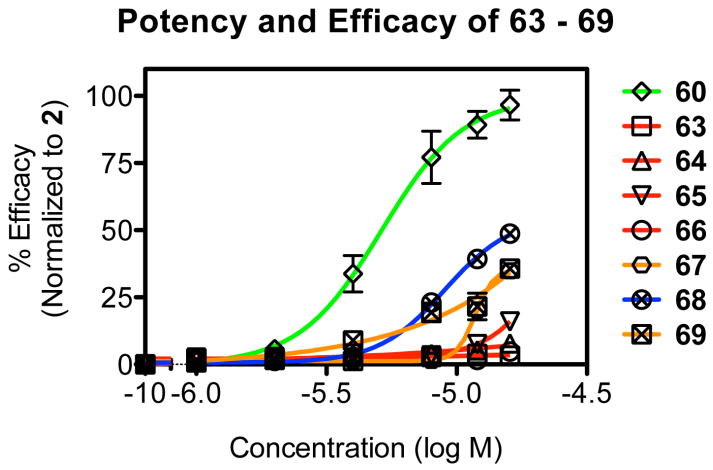

Figure 3.7. SAR of alanine scan compounds **63** – **69** compared to the parent sequence **60** in Jurkat lymphocytes. Potency and efficacy based on the release of **3** after 14 h.

Cpd.	Sequence	Potency (EC_{50}, μM)	Efficacy (% of 2)	Toxicity (IC_{50}, μM)	Sol. (μM)
60	UUUUWWAYWPPVV-NH_2	5.1 ± 0.6	98 ± 2	>16	22
63	UUUUAWAYWPPVV-NH_2	*ND*	<5	*ND*	86
64	UUUUWAAYWPPVV-NH_2	*ND*	<10	*ND*	86
65	UUUUWWAAWPPVV-NH_2	*ND*	*ND*	*ND*	63
66	UUUUWWAYAPPVV-NH_2	*ND*	<5	*ND*	86
67	UUUUWWAYWAPVV-NH_2	*ND*	~35	*ND*	21
68	UUUUWWAYWPAVV-NH_2	9.0 ± 2.7	54 ± 4	*ND*	22
69	UUUUWWAYWPPAV-NH_2	*ND*	~35	*ND*	48

Table 3.3. SAR data for alanine scan analogues **63** – **69**. Potency and efficacy (± standard deviation) were calculated based on non-linear regression of fluorescence (as a percentage of **2**) plotted versus concentration. *ND* = Not Determined.

Based on the dramatic loss of activity for peptides **63** – **66**, the alanine scan indicated that the aromatic residues were critical for activity. Thus, we tested several analogues to probe the sequence of the aromatic residues. Compounds **70** – **73** substituted each tryptophan residue with tyrosine, and compounds **74** and **75** substituted the central alanine residue to tryptophan and tyrosine, respectively, to increase the total aromatic content (Figure 3.8).

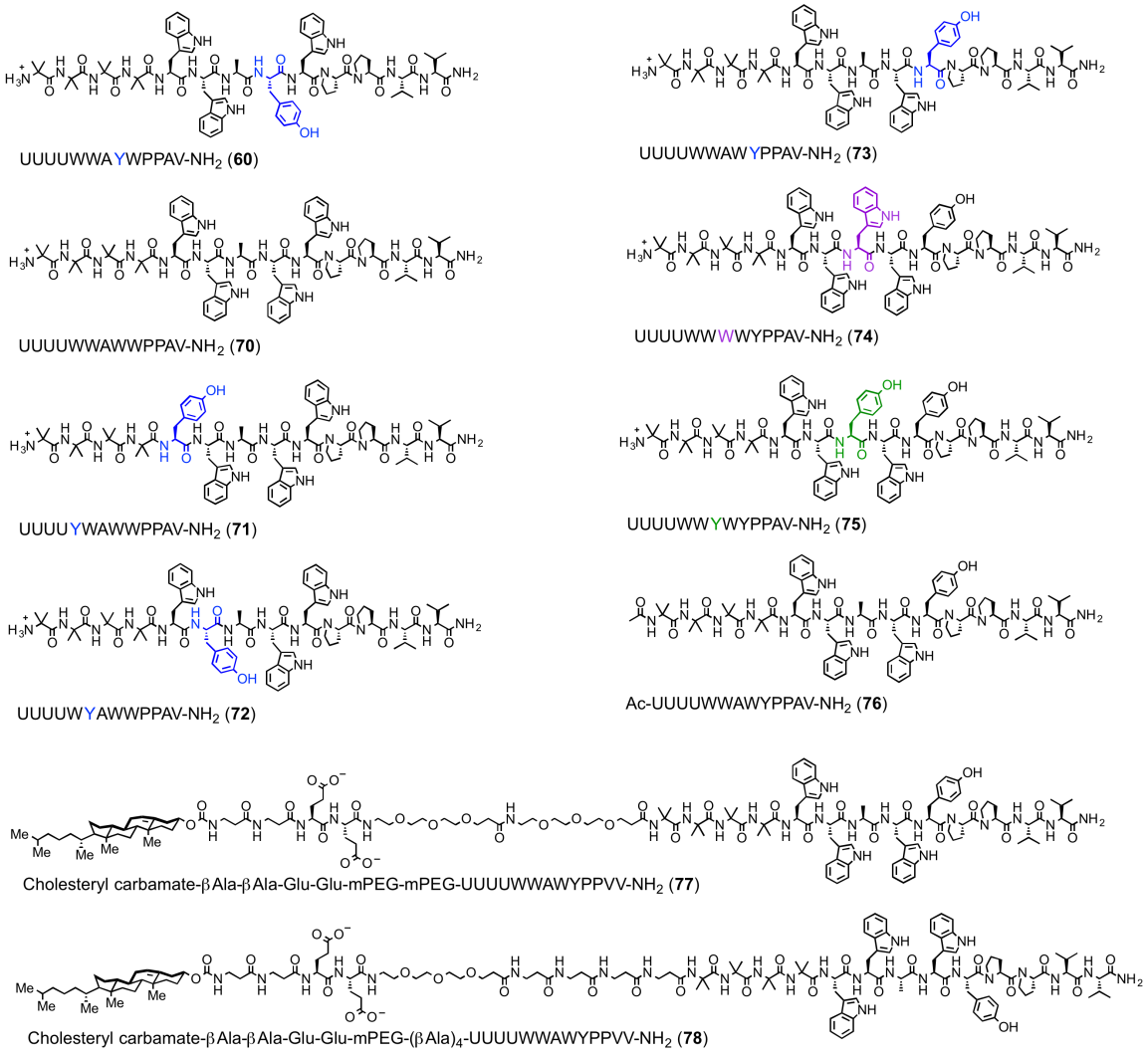

Figure 3.8. Structures of the endosome disruptor analogues **70** – **78**. Tyrosine (blue) was substituted along the aromatic residues in **71** – **73**. The central alanine was also substituted for either tryptophan (**74**, purple) or tyrosine (**75**, green).

Substitution of tryptophan with tyrosine for compounds **70** – **73** did not significantly change either potency or efficacy. Interestingly, compounds **74** and **75** showed a dramatic loss of efficacy, indicating that the addition of a larger amino acid at this position was not tolerated (Table 3.4). The sequence of peptide **73** was integrated into compounds **77** and **78** containing the cholesteryl carbamate membrane anchor. Again, these compounds demonstrated approximately a 50-to 200-fold increase in potency versus the peptide sequence alone.

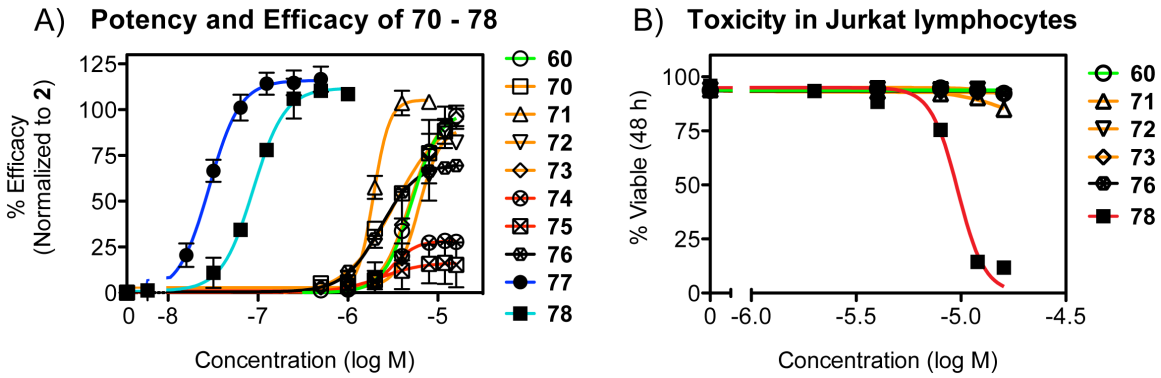

Figure 3.9. SAR of compounds **70** – **78** in Jurkat lymphocytes. A) Potency and efficacy based on the release of **3** after 14 h. B) Toxicity of select analogues in Jurkat lymphocytes after 48 h.

Cpd.	Sequence	Potency (EC_{50}, μM)	Efficacy (% of 2)	Toxicity (IC_{50}, μM)	Sol. (μM)
60	UUUUWWAYWPPVV-NH_2	5.1 ± 0.6	98 ± 2	>16	22
70	UUUUWWAWWPPVV-NH_2	3.4 ± 1.0	100 ± 5	*ND*	*ND*
71	UUUUYWAWWPPVV-NH_2	3.2 ± 1.4	105 ± 19	>16	21
72	UUUUWYAWWPPVV-NH_2	6.7 ± 2.0	96 ± 12	>16	28
73	UUUUWWAWYPPVV-NH_2	5.4 ± 1.6	101 ± 2	>16	13
74	UUUUWWWWYPPVV-NH_2	3.1 ± 0.9	27 ± 1	*ND*	*ND*
75	UUUUWWYWYPPVV-NH_2	2.5 ± 1.2	18 ± 12	*ND*	*ND*
76	Ac-UUUUWWAWYPPVV-NH_2	2.3 ± 0.7	70 ± 1	>16	5
77	*MA*-UUUUWWAWYPPVV-NH_2	0.06 ± 0.02	118 ± 7	10 ± 0.4	*ND*
78	*MA*-UUUUWWAWYPPVV-NH_2	0.08 ± 0.02	111 ± 2	10 ± 0.1	*ND*

Table 3.4. SAR data for analogues **70** – **78**. Potency and efficacy (± standard deviation) were calculated based on non-linear regression of fluorescence (as a percentage of **2**) plotted versus concentration. *MA* = Membrane anchored. *ND* = Not Determined.

3.4 Evaluation of Helicity by Circular Dichroism

To evaluate the hypothesis that helicity of these peptides is responsible for the observed activity, we obtained electronic circular dichroism (CD) spectra of selected analogues. These experiments were conducted in buffer at pH 7 to mimic the extracellular environment, at pH 5 to mimic the acidic lumen of endosomes, and in methanol to mimic the hydrophobic environment of membranes. CD spectra of α- and 3_{10}-helical peptides typically exhibit negative minima at ~208 and ~222 nm and a positive maximum at ~195 nm.[29, 30] This type of spectroscopy cannot readily distinguish between these types of helices,[31] and peptides containing helix-promoting residues are often comprised of mixtures of

α- and 3_{10}-helices in equilibrium, or these helices may co-exist in the same molecule.[32]

As shown in Figure 3.10, CD spectra of the inactive peptides **53** and **54** showed negative minima near 200 nm in both aqueous buffer and methanol, consistent with a lack of secondary structure. In pH 7 buffer, the active peptides **73** and **76** also showed a lack of secondary structure. However, in aqueous solution at pH 5, peptide **73** containing a protonated N-terminus, but not its acetylated analogue **76**, showed increased negative ellipticity near 208 and 222 nm, suggesting increased ordering. The intensities of these minima were increased in methanol for both **73** and **76**. Moreover, **73** exhibited a prominent maximum at 195 nm, consistent with the adoption of a helical secondary structure.

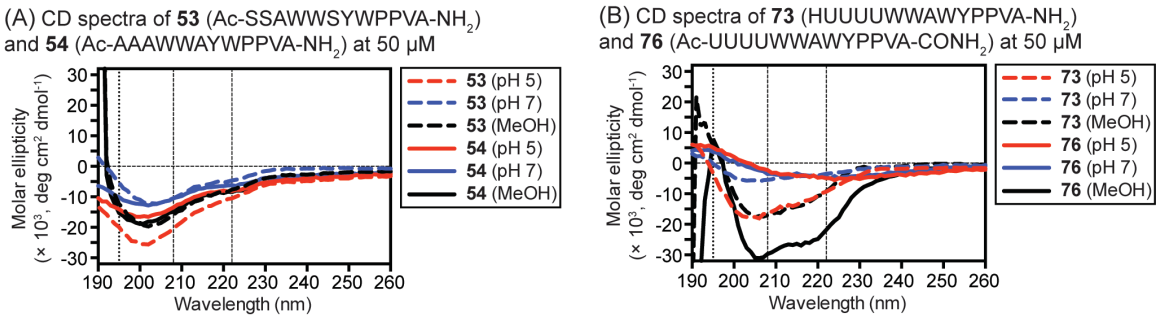

Figure 3.10. Circular dichroism spectra of **53**, **54**, **73**, and **76**. Spectra generated in aqueous buffer at pH 5 and pH 7 were obtained in phosphate buffer (10 mM) containing 5% MeOH. Markers (thin dashed lines) are shown at 195, 208, and 222 nm, and molar ellipticity = 0 to illustrate bands commonly associated with helical secondary structure.

3.5 Molecular Modeling of Endosome Disruptive Peptides

SAR and CD studies provided valuable information regarding the mechanism of endosome disruptive activity. Introduction of aminoisobutyric acid

(Aib) residues significantly increased potency, likely by inducing a helical conformation in the hydrophobic environment of the lipid bilayer. Alanine scanning illustrated that the aromatic residues were critical to activity. These aromatic positions could contain either tryptophan or tyrosine and maintain similar potency and efficacy. However the sequence of these residues was observed to be highly specific, requiring an "XXAXX" motif where X represents either tryptophan or tyrosine. Substitution of the alanine residue in this motif also resulted in a significant loss in efficacy.

Using this information, we modeled the sequence of compound **76** as idealized α- and 3_{10}-helices (Figure 3.10, Panels A and B). Literature precedent and CD spectroscopy suggested that the Aib residues increased the propensity for peptides to adopt either conformation.[24, 25] When modeled as an α-helix, **76** is approximately 26 Å in length, which is much shorter than the thickness of a mammalian cell lipid bilayer (phosphate-phosphate distance of 35 – 43 Å when measured by X-ray scattering).[33] This conformation also projects the crucial aromatic side chains at four different angles around the helical axis. However when modeled as a 3_{10} helix, the peptide length increases to approximately 32 Å, which is only slightly shorter than the thickness of a lipid bilayer. More importantly, this conformation orients the aromatic side chains at 120° angles from each other, with the alanine residue occupying a hydrophobic face of the helix. Based on this modeling, we hypothesized that the 3_{10}-helical conformation of this peptide could self-assemble into a hexameric pore structure in the membranes of acidic compartments. In this model, an antiparallel assembly

would allow pi-stacking interactions between the aromatic side chains to define the walls of the pore, whereas the aliphatic residues would occupy a hydrophobic face projecting towards the lipid bilayer (Figure 3.11, Panel C). In support of this concept, related antiparallel peptide hexamers that form conductive channels in membranes have been identified in biological systems.[34] Additionally, designed 32-amino acid peptides that self-assemble as a hexamer of parallel alpha helices to form a 6 Å channel have been reported.[35]

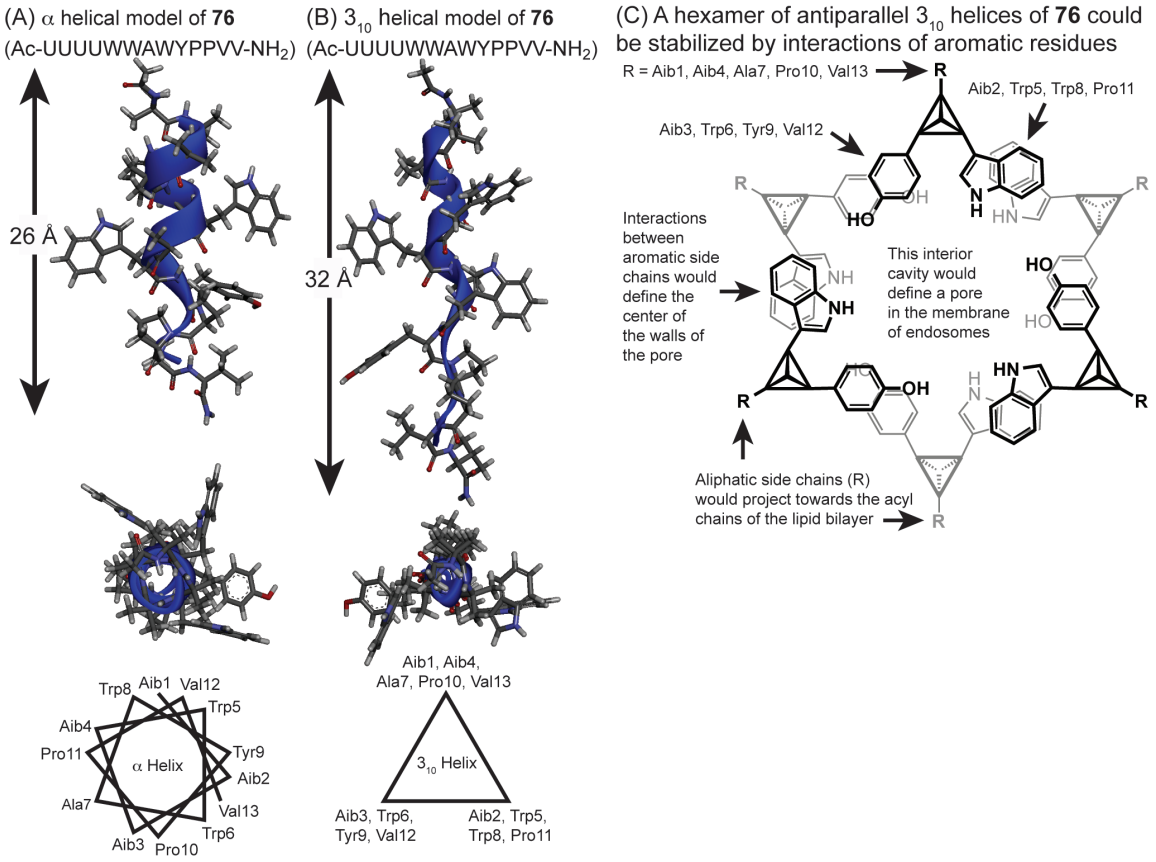

Figure 3.11. Models of **76** as an idealized α- or 3_{10}-helix (Panel A, B). A model assembly of an antiparallel hexamer stabilized by intermolecular interactions of aromatic side chains.

3.5 Optimized Endosome Disruptive Peptides

To test the model shown in Figure 3.11, we designed new peptides based on the idealized 3_{10} helix. We hypothesized that introducing three amino acids to the peptide sequence would extend the helix by one full turn, increasing the peptide length and possibly providing more stability to the hexameric assembly. The critical "XXAXX" sequence was extended to "XXAXXAXX" to produce compounds **79** – **82** with two more aromatic side chains in the correct orientation to provide additional pi-stacking interactions to the current model.

The extended peptide **79** bears an additional WWA sequence to add a tryptophan reside to each aromatic face. This peptide showed a 13-fold increase in potency compared to **73** with only a slight decrease in efficacy, however its solubility was quite low. Peptides **80** and **81** replaced two or three of the tryptophan residues with tyrosine to improve solubility. These peptides demonstrated 20- and 10-fold improved potency, respectively, as well as improved efficacy and solubility. Additionally, CD spectra of **80** and its acetylated analogue **82** were similar to the shorter peptides **73** and **76**, and provided evidence of a helical secondary structure in methanol (Figure 3.13, Panel C). As a control, compound **83** was designed to possess the same amino acids as **80**, but as a scrambled sequence that does not contain the crucial "XXAXXAXX" motif. As shown in Table 3.5, this compound showed a significant loss of activity (~25-fold), consistent with the proposed model. Conjugation of the extended peptide sequence of **81** to the cholesteryl carbamate membrane anchor provided compound **84**. This compound produced nearly 100-fold greater potency than the

original PC-4 endosome disruptor (**2**), along with improved efficacy and no increase in cellular toxicity.

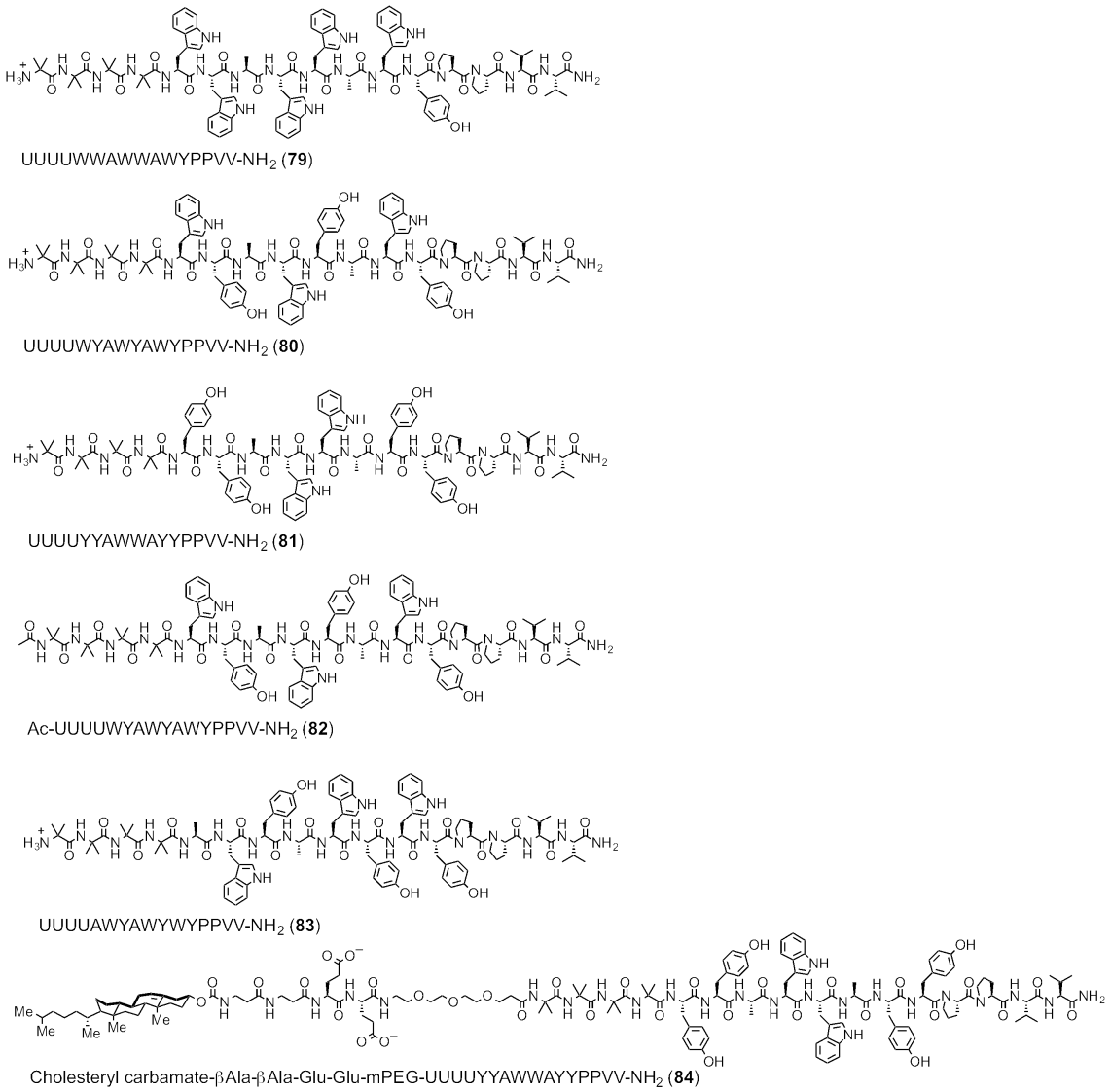

Figure 3.12. Structures of endosome disruptor analogues **79** – **84**.

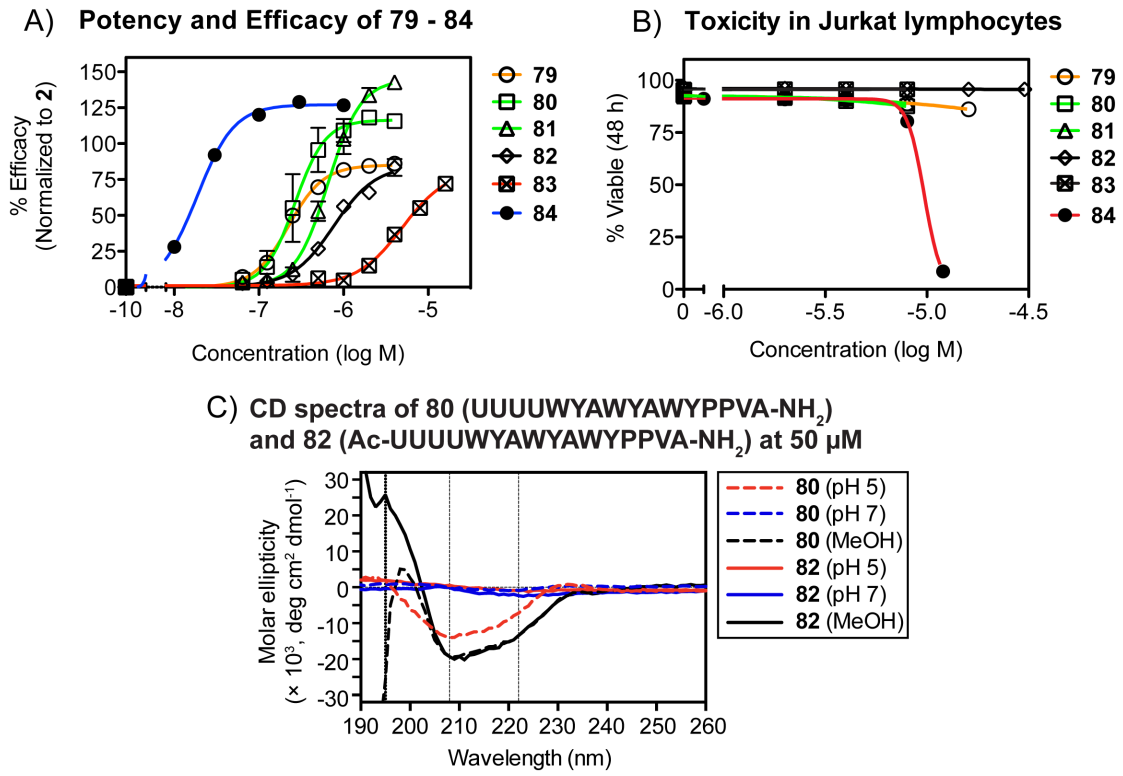

Figure 3.13. SAR of compounds **79** – **84** in Jurkat lymphocytes. A) Potency and efficacy based on the release of **3** after 14 h. B) Toxicity in Jurkat lymphocytes after 48 h. C) Circular dichroism spectra for **80** and **82**.

Cpd.	Sequence	Potency (EC_{50}, µM)	Efficacy (% of 2)	Toxicity (IC_{50}, µM)	Sol. (µM)
73	UUUUWWAWYPPVV-NH_2	5.4 ± 1.6	101 ± 2	>16	8
79	UUUUWWAWWAWYPPVV-NH_2	0.22 ± 0.01	86 ± 54	>16	2
80	UUUUWYAWYAWYPPVV-NH_2	0.28 ± 0.10	113 ± 4	>16	5
81	UUUUYYAWWAYYPPVV-NH_2	0.33 ± 0.10	145 ± 5	>16	6
82	Ac-UUUUWYAWYAWYPPVV-NH_2	0.77 ± 0.23	85 ± 7	>16	1
83	UUUUAWYAWYWYPPVV-NH_2	8.9 ± 5.6	83 ± 12	>16	3
84	*MA*-UUUUYYAWWAYYPPVV-NH_2	0.02 ± 0.01	128 ± 2	11 ± 0.2	66

Table 3.5. SAR data for analogues **79** – **84**. Potency and efficacy (± standard deviation) were calculated based on non-linear regression of fluorescence (as a percentage of **2**) plotted versus concentration. *MA* = Membrane anchor. *ND* = Not Determined.

3.6 Cell-Based Assay for Functional Determination of Pore Size

To further validate the model shown in Figure 3.11, we synthesized the cholesterol-linked fluorescent probes **85** – **87**. These probes were designed to release fluorescent cargo that systematically increased in molecular size. We hypothesized that the efficacy of endosome disruption would dramatically decrease as we increased the size of the releasable cargo beyond the diameter of the proposed pore structure. As shown in Figure 3.14, the size of the released cargo ranged from a minimal projection diameter (MPD) of 12.4 Å (**3**) to 17.9 Å (**87**), as calculated with ChemAxon software (MMFF94 force field). The cholesteryl carbamate membrane anchor in compounds **85** – **87** was chosen as a more easily synthesized alternative to the cholesterylamine of **3**.

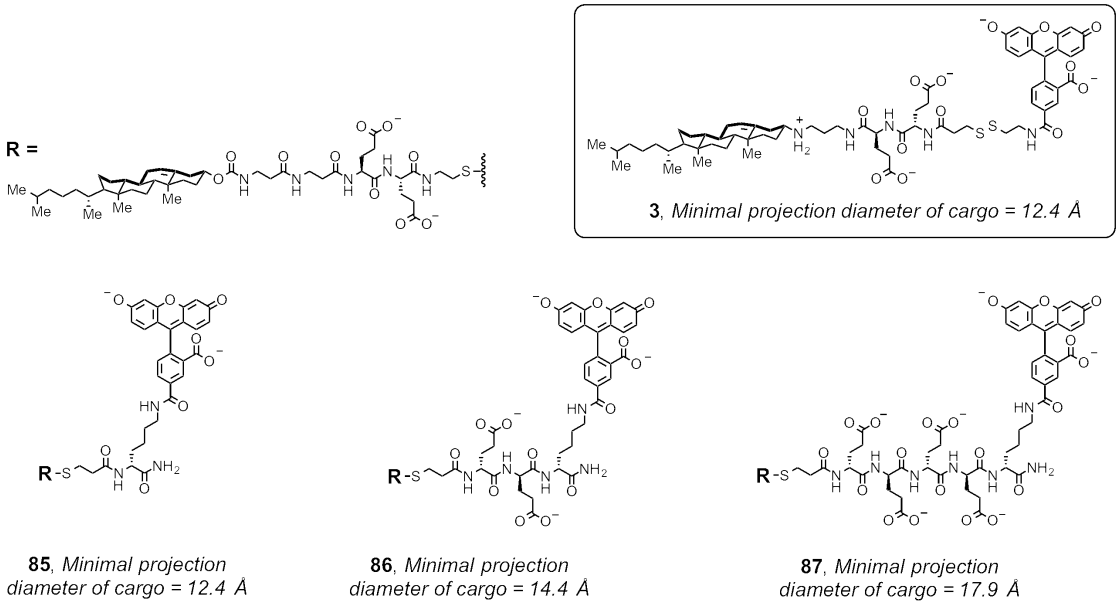

Figure 3.14. Structures of the fluorescent disulfide probes **85** – **87** containing glutamic acid residues to increase molecular size of the released cargo. D-amino acids were used to synthesize the cargo to avoid potential proteolysis. Values for the minimal projection diameter of the thiol cleavage products were calculated using the geometry plugin of ChemAxon MarvinView v. 6.2.3 after conformational sampling with the MMFF94 force field (www.chemaxon.com).

These probes were used to measure the diameter of the pore induced in endosomes by the peptides **2** (cholesterylamine-PC-4), **73**, and **80**. The fluorescent probe **3** was included in the evaluation and used to normalize the efficacy of release (Figure 3.15). In these experiments, the smallest cargo of compounds **3** and **85** was released from endosomes to the greatest extent. The largest cargo of **87** was not released by any of the peptides tested. Linear regression analysis of efficacy versus MPD of the cargo for the related compounds **85** – **87** indicated that a calculated MPD of ≤ 15 Å is required for at least 50% release of these types of probes. This data provides experimental evidence that the maximum inner diameter of the pore induced by these endosome disruptive peptides is ~ 15 Å.

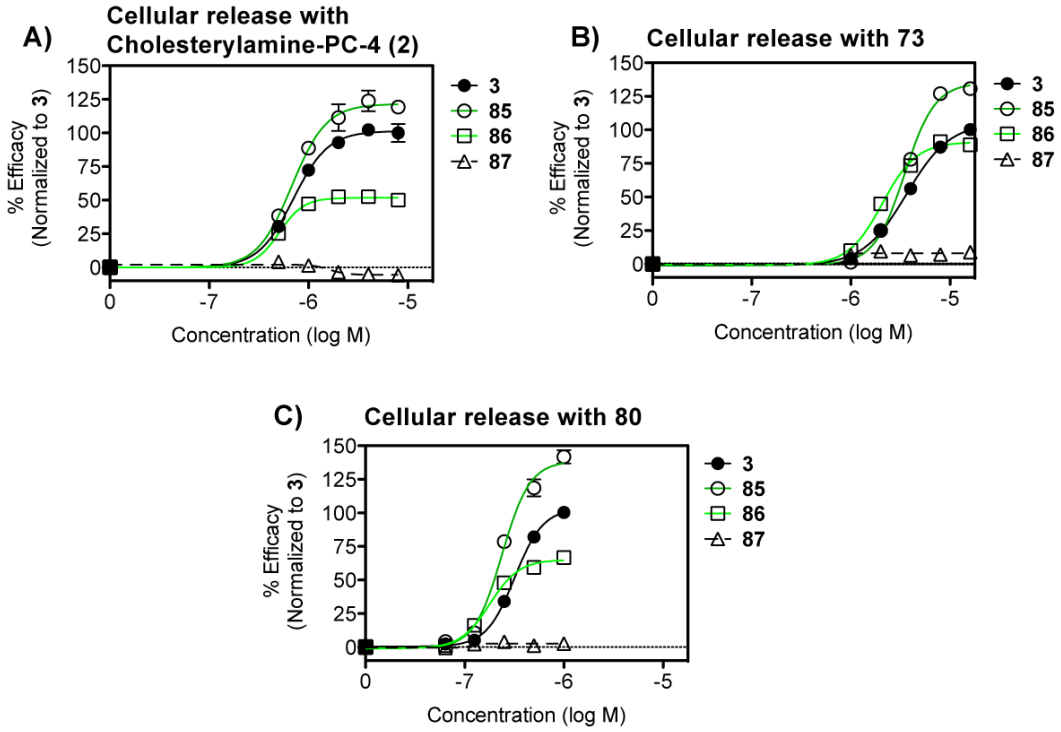

Figure 3.15. Evaluation of pore size using fluorescent probes **85** – **87** (2.5 μM). Endosome disruptors **2** (cholesterylamine-PC-4, Panel A), **73** (Panel B), and **80** (Panel C) were used to evaluate cellular release by flow cytometry. Potency and efficacy based on release after 14 h.

		3		85		86		87	
ED	**Sequence**	**Pot. (EC_{50}, μM)**	**Eff. (%)**	**Pot. (EC_{50}, μM)**	**Eff. (%)**	**Pot. (EC_{50}, μM)**	**Eff. (%)**	**Pot. (EC_{50}, μM)**	**Eff. (%)**
2	*MA*-SSAWWSYWPPVA-NH_2	0.7	*100**	0.7	122	0.5	52	*ND*	<5
73	UUUUWWAWYPPVV-NH_2	3.6	*100**	3.5	135	2.1	91	*ND*	<10
84	UUUUWYAWYAWYPPVV-NH_2	0.3	*100**	0.2	139	0.2	65	*ND*	<5

Table 3.6. Cellular release of fluorescent probes **85** – **87** containing glutamic acid residues as a measure of endosome disruptor pore size. *Efficacy values for each endosome disruptor were normalized to release of **3** at 100%. Potency and efficacy were calculated based on non-linear regression of efficacy plotted versus concentration. Measurements were determined in duplicate and standard deviation values were ~30% for potency and <5% for efficacy. *MA* = Membrane anchored. *ND* = Not Determined due to lack of efficacy.

3.7 Molecular Dynamics Simulations of the Proposed Model

Our collaborator, Dr. Gerry Lushington, performed molecular dynamics (MD) simulations to evaluate the structures of anti-parallel hexamers of peptides **76** and **82** in a model membrane. Dynamic stability of the model pore complexes was evaluated via Nanoscale Molecular Dynamics (NAMD)[36] simulations according to the CHARMM[37] force field and electrostatics with recently described parameters for peptides containing Aib.[38] As shown in Figure 3.16, these studies revealed that peptides **76** and **82** could form relatively stable pores comprising anti-parallel hexamers. Analysis of phi and psi angles indicates that contributions from both α- and 3_{10}-helices play major roles in the stability of these assemblies. Based on measurements of pore geometry during the MD simulations, these studies calculated pore diameters of 12.8 ± 7.6 Å for **76** and 12.2 ± 5.6 Å for **82** with mean bottleneck diameter of 7.0 Å for **76** and 7.6 Å for **82**. These calculated values are consistent with the experimental data shown in Figure 3.15 and Table 3.6, where anionic cargo with a calculated MPD of ≤ 15 Å could escape through

the pore into the cytosol whereas cargo of MPD ≥ 18 Å remained trapped in the lumen of endosomes.

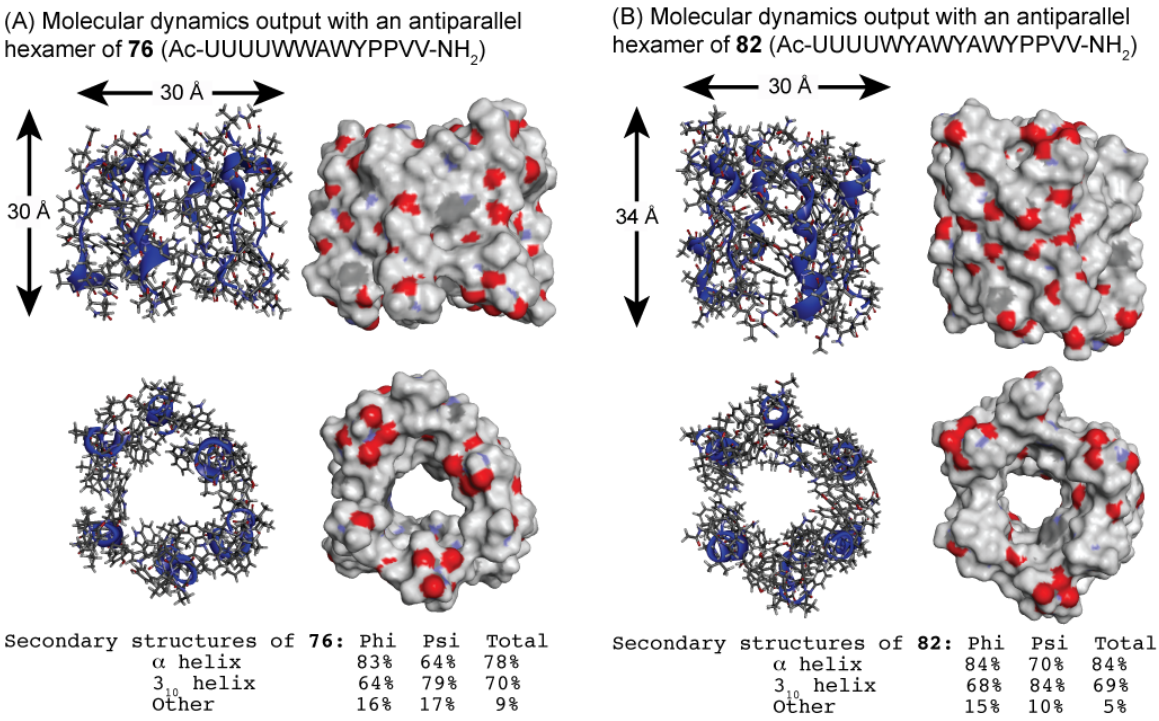

Figure 3.16. Output from molecular dynamics simulations of endosome disruptors **76** and **82** as anti-parallel hexamers of 3_{10} helices. Structures were extracted after 20,000-step MD simulations surrounded by lipids of a model membrane with explicit solvation by water. Membrane lipids and water molecules included in the simulation were removed for clarity. Values for secondary structure calculations do not sum to 100% due to overlap (± 27.5 degree error threshold) in definitions of alpha and 3_{10}-helices for dynamic structures.

3.8 Conclusions

The Peterson lab has previously demonstrated that a pH-dependent membrane disruptive peptide can be targeted to early/recycling endosomes to allow for efficient release of disulfide-linked cargo.[3] However in order to expand this delivery system beyond proof-of-concept, several limitations needed to be

addressed including the narrow toxicity index, limited *in vivo* applicability, and a poor understanding of the mechanism of action.

Through extensive SAR evaluation we have produced endosome targeted peptides containing cholesterol-based membrane anchors that are nearly 100-fold more potent than the parent cholesterylamine-PC-4 compound. More importantly, we have developed several active peptides with sub-micromolar potency that do not require the membrane targeting cholesterol moiety. None of the compounds highlighted by this SAR study have shown any significant increase in toxicity compared to the parent cholesterylamine-PC-4 compound. Because of this work, we have greatly improved the toxicity index and begun to address the limitations of *in vivo* applicability by eliminating the potential pharmacokinetic problems associated with lipid-conjugated molecules.

We also made significant progress toward understanding the mechanism of endosome disruptive activity. Based on key structure-activity relationships and circular dichroism studies, we hypothesized that these peptides formed helices in lipid membranes and self-assembled into a hexameric pore structure with aromatic residues forming critical stabilizing interactions. This model guided the design of extended peptide sequences that significantly improved cellular activity. We began to validate this model by probing the diameter of the proposed pore structure using fluorescent cargo with increasing molecular size. These results provided experimental evidence that the proposed pore structure was ~ 15 Å in diameter. In collaboration with Dr. Gerry Lushington, we provided further evidence for this model using molecular dynamics simulations. This analysis

illustrated that helical peptides could form a stable, hexameric pore structure in model lipid membranes with pore geometry consistent with the proposed model. Further structural validation is currently ongoing using NMR spectroscopy and crystallization trials to attempt to produce an X-ray crystal structure.

In summary, we have developed endosome disruptive peptides with significantly improved activity and toxicity index. These compounds allow for efficient release of small molecule cargo from early endosomes and possess numerous potential applications for the delivery of cell-impermeable therapeutic agents. Currently efforts are focused on utilizing these peptides for the selective delivery of cytotoxic agents to tumor cells and this work will be discussed in Chapter 4.

3.9 Experimental Section

3.9.1 General

Chemical reagents were purchased from Apptec, Acros, Aldrich, Alfa Aesar, EMD Biosciences, or TCI America, and were used without further purification. Solvents were from Aldrich or Fisher Scientific. Fmoc-protected 3-((2-aminoethyl)disulfanyl)propanoic acid[3], 3β-cholesterylamino-N-valeric acid[3], 3-((((cholester-3-yl)oxy)carbonyl) amino)propanoic acid[39], 5-carboxyfluorescein NHS ester[40], and the fluorescent disulfide probe (**3**)[3] were prepared as previously described. All endosome disruptor compounds were synthesized by Dr. Chamani Perera or Dr. Ze Li and provided with >95% purity based on analytical HPLC profiling. Column chromatography employed Silica Gel (SiliCycle, 40-63 μm).

Preparative HPLC employed an Agilent 1200 Series preparative pump / gradient extension with a Hamilton PRP-1 (polystyrene-divinylbenzene) reverse-phase preparative column (10-12 μm particle size, 21.5 mm x 25 cm) with a flow rate of 25.0 mL/min. HPLC fractions containing water were dried using a Labconco FreeZone 4.5 lyophilizer. Compounds containing basic amines were isolated as TFA salts. Analytical HPLC traces were acquired using an Agilent 1100 Series quaternary pump and a Hamilton PRP-1 (polystyrene-divinylbenzene) reverse phase analytical column (7 μm particle size, 4 mm x 25 cm) with diode-array detection at either 215 or 254 nm. Chromatograms were acquired at 45 °C to minimize rotational isomers, however in some cases small peak shoulders can be observed in the analytical HPLC trace. Coalescence of these shoulders was significantly improved by increasing the analysis temperature and also provided equivalent m/z by LR-MS consistent with rotational isomers. Analytical HPLC traces employed a gradient elution of H_2O:CH_3CN (90:10 to 0:100) with added TFA (0.1%) over 20 min and a 100% CH_3CN wash for an additional 5 min. Purity was determined by integration of the chromatogram. Low-resolution mass spectra (LRMS) were obtained using a Waters Micromass ZQ instrument with ESI+ or ESI-. Peaks are reported as *m/z*.

3.9.2 Synthetic Procedures and Characterization

General Procedure for Solid Phase Peptide Synthesis (SPPS). SPPS for compounds **50** – **84** was performed on a Mettler Toledo MiniBlock reactor (Model No: Bohdan 2080; 12-well block with glass reaction vessels, 600 rpm) utilizing

standard Fmoc chemistry employing Rink amide MBHA resin (0.5 mmol/g, 100 mg, 0.05 mmol). The following amino acids were used in the syntheses: Fmoc-Ser(O*t*-Bu)-OH, Fmoc-Ala-OH, Fmoc-Trp(Boc)-OH, Fmoc-Tyr(O*t*-Bu)-OH, Fmoc-Pro-OH, Fmoc-Val-OH, Fmoc-Glu(O*t*-Bu)-OH, Fmoc-Ahx-OH, Fmoc-β-Ala-OH, and Fmoc-Aib-F. The resin was swelled in DMF for 2 h and the Fmoc group removed by agitating with deblocking solution (20% piperidine in DMF (2 mL), two times, for 4 minutes each). The resin was washed four times with DMF (2 mL) to remove any traces of piperidine, and treated with Fmoc-amino acids (4 eq.), HATU coupling reagents (3.8 eq.), and DIEA (8 eq.) in 2 ml of DMF with agitation until coupling was completed by Kaiser Test (3h , 6h, or 12 h). Once the coupling was complete, the reaction solution was removed and resin was washed four times with DMF (2 mL). This coupling protocol was repeated for each additional Fmoc-amino acid. The hindered 2-aminoisobutyric acid (Aib) was coupled via acid fluoride chemistry. Fmoc-Aib-F was synthesized using DAST chemistry.[41] Fmoc-Aib-F (4 eq.) was dissolved in 0.5 mL of DMF, added to the resin, and agitated for 2 h. For acetylated peptides, the final amine was capped by agitating with acetic anhydride/DIEA/DMF (1:2:7) for 1 h. For cholesterol modified peptides, the peptide was capped with either 3β-cholesterylamino-N-valeric acid[3] or 3-((((cholester-3-yl)oxy)carbonyl) amino)propanoic acid[39] using the general coupling protocol with HATU. Synthesis of compounds **85** – **87** and **89** employed a 50 mL peptide synthesis vessel (Quark Glassware) with a wrist action shaker and standard Fmoc amino acid methodology described above. Cleavage from Rink amide MBHA resin (compounds **50** – **87**) was done using a

mixture of TFA/H_2O/TIPS (95/2.5/2.5) with agitation for 2 h. Cleavage from 2-chlorotrityl resin (compound **89**) was done by treatment with a mixture of DCM/TFE/acetic acid (7/2/1) with shaking for 2 h. The resin was removed by filtration and washed with DCM (2 mL, 3x) or DMF (2 mL, 3x). The filtrates were combined and concentrated under vacuum to give crude products. Purification was done using preparative reverse-phase HPLC (gradient: 90/10 H_2O/MeCN to 100% MeCN over 20 min with 0.1% TFA added).

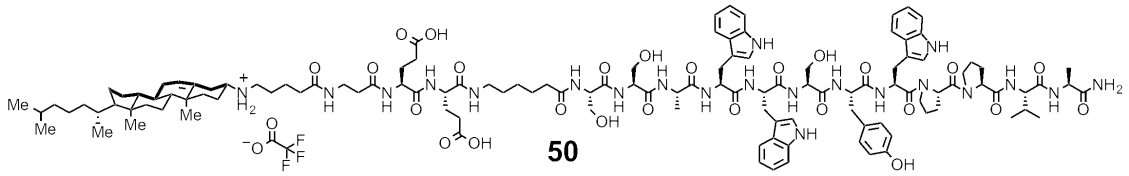

50

***N*-(5-(3β-cholest-5-en-3-ylammonio)pentanoyl)-β-Alanyl-L-Glutamyl-L-Glutamyl-Aminohexanoyl-L-Seryl-L-Seryl-L-Alanyl-L-Tryptophyl-L-Tryptophyl-L-Seryl-L-Tyrosyl-L-Tryptophyl-L-Prolyl-L-Prolyl-L-Valyl-L-Alaninamide (50).** Using the general SPPS procedure, Rink amide MBHA resin (0.5 mmol/g, 100 mg, 0.05 mmol) was used to produce **50** (42 mg, 0.017 mmol, 36% yield overall) as a white solid. LR-MS (ESI-) m/z 2344.2 ($M\text{-}H^+$, $C_{123}H_{173}N_{21}O_{25}$ requires 2344.3).

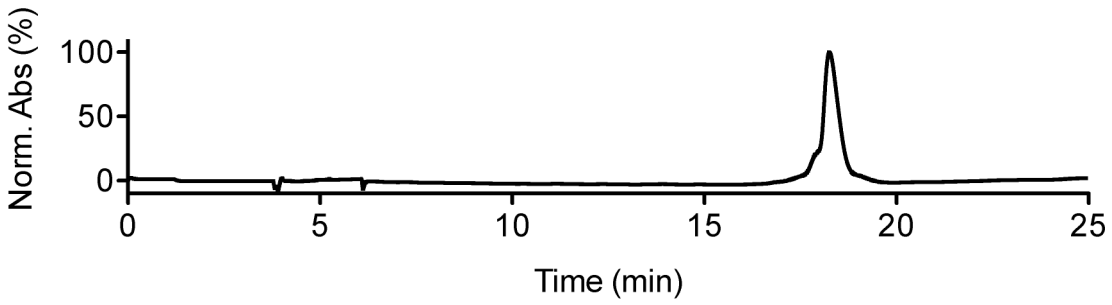

Figure 3.17. Analytical HPLC profile of **50** after preparative HPLC. Retention time = 18 min monitored by UV absorbance at 254 nm. Purity >95% by HPLC.

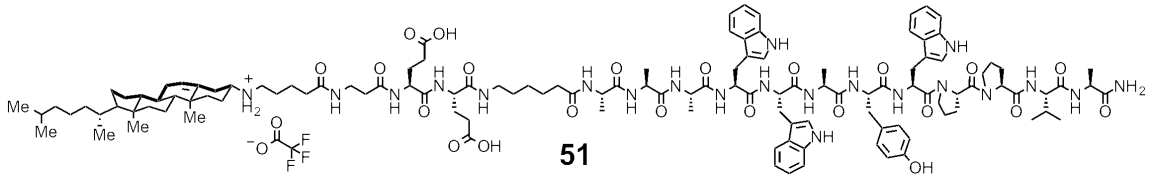

51

***N*-(5-(3β-cholest-5-en-3-ylammonio)pentanoyl)-β-Alanyl-L-Glutamyl-L-Glutamyl-Aminohexanoyl-L-Alanyl-L-Alanyl-L-Alanyl-L-Tryptophyl-L-Tryptophyl-L-Alanyl-L-Tyrosyl-L-Tryptophyl-L-Prolyl-L-Prolyl-L-Valyl-L-Alaninamide (51).** Using the general SPPS procedure, Rink amide MBHA resin (0.5 mmol/g, 100 mg, 0.05 mmol) was used to produce **51** (28 mg, 0.012 mmol, 24% yield overall) as a white solid. LR-MS (ESI-) m/z 2297.0 ($M\text{-}H^+$, $C_{123}H_{173}N_{21}O_{22}$ requires 2296.8).

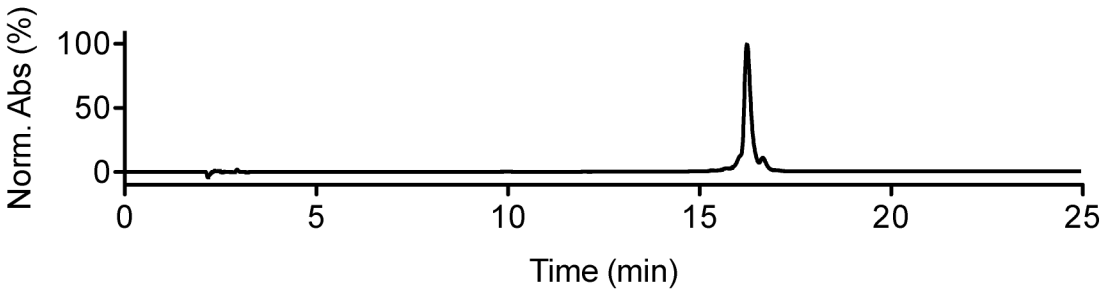

Figure 3.18. Analytical HPLC profile of **51** after preparative HPLC. Retention time = 16 min monitored by UV absorbance at 254 nm. Purity >95% by HPLC.

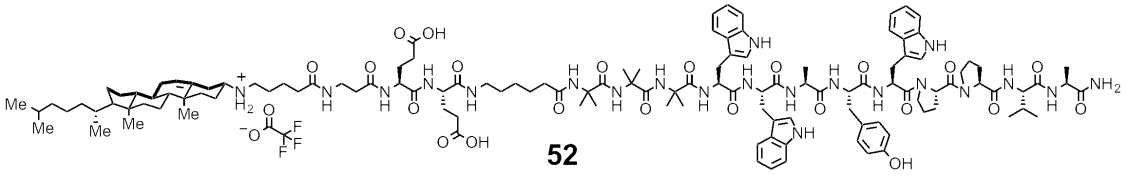

52

***N*-(5-(3β-cholest-5-en-3-ylammonio)pentanoyl)-β-Alanyl-L-Glutamyl-L-Glutamyl-Aminohexanoyl-Aminoisobutyl-Aminoisobutyl-Aminoisobutyl-L-Tryptophyl-L-Tryptophyl-L-Alanyl-L-Tyrosyl-L-Tryptophyl-L-Prolyl-L-Prolyl-L-Valyl-L-Alaninamide (52).** Using the general SPPS procedure, Rink amide

MBHA resin (0.5 mmol/g, 100 mg, 0.05 mmol) was used to produce **52** (17 mg, 0.007 mmol, 15% yield overall) as a white solid. LR-MS (ESI-) m/z 2338.4 (M-H^+, $C_{126}H_{179}N_{21}O_{22}$ requires 2338.9).

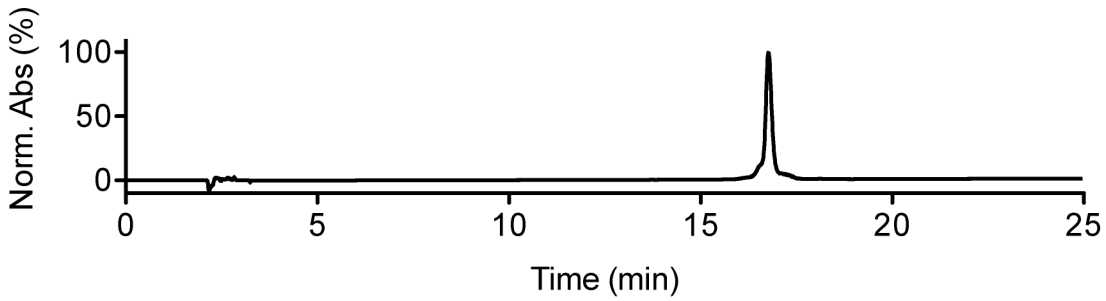

Figure 3.19. Analytical HPLC profile of **52** after preparative HPLC. Retention time = 16 min monitored by UV absorbance at 254 nm. Purity >95% by HPLC.

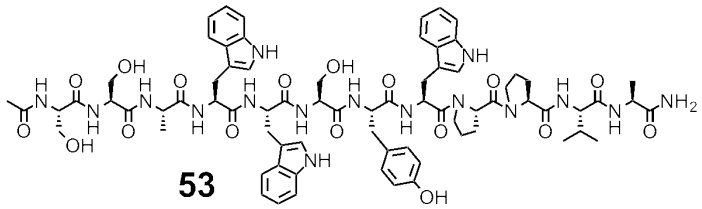

53

***N*-(Acetyl)-L-Seryl-L-Seryl-L-Alanyl-L-Tryptophyl-L-Tryptophyl-L-Seryl-L-Tyrosyl-L-Tryptophyl-L-Prolyl-L-Prolyl-L-Valyl-L-Alaninamide (53).** Using the general SPPS procedure, Rink amide MBHA resin (0.5 mmol/g, 100 mg, 0.05 mmol) was used to produce **53** (47 mg, 0.032 mmol, 64% yield overall) as a white solid. LR-MS (ESI-) m/z 1476.1 (M-H^+, $C_{74}H_{92}N_{16}O_{17}$ requires 1476.6).

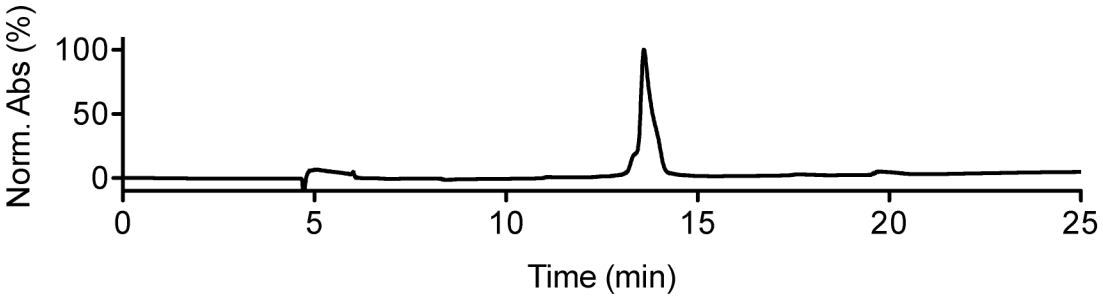

Figure 3.20. Analytical HPLC profile of **53** after preparative HPLC. Retention time = 14 min monitored by UV absorbance at 254 nm. Purity >95% by HPLC.

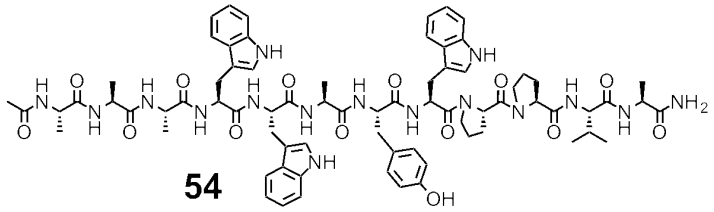

54

***N*-(Acetyl)-L-Alanyl-L-Alanyl-L-Alanyl-L-Tryptophyl-L-Tryptophyl-L-Alanyl-L-Tyrosyl-L-Tryptophyl-L-Prolyl-L-Prolyl-L-Valyl-L-Alaninamide (54).** Using the general SPPS procedure, Rink amide MBHA resin (0.5 mmol/g, 100 mg, 0.05 mmol) was used to produce **54** (20 mg, 0.014 mmol, 28% yield overall) as a white solid. LR-MS (ESI-) m/z 1428.1 ($M\text{-}H^+$, $C_{74}H_{92}N_{16}O_{14}$ requires 1427.7).

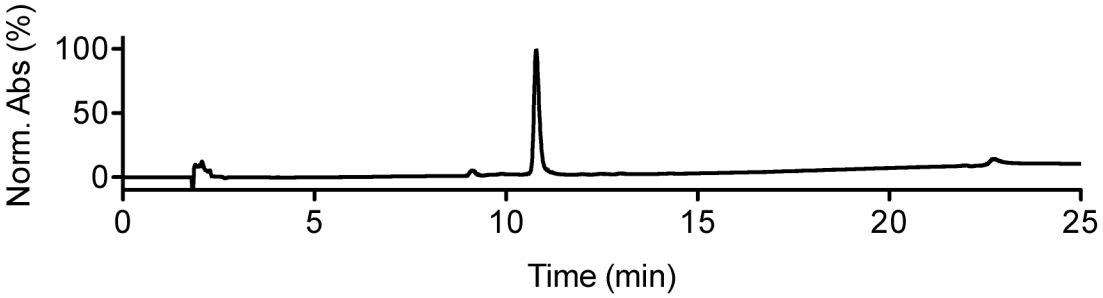

Figure 3.21. Analytical HPLC profile of **54** after preparative HPLC. Retention time = 11 min monitored by UV absorbance at 254 nm. Purity >95% by HPLC.

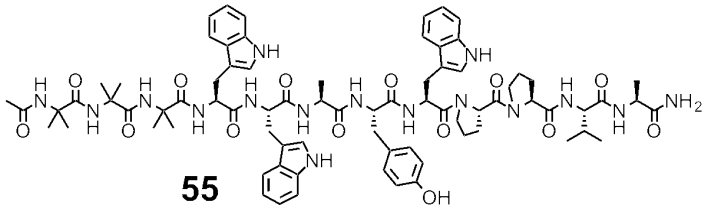

55

***N*-(Acetyl)-Aminoisobutyl-Aminoisobutyl-Aminoisobutyl-L-Tryptophyl-L-Tryptophyl-L-Alanyl-L-Tyrosyl-L-Tryptophyl-L-Prolyl-L-Prolyl-L-Valyl-L-Alaninamide (55).** Using the general SPPS procedure, Rink amide MBHA resin (0.5 mmol/g, 100 mg, 0.05 mmol) was used to produce **55** (32 mg, 0.022 mmol, 44% yield overall) as a white solid. LR-MS (ESI-) m/z 1470.2 ($M\text{-}H^+$, $C_{77}H_{98}N_{16}O_{14}$ requires 1469.7).

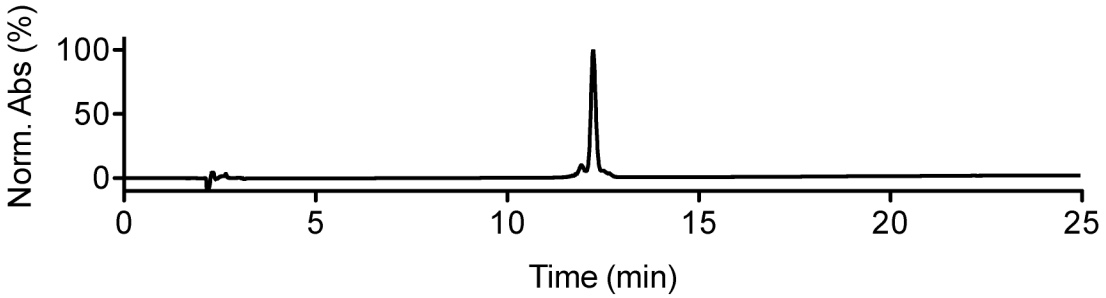

Figure 3.22. Analytical HPLC profile of **55** after preparative HPLC. Retention time = 12 min monitored by UV absorbance at 254 nm. Purity >95% by HPLC.

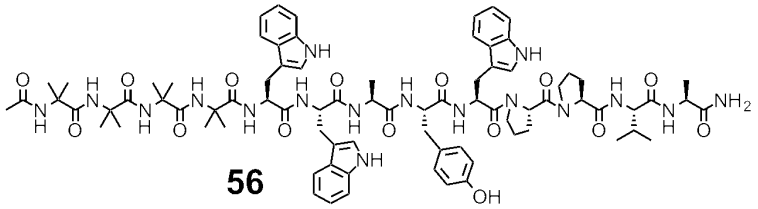

56

***N*-(Acetyl)-Aminoisobutyl-Aminoisobutyl-Aminoisobutyl-Aminoisobutyl-L-Tryptophyl-L-Tryptophyl-L-Alanyl-L-Tyrosyl-L-Tryptophyl-L-Prolyl-L-Prolyl-L-Valyl-L-Alaninamide (56).** Using the general SPPS procedure, Rink amide MBHA resin (0.5 mmol/g, 100 mg, 0.05 mmol) was used to produce **56** (33 mg,

0.021 mmol, 42% yield overall) as a white solid. LR-MS (ESI-) m/z 1555.3 (M-H^+, $C_{81}H_{105}N_{17}O_{15}$ requires 1554.8).

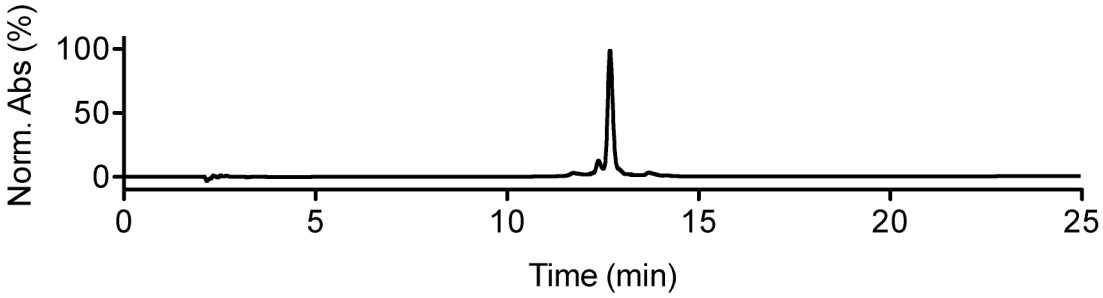

Figure 3.23. Analytical HPLC profile of **56** after preparative HPLC. Retention time = 13 min monitored by UV absorbance at 254 nm. Purity >95% by HPLC.

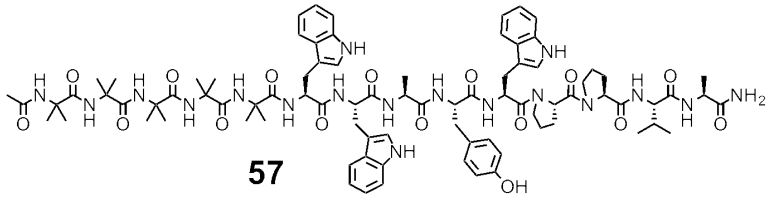

57

***N*-(Acetyl)-Aminoisobutyl-Aminoisobutyl-Aminoisobutyl-Aminoisobutyl-Aminoisobutyl-L-Tryptophyl-L-Tryptophyl-L-Alanyl-L-Tyrosyl-L-Tryptophyl-L-Prolyl-L-Prolyl-L-Valyl-L-Alaninamide (57).** Using the general SPPS procedure, Rink amide MBHA resin (0.5 mmol/g, 100 mg, 0.05 mmol) was used to produce **57** (23 mg, 0.014 mmol, 28% yield overall) as a white solid. LR-MS (ESI-) m/z 1640.2 (M-H^+, $C_{85}H_{112}N_{18}O_{16}$ requires 1639.8).

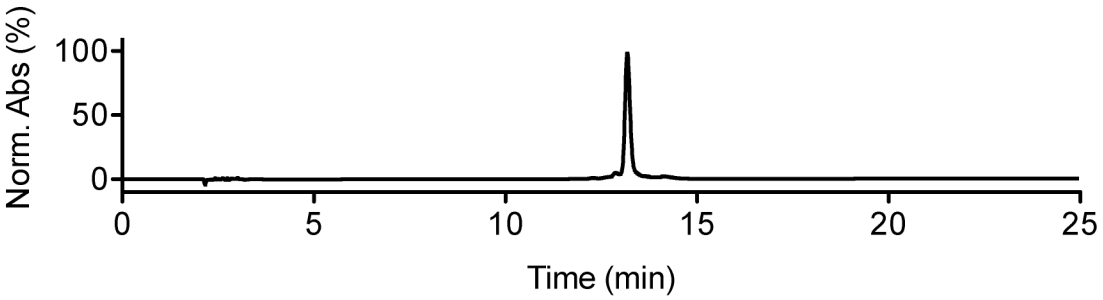

Figure 3.24. Analytical HPLC profile of **57** after preparative HPLC. Retention time = 13 min monitored by UV absorbance at 254 nm. Purity >95% by HPLC.

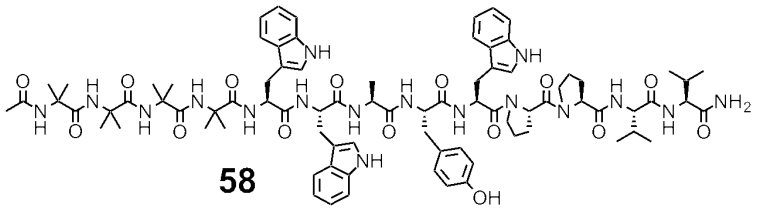

58

***N*-(Acetyl)-Aminoisobutyl-Aminoisobutyl-Aminoisobutyl-Aminoisobutyl-L-Tryptophyl-L-Tryptophyl-L-Alanyl-L-Tyrosyl-L-Tryptophyl-L-Prolyl-L-Prolyl-L-Valyl-L-Valinamide (58).** Using the general SPPS procedure, Rink amide MBHA resin (0.5 mmol/g, 100 mg, 0.05 mmol) was used to produce **58** (32 mg, 0.020 mmol, 40% yield overall) as a white solid. LR-MS (ESI+) m/z 1607.4 ($M+Na^+$, $C_{83}H_{109}N_{17}O_{15}Na$ requires 1606.8).

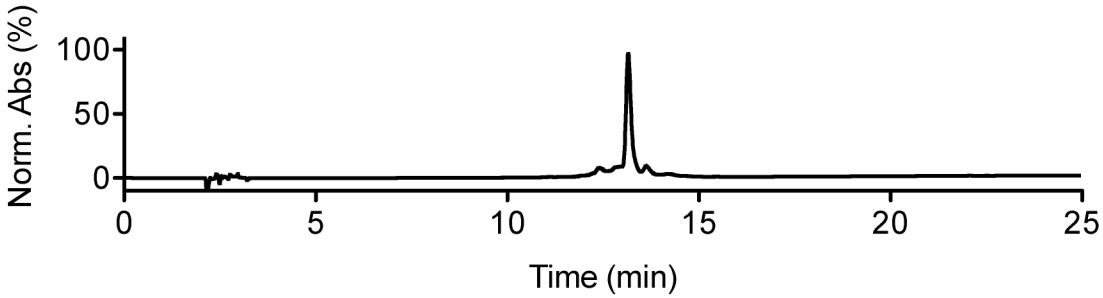

Figure 3.25. Analytical HPLC profile of **58** after preparative HPLC. Retention time = 13 min monitored by UV absorbance at 254 nm. Purity >95% by HPLC.

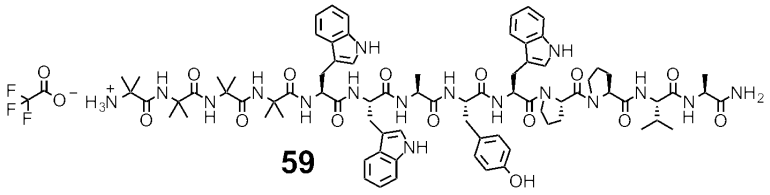

59

Aminoisobutyl-Aminoisobutyl-Aminoisobutyl-Aminoisobutyl-L-Tryptophyl-L-Tryptophyl-L-Alanyl-L-Tyrosyl-L-Tryptophyl-L-Prolyl-L-Prolyl-L-Valyl-L-Alaninamide (59). Using the general SPPS procedure, Rink amide MBHA resin (0.5 mmol/g, 100 mg, 0.05 mmol) was used to produce **59** (30 mg, 0.019 mmol,

38% yield overall) as a white solid. LR-MS (ESI-) m/z 1513.5 ($M-H^+$, $C_{81}H_{105}N_{17}O_{15}$ requires 1512.8).

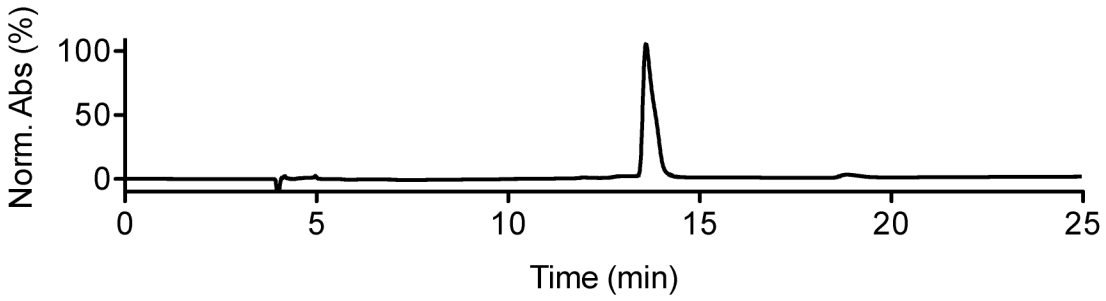

Figure 3.26. Analytical HPLC profile of **59** after preparative HPLC. Retention time = 14 min monitored by UV absorbance at 254 nm. Purity >95% by HPLC.

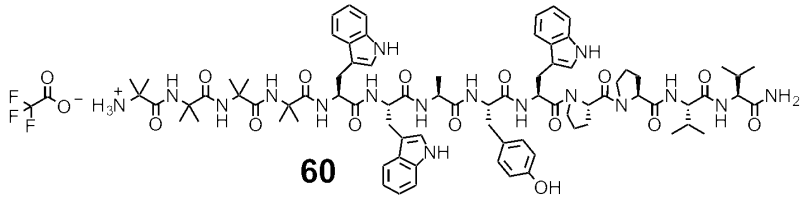

60

Aminoisobutyl-Aminoisobutyl-Aminoisobutyl-Aminoisobutyl-L-Tryptophyl-L-Tryptophyl-L-Alanyl-L-Tyrosyl-L-Tryptophyl-L-Prolyl-L-Prolyl-L-Valyl-L-Valinamide (60). Using the general SPPS procedure, Rink amide MBHA resin (0.5 mmol/g, 100 mg, 0.05 mmol) was used to produce **60** (43 mg, 0.028 mmol, 56% yield overall) as a white solid. LR-MS (ESI+) m/z 1543.2 ($M+H^+$, $C_{81}H_{107}N_{17}O_{14}$ requires 1542.8).

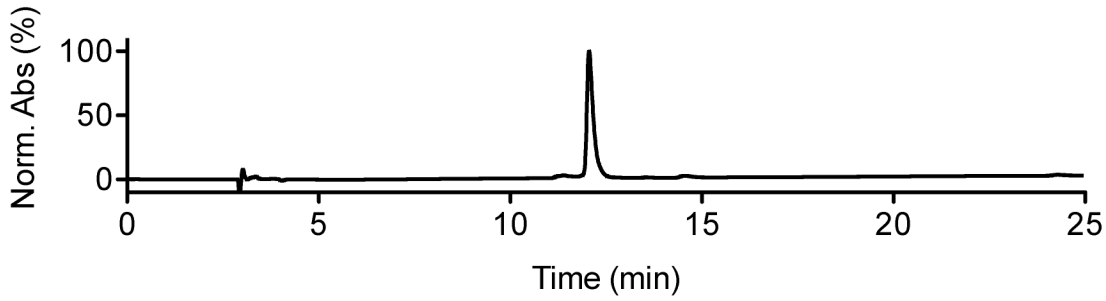

Figure 3.27. Analytical HPLC profile of **60** after preparative HPLC. Retention time = 12 min monitored by UV absorbance at 254 nm. Purity >95% by HPLC.

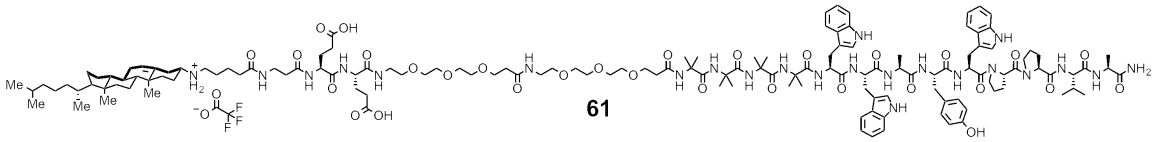

61

***N*-(5-(3β-cholest-5-en-3-ylammonio)pentanoyl)-β-Alanyl-L-Glutamyl-L-Glutamyl-mPEG-mPEG-Aminoisobutyl-Aminoisobutyl-Aminoisobutyl-Aminoisobutyl-L-Tryptophyl-L-Tryptophyl-L-Alanyl-L-Tyrosyl-L-Tryptophyl-L-Prolyl-L-Prolyl-L-Valyl-L-Alaninamide (61).** Using the general SPPS procedure, Rink amide MBHA resin (0.5 mmol/g, 100 mg, 0.05 mmol) was used to produce **61** (47 mg, 0.017 mmol, 34% yield overall) as a white solid. LR-MS (ESI-) m/z 2717.3 ($M-H^+$, $C_{142}H_{209}N_{23}O_{30}$ requires 2716.6).

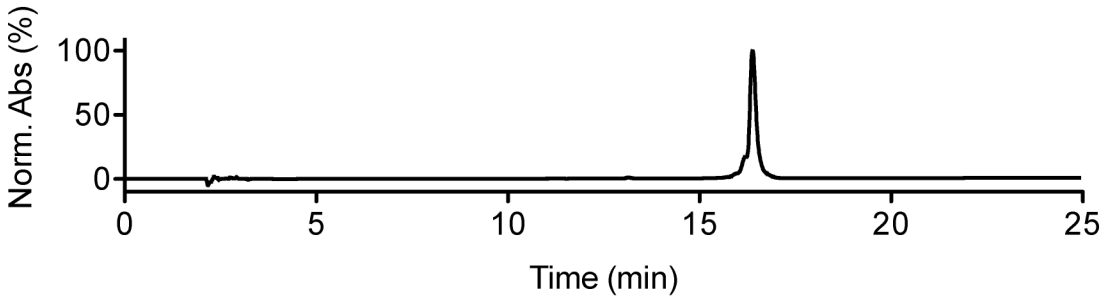

Figure 3.28. Analytical HPLC profile of **61** after preparative HPLC. Retention time = 17 min monitored by UV absorbance at 254 nm. Purity >95% by HPLC.

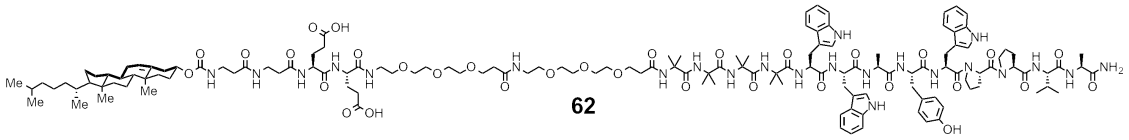

62

((3β-cholest-5-en-3-yl)carbonyl)-β-Alanyl-β-Alanyl-L-Glutamyl-L-Glutamyl-mPEG-mPEG-Aminoisobutyl-Aminoisobutyl-Aminoisobutyl-Aminoisobutyl-L-Tryptophyl-L-Tryptophyl-L-Alanyl-L-Tyrosyl-L-Tryptophyl-L-Prolyl-L-Prolyl-L-Valyl-L-Alaninamide (62). Using the general SPPS procedure, Rink amide MBHA resin (0.5 mmol/g, 100 mg, 0.05 mmol) was used to produce **62** (19

mg, 0.007 mmol, 14% yield overall) as a white solid. LR-MS (ESI-) m/z 2732.7 ($M\text{-}H^+$, $C_{141}H_{205}N_{23}O_{32}$ requires 2732.5).

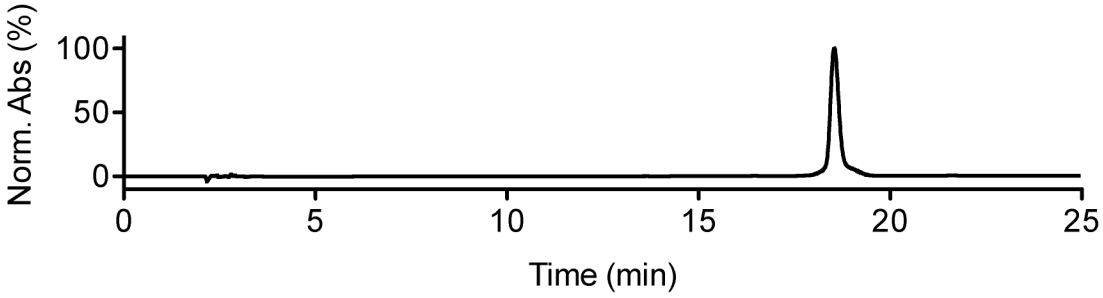

Figure 3.29. Analytical HPLC profile of **62** after preparative HPLC. Retention time = 19 min monitored by UV absorbance at 254 nm. Purity >95% by HPLC.

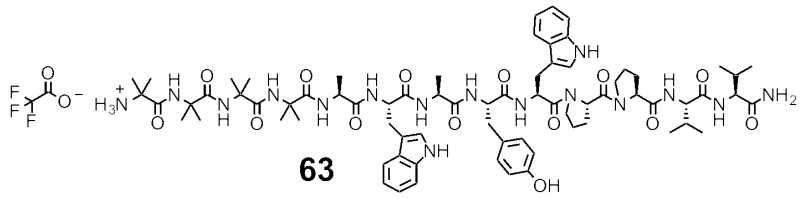

63

Aminoisobutyl-Aminoisobutyl-Aminoisobutyl-Aminoisobutyl-L-Alanyl-L-Tryptophyl-L-Alanyl-L-Tyrosyl-L-Tryptophyl-L-Prolyl-L-Prolyl-L-Valyl-L-Valinamide (63). Using the general SPPS procedure, Rink amide MBHA resin (0.5 mmol/g, 70 mg, 0.035 mmol) was used to produce **63** (26 mg, 0.018 mmol, 51% yield overall) as a white solid. LR-MS (ESI-) m/z 1540.0 ($M\text{-}H^+ \bullet TFA$, $C_{73}H_{102}N_{16}O_{14} \bullet CF_3CO_2H$ requires 1539.7).

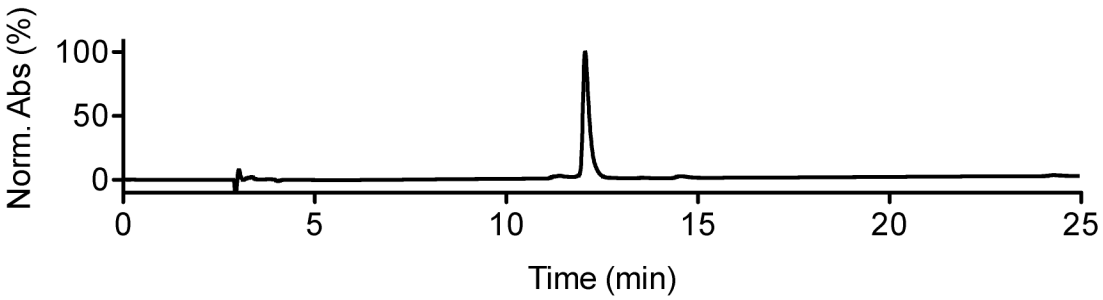

Figure 3.30. Analytical HPLC profile of **63** after preparative HPLC. Retention time = 12 min monitored by UV absorbance at 254 nm. Purity >95% by HPLC.

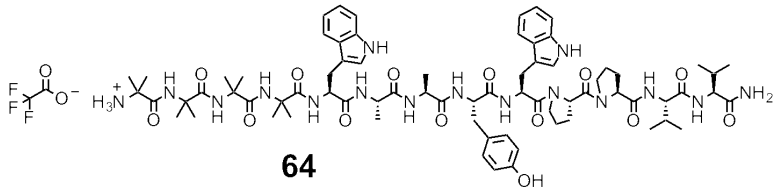

64

Aminoisobutyl-Aminoisobutyl-Aminoisobutyl-Aminoisobutyl-L-Tryptophyl-L-Alanyl-L-Alanyl-L-Tyrosyl-L-Tryptophyl-L-Prolyl-L-Prolyl-L-Valyl-L-Valinamide (64). Using the general SPPS procedure, Rink amide MBHA resin (0.5 mmol/g, 70 mg, 0.035 mmol) was used to produce **64** (18 mg, 0.013 mmol, 37% yield overall) as a white solid. LR-MS (ESI-) m/z 1426.0 ($M\text{-}H^+$, $C_{73}H_{102}N_{16}O_{14}$ requires 1425.7).

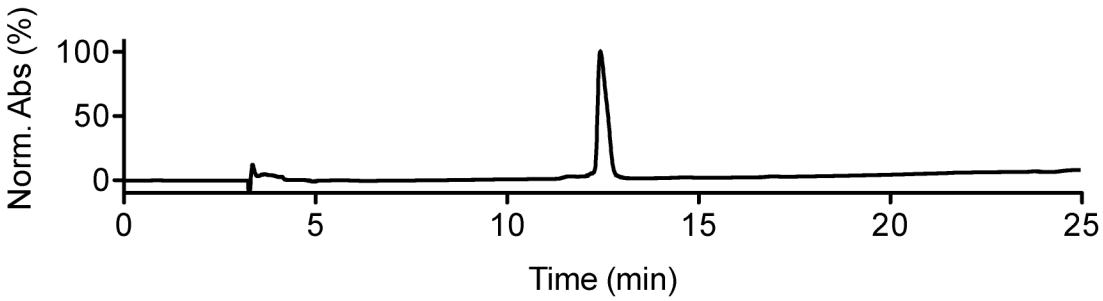

Figure 3.31. Analytical HPLC profile of **64** after preparative HPLC. Retention time = 13 min monitored by UV absorbance at 254 nm. Purity >95% by HPLC.

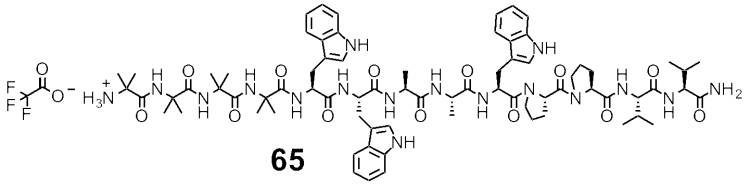

65

Aminoisobutyl-Aminoisobutyl-Aminoisobutyl-Aminoisobutyl-L-Tryptophyl-L-Tryptophyl-L-Alanyl-L-Alanyl-L-Tryptophyl-L-Prolyl-L-Prolyl-L-Valyl-L-Valinamide (65). Using the general SPPS procedure, Rink amide MBHA resin (0.5 mmol/g, 70 mg, 0.035 mmol) was used to produce **65** (19 mg, 0.013 mmol,

37% yield overall) as a white solid. LR-MS (ESI-) m/z 1449.4 ($M\text{-}H^+$, $C_{75}H_{103}N_{17}O_{13}$ requires 1448.8).

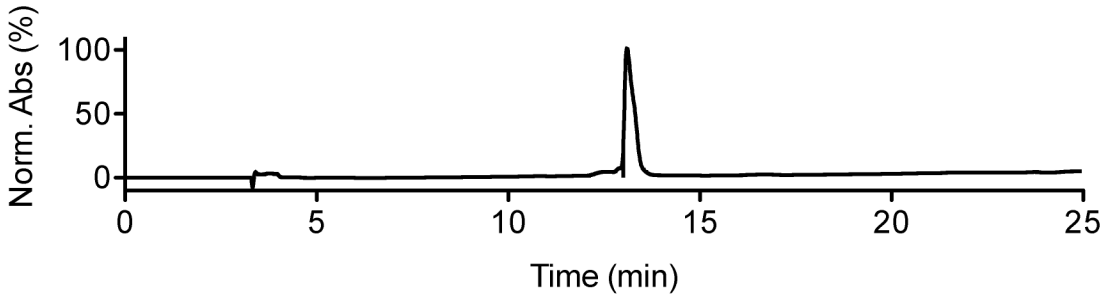

Figure 3.32. Analytical HPLC profile of **65** after preparative HPLC. Retention time = 13 min monitored by UV absorbance at 254 nm. Purity >95% by HPLC.

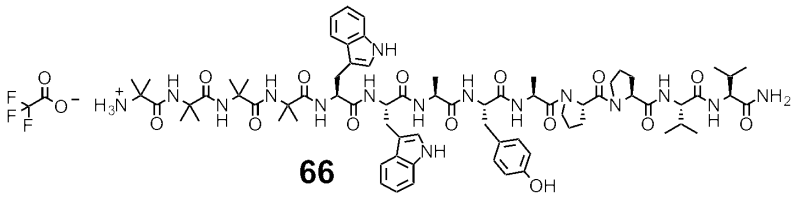

66

Aminoisobutyl-Aminoisobutyl-Aminoisobutyl-Aminoisobutyl-L-Tryptophyl-L-Tryptophyl-L-Alanyl-L-Tyrosyl-L-Alanyl-L-Prolyl-L-Prolyl-L-Valyl-L-Valinamide (66). Using the general SPPS procedure, Rink amide MBHA resin (0.5 mmol/g, 70 mg, 0.035 mmol) was used to produce **66** (30 mg, 0.021 mmol, 60% yield overall) as a white solid. LR-MS (ESI-) m/z 1426.2 ($M\text{-}H^+$, $C_{73}H_{102}N_{16}O_{14}$ requires 1425.8).

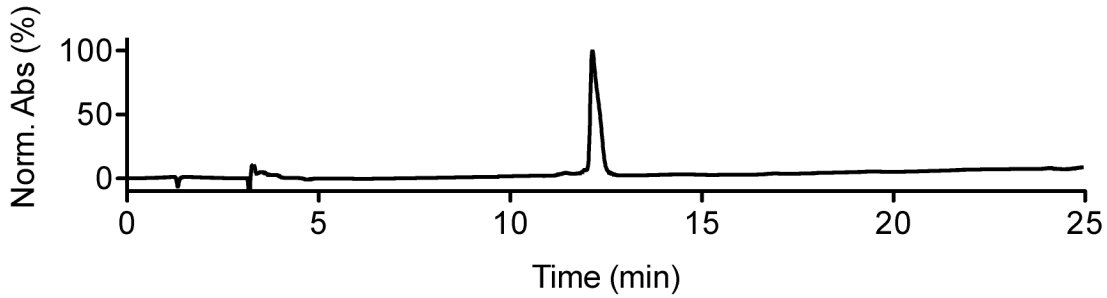

Figure 3.33. Analytical HPLC profile of **66** after preparative HPLC. Retention time = 12 min monitored by UV absorbance at 254 nm. Purity >95% by HPLC.

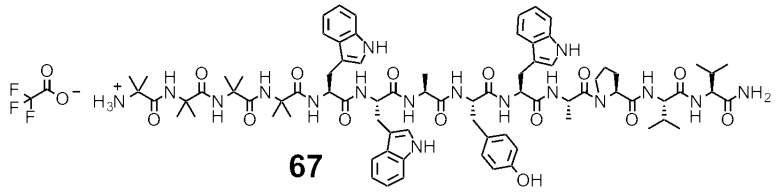

67

Aminoisobutyl-Aminoisobutyl-Aminoisobutyl-Aminoisobutyl-L-Tryptophyl-L-Tryptophyl-L-Alanyl-L-Tyrosyl-L-Tryptophyl-L-Alanyl-L-Prolyl-L-Valyl-L-Valinamide (67). Using the general SPPS procedure, Rink amide MBHA resin (0.5 mmol/g, 70 mg, 0.035 mmol) was used to produce **67** (15 mg, 0.010 mmol, 28% yield overall) as a white solid. LR-MS (ESI-) m/z 1515.6 ($M\text{-}H^+$, $C_{79}H_{105}N_{17}O_{14}$ requires 1514.8).

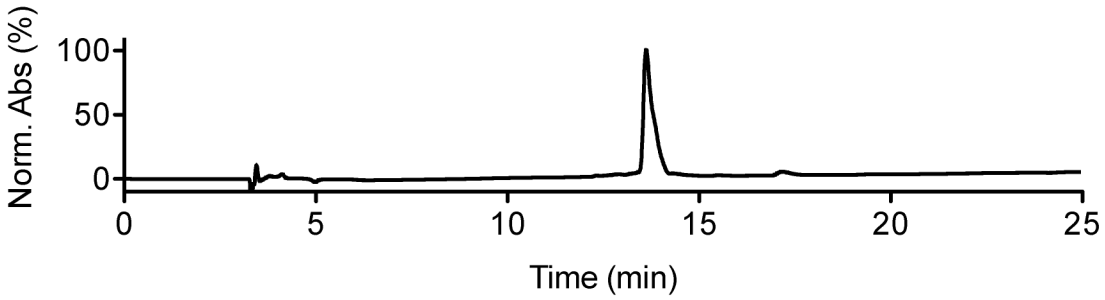

Figure 3.34. Analytical HPLC profile of **67** after preparative HPLC. Retention time = 14 min monitored by UV absorbance at 254 nm. Purity >95% by HPLC.

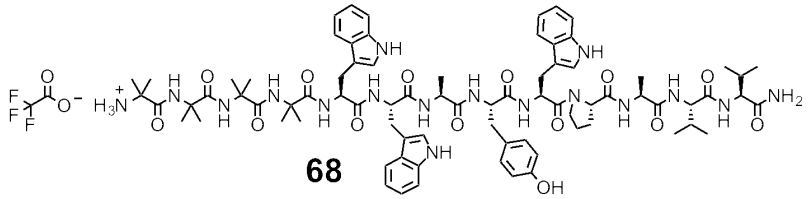

68

Aminoisobutyl-Aminoisobutyl-Aminoisobutyl-Aminoisobutyl-L-Tryptophyl-L-Tryptophyl-L-Alanyl-L-Tyrosyl-L-Tryptophyl-L-Prolyl-L-Alanyl-L-Valyl-L-Valinamide (68). Using the general SPPS procedure, Rink amide MBHA resin (0.5 mmol/g, 70 mg, 0.035 mmol) was used to produce **68** (20 mg, 0.013 mmol,

37% yield overall) as a white solid. LR-MS (ESI-) m/z 1515.2 ($M\text{-}H^+$, $C_{79}H_{105}N_{17}O_{14}$ requires 1514.8).

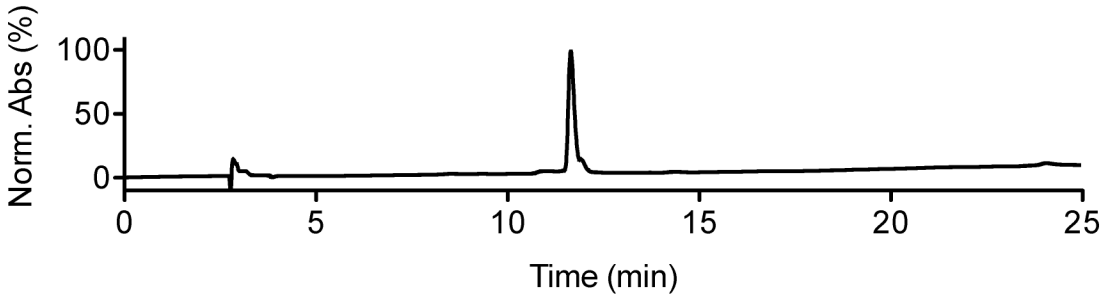

Figure 3.35. Analytical HPLC profile of **68** after preparative HPLC. Retention time = 12 min monitored by UV absorbance at 254 nm. Purity >95% by HPLC.

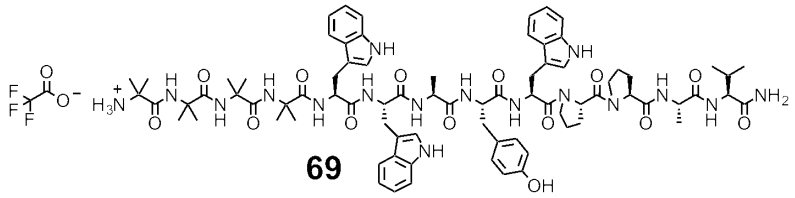

69

Aminoisobutyl-Aminoisobutyl-Aminoisobutyl-Aminoisobutyl-L-Tryptophyl-L-Tryptophyl-L-Alanyl-L-Tyrosyl-L-Tryptophyl-L-Prolyl-L-Prolyl-L-Alanyl-L-Valinamide (69). Using the general SPPS procedure, Rink amide MBHA resin (0.5 mmol/g, 70 mg, 0.035 mmol) was used to produce **69** (25 mg, 0.016 mmol, 47% yield overall) as a white solid. LR-MS (ESI-) m/z 1627.6 ($M\text{-}H^+ \bullet TFA$, $C_{79}H_{103}N_{17}O_{14} \bullet CF_3CO_2H$ requires 1626.8).

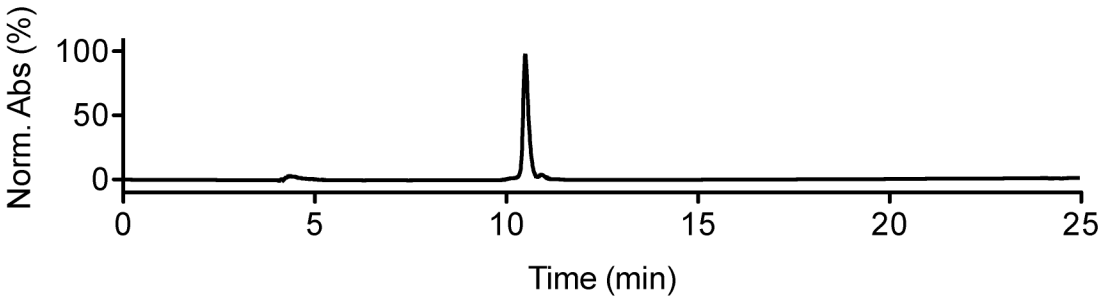

Figure 3.36. Analytical HPLC profile of **69** after preparative HPLC. Retention time = 11 min monitored by UV absorbance at 254 nm. Purity >95% by HPLC.

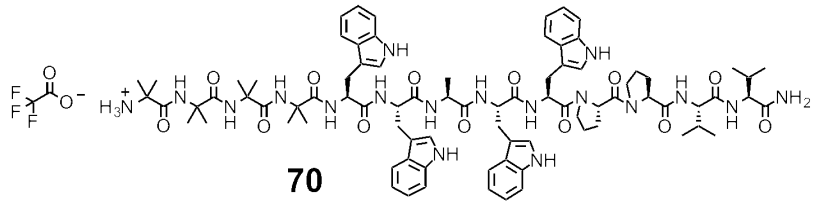

70

Aminoisobutyl-Aminoisobutyl-Aminoisobutyl-Aminoisobutyl-L-Tryptophyl-L-Tryptophyl-L-Alanyl-L-Tryptophyl-L-Tryptophyl-L-Prolyl-L-Prolyl-L-Valyl-L-Valinamide (70). Using the general SPPS procedure, Rink amide MBHA resin (0.5 mmol/g, 60 mg, 0.03 mmol) was used to produce **70** (14 mg, 0.009 mmol, 30% yield overall) as a white solid. LR-MS (ESI+) m/z 1566.2 ($M+H^+$, $C_{83}H_{108}N_{18}O_{13}$ requires 1565.8).

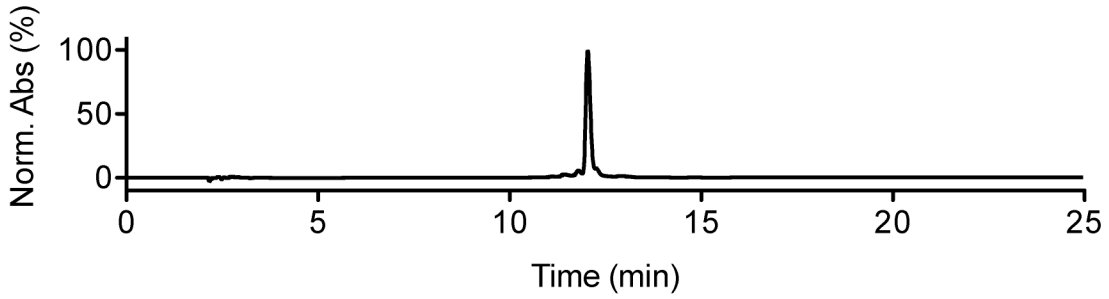

Figure 3.37. Analytical HPLC profile of **70** after preparative HPLC. Retention time = 12 min monitored by UV absorbance at 254 nm. Purity >95% by HPLC.

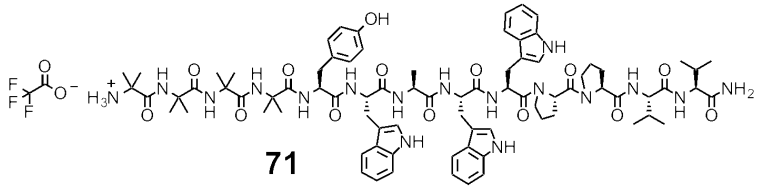

71

Aminoisobutyl-Aminoisobutyl-Aminoisobutyl-Aminoisobutyl-L-Tyrosyl-L-Tryptophyl-L-Alanyl-L-Tryptophyl-L-Tryptophyl-L-Prolyl-L-Prolyl-L-Valyl-L-Valinamide (71). Using the general SPPS procedure, Rink amide MBHA resin (0.5 mmol/g, 60 mg, 0.03 mmol) was used to produce **71** (23 mg, 0.015 mmol,

50% yield overall) as a white solid. LR-MS (ESI-) m/z 1541.6 ($M\text{-}H^+$, $C_{81}H_{107}N_{17}O_{14}$ requires 1540.8).

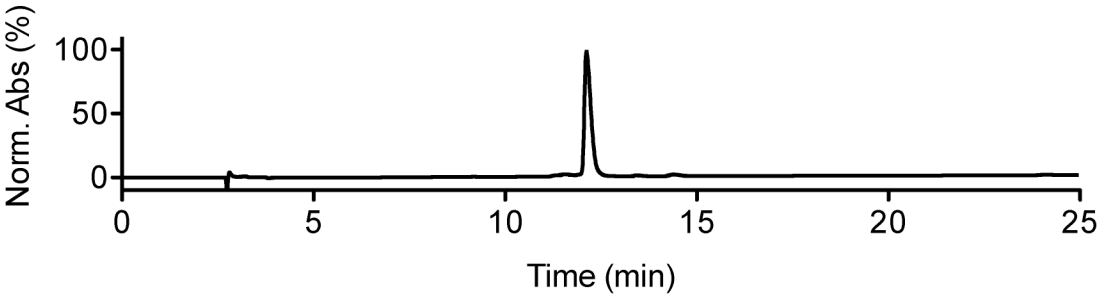

Figure 3.38. Analytical HPLC profile of **71** after preparative HPLC. Retention time = 12 min monitored by UV absorbance at 254 nm. Purity >95% by HPLC.

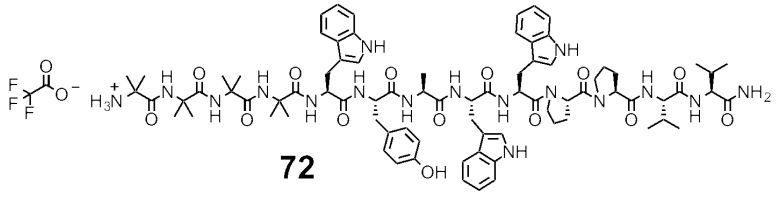

72

Aminoisobutyl-Aminoisobutyl-Aminoisobutyl-Aminoisobutyl-L-Tryptophyl-L-Tyrosyl-L-Alanyl-L-Tryptophyl-L-Tryptophyl-L-Prolyl-L-Prolyl-L-Valyl-L-Valinamide (72). Using the general SPPS procedure, Rink amide MBHA resin (0.5 mmol/g, 60 mg, 0.03 mmol) was used to produce **72** (21 mg, 0.014 mmol, 45% yield overall) as a white solid. LR-MS (ESI-) m/z 1541.2 ($M\text{-}H^+$, $C_{81}H_{107}N_{17}O_{14}$ requires 1540.8).

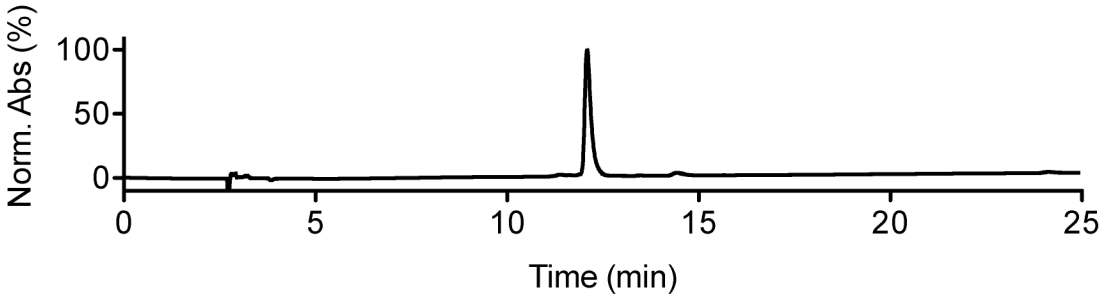

Figure 3.39. Analytical HPLC profile of **72** after preparative HPLC. Retention time = 12 min monitored by UV absorbance at 254 nm. Purity >95% by HPLC.

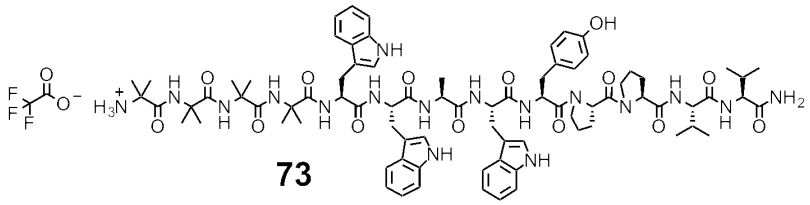

73

Aminoisobutyl-Aminoisobutyl-Aminoisobutyl-Aminoisobutyl-L-Tryptophyl-L-Tryptophyl-L-Alanyl-L-Tryptophyl-L-Tyrosyl-L-Prolyl-L-Prolyl-L-Valyl-L-Valinamide (73). Using the general SPPS procedure, Rink amide MBHA resin (0.5 mmol/g, 60 mg, 0.03 mmol) was used to produce **73** (20 mg, 0.013 mmol, 43% yield overall) as a white solid. LR-MS (ESI-) m/z 1541.3 ($M\text{-}H^+$, $C_{81}H_{107}N_{17}O_{14}$ requires 1540.8).

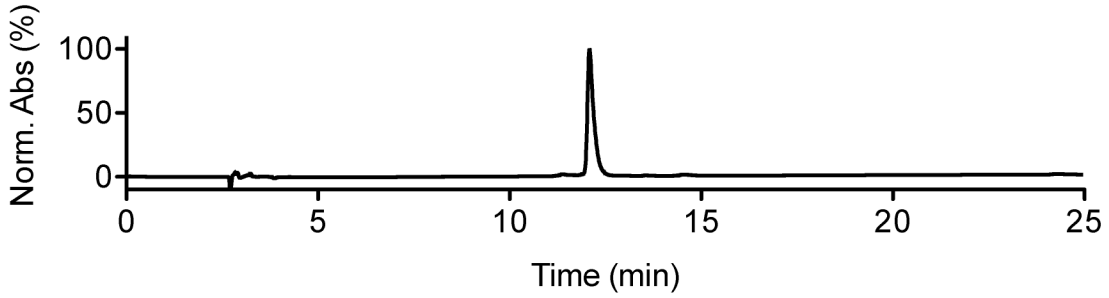

Figure 3.40. Analytical HPLC profile of **73** after preparative HPLC. Retention time = 12 min monitored by UV absorbance at 254 nm. Purity >95% by HPLC.

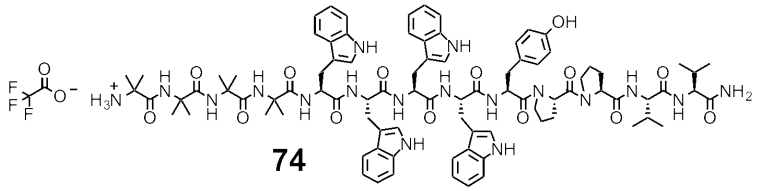

74

Aminoisobutyl-Aminoisobutyl-Aminoisobutyl-Aminoisobutyl-L-Tryptophyl-L-Tryptophyl-L-Tryptophyl-L-Tryptophyl-L-Tryptophyl-L-Tyrosyl-L-Prolyl-L-Prolyl-L-Valyl-L-Valinamide (74). Using the general SPPS procedure, Rink amide MBHA resin (0.5 mmol/g, 60 mg, 0.03 mmol) was used to produce **74** (19 mg, 0.011 mmol,

38% yield overall) as a white solid. LR-MS (ESI+) m/z 1657.7 ($M+H^+$, $C_{89}H_{112}N_{18}O_{14}$ requires 1657.9).

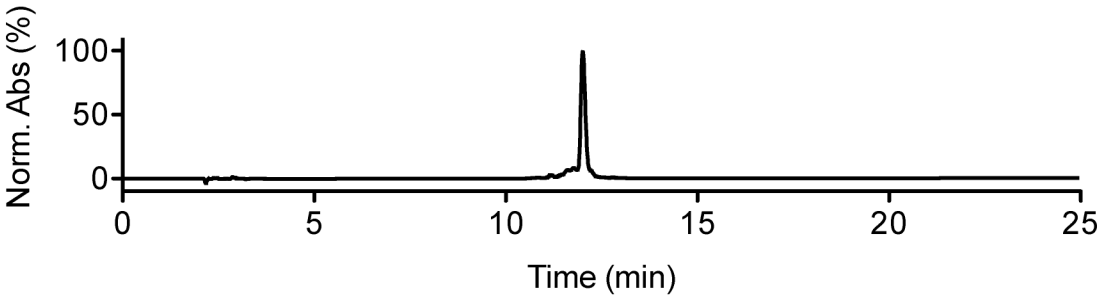

Figure 3.41. Analytical HPLC profile of **74** after preparative HPLC. Retention time = 12 min monitored by UV absorbance at 254 nm. Purity >95% by HPLC.

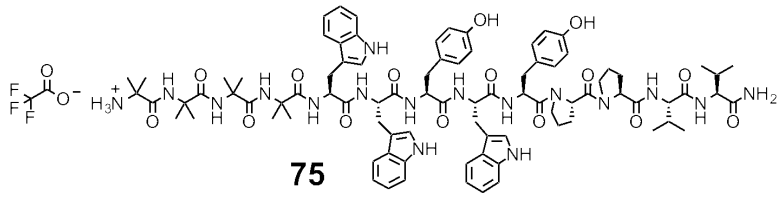

75

Aminoisobutyl-Aminoisobutyl-Aminoisobutyl-Aminoisobutyl-L-Tryptophyl-L-Tryptophyl-L-Tyrosyl-L-Tryptophyl-L-Tyrosyl-L-Prolyl-L-Prolyl-L-Valyl-L-Valinamide (75). Using the general SPPS procedure, Rink amide MBHA resin (0.5 mmol/g, 60 mg, 0.03 mmol) was used to produce **75** (19 mg, 0.011 mmol, 39% yield overall) as a white solid. LR-MS (ESI+) m/z 1635.4 ($M+H^+$, $C_{87}H_{111}N_{17}O_{15}$ requires 1634.9).

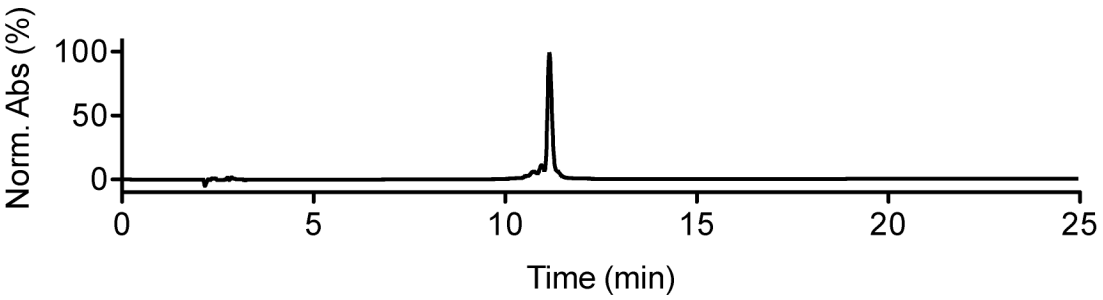

Figure 3.42. Analytical HPLC profile of **75** after preparative HPLC. Retention time = 11 min monitored by UV absorbance at 254 nm. Purity >95% by HPLC.

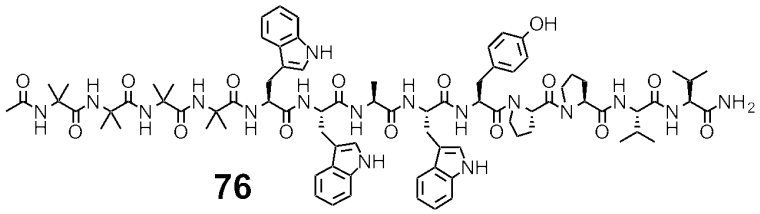

76

***N*-(Acetyl)-Aminoisobutyl-Aminoisobutyl-Aminoisobutyl-Aminoisobutyl-L-Tryptophyl-L-Tryptophyl-L-Alanyl-L-Tryptophyl-L-Tyrosyl-L-Prolyl-L-Prolyl-L-Valyl-L-Valinamide (76).** Using the general SPPS procedure, Rink amide MBHA resin (0.5 mmol/g, 60 mg, 0.03 mmol) was used to produce **76** (14 mg, 0.009 mmol, 29% yield overall) as a white solid. LR-MS (ESI-) m/z 1696.7 (M-H^+•TFA, $C_{83}H_{109}N_{17}O_{15}$ •CF_3CO_2H requires 1696.8).

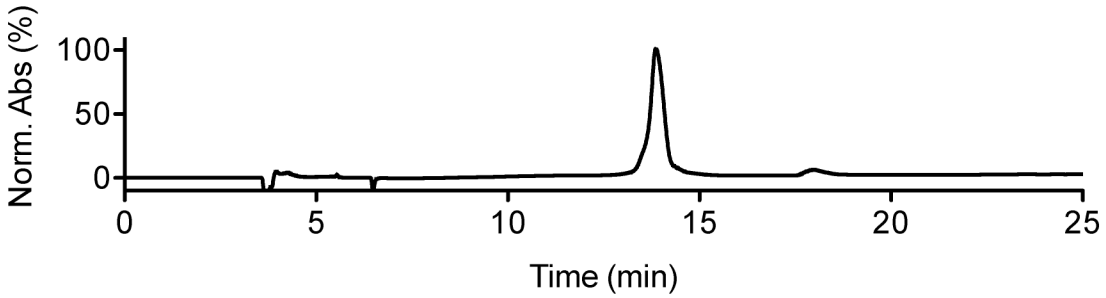

Figure 3.43. Analytical HPLC profile of **76** after preparative HPLC. Retention time = 14 min monitored by UV absorbance at 254 nm. Purity >95% by HPLC.

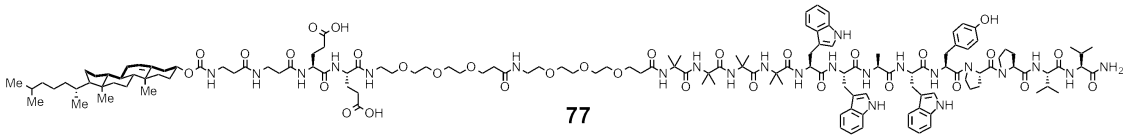

77

((3β-cholest-5-en-3-yl)carbonyl)-β-Alanyl-β-Alanyl-L-Glutamyl-L-Glutamyl-mPEG-mPEG-Aminoisobutyl-Aminoisobutyl-Aminoisobutyl-Aminoisobutyl-L-Tryptophyl-L-Tryptophyl-L-Alanyl-L-Tryptophyl-L-Tyrosyl-L-Prolyl-L-Prolyl-L-Valyl-L-Valinamide (77). Using the general SPPS procedure, Rink amide MBHA resin (0.5 mmol/g, 60 mg, 0.03 mmol) was used to produce **77** (10

mg, 0.004 mmol, 12% yield overall) as a white solid. LR-MS (ESI-) m/z 1380.4 ($M-2H^+/2$, $C_{143}H_{209}N_{23}O_{32}$ requires 1379.8).

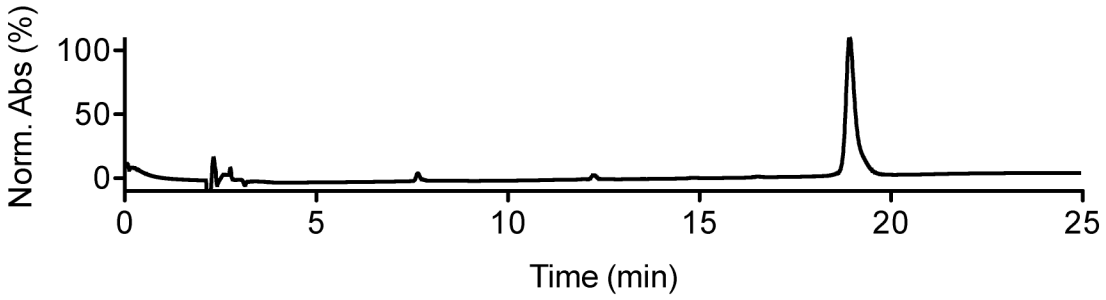

Figure 3.44. Analytical HPLC profile of **77** after preparative HPLC. Retention time = 19 min monitored by UV absorbance at 254 nm. Purity >95% by HPLC.

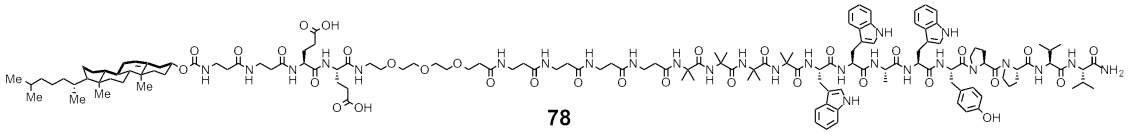

78

((3β-Cholest-5-en-3-yl)carbonyl)-β-Alanyl-β-Alanyl-L-Glutamyl-L-Glutamyl-mPEG-(β-Alanyl)$_4$-Aminoisobutyl-Aminoisobutyl-Aminoisobutyl-Aminoisobutyl-L-Tryptophyl-L-Tryptophyl-L-Alanyl-L-Tryptophyl-L-Tyrosyl-L-Prolyl-L-Prolyl-L-Valyl-L-Valinamide (78). Using the general SPPS procedure, Rink amide MBHA resin (0.5 mmol/g, 60 mg, 0.03 mmol) was used to produce **78** (15 mg, 0.005 mmol, 18% yield overall) as a white solid. LR-MS (ESI-) m/z 1420.7 ($M-H^+/2$, $C_{146}H_{212}N_{26}O_{32}$ requires 1420.3).

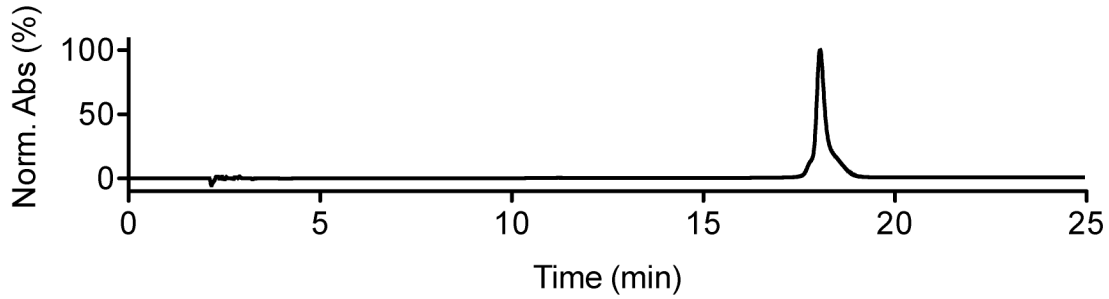

Figure 3.45. Analytical HPLC profile of **78** after preparative HPLC. Retention time = 18 min monitored by UV absorbance at 254 nm. Purity >95% by HPLC.

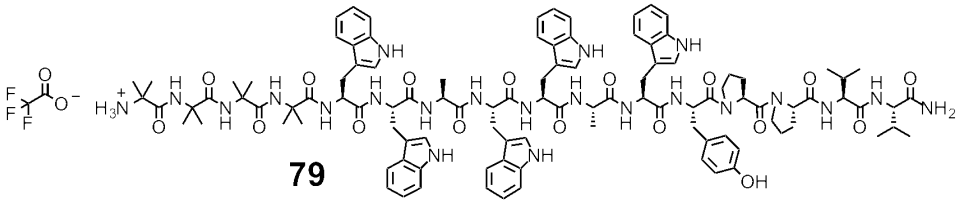

79

Aminoisobutyl-Aminoisobutyl-Aminoisobutyl-Aminoisobutyl-L-Tryptophyl-L-Tryptophyl-L-Alanyl-L-Tryptophyl-L-Tryptophyl-L-Alanyl-L-Tryptophyl-L-Tyrosyl-L-Prolyl-L-Prolyl-L-Valyl-L-Valinamide (79). Using the general SPPS procedure, Rink amide MBHA resin (0.5 mmol/g, 60 mg, 0.03 mmol) was used to produce **79** (20 mg, 0.010 mmol, 33% yield overall) as a white solid. LR-MS (ESI-) m/z 1985.6 ($M-H^+$, $C_{106}H_{132}N_{22}O_{17}$ requires 1985.0).

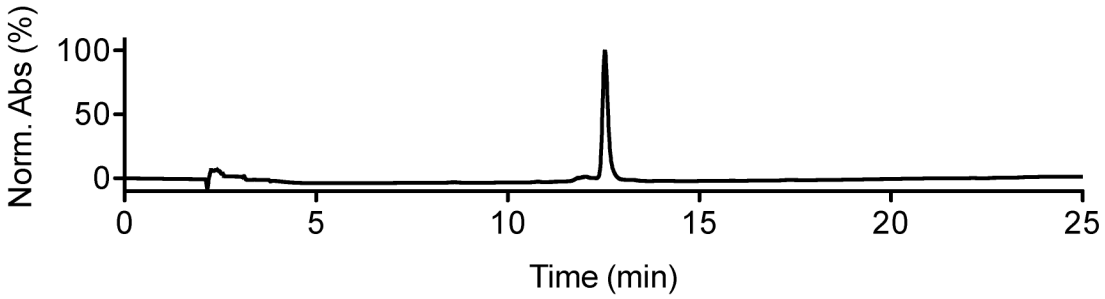

Figure 3.46. Analytical HPLC profile of **79** after preparative HPLC. Retention time = 13 min monitored by UV absorbance at 254 nm. Purity >95% by HPLC.

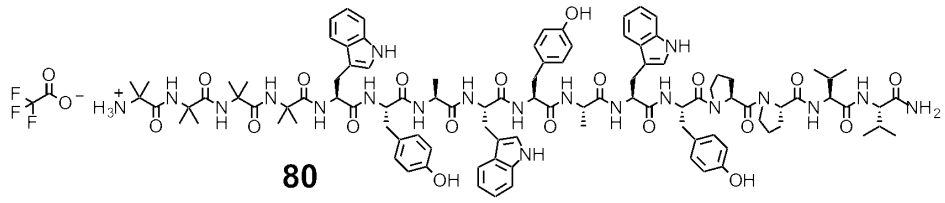

80

Aminoisobutyl-Aminoisobutyl-Aminoisobutyl-Aminoisobutyl-L-Tryptophyl-L-Tyrosyl-L-Alanyl-L-Tryptophyl-L-Tyrosyl-L-Alanyl-L-Tryptophyl-L-Tyrosyl-L-Prolyl-L-Prolyl-L-Valyl-L-Valinamide (80). Using the general SPPS procedure, Rink amide MBHA resin (0.5 mmol/g, 60 mg, 0.03 mmol) was used to

produce **80** (25 mg, 0.013 mmol, 42% yield overall) as a white solid. LR-MS (ESI+) m/z 1941.1 ($M+H^+$, $C_{102}H_{130}N_{20}O_{19}$ requires 1941.0).

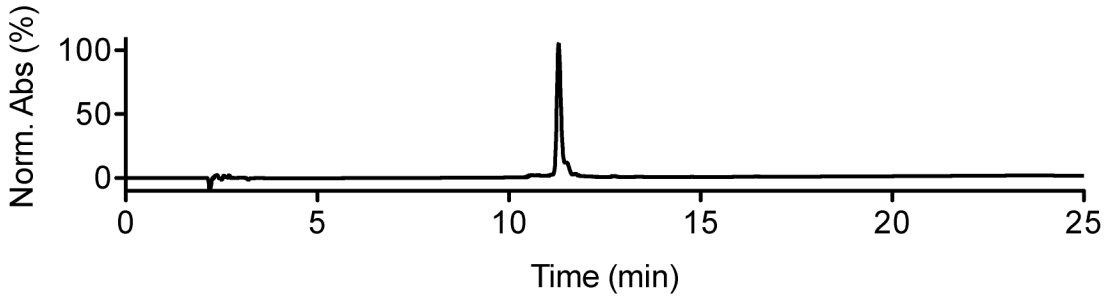

Figure 3.47. Analytical HPLC profile of **80** after preparative HPLC. Retention time = 11 min monitored by UV absorbance at 254 nm. Purity >95% by HPLC.

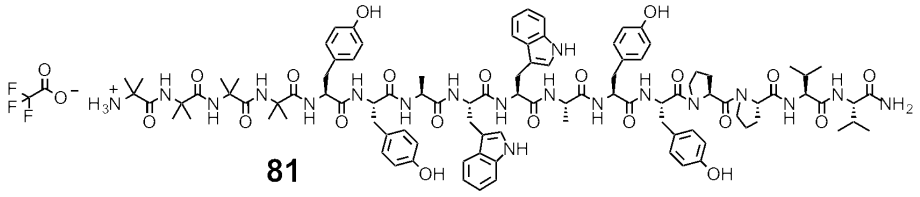

81

Aminoisobutyl-Aminoisobutyl-Aminoisobutyl-Aminoisobutyl-L-Tyrosyl-L-Tyrosyl-L-Alanyl-L-Tryptophyl-L-Tryptophyl-L-Alanyl-L-Tyrosyl-L-Tyrosyl-L-Prolyl-L-Prolyl-L-Valyl-L-Valinamide (81). Using the general SPPS procedure, Rink amide MBHA resin (0.5 mmol/g, 60 mg, 0.03 mmol) was used to produce **81** (30 mg, 0.016 mmol, 52% yield overall) as a white solid. LR-MS (ESI+) m/z 1917.5 ($M+H^+$, $C_{100}H_{129}N_{19}O_{20}$ requires 1918.0).

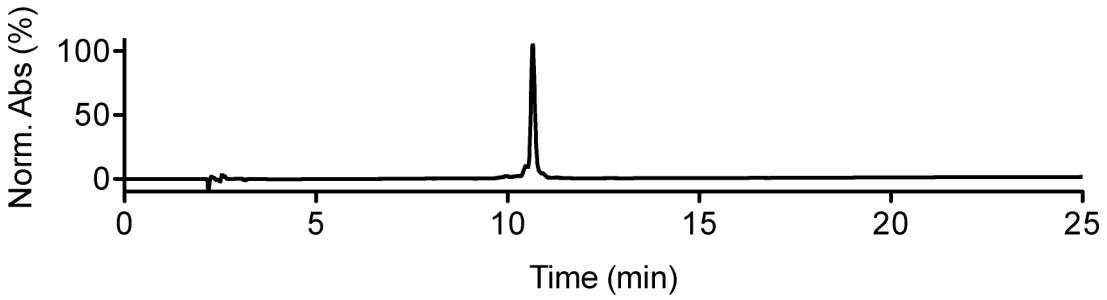

Figure 3.48. Analytical HPLC profile of **81** after preparative HPLC. Retention time = 11 min monitored by UV absorbance at 254 nm. Purity >95% by HPLC.

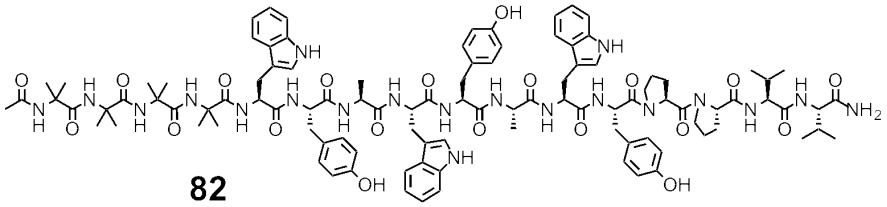

82

***N*-(Acetyl)-Aminoisobutyl-Aminoisobutyl-Aminoisobutyl-Aminoisobutyl-L-Tryptophyl-L-Tyrosyl-L-Alanyl-L-Tryptophyl-L-Tyrosyl-L-Alanyl-L-Tryptophyl-L-Tyrosyl-L-Prolyl-L-Prolyl-L-Valyl-L-Valinamide (82).** Using the general SPPS procedure, Rink amide MBHA resin (0.5 mmol/g, 60 mg, 0.03 mmol) was used to produce **82** (15 mg, 0.008 mmol, 25% yield overall) as a white solid. LR-MS (ESI+) m/z 2005.4 ($M+Na^+$, $C_{104}H_{132}N_{20}O_{20}Na$ requires 2005.0).

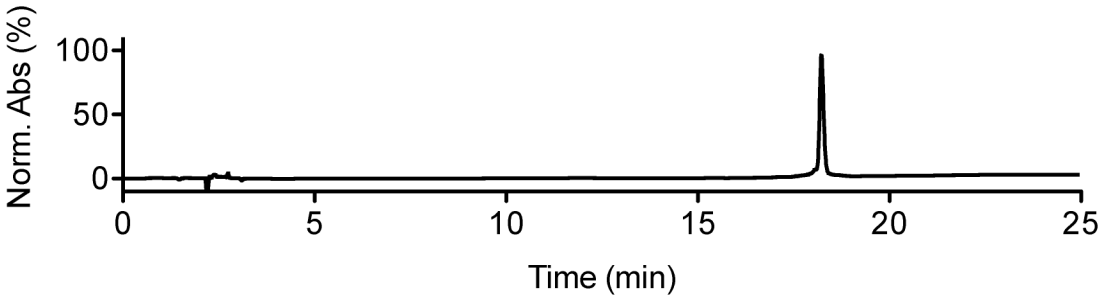

Figure 3.49. Analytical HPLC profile of **82** after preparative HPLC. Retention time = 18 min monitored by UV absorbance at 254 nm. Purity >95% by HPLC.

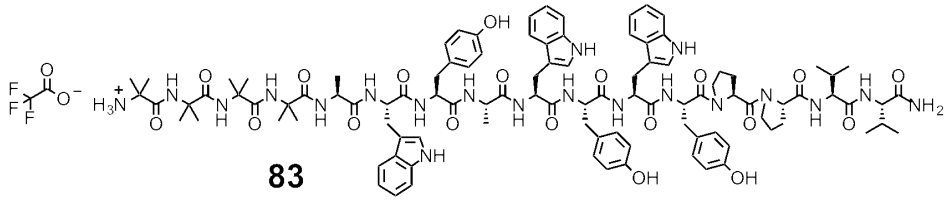

83

Aminoisobutyl-Aminoisobutyl-Aminoisobutyl-Aminoisobutyl-L-Alanyl-L-Tryptophyl-L-Tyrosyl-L-Alanyl-L-Tryptophyl-L-Tyrosyl-L-Tryptophyl-L-Tyrosyl-L-Prolyl-L-Prolyl-L-Valyl-L-Valinamide (83). Using the general SPPS

procedure, Rink amide MBHA resin (0.5 mmol/g, 60 mg, 0.03 mmol) was used to produce **79** (18 mg, 0.009 mmol, 31% yield overall) as a white solid. LR-MS (ESI+) m/z 1941.2 ($M+H^+$, $C_{102}H_{130}N_{20}O_{19}$ requires 1941.0).

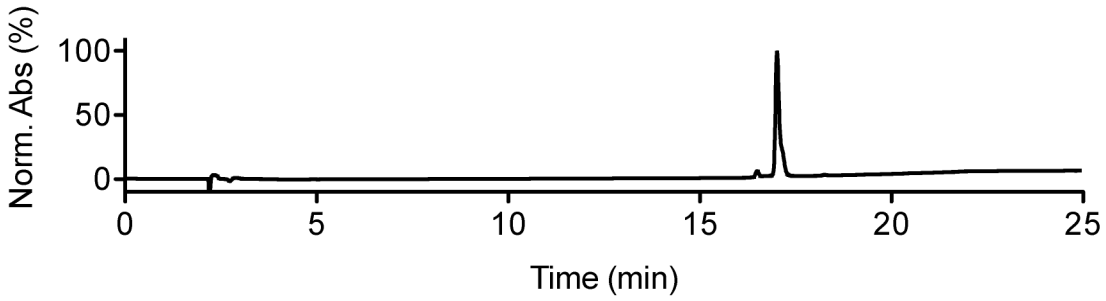

Figure 3.50. Analytical HPLC profile of **83** after preparative HPLC. Retention time = 17 min monitored by UV absorbance at 254 nm. Purity >95% by HPLC.

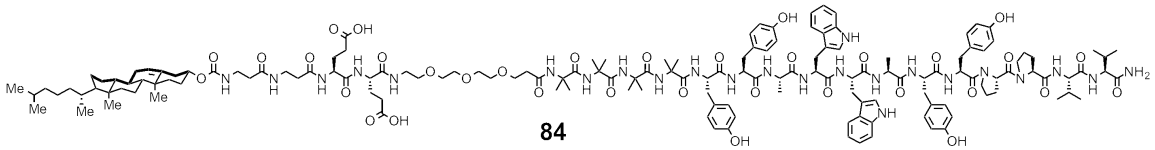

84

((3β-cholest-5-en-3-yl)carbonyl)-β-Alanyl-β-Alanyl-L-Glutamyl-L-Glutamyl-mPEG-Aminoisobutyl-Aminoisobutyl-Aminoisobutyl-Aminoisobutyl-L-Tyrosyl-L-Tyrosyl-L-Alanyl-L-Tryptophyl-L-Tryptophyl-L-Alanyl-L-Tyrosyl-L-Tyrosyl-L-Prolyl-L-Prolyl-L-Valyl-L-Valinamide (84). Using the general SPPS procedure, Rink amide MBHA resin (0.5 mmol/g, 60 mg, 0.03 mmol) was used to produce **84** (10 mg, 0.004 mmol, 11% yield overall) as a white solid. LR-MS (ESI-) m/z 1465.8 ($M-H^+/2$, $C_{153}H_{214}N_{24}O_{34}$ requires 1465.3).

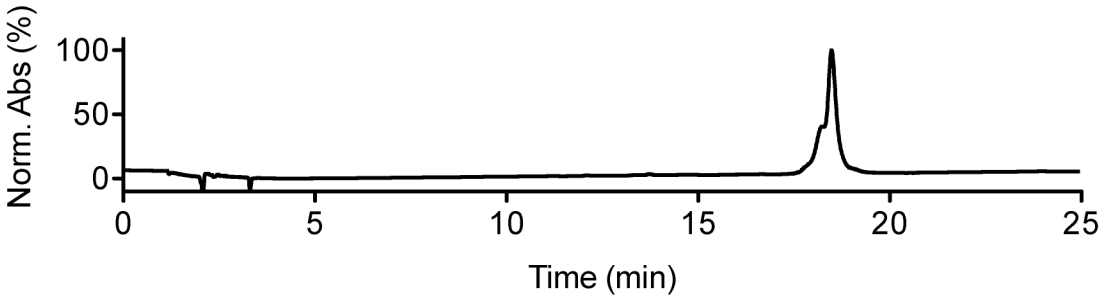

Figure 3.51. Analytical HPLC profile of **84** after preparative HPLC. Retention time = 18 min monitored by UV absorbance at 254 nm. Purity >95% by HPLC. Peak shoulder consistent with rotational isomer.

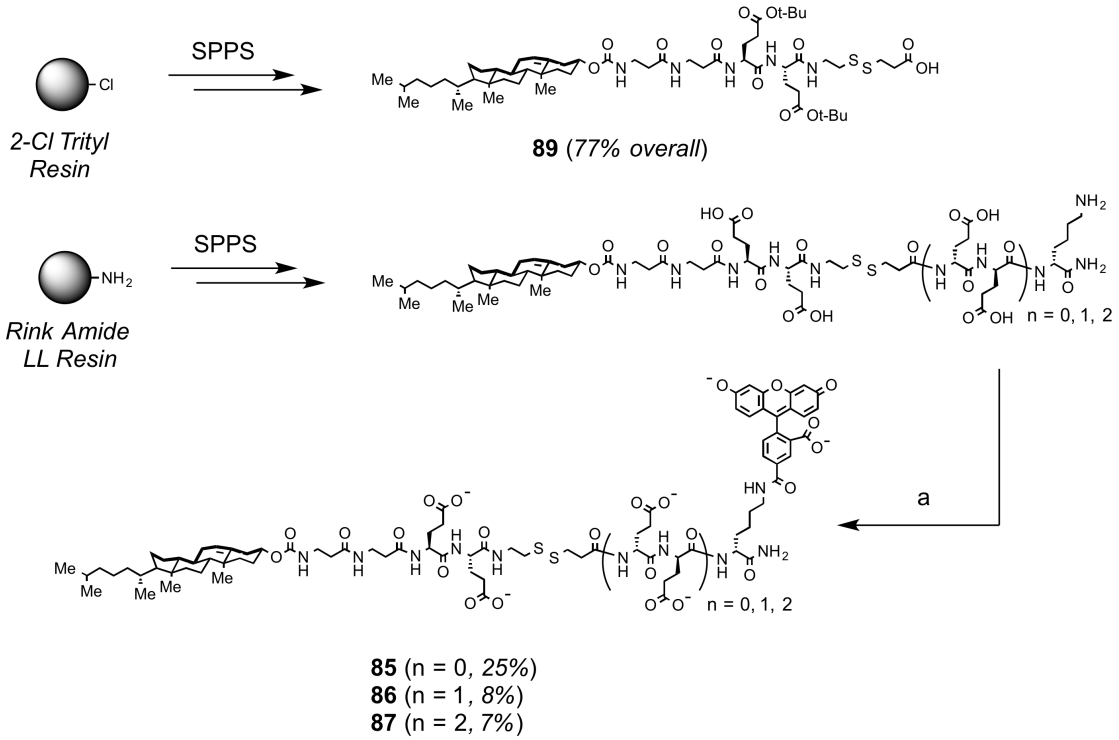

Figure 3.52. Reagents and Conditions: a) 5-carboxyfluorescein NHS-ester, DIEA, DMF, 22 °C, 16 h.

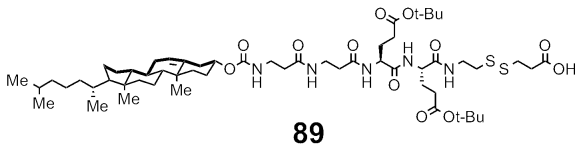

89

(11*S*,14*S*)-11,14-bis(2-carboxyethyl)-1-((cholester3-yl)oxy)-1,5,9,12,15-pentaoxo-19,20-dithia-2,6,10,13,16-pentaazatricosan-23-oic acid (89). Compound **89** was constructed using SPPS with 2-Chlorotrityl resin (1.3 mmol/g, 385 mg, 0.5 mmol) using Fmoc-protected 3-((2-aminoethyl)disulfanyl)propanoic acid[3], 3-((((Cholester-3-yl)oxy)carbonyl) amino)propanoic acid[39], and the following Fmoc-protected amino acids: Fmoc-β-Ala-OH, Fmoc-L-Glu(O*t*-Bu)-OH. The crude product was purified using flash chromatography (gradient elution of DCM to DCM/MeOH 95/5) to yield compound **89** (425 mg, 0.38 mmol, 77% overall yield) as an off-white solid. LR-MS (ESI-) m/z 1105.0 ($M-H^+$, $C_{57}H_{95}N_5O_{12}S_2$ requires 1104.6).

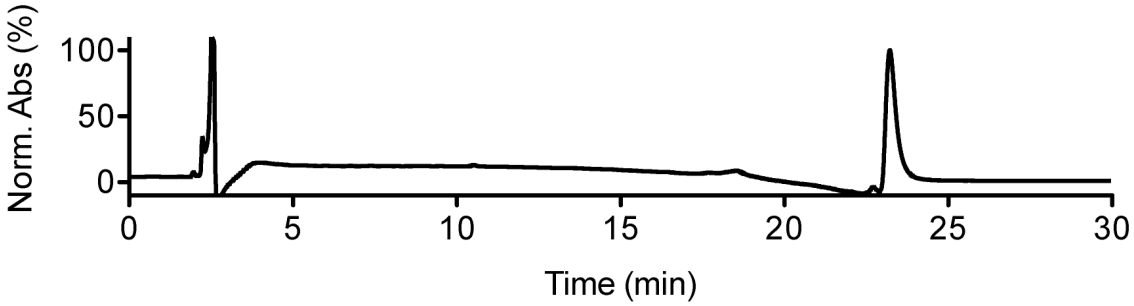

Figure 3.53. Analytical HPLC profile of **89** after column chromatography. Retention time = 24.0 min. Monitored by UV absorbance at 215 nm. Purity >90% by integration of chromatogram.

General Procedure for Synthesis of D-Glu Fluorescent Probes. Compounds **85** – **87** were constructed using SPPS with Rink amide LL resin with Fmoc-D-Lys(Boc)-OH, Fmoc-D-Glu(O*t*-Bu)-OH, and purified compound **89**. The crude peptides were dried under vacuum and azeotroped using a mixture of toluene/MeOH (3/1, 3 mL, 3x) to ensure complete removal of TFA and H_2O. The crude peptides were dissolved in 2mL dry DMF, then DIEA (0.2 mL) and 5-

carboxyfluorescein NHS-ester (2 eq.) were added and allow to stir at 22 °C for 16 h. The solvent was removed, and the residue was dissolved in DMSO (1.5 mL) and subjected to preparative RP-HPLC (Gradient: H_2O:CH_3CN (9:1) to (0:100) with added TFA (0.1%) over 20 min; elution time = 16-18 min). Pure fractions were collected, combined, and lyophilized to provide product as a yellow solid.

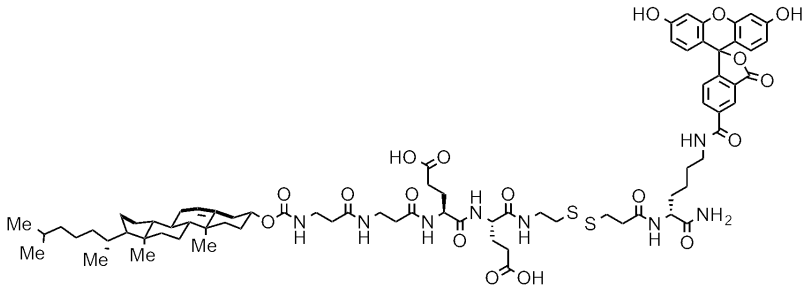

85

(11*S*,14*S*)-11,14-bis(2-carboxyethyl)-1-((cholester-3-yl)oxy)-1,5,9,12,15-pentaoxo-19,20-dithia-2,6,10,13,16-pentaazatricosan-23-yl-[D-Lysyl(ε-*N*-(6-hydroxy-3-oxo-3*H*-xanthen-9-yl)benzoic acid)] (85). Using the general procedure described above, Rink amide LL resin (0.36 mmol/g, 63 mg, 0.0225 mmol) was used to produce compound **85** (8.4 mg, 0.0057 mmol, 25% yield overall) as a yellow solid. LR-MS (ESI-) m/z 1478.1 ($M\text{-}H^+$, $C_{76}H_{102}N_8O_{18}S_2$ requires 1477.7).

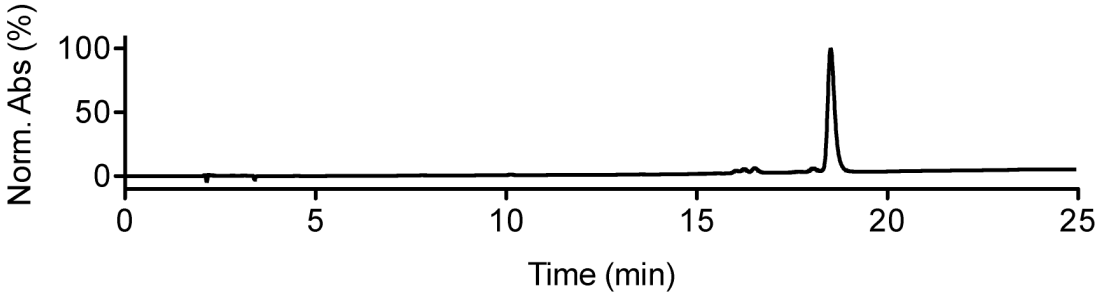

Figure 3.54. Analytical HPLC profile of **85** after preparative HPLC. Retention time = 19.1 min. Monitored by UV absorbance at 254 nm. Purity >90% by

integration of chromatogram. Peak shoulders provided equivalent m/z consistent with rotational isomers.

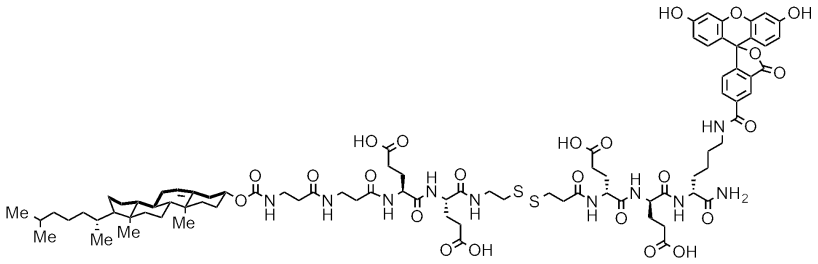

86

(11*S*,14*S*)-11,14-bis(2-carboxyethyl)-1-((cholester-3-yl)oxy)-1,5,9,12,15-pentaoxo-19,20-dithia-2,6,10,13,16-pentaazatricosan-23-yl-[D-Glutamyl-D-Glutamyl-D-Lysyl(ε-*N*-(6-hydroxy-3-oxo-3*H*-xanthen-9-yl)benzoic acid)] (86). Using the general procedure described above, Rink amide LL resin (0.36 mmol/g, 104 mg, 0.0375 mmol) was used to produce compound **86** (5.6 mg, 0.0032 mmol, 8% yield overall) as a yellow solid. LR-MS (ESI-) m/z 868.1 (M-2H$^+$/2, $C_{86}H_{117}N_{10}O_{24}S_2$ requires 867.4).

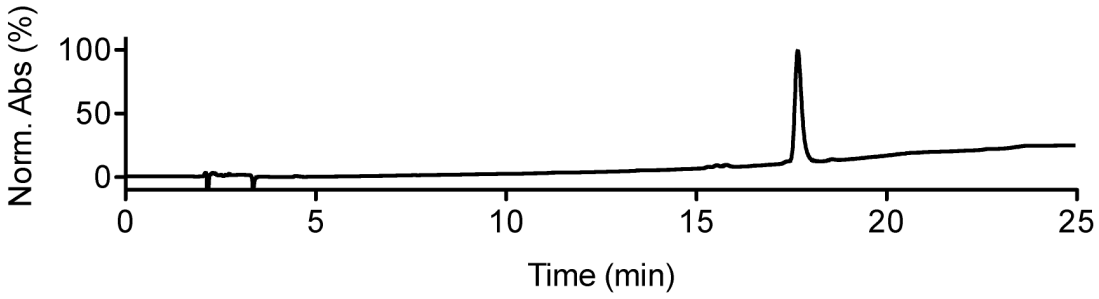

Figure 3.55. Analytical HPLC profile of **86** after preparative HPLC. Retention time = 18.0 min. Monitored by UV absorbance at 254 nm. Purity >90% by integration of chromatogram. Peak shoulders provided equivalent m/z consistent with rotational isomers.

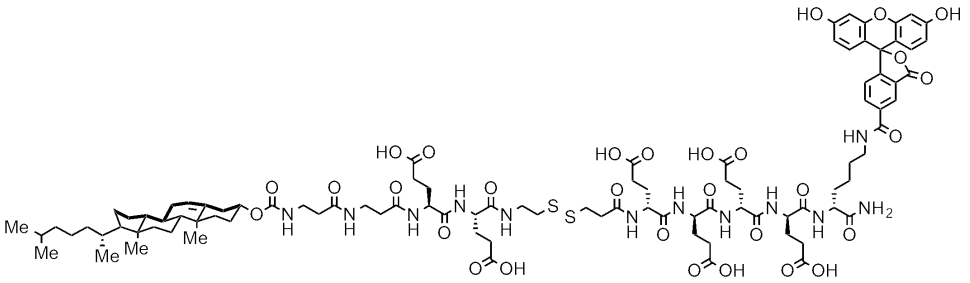

87

(11*S*,14*S*)-11,14-bis(2-carboxyethyl)-1-((cholester-3-yl)oxy)-1,5,9,12,15-pentaoxo-19,20-dithia-2,6,10,13,16-pentaazatricosan-23-yl-[D-Glutamyl-D-Glutamyl-D-Glutamyl-D-Glutamyl-D-Lysyl(ε-*N*-(6-hydroxy-3-oxo-3*H*-xanthen-9-yl)benzoic acid)] (87). Using the general procedure described above, Rink amide LL resin (0.36 mmol/g, 125 mg, 0.045 mmol) was used to produce compound **87** (6.2 mg, 0.0031 mmol, 7% yield overall) as a yellow solid. LR-MS (ESI-) m/z 997.4 ($M-2H^+/2$, $C_{96}H_{133}N_{12}O_{30}S_2$ requires 996.9).

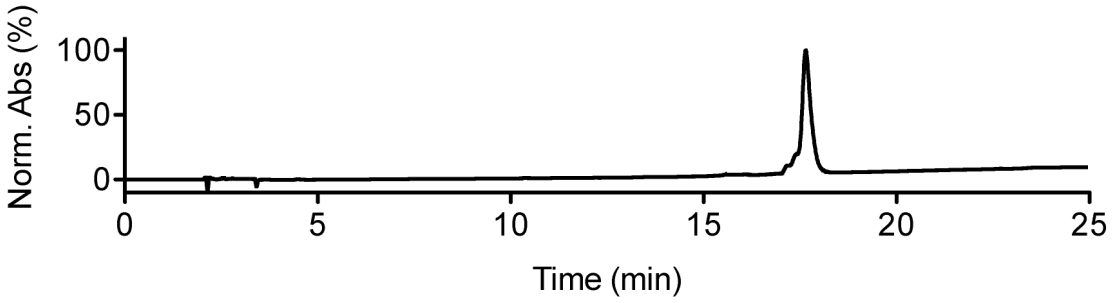

Figure 3.56. Analytical HPLC profile of **87** after preparative HPLC. Retention time = 17.5 min. Monitored by UV absorbance at 254 nm. Purity >90% by integration of chromatogram. Peak shoulders provided equivalent m/z consistent with rotational isomers.

3.9.3 Biological Assays and Protocols

General. Reagents were purchased from Sigma-Aldrich, Fisher Scientific, and Acros Organics. Cell culture reagents were from Sigma-Aldrich. UV/Vis measurements employed an Agilent 8452A diode array spectrophotometer.

Cell culture. Jurkat lymphocytes (human acute leukemia, ATCC #TIB-152) were cultivated in Roswell Park Memorial Institute (RPMI) 1640 medium supplemented with Fetal Bovine Serum (FBS, 10%), penicillin (100 units/mL), and streptomycin (100 µg/mL) and incubated in a humidified 5% CO_2 incubator at 37 °C. Media used for cell culture and all wash steps contained antibiotics and 10% FBS unless otherwise noted.

Microscopy. An inverted Leica TCS SPE confocal laser-scanning microscope fitted with a Leica 63X oil-immersion objective was employed for imaging. Fluorescent probes were excited with either a 405 nm or 488 nm solid-state laser and emitted photons were collected from 410-470 nm or 495-600 nm, respectively. To image living cells, 50 µL of cells in media was pipetted to form a small droplet in the center of a coverslip fitted with a press-to-seal silicone isolator (Invitrogen). A microscope slide was added to the top of the coverslip to create a column of media containing living cells. To allow accurate comparisons of differences in cellular fluorescence, laser power and PMT gain settings were identical for all samples shown in a given figure.

Flow Cytometry. Populations of 10,000 Jurkat cells were analyzed for each sample using an Accuri C6 flow cytometer equipped with 488 nm and 640 nm solid-state lasers. Live cells were gated using forward scattering (FSC) and side

scattering (SSC) dot plots to identify cellular physical properties of size and granularity.

Analysis of Endosome Disruption by Release of Fluorescent Probes. Jurkat lymphocytes were suspended at 350,000 cells per mL in media. The fluorescent probe (**3**, or **85** – **87**) was added at 2.5 μM (diluted from a 10 mM DMSO stock). Endosome disruptor was added at various concentrations from 10 nM to 16 μM (diluted from a 1000x DMSO stock). The samples were aliquoted into two eppendorf tubes at 500 μL each to provide replicates and incubated for 14 h in a 37 °C incubator with gentle rotation to maintain cell suspension. Following incubation, the cells were pelleted by centrifugation at 2,000 rpm for 2 minutes, re-suspended in 500 μL media, and allowed to incubate at 22 °C for 30 minutes to allow efflux of excess fluorescent probe from the plasma membrane. The cells were washed once more in media and analyzed for cellular fluorescence by flow cytometry.

Data analysis. Cells that were not treated with endosome disruptor (fluorescent probe alone) were analyzed to provide baseline fluorescence values. Following baseline subtraction, replicates for each compound were plotted versus concentration and analyzed by non-linear regression in Prism 5 using the "log(agonist) vs response – four parameter" model. To normalize the efficacy of each replicate, the span of the resulting curve was normalized to the activity of cholesterylamine-PC-4 (**2**) at 100%. To ensure the accuracy of efficacy measurements, each round of testing included either cholesterylamine-PC-4 (**2**)

or another previously normalized compound to serve as a known efficacy value to which additional compounds were normalized. The calculated EC_{50} values from the resulting curves were averaged to provide the mean EC_{50} ± standard deviation (SD). The average standard deviation of EC_{50} values for a given peptide was ~30% of the mean, based on multiple independent experiments for a subset of peptides. Analysis of each peptide contained at least two replicates, however for peptides that contained only two replicates and a SD <30% of the mean, the SD was adjusted to 30% of the mean. Efficacy values for each peptide were averaged to provide mean efficacy (as % of **2**) ± SD.

Toxicity Analysis of Endosome Disruptors. Jurkat lymphocytes were suspended at 350,000 cells per mL in media and aliquoted into a 48-well plate at 500 µL per well. Endosome disruptor was added at various concentrations from 1 µM to 32 µM (diluted from a 500x DMSO stock) in duplicate. The samples were incubated for 48 h at 37 °C. Following incubation, the cells were analyzed by flow cytometry. Live gating by FSC and SSC provided the cell viability for each condition. Cell viability at 48 h was plotted versus concentration and analyzed by non-linear regression in GraphPad Prism 6 to provide IC_{50} values.

Analysis of Endosome Disruptor Solubility. Endosome disruptor peptides (0.5 – 1.5 mg) were added to eppendorf tubes in triplicate. Each tube received 1 mL of PBS 7.4 and was placed in a sonication bath for 30 minutes at 22 °C to disperse the solid material. The tubes were incubated for 24 h at 22 °C with

agitation. Following incubation, the samples were centrifuged at 16,000 x G for 1 h to pellet any un-dissolved material. The supernatant was analyzed by UV absorbance at 280 nm and the concentration was determined using the calculated extinction coefficient for each peptide sequence (Table 3.7, http://www.basic.northwestern.edu/biotools/proteincalc.html). Concentration values for each compound were averaged from three independent replicates to provide thermodynamic solubility with error values typically <10%.

Cpd.	Sequence	Ext. Coeff. (ε, M^{-1} cm^{-1})	Cpd.	Sequence	Ext. Coeff. (ε, M^{-1} cm^{-1})
2	*MA*-SSAWWSYWPPVA-NH_2	18350	**67**	UUUUWWAYWAPVV-NH_2	18350
50	*MA*-SSAWWSYWPPVA-NH_2	18350	**68**	UUUUWWAYWPAVV-NH_2	18350
51	*MA*-AAAWWAYWPPVA-NH_2	18350	**69**	UUUUWWAYWPPAV-NH_2	18350
52	*MA*-UUUWWAYWPPVA-NH_2	18350	**70**	UUUUWWAWWPPVV-NH_2	22760
53	Ac-SSAWWSYWPPVA-NH_2	18350	**71**	UUUUYWAWWPPVV-NH_2	18350
54	Ac-AAAWWAYWPPVA-NH_2	18350	**72**	UUUUWYAWWPPVV-NH_2	18350
55	Ac-UUUWWAYWPPVA-NH_2	18350	**73**	UUUUWWAWYPPVV-NH_2	18350
56	Ac-UUUUWWAYWPPVA-NH_2	18350	**74**	UUUUWWWWYPPVV-NH_2	24040
57	Ac-UUUUUWWAYWPPVA-NH_2	18350	**75**	UUUUWWYWYPPVV-NH_2	19630
58	Ac-UUUUWWAYWPPVV-NH_2	18350	**76**	Ac-UUUUWWAWYPPVV-NH_2	18350
59	UUUUWWAYWPPVA-NH_2	18350	**77**	*MA*-UUUUWWAWYPPVV-NH_2	18350
60	UUUUWWAYWPPVV-NH_2	18350	**78**	*MA*-UUUUWWAWYPPVV-NH_2	18350
61	*MA*-UUUUWWAYWPPVA-NH_2	18350	**79**	UUUUWWAWWAWYPPVV-NH_2	29730
62	*MA*-UUUUWWAYWPPVA-NH_2	18350	**80**	UUUUWYAWYAWYPPVV-NH_2	20910
63	UUUUAWAYWPPVV-NH_2	12660	**81**	UUUUYYAWWAYYPPVV-NH_2	16500
64	UUUUWAAYWPPVV-NH_2	12660	**82**	Ac-UUUUWYAWYAWYPPVV-NH_2	20910
65	UUUUWWAAWPPVV-NH_2	17070	**83**	UUUUAWYAWYWYPPVV-NH_2	20910
66	UUUUWWAYAPPVV-NH_2	12660	**84**	*MA*-UUUUYYAWWAYYPPVV-NH_2	16500

Table 3.7. Calculated extinction coefficients (ε) for endosome disruptors **50** – **84** based on tryptophan and tyrosine content and absorbance at 280 nm.

Molecular Dynamics Simulations. MD simulations were performed by Dr. Gerry Lushington. For these simulations, close analogues of each peptide (e.g. sequence: AAAAWWAWYPPVV) were constructed via the Avogadro[42] polymer builder, specifying backbone torsion angles corresponding to the 3_{10} amino acid

helix. The first four N-terminal alanine residues were mutated to Aib in PyMol.[43] Pymol was further used to assemble the putative multi-peptide pore models and add flanking 1-palmitoyl-2-oleoylphosphatidylcholine (POPC) lipids. The ratio of peptide to lipid molecules was 1:2, and the lipid molecules were positioned to surround the multi-peptide pore model and ensure that no two pores would directly border each other under periodic boundary conditions. Aromatic amino acid side chains were hand-edited to devise a regular lattice of aromatic-aromatic interactions designed to stabilize the walls of the pore, with the aliphatic side chains oriented outwards into the lipid medium. Dynamic stability of the pore model complexes was evaluated via NAMD[36] molecular dynamics simulations according to the CHARMM[37] force field and electrostatics, but this force field was modified to include recently described[38] parameters for peptides containing Aib. NAMD topology files were created using VMD[44] as the basis for force field parameter specification, standardization of peptide termini (the N-terminus was capped with an acyl group, whereas the C-terminus was converted into an amide), and creation of a water saturated box. Water was introduced per default density specifications into a periodic unit cell for the simulation chosen to extend by 5.0 Angstroms both above and below the pore, but with no buffer within the plane of the simulated membrane. Pore stability was ultimately gauged via a standard protocol as follows: 1) interatomic interactions within the unit cell were relaxed via 1000 steps of temperature-agnostic molecular mechanics refinement, 2) unit cell dimensions were optimized via a 10000 step molecular dynamics simulation implementing the default Langevin piston pumping protocol specified

by VMD (standard atmospheric pressure; T = 298K), and finally 3) Constant temperature and volume analysis via a 20000 step molecular dynamics simulation according to the default production run specifications specified by VMD. Uniform decile time-sampling of molecular dynamics simulations of the hexapeptide embedded in the periodic endosomal membrane environment was performed to characterize the pore geometry and estimate its radius. For each analyzed geometry snapshot, MolAxis[45] software was used to quantify the pore radius as a function of time and of distance from the center of the channel. Using 4.0 Angstrom probe radius and 0.5 Angstrom resolution (all other parameters retained at default values), the intelligent sampling encoded within the MolAxis program produced radius sampling of between 35-45 points at different locations along the pore-perpendicular axis. From this combined spatial and temporal sampling, Dr. Lushington computed mean values for the overall pore radius, the bottleneck radius (single smallest radius per timestep).

3.10 References

1. Peterson, B. R., Synthetic mimics of mammalian cell surface receptors: prosthetic molecules that augment living cells. *Org. Biomol. Chem.* **2005,** *3*, 3607-3612.

2. Hymel, D.; Peterson, B. R., Synthetic cell surface receptors for delivery of therapeutics and probes. *Adv. Drug Deliv. Rev.* **2012,** *64*, 797-810.

3. Sun, Q.; Cai, S.; Peterson, B. R., Selective disruption of early/recycling endosomes: Release of disulfide-linked cargo mediated by a N-alkyl-3 beta-cholesterylamine-capped peptide. *J. Am. Chem. Soc.* **2008,** *130*, 10064-10065.

4. Nakase, I.; Kobayashi, S.; Futaki, S., Endosome-Disruptive Peptides for Improving Cytosolic Delivery of Bioactive Macromolecules. *Biopolymers* **2010,** *94*, 763-770.

5. Varkouhi, A. K.; Scholte, M.; Storm, G.; Haisma, H. J., Endosomal escape pathways for delivery of biologicals. *J. Control. Release* **2011,** *151*, 220-228.

6. Mudhakir, D.; Harashima, H., Learning from the Viral Journey: How to Enter Cells and How to Overcome Intracellular Barriers to Reach the Nucleus. *AAPS J.* **2009,** *11*, 65-77.

7. Han, X.; Bushweller, J. H.; Cafiso, D. S.; Tamm, L. K., Membrane structure and fusion-triggering conformational change of the fusion domain from influenza hemagglutinin. *Nat. Struct. Biol.* **2001,** *8*, 715-720.

8. Smith, A. E.; Helenius, A., How viruses enter animal cells. *Science* **2004,** *304*, 237-242.

9. Galloux, M.; Libersou, S.; Alves, I. D.; Marquant, R.; Salgado, G. F.; Rezaei, H.; Lepault, J.; Delmas, B.; Bouaziz, S.; Morellet, N., NMR Structure of a Viral Peptide Inserted in Artificial Membranes: A View on the Early Steps of the Birnavirus Entry Process. *J. Biol. Chem.* **2010,** *285*, 19409-19421.

10. Maia, L. F.; Soares, M. R.; Valente, A. P.; Almeida, F. C. L.; Oliveira, A. C.; Gomes, A. M. O.; Freitas, M. S.; Schneemann, A.; Johnson, J. E.; Silva, J. L., Structure of a membrane-binding domain from a non-enveloped animal virus -

Insights into the mechanism of membrane permeability and cellular entry. *J. Biol. Chem.* **2006,** *281*, 29278-29286.

11. Dormitzer, P. R.; Nason, E. B.; Prasad, B. V. V.; Harrison, S. C., Structural rearrangements in the membrane penetration protein of a non-enveloped virus. *Nature* **2004,** *430*, 1053-1058.

12. Schuerch, D. W.; Wilson-Kubalek, E. M.; Tweten, R. K., Molecular basis of listeriolysin O pH dependence. *Proc. Natl. Acad. Sci. U. S. A.* **2005,** *102*, 12537-12542.

13. Hamon, M. A.; Ribet, D.; Stavru, F.; Cossart, P., Listeriolysin O: the Swiss army knife of Listeria. *Trends Microbiol.* **2012,** *20*, 360-368.

14. Park, S. H.; Kim, H. E.; Kim, C. M.; Yun, H. J.; Choi, E. C.; Lee, B. J., Role of proline, cysteine and a disulphide bridge in the structure and activity of the anti-microbial peptide gaegurin 5. *Biochem. J.* **2002,** *368*, 171-182.

15. Chia, B. C. S.; Carver, J. A.; Mulhern, T. D.; Bowie, J. H., Maculatin 1.1, an anti-microbial peptide from the Australian tree frog, Litoria genimaculata. Solution structure and biological activity. *Eur. J. Biochem.* **2000,** *267*, 5265-5265.

16. Park, C. B.; Yi, K. S.; Matsuzaki, K.; Kim, M. S.; Kim, S. C., Structure-activity analysis of buforin II, a histone H2A-derived antimicrobial peptide: The proline hinge is responsible for the cell-penetrating ability of buforin II. *Proc. Natl. Acad. Sci. U. S. A.* **2000,** *97*, 8245-8250.

17. Hristova, K.; Dempsey, C. E.; White, S. H., Structure, location, and lipid perturbations of melittin at the membrane interface. *Biophys. J.* **2001,** *80*, 801-811.

18. Li, W. J.; Nicol, F.; Szoka, F. C., GALA: a designed synthetic pH-responsive amphipathic peptide with applications in drug and gene delivery. *Adv. Drug Deliv. Rev.* **2004,** *56*, 967-985.

19. Tu, Y.; Kim, J. S., A fusogenic segment of glycoprotein H from herpes simplex virus enhances transfection efficiency of cationic liposomes. *J. Gene. Med.* **2008,** *10*, 646-654.

20. Parente, R. A.; Nir, S.; Szoka, F. C., Mechanism of Leakage of Phospholipid Vesicle Contents Induced by the Peptide GALA. *Biochemistry* **1990,** *29*, 8720-8728.

21. Hirosue, S.; Weber, T., pH-dependent lytic peptides discovered by phage display. *Biochemistry* **2006,** *45*, 6476-6487.

22. Austin, C. D.; Wen, X. H.; Gazzard, L.; Nelson, C.; Scheller, R. H.; Scales, S. J., Oxidizing potential of endosomes and lysosomes limits intracellular cleavage of disulfide-based antibody-drug conjugates. *Proc. Natl. Acad. Sci. U. S. A.* **2005,** *102*, 17987-17992.

23. Graber, M. L.; Dilillo, D. C.; Friedman, B. L.; Pastorizamunoz, E., Characteristics of Fluorophores for Measuring Intracellular pH. *Anal. Biochem.* **1986,** *156*, 202-212.

24. Prasad, B. V. V.; Balaram, P., The Stereochemistry of Peptides Containing Alpha-Aminoisobutyric Acid. *Crc Critical Reviews in Biochemistry* **1984,** *16*, 307-348.

25. Karle, I. L.; Balaram, P., Structural Characteristics of Alpha-Helical Peptide Molecules Containing Aib Residues. *Biochemistry* **1990,** *29*, 6747-6756.

26. Wolfrum, C.; Shi, S.; Jayaprakash, K. N.; Jayaraman, M.; Wang, G.; Pandey, R. K.; Rajeev, K. G.; Nakayama, T.; Charrise, K.; Ndungo, E. M.; Zimmermann, T.; Koteliansky, V.; Manoharan, M.; Stoffel, M., Mechanisms and optimization of in vivo delivery of lipophilic siRNAs. *Nat. Biotechnol.* **2007,** *25*, 1149-1157.

27. Wu, S. Y.; McMillan, N. A. J., Lipidic Systems for In Vivo siRNA Delivery. *Aaps J.* **2009,** *11*, 639-652.

28. Raouane, M.; Desmaele, D.; Urbinati, G.; Massaad-Massade, L.; Couvreur, P., Lipid Conjugated Oligonucleotides: A Useful Strategy for Delivery. *Bioconjugate Chem.* **2012,** *23*, 1091-1104.

29. Mayr, W.; Oekonomopulos, R.; Jung, G., Synthesis and Conformation of a Polyoxyethylene-Bound Undecapeptide of the Alamethicin Helix and (2-Methylalanyl-L-Alanine)1-7. *Biopolymers* **1979,** *18*, 425-450.

30. Sudha, T. S.; Vijayakumar, E. K. S.; Balaram, P., Circular-Dichroism Studies of Helical Oligopeptides - Can 3(10) and Alpha-Helical Conformations be Chiroptically Distinguished. *Int. J. Pept. Protein Res.* **1983,** *22*, 464-468.

31. Silva, R.; Yasui, S. C.; Kubelka, J.; Formaggio, F.; Crisma, M.; Toniolo, C.; Keiderling, T. A., Discriminating 3(10)- from alpha helices: Vibrational and electronic CD and IR absorption study of related Aib-containing oligopeptides. *Biopolymers* **2002,** *65*, 229-243.

32. Toniolo, C.; Polese, A.; Formaggio, F.; Crisma, M.; Kamphuis, J., Circular dichroism spectrum of a peptide 3(10)-helix. *J. Am. Chem. Soc.* **1996,** *118*, 2744-2745.

33. Mitra, K.; Ubarretxena-Belandia, T.; Taguchi, T.; Warren, G.; Engelman, D. M., Modulation of the bilayer thickness of exocytic pathway membranes by membrane proteins rather than cholesterol. *Proc. Natl. Acad. Sci. U. S. A.* **2004,** *101*, 4083-4088.

34. Song, C.; Weichbrodt, C.; Salnikov, E. S.; Dynowski, M.; Forsberg, B. O.; Bechinger, B.; Steinem, C.; de Groot, B. L.; Zachariae, U.; Zeth, K., Crystal structure and functional mechanism of a human antimicrobial membrane channel. *Proc. Natl. Acad. Sci. U. S. A.* **2013,** *110*, 4586-4591.

35. Zaccai, N. R.; Chi, B.; Thomson, A. R.; Boyle, A. L.; Bartlett, G. J.; Bruning, M.; Linden, N.; Sessions, R. B.; Booth, P. J.; Brady, R. L.; Woolfson, D. N., A de novo peptide hexamer with a mutable channel. *Nat. Chem. Biol.* **2011,** *7*, 935-941.

36. Phillips, J. C.; Braun, R.; Wang, W.; Gumbart, J.; Tajkhorshid, E.; Villa, E.; Chipot, C.; Skeel, R. D.; Kale, L.; Schulten, K., Scalable molecular dynamics with NAMD. *J. Comput. Chem.* **2005,** *26*, 1781-1802.

37. Vanommeslaeghe, K.; Hatcher, E.; Acharya, C.; Kundu, S.; Zhong, S.; Shim, J.; Darian, E.; Guvench, O.; Lopes, P.; Vorobyov, I.; MacKerell, A. D., CHARMM General Force Field: A Force Field for Drug-Like Molecules Compatible with the CHARMM All-Atom Additive Biological Force Fields. *J. Comput. Chem.* **2010,** *31*, 671-690.

38. Grubisic, S.; Brancato, G.; Barone, V., An improved AMBER force field for alpha,alpha-dialkylated peptides: intrinsic and solvent-induced conformational

preferences of model systems. *Phys. Chem. Chem. Phys.* **2013,** *15*, 17395-17407.

39. Yu, X. D.; Liu, Q. A.; Wu, J. C.; Zhang, M. M.; Cao, X. H.; Zhang, S.; Wang, Q.; Chen, L. M.; Yi, T., Sonication-Triggered Instantaneous Gel-to-Gel Transformation. *Chem.-Eur. J.* **2010,** *16*, 9099-9106.

40. Ueno, Y.; Jiao, G. S.; Burgess, K., Preparation of 5-and 6-carboxyfluorescein. *Synthesis-Stuttgart* **2004**, 2591-2593.

41. Kaduk, C.; Wenschuh, H.; Beyermann, M.; Forner, K.; Carpino, L.; Bienert, M., Synthesis of Fmoc-amino acid fluorides via DAST, an alternative fluorinating agent. *Lett. Pept. Sci.* **1996,** *2*, 285-288.

42. Hanwell, M. D.; Curtis, D. E.; Lonie, D. C.; Vandermeersch, T.; Zurek, E.; Hutchison, G. R., Avogadro: an advanced semantic chemical editor, visualization, and analysis platform. *J. Cheminformatics* **2012,** *4*, 17.

43. Schrödinger, L., The PyMOL Molecular Graphics System. *Version 1.6 (2013)*.

44. Humphrey, W.; Dalke, A.; Schulten, K., VMD: Visual molecular dynamics. *J. Mol. Graph.* **1996,** *14*, 33-38.

45. Yaffe, E.; Fishelovitch, D.; Wolfson, H. J.; Halperin, D.; Nussinov, R., MolAxis: Efficient and accurate identification of channels in macromolecules. *Proteins* **2008,** *73*, 72-86.

Chapter 4

Toward Tumor Selective Toxicity using Small Molecule-Protein Conjugates and Endosome Disruptive Peptides

4.1 Introduction

Optimized endosome disruptive peptides developed by the Peterson lab provide chemically-defined tools for the delivery of cell-impermeable small molecules into the cytosol of living mammalian cells. Structure-activity relationships (SAR), experimental data, and molecular modeling provided evidence that these peptides form a hexameric pore structure in the lipid bilayers of early endosomes with a diameter of ~15 Å. This pore assembly allows the efficient release of disulfide-linked small molecules targeted to early endosomes by cholesterol-based membrane anchors.

During the course of developing improved endosome disruptors, our lab also investigated the application of these compounds as a drug delivery system for cancer therapeutics. The preliminary work for this application, performed by Dr. Qi Sun and Ning Yang, involved the controlled release of cytotoxins using endosome disruptors. Dr. Sun's initial work utilized disulfide-linked colchicine,[1, 2] a tubulin-destablilizing cytotoxin, targeted to membranes of early endosomes by cholesterylamines and conjugated via a disulfide. Co-treatment with the endosome disruptor cholesterylamine-PC-4 (**2**)[3] produced a 5-fold increase in

cellular toxicity, providing proof-of-concept that endosome disruption could induce cellular toxicity through release of a cytotoxic warhead.

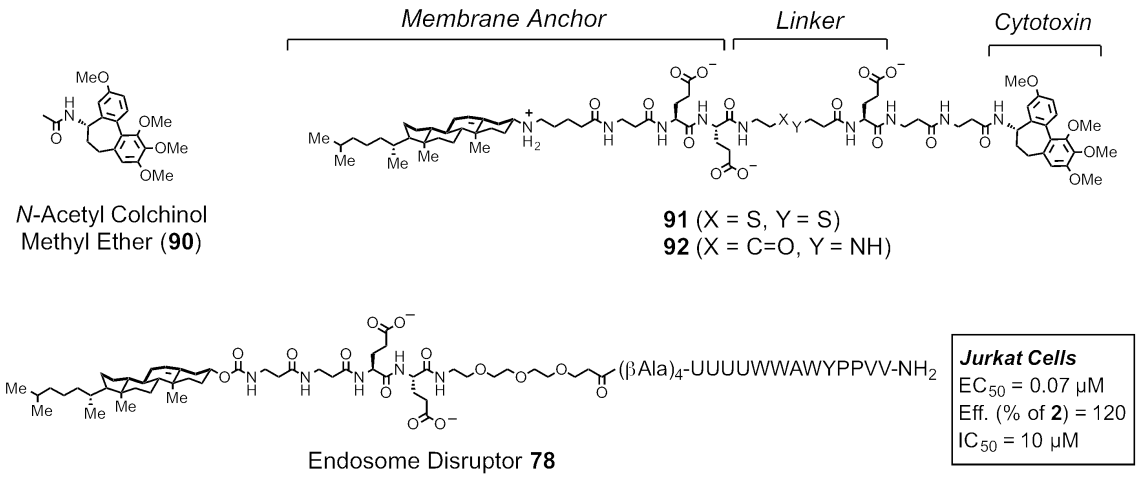

Figure 4.1. Structures of *N*-acetyl colchinol methyl ether (**90**, NACME), the membrane anchored disulfide (**91**) and amide (**92**) linked CME compounds, and endosome disruptor **78**.

As part of his Master's thesis, Ning Yang synthesized compounds **91** and **92** (Figure 4.1) with colchinol methyl ether (CME) as the cytotoxic warhead.[4, 5] In the absence of endosome disruption, these CME analogues demonstrated less cytotoxicity than the previous colchicine analogue, presumably by limiting off-target toxicity seen with the membrane-anchored colchicine compound. He also found that inclusion of the anionic glutamic acid residue proximal to the disulfide enhanced cytotoxicity, presumably by increasing retention of the warhead in the cytosol following release from endosomes. As shown in Figure 4.2, a 50-fold increase in cytotoxicity is observed for compound **91** when endosome disruptor **78** is co-administered in two different cell lines. Compound **92** contains a much more stable amide linkage and shows significantly less toxicity in the presence of the endosome disruptor.

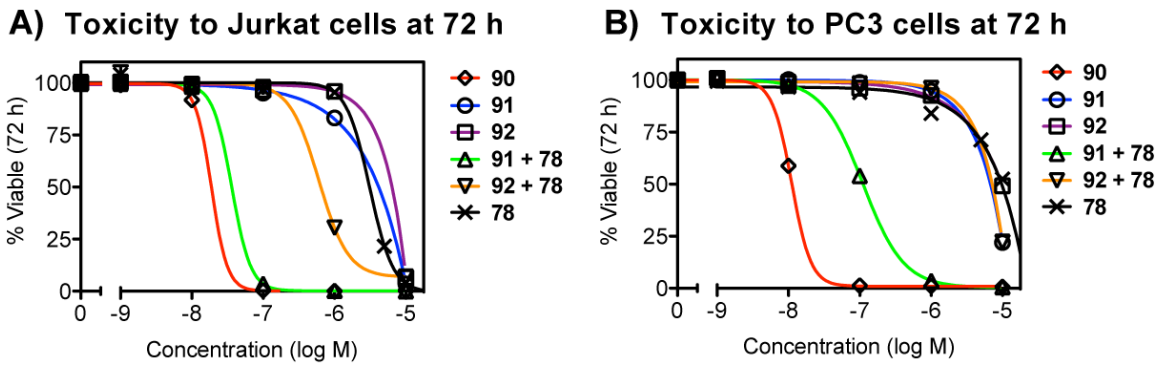

Figure 4.2. Toxicity analysis of compounds **90** – **92** in the presence and absence of endosome disruptor **78**. Jurkat lymphocytes (A) or PC3 cells (B) were treated for 72 h with and without **78** (1 μM). Analysis performed by flow cytometry and fit by non-linear regression to provide IC_{50} values.

Compound Added		Jurkat cells (IC_{50}, μM)	PC3 cells (IC_{50}, μM)
90	(NACME)	0.02	0.01
91	(*MA*-Disulfide-CME)	2.2	5.0
92	(*MA*-Amide-CME)	3.7	9.9
91 + 78	(*MA*-Disulfide-CME + ED)	0.04	0.11
92 + 78	(*MA*-Amide-CME + ED)	0.63	5.4
78	(ED alone)	3.1	9.5

Table 4.1. IC_{50} values of compounds **90** – **92** in Jurkat or PC3 cells. Endosome disruptor **78** was used to induce release of the cytotoxic CME warhead. *MA* = Membrane Anchor. ED = Endosome Disruptor.

This work further demonstrated that endosome disruption can be used to release bioactive molecules and produce a physiological effect. Moreover, development of the optimized disulfide-linked colchinol produced a warhead that is nearly equipotent to the parent cytotoxin *N*-acetyl cholchinol methyl ether (NACME, **90**) in Jurkat cells. However, the application of this system to cancer chemotherapy is hindered by a major limitation; since the cholesterol-based

membrane anchor is efficiently taken up by nearly all mammalian cell types, conjugated cytotoxins such as **91** would not produce selective toxicity to tumor cells versus normal cells.

To address this limitation, we began to investigate conjugation to antibodies as a means to selectively deliver a disulfide-linked cytotoxic warhead to tumor cells that overexpress targeted cell surface receptors. These conjugates would bind their cell surface antigen and undergo receptor-mediated endocytosis to accumulate in endosomes similar to the cholesterol-based membrane anchors.[6] Release of the warhead could then be induced by co-treatment with endosome disruptive peptides to produce tumor-specific toxicity.

4.2 Antibody-Drug Conjugates in Cancer Chemotherapy

Antibody-drug conjugates (ADCs) are becoming widely used in cancer chemotherapy because of their ability to accumulate and release potent cytotoxic agents in tumor cells that overexpress targeted cell surface receptors.[7-9] ADCs essentially act as prodrugs while in systemic circulation. They can remain in circulation for several days by cycling in and out of the vascular endothelium through binding to the neonatal Fc receptor (FcRn).[10-12] ADCs generally comprise an antibody, a cleavable or non-cleavable linker, and a potent cytotoxin.[13] Examples of three FDA-approved ADCs are shown in Figure 4.3. An ideal antibody is targeted to a cell surface receptor that is exclusively or abundantly expressed on tumor cells versus normal tissues. This receptor should undergo rapid internalization, typically through receptor-mediated endocytosis, as

well as appropriate intracellular trafficking to allow for release of the cytotoxic payload. Receptors commonly targeted by monoclonal antibodies for cancer therapy include the epidermal growth factor receptor (EGFR),[14, 15] vascular endothelial growth factor (VEGF),[16, 17] human epidermal growth factor receptor 2 (HER2),[18, 19] CD-20,[20] CD-30,[21] and CD-33.[22]

Release of the cytotoxin can be achieved though chemical or enzymatic means.[23-25] Due to the long half-life of ADCs, the stability of the linker is critically important. Some ADCs utilize cleavable linkers such as acid-labile hydrazones or disulfides. These linkers are typically more labile in systemic circulation, however their stability can be increased by addition of steric bulk or modulation of the electronic properties near the cleavage site. Non-cleavable linkers typically require proteolysis of either a peptide substrate in the linker, such as Adcetris[21, 26, 27] containing a valine-citruline dipeptide linker (Figure 4.3), or degradation of the entire antibody in the lysosome. Regardless of the cleavage mechanism, the design of the linker must also allow release of an active cytotoxic drug.

Another important design aspect of ADCs is the method of conjugation between the antibody and the linker-drug payload. The most common methods are alkylation of reduced cysteine residues, acylation of lysine residues, or genetically engineering the antibody for site-specific conjugation. The first two methods produce heterogeneous mixtures with several payload molecules linked per antibody. Genetically engineered sites allow for specific conjugation of a single payload, however each of these methods has demonstrated therapeutic efficacy. The stoichiometry of the linked payload is also important. ADCs with 2 –

4 drugs per IgG show the greatest efficacy, while more heavily loaded antibodies are cleared more rapidly from circulation.[28]

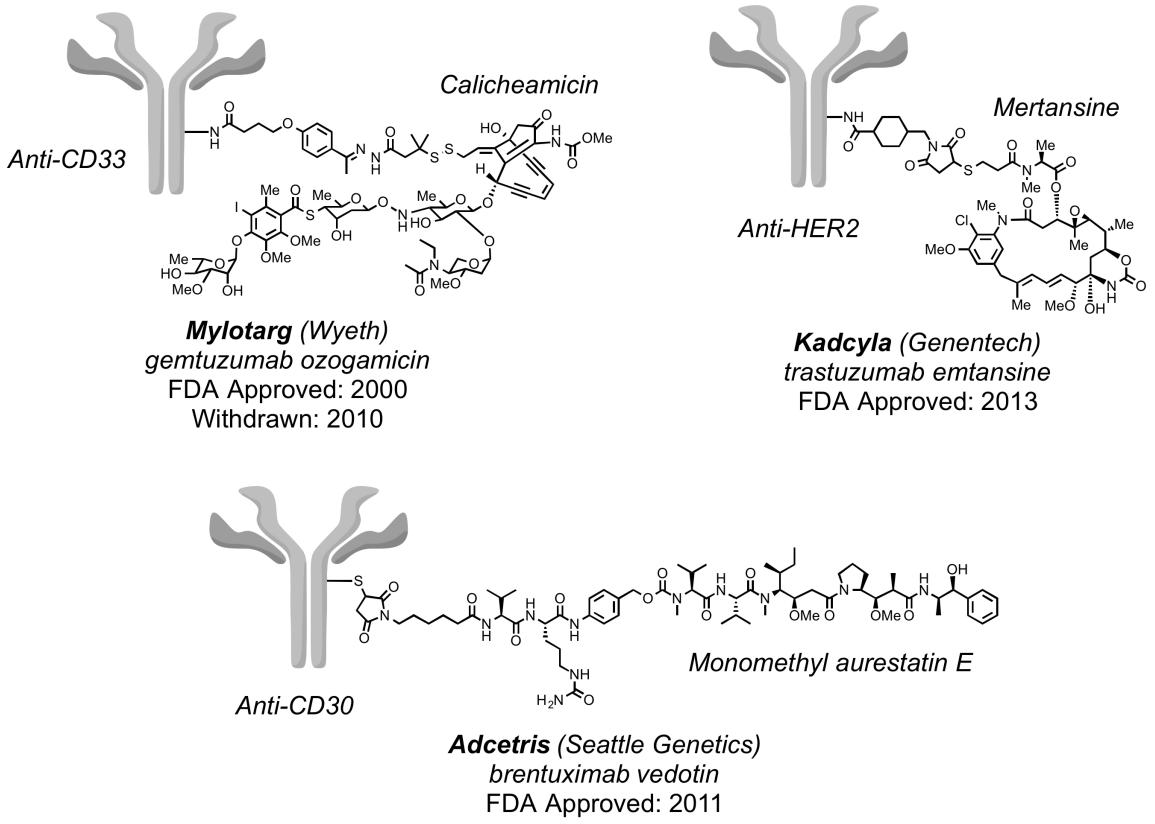

Figure 4.3. Structure and composition of current FDA-approved antibody-drug conjugates. ADCs contain an antibody targeted to a cell surface receptor, a cleavable or non-cleavable linker, and a cytotoxic warhead.

Despite the selectivity of an ADC for tumor cells versus normal tissue, its exposure to systemic circulation is far greater than its exposure to the tumor environment. As a result, the vast majority of a given dose is cleared in systemic circulation and very little of a given dose is localized to tumor cells. Because of this, ADCs require highly cytotoxic agents, typically sub-nanomolar potency, to produce therapeutic efficacy. Mylotarg utilizes the DNA-cleaving enediyne calicheamicin as its cytotoxin along with an acid-labile hydrazone linker.[22, 29]

Although this was the first ADC approved by the FDA, this drug was voluntarily withdrawn due to a narrow therapeutic index caused by non-specific cleavage to release the highly potent warhead. Subsequent generations of ADCs, represented by Adcetris[21, 26, 27] and Kadcyla[18, 30, 31], utilize potent tubulin-binding agents as their cytotoxins and contain more stable linkers that require proteolysis. These next-generation ADCs have significantly improved therapeutic indices, however the highly potent cytotoxin still causes some dose-limiting toxicities.

We hypothesized that we could improve the potency of ADCs by inducing release of the conjugated cytotoxin through endosome disruption. This method could be advantageous for two reasons: 1) inducing cleavage of a disulfide bond to release a cytotoxic payload would be more efficient than proteolytic mechanisms, and 2) this increase in efficiency would allow the use of cytotoxins with lower potency, such as our optimized colchinol methyl ether (CME), and thus reduce dose-limiting toxicities caused by systemic exposure.

In this chapter, we report the further evaluation of compounds **90** – **92** using optimized endosome disruptors to induce toxicity. We also report proof-of-concept experiments to characterize the release of disulfide-linked cargo from conjugated antibodies. Furthermore, we describe current and future work involving conjugation of endosome disruptive peptides with antibodies to generate dual-antibody delivery systems targeting tumor cells that overexpress two different cell surface receptors.

4.3 Release of Cytotoxic Cargo using Optimized Endosome Disruptors

In order to further characterize the release of bioactive molecules, we evaluated compounds **90** – **92** in two different cell lines using optimized endosome disruptors. Endosome disruptor **80** does not contain the membrane anchor, but still demonstrated sub-micromolar endosome disruption activity based on release of the fluorescent probe **3** in Jurkat lymphocytes. As shown in Table 4.2, co-treatment of **91** with endosome disruptor **80** shows >100-fold induction of toxicity versus **91** alone in Jurkat lymphocytes. As a control, the colchinol probe **92** shows greatly reduced toxicity when co-treated with **80** due to the increased stability of the amide-containing linker. In SKBr3 breast cancer cells, co-treatment of **91** with **80** shows significantly less potency, with only a 7-fold induction of toxicity observed versus **91** alone. Because of this result, we evaluated **80** and other endosome disruptors that lack a membrane anchor in multiple adherent cell lines. For reasons that are unclear, it was found that the endosome disruptive activity of compounds lacking the membrane anchor is greatly reduced in most adherent cell lines. This difference may relate to differential rates of pinocytosis of the endosome disruptive peptide.

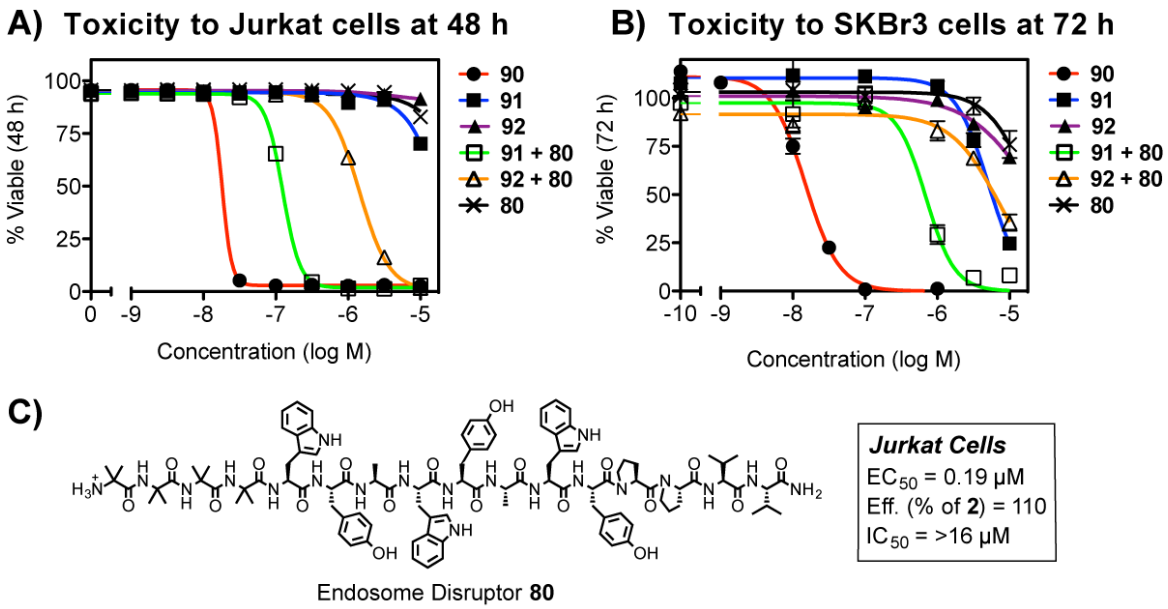

Figure 4.4. Toxicity analysis of compounds **90** – **92** in the presence and absence of endosome disruptor **80**. Jurkat lymphocytes (A) treated for 48 h or SKBr3 cells (B) treated for 72 h with and without **80** (1 µM). Analysis performed by flow cytometry and fit by non-linear regression to provide IC_{50} values. C) Structure and activity data for endosome disruptor **80**.

Compound Added		Jurkat cells (IC_{50}, µM)	SKBr3 cells (IC_{50}, µM)
90	(NACME)	0.02	0.02
91	(*MA*-Disulfide-CME)	18	5.1
92	(*MA*-Amide-CME)	>>10	21
91 + 80	(*MA*-Disulfide-CME + ED)	0.13	0.7
92 + 80	(*MA*-Amide-CME + ED)	1.5	7.2
80	(ED alone)	23	20

Table 4.2. IC_{50} values of compounds **90** – **92** in Jurkat or SKBr3 cells. Endosome disruptor **80** was used to induce release of the cytotoxic CME warhead. *MA* = Membrane Anchor. ED = Endosome Disruptor.

In contrast to **80**, the membrane anchored endosome disruptor **84** demonstrated robust activity in both the Jurkat and SKBr3 cell lines (Figure 4.5

and Table 4.3). In Jurkat lymphocytes, a 200-fold increase in toxicity was observed for **91** when co-treated with **84**. In SKBr3 cells, a 100-fold increase in toxicity was observed. In both of these cell lines, the combination of **91** and **84** produced toxicity nearly equipotent to the parent drug NACME (**90**). Again, the more stable amide-linked compound **92** demonstrated greatly reduced toxicity in both cell lines.

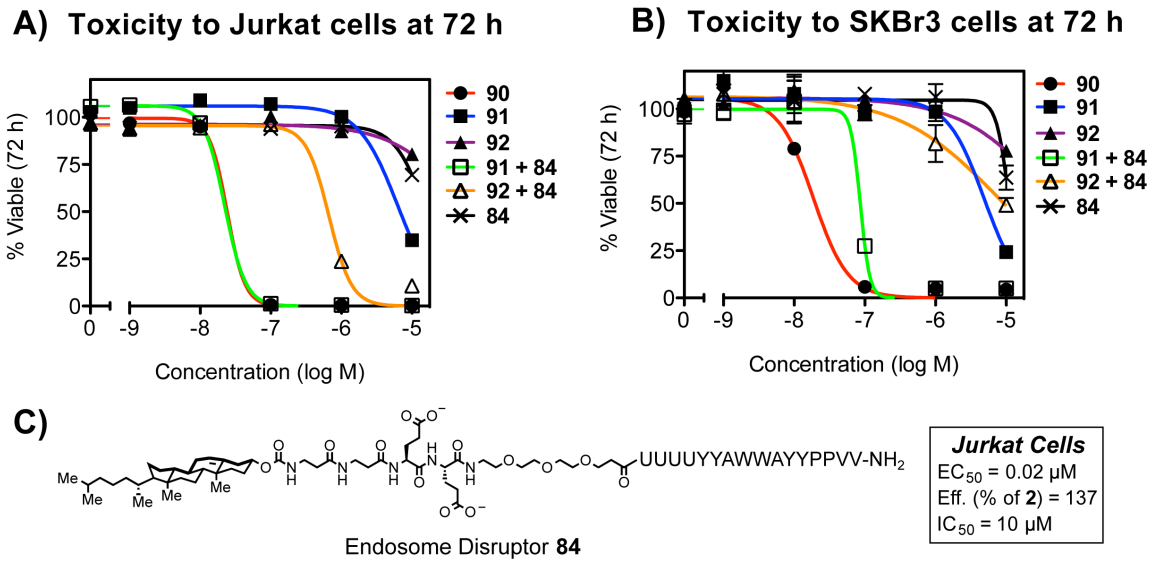

Figure 4.5. Toxicity analysis of compounds **90** – **92** in the presence and absence of endosome disruptor **80**. Jurkat lymphocytes (A) treated for 48 h or SKBr3 cells (B) treated for 72 h with and without **80** (1 μM). Analysis performed by flow cytometry and fit by non-linear regression to provide IC_{50} values. C) Structure and activity data for endosome disruptor **84**.

Compound Added		Jurkat cells (IC_{50}, μM)	SKBr3 cells (IC_{50}, μM)
90	(NACME)	0.02	0.02
91	(*MA*-Disulfide-CME)	6.3	4.9
92	(*MA*-Amide-CME)	>50	>10
91 + 84	(*MA*-Disulfide-CME + ED)	0.02	0.08
92 + 84	(*MA*-Amide-CME + ED)	0.67	7.5
84	(ED alone)	16	11

Table 4.3. IC_{50} values of compounds **90** – **92** in Jurkat or SKBr3 cells. Endosome disruptor **84** was used to induce release of the cytotoxic CME warhead. *MA* = Membrane Anchor. ED = Endosome Disruptor.

Based on these results, we moved forward to preliminary studies with antibody conjugates using membrane anchored endosome disruptors. For reasons discussed in the previous chapter, the requirement of the cholesterol-based membrane anchor was not ideal. However for proof-of-concept experiments, these compounds were necessary to produce robust release of small molecule cargo in adherent cell lines. Elimination of the membrane anchor will be addressed later in this chapter as part of the future directions.

4.4 Release of Disulfide-Linked Cargo from an Antibody Targeted to a Cell Surface Receptor

For proof-of-concept experiments aimed at releasing small molecule cargo from an antibody, we first synthesized compound **93** containing carboxy-fluorescein linked through a disulfide to an NHS ester. This amine-reactive compound can be used to label lysine residues of an antibody and cleavage of

the disulfide produces the same fluorescent cargo as compound **3** described in the previous chapter.

Several unconjugated or 'naked' antibodies are FDA-approved and used clinically in cancer chemotherapy. For our initial experiments we chose Herceptin (Trastuzumab, Genentech), a humanized IgG targeting human epidermal growth factor receptor 2 (HER2). This antibody has been used for over a decade to treat HER2 positive breast cancer and is also used in several ADCs including Kadcyla (Figure 4.3).

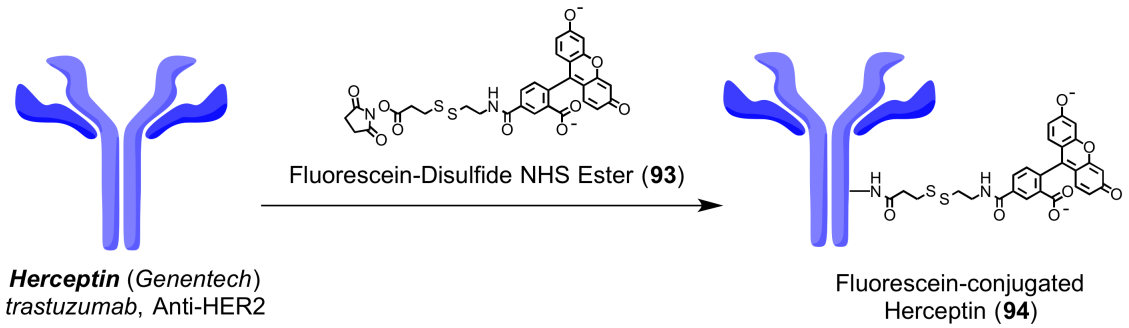

Figure 4.6. Structures of the fluorescein-disulfide NHS ester (**93**) and the conjugated anti-HER2 antibody Herceptin (**94**).

Using a standard protein labeling protocol and size-exclusion chromatography, Herceptin was conjugated with compound **93** to produce the fluorescent protein conjugate **94** (Figure 4.6). We first evaluated the binding and trafficking properties of this conjugate by confocal microscopy using HEK-293T cells that were transiently transfected with a plasmid expressing HER2 fused to cyan fluorescent protein (HER2-CFP, Figure 4.7, Panel B). HEK-293 cells express very low levels of HER2 and therefore do not bind Herceptin to a large extent. Upon treatment with **94**, strong co-localization can be observed between the green fluorescent Herceptin conjugate and cells expressing the cyan HER2

fusion protein (Figure 4.7, Panel C). To evaluate release of the conjugated fluorophore, transfected cells were then co-treated with **94** and endosome disruptor **61**. Co-treatment produced strong fluorescence in the cytosol and nucleus indicative of release of the fluorescent cargo (Figure 4.7, Panel D).

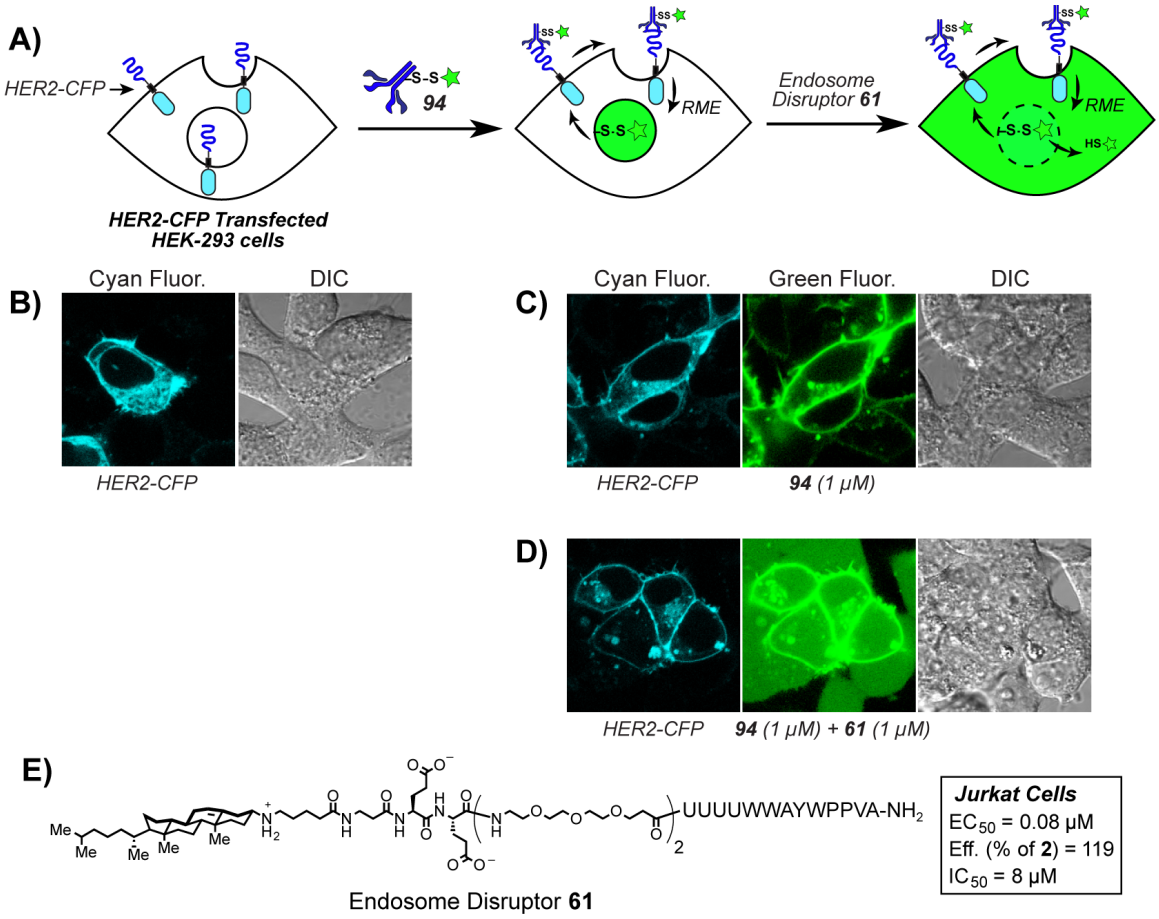

Figure 4.7. Cellular release of carboxyfluorescein from Herceptin in HEK-293 cells that transiently express HER2-CFP. A) Schematic representation of Herceptin uptake and release of the free fluorophore. B) Confocal micrographs of HEK-293 cells transiently transfected with HER2-CFP for 48 h. C) Treatment of HER2-CFP expressing cells with **94** (1 μM) for 24 h. D) Co-treatment of **94** (1 μM) with endosome disruptor **61** (1 μM) for 24 h.

We performed a similar experiment in SKBr3 cells, which endogenously overexpress HER2 on the cell surface. As shown in Figure 4.8, strong

fluorescence is observed on the plasma membrane of these cells when treated with **94**. Upon co-treatment with endosome disruptor **78** (Figure 4.1), fluorescence is observed in the cytosol and nucleus (Figure 4.8, Panel C). These results demonstrate that an antibody targeted to a cell surface receptor can be used in conjunction with endosome disruptors such as **78** to efficiently deliver disulfide-linked small molecules.

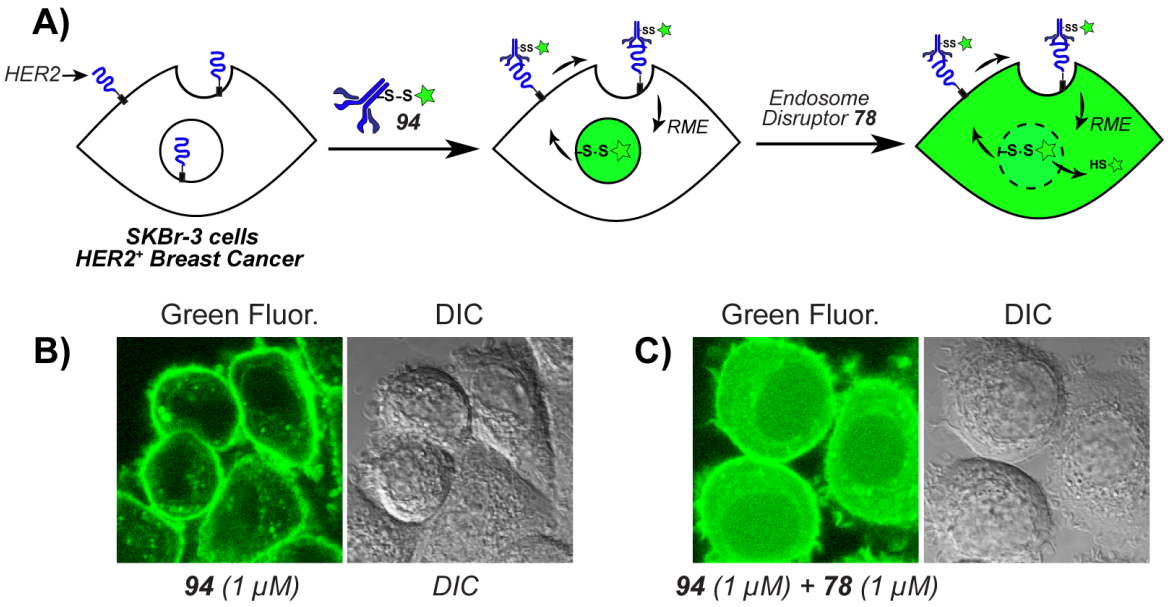

Figure 4.8. Cellular release of carboxyfluorescein from Herceptin in HER2 positive SKBr3 cells. A) Schematic representation of Herceptin uptake and release of the free fluorophore. B) Confocal micrographs of SKBr3 cells treated with **94** (1 μM) for 24 h. C) Co-treatment of **94** (1 μM) with endosome disruptor **78** (1 μM) for 24 h.

To expand on the previous results, we designed and synthesized compound **95**, which allows antibody conjugation of our optimized colchinol methyl ether (CME) cytotoxin to antibodies. We labeled Herceptin with this compound to produce the antibody-drug conjugate **96** (Figure 4.9). Again using HER2-positive SKBr3 cells, we evaluated the toxicity of **96** by flow cytometry in

the presence and absence of endosome disruptor **78**. Similar to the membrane-anchored compound **91**, we observed a >200-fold increase in toxicity of **96** in the presence of the endosome disruptor (Figure 4.8). This result indicates that we can significantly improve the toxicity of an ADC using endosome disruptors to facilitate the release of a conjugated cytotoxin.

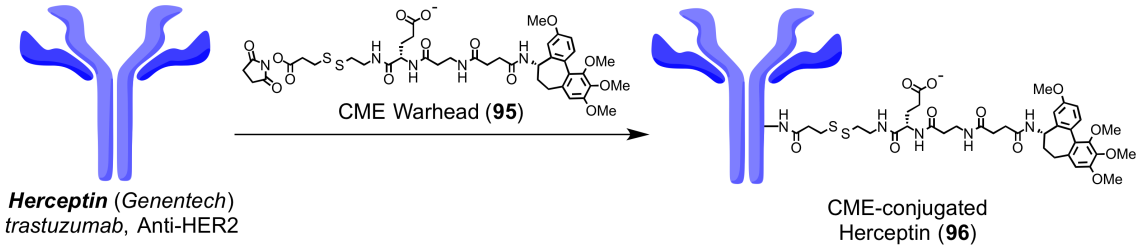

Figure 4.9. Structures of the CME-disulfide NHS ester (**95**) and the conjugated anti-HER2 antibody Herceptin (**96**).

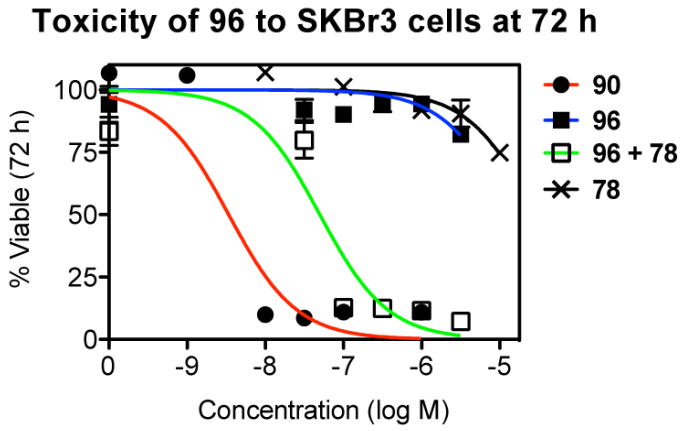

Figure 4.10. Toxicity analysis of CME-conjugated Herceptin (**96**) in the absence and presence of endosome disruptor **78**. SKBr3 cells treated for 72 h with and without **78** (1 μM). Analysis performed by flow cytometry and fit by non-linear regression to provide IC_{50} values.

Compound Added		SKBr3 cells (IC_{50}, μM)
90	(NACME)	0.005
96	(*Herceptin*-S-S-CME)	14
96 + 78	(*Herceptin*-S-S-CME + ED)	0.05
78	(ED alone)	29

Table 4.4. IC_{50} values of compound **96** in the absence and presence of endosome disruptor **78** in SKBr3 cells. Endosome disruptor **78** was used to induce release of the cytotoxic CME warhead. ED = Endosome Disruptor.

4.5 Future Directions: Specific Delivery of Small Molecule Cargo using Endosome Disruptor-Antibody Conjugates

Disruption of endosomes produces a significant increase in the potency of a disulfide-linked antibody-drug conjugate. This induction requires the use of membrane-anchored endosome disruptive peptides in adherent cell lines. The cholesterol moiety dramatically increases endosomal accumulation and consequently increases the potency of the conjugated peptide. However, it also significantly limits potential *in vivo* applications of endosome disruption due to poor pharmacokinetics and a lack of selectivity.

To address both of these limitations, we are currently focused on the development of peptides that can be conjugated to an antibody and produce endosome disruption in cells that overexpress a cell surface receptor (Figure 4.11). Similar to cholesterol conjugation or ADCs, the antibody would provide significant accumulation of a linked peptide in endosomes and increase

endosome disruptive activity compared to the peptide alone. The design of the linker between the antibody and the peptide is perhaps the most critical aspect of this approach. The linker needs to be sufficiently stable to remain intact while in systemic circulation, but allow cleavage once a significant amount has accumulated in the target cells. Using fluorescence-based screening assays, we are currently focused on evaluating several linkers between Erbitux[15, 32, 33], an FDA-approved antibody targeting the epidermal growth factor receptor (EGFR), and the peptide sequence of endosome disruptor **80**.

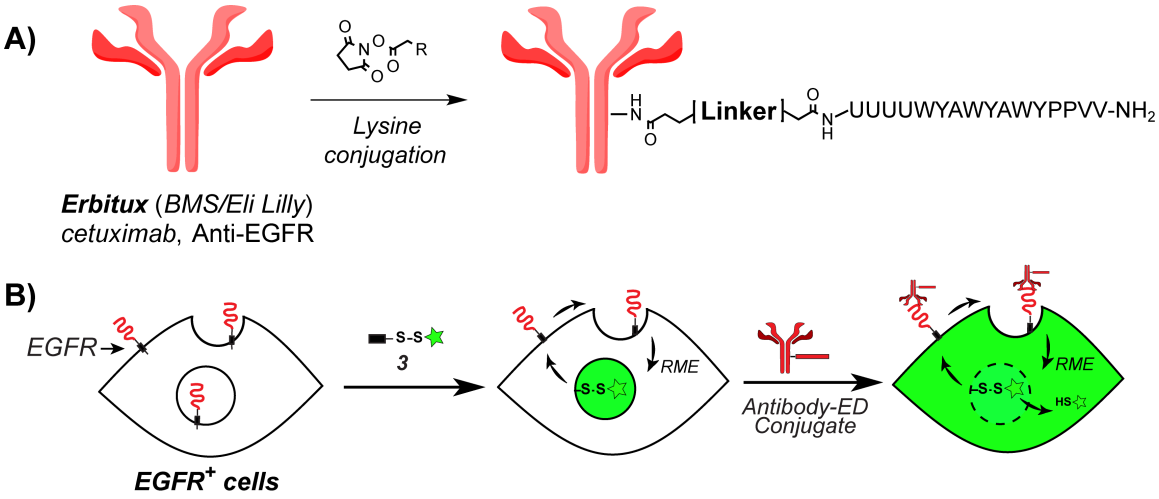

Figure 4.11. Evaluation of endosome disruptors conjugated to an antibody targeted to the epidermal growth factor receptor (EGFR). A) Erbitux (anti-EGFR) is conjugated through lysine residues to the peptide sequence of **80** to screen various linkers. B) Schematic representation of the fluorescence-based screen using **3** to identify linkers that produce robust endosome disruption.

Given that several cancer types overexpress multiple cell surface receptors[14, 34, 35], it would be possible to use two different antibodies as part of the same therapy. An endosome disruptive antibody targeting a cell surface receptor coupled with a disulfide-linked antibody-drug conjugate targeting a second cell surface receptor could provide a chemotherapeutic system

potentially with excellent selectivity and minimal side effects (Figure 4.12). Since the toxicity of the ADC would be induced by endosome disruption, this dual-antibody system may require lower doses than current ADCs for inhibition of tumor growth.

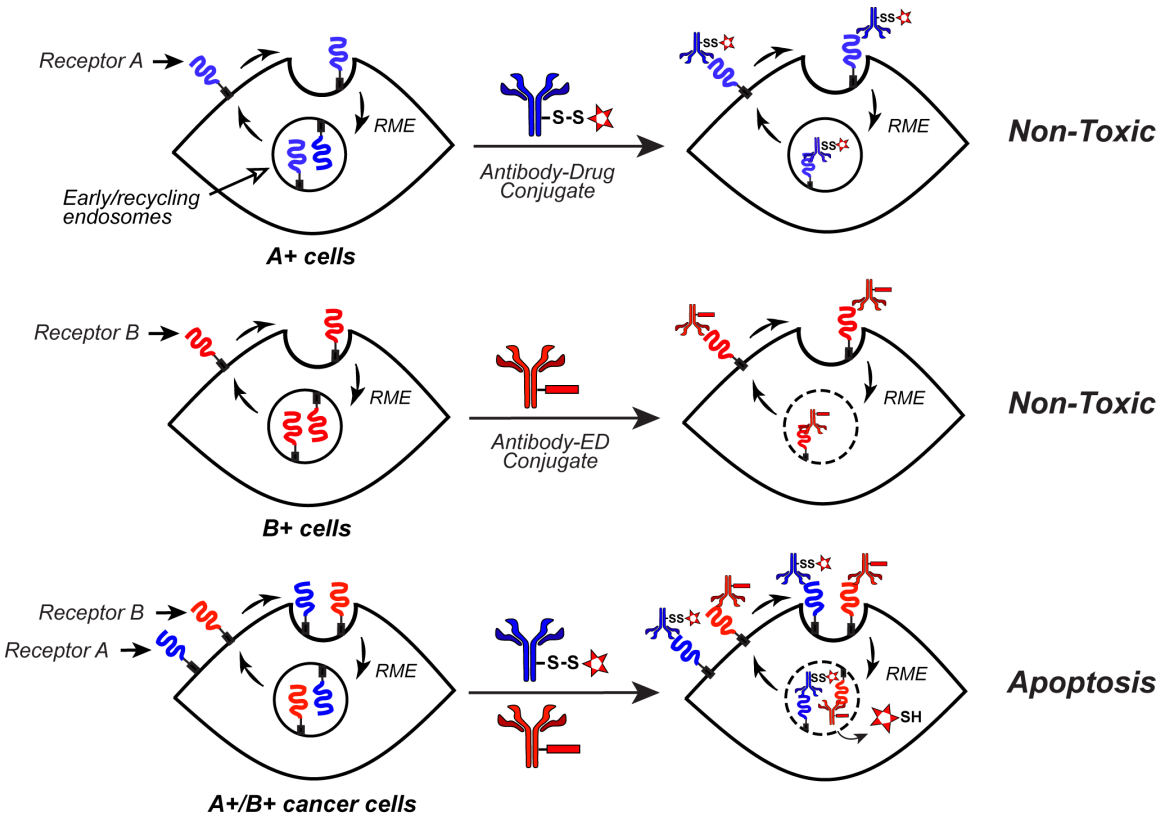

Figure 4.12. A novel strategy to produce tumor-specific toxicity based on co-treatment with two antibodies targeted to cell surface recpetors. Either an antibody-drug conjugate or an antibody-endosome disruptor conjugate alone would produce no toxicity. The combination in endosomes would induce release of the disulfide-linked warhead and result in apoptosis.

4.6 Conclusions

We evaluated a disulfide-linked cytotoxin in two different cell lines using optimized endosome disruptors to induce its release and produce cellular toxicity. It was found that endosome disruptors that do not contain the cholesterol-based membrane anchor were less effective at inducing toxicity in adherent cell lines.

The cholesterol-conjugated derivatives, however, were effective at inducing toxicity, producing approximately a 100- to 200-fold increase in potency when co-treated with the disulfide-linked cytotoxin **91**. We then evaluated the release of small molecule cargo from an antibody targeted to a cell surface receptor. Using confocal microscopy, we observed robust release of fluorescent cargo conjugated to the anti-HER2 antibody Herceptin. The optimized colchinol cytoxin was then conjugated to Herceptin and evaluated for toxicity in HER2-positive SKBr3 cells. Similar to the cholesterol-linked system, the CME-Herceptin ADC produced a >200-fold increase in toxicity when co-treated with an endosome disruptor. This result indicates that the efficacy of an ADC can be enhanced by using endosome disruption to induce the release of a cytotoxin, while still maintaining selectivity provided by the antibody-receptor interaction. Current studies are focused on improving the activity of endosome disruptive peptides conjugated to an antibody by investigating the SAR in the linker. We envision utilizing this type of antibody conjugate to induce the toxicity of a second ADC to produce tumor-specific toxicity. This dual-antibody approach could lead to a chemotherapy system with a greatly improved therapeutic index compared to current ADC therapies.

4.7 Experimental Section

4.7.1 General

Reagents were purchased from Sigma-Aldrich, Fisher Scientific, Acros, Aapptec, or EMD Biosciences. Colchicine (**97**) was purchased from Sigma-

Aldrich. N-acetyl colchinol methyl ether (**90**)[36, 37], de-acetyl colchinol methyl ether (**98**)[36, 37], and Fmoc-protected 3-((2-aminoethyl)disulfanyl)propanoic acid[3] were prepared according to previously published methods. All endosome disruptor compounds were synthesized by Dr. Chamani Perera and characterization is provided in Chapter 3 of this dissertation. The colchinol methyl ether compounds **91** and **92** were provided by Ning Yang in >95% purity and their corresponding syntheses and characterization are described in his Master's thesis. ^{1}H (400 MHz) and ^{13}C (101 MHz) NMR spectra were acquired a Bruker Avance 400 instrument. Chemical shifts are reported in ppm and are referenced to $CDCl_3$ (^{1}H 7.26 ppm; ^{13}C 77.2 ppm). Coupling constants J_{HH} are in hertz and are reported as follows: chemical shift, multiplicity (app = apparent, s = singlet, d = doublet, t = triplet, q = quartet, dd = doublet of doublets), coupling constant, and integration. Melting points were acquired using a Thomas Hoover Capillary Melting Point Apparatus and are uncorrected. Infrared spectra (IR) were recorded with a Perkin-Elmer Spectrum 100 FT-IR spectrophotometer. UV/Vis measurements employed an Aligent 8452A diode array spectrophotometer. High-resolution mass spectra were obtained at the Mass Spectrometry Laboratory at the University of Kansas. Low-resolution mass spectra were acquired on a Waters Micromass ZQ instrument with electrospray ionization (ESI+). Thin layer chromatography (TLC) used EMD aluminum-backed silica plates (0.20 mm, 60 F-254), and flash chromatography used ICN silica gel (200-400 mesh). Plates were visualized by UV or staining with phosphomolybdic acid. Preparative HPLC was performed with an Agilent 1200 instrument equipped with a Hamilton PRP-1

reverse phase column (250 mm length, 21 mm ID, 12-20 μm particle size) with detection by absorbance at 215, 254, and 350 nm. All non-aqueous reactions were carried out using flame- or oven-dried glassware under an atmosphere of dry argon or nitrogen. Reaction solvents were purified via filtration through two columns of activated basic alumina under an atmosphere of Ar using a solvent purification system from Glass Contour. Other commercial reagents were used as received unless otherwise noted. Yields are reported based on isolated material.

4.7.2 Synthetic Procedures and Characterization Data

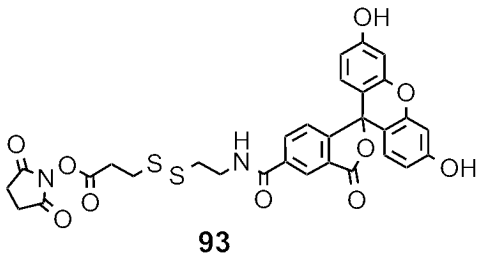

93

5-((2-((3-((2,5-dioxopyrrolidin-1-yl)oxy)-3-oxopropyl)disulfanyl)ethyl) carbamoyl)-2-(6-hydroxy-3-oxo-3*H*-xanthen-9-yl)benzoic acid (93). Fmoc-3-((2-aminoethyl)disulfanyl)propanoic acid[3] (28 mg, 0.070 mmol) was dissolved in DMF (1 mL) containing 20% piperidine and stirred at 22 °C for 30 min. The solvent was removed under vacuum to provide the primary amine. 5-Carboxy fluorescein NHS ester (17 mg, 0.035 mmol) was dissolved in dry DMF (2 mL) and added to the primary amine along with DIEA (0.2 mL). The reaction was stirred at 22 °C for 16 h. Following completion, the solvent was removed under vacuum, the residue was re-dissolved in DCM containing 5% methanol, applied

to a short silica plug, and eluted with 90/10 DCM/MeOH. The solvent was removed to give the crude carboxylic acid product. This product (~15 mg) was dissolved in DMF (2 mL) and EDC (11 mg, 0.06 mmol) and N-hydroxysuccinimide (NHS, 7 mg, 0.06 mmol) were added. The reaction was allowed to stir at 22 °C for 16 h. The solvent was removed under vacuum, and the residue was dissolved in DMSO (2 mL) and purified by preperative RP-HPLC (Gradient: H_2O:CH_3CN (9:1) to (0:100) with added TFA (0.1%) over 20 min; elution time = 12 min). Pure fractions were collected, combined, and dried under vacuum to give **93** (9 mg, 0.014 mmol, 39% overall yield) as a yellow solid. ^{1}H NMR (400 MHz, CD_3OD) δ 8.44 (s, 1H), 8.21 (d, *J* = 9.6 Hz, 1H), 7.31 (d, *J* = 8.0 Hz, 1H), 6.71 (d, *J* = 2.4 Hz, 2H), 6.67 – 6.51 (m, 5H), 3.76 (t, *J* = 6.6 Hz, 2H), 3.17 – 2.99 (m, 5H), 2.83 (s, 4H); ^{13}C NMR (101 MHz, CD_3OD) δ 174.9, 172.5, 171.8, 171.6, 168.8, 168.5, 162.3, 154.2, 154.1, 130.4, 130.3, 129.9, 129.2, 126.3, 125.8, 124.9, 103.6, 40.4, 38.5, 33.4, 31.8, 26.3; IR (film) ν_{max} 3340, 2926, 2853, 1735, 1618, 1454, 1203, 1115, 1070, 994, 851, 761 cm^{-1}; HRMS (ESI+) m/z 659.0740 ($M+Na^+$, $C_{30}H_{24}N_2O_{10}S_2Na$ requires 659.0765).

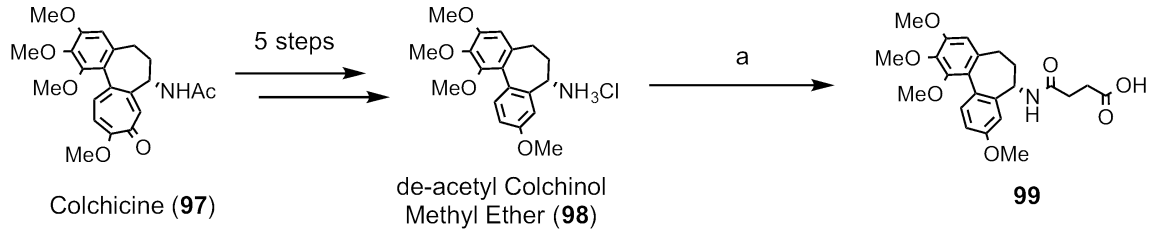

Figure 4.13. Synthesis of compound **99**. Reagents and Conditions: a) succinic anhydride, DCM, DIEA, 16 h, 22 °C.

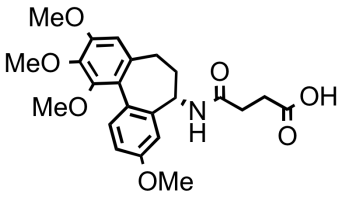

99

4-oxo-4-(((5*S*)-3,9,10,11-tetramethoxy-6,7-dihydro-5*H*-dibenzo[*a*,*c*][7] annulen-5-yl)amino)butanoic acid (99). Detailed synthetic procedures and characterization data of de-acetyl colchinol methyl ether hydrochloride (**98**) have been previously described.[36, 37] De-acetyl colchinol methyl ether hydrochloride (**98**, 97 mg, 0.264 mmol) was dissolved in dichloromethane (10 mL) and washed with 1 M aq. NaOH (5 mL) to provide the free primary amine. The organic phase was collected, dried over Na_2SO_4, and concentrated under vacuum. The primary amine was re-dissolved in dry DCM (2 mL) containing diisopropylethylamine (DIEA, 0.2 mL). Succinic anhydride (53 mg, 0.526 mmol, 2 equiv.) was added and the reaction was allowed to stir overnight at room temperature. Upon completion, the reaction mixture was loaded directly onto silica and subjected to flash chromatography (gradient elution of 99/1 to 9/1 DCM/MeOH) to yield **99** (92 mg, 0.214 mmol, 81% yield) as an off-white solid. ^{1}H NMR (400 MHz, $CDCl_3$) δ 7.39 (d, *J* = 8.4 Hz, 1H), 6.84 (s, 1H), 6.74 (d, *J* = 7.9 Hz, 1H), 6.56 (s, 1H), 4.72 (m, 1H), 3.90 (s, 3H), 3.88 (s, 3H), 3.79 (s, 3H), 3.52 (s, 3H), 2.62 – 2.22 (m, 7H), 1.80 (m, 1H); ^{13}C NMR (101 MHz, $CDCl_3$) δ 176.3, 171.9, 159.0, 152.6, 151.3, 141.4, 140.6, 134.9, 131.4, 126.8, 125.0, 111.2, 109.2, 107.9, 77.5, 77.2, 76.9, 61.4, 61.1, 56.3, 55.4, 49.8, 39.4, 30.9, 30.7, 29.7; IR (film) ν_{max} 2934, 1717, 1651, 1607, 1544, 1484, 1456, 1402, 1292, 1267, 1237, 1194, 1144, 1100, 1003,

914, 827, 732, 701 cm^{-1}; HRMS (ESI+) m/z 452.1659 ($M+Na^+$, $C_{23}H_{27}NO_7Na$ requires 452.1685).

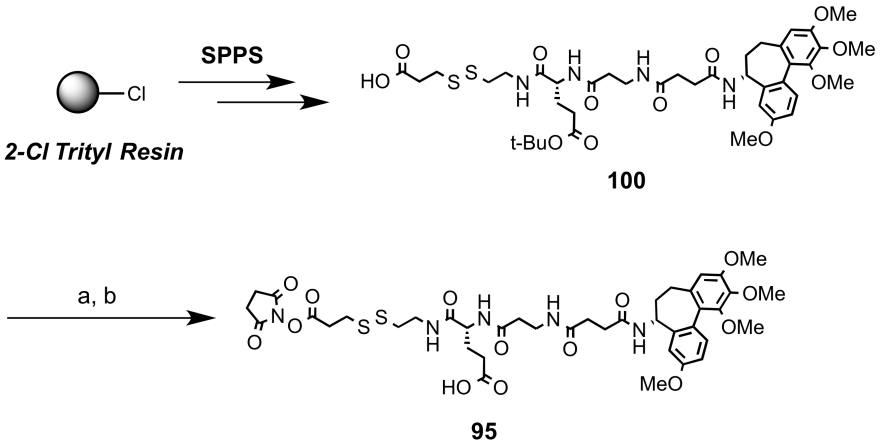

Figure 4.14. Synthesis of compound **95**. Reagents and Conditions: a) EDC, NHS, DIEA, DMF, 16 h, 22 °C; b) 30% TFA in DCM, 1 h, 22 °C.

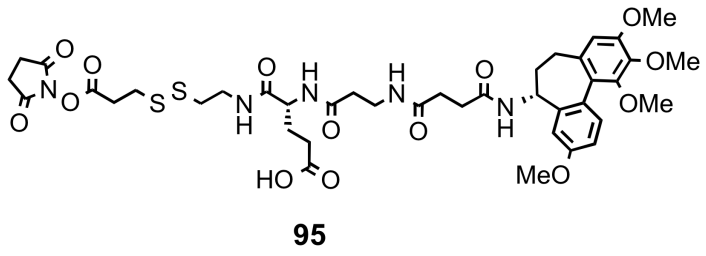

95

(4*R*)-5-((2-((3-((2,5-dioxopyrrolidin-1-yl)oxy)-3-oxopropyl)disulfanyl)ethyl) amino)-5-oxo-4-(3-(4-oxo-4-(((5*R*)-3,9,10,11-tetramethoxy-6,7-dihydro-5*H*-dibenzo[*a*,*c*][7]annulen-5-yl)amino)butanamido)propanamido)pentanoate N-hydroxysuccinimidyl ester (95). Solid phase peptide synthesis (SPPS) employed a 50 mL peptide synthesis vessel (Quark Glassware) with a wrist action shaker and standard Fmoc amino acid methodology. The peptide was constructed with 2-chlorotrityl resin (0.89 mmol/g, 112 mg, 0.1 mmol) using Fmoc-protected 3-((2-aminoethyl)disulfanyl)propanoic acid[3], compound **99**, and the following Fmoc-protected amino acids: Fmoc-β-Ala-OH, Fmoc-Glu(O*t*-Bu)-

OH. Amino acids were consecutively coupled to the resin by addition of DMF solution (2 mL) of amino acid (4.0 eq.), HATU (3.8 eq.) and DIEA (8.0 eq.) with shaking at 22 ^{o}C for 3 h. Deprotection of Fmoc carbamates on the resin was carried out by addition of piperidine (20%) in DMF (1.5 mL for 1 min (4x) with bubbling nitrogen for agitation). After completing all the steps of coupling reactions, the peptide was cleaved from the resin by treatment with a mixture of DCM/TFE/acetic acid (7:2:1) with shaking for 2 h. The resin was removed by filtration and washed with DCM (2 mL, 3x). The filtrates were combined and concentrated under vacuum. To ensure complete removal of acetic acid, the crude product (**100**) residue was azeotroped under vacuum from a mixture of methanol/toluene (1:3, 3 x 2 mL).

The crude peptide (**100**, 16 mg) containing a free C-terminal carboxylic acid was dissolved in dry DCM (2 mL). Ethyl-3-(3-dimethylaminopropyl) carbodiimide (EDC, 10 mg, 0.052 mmol) was added and allowed to stir at room temperature for 15 min. N-Hydroxysuccinimide (NHS, 7 mg, 0.060 mmol) was then added and the reaction was allowed to stir overnight. Upon completion, the reaction mixture was dried under vacuum, re-dissolved in DCM containing 30% TFA and allowed to stir for 1 h to remove the *tert*-butyl ester protecting group. The solvent was removed under vacuum, and the residue was dissolved in DMSO (1.5 mL) and purified by preparative RP-HPLC (Gradient: H_2O:CH_3CN (9:1) to (0:100) with added TFA (0.1%) over 20 min; elution time = 12 min). Pure fractions were collected, combined, and dried under vacuum to give **95** (5 mg,

0.006 mmol, 6% overall yield) as a white solid. HRMS (ESI+) m/z 912.2705 ($M+Na^+$, $C_{40}H_{51}N_5O_{14}S_2Na$ requires 912.2772).

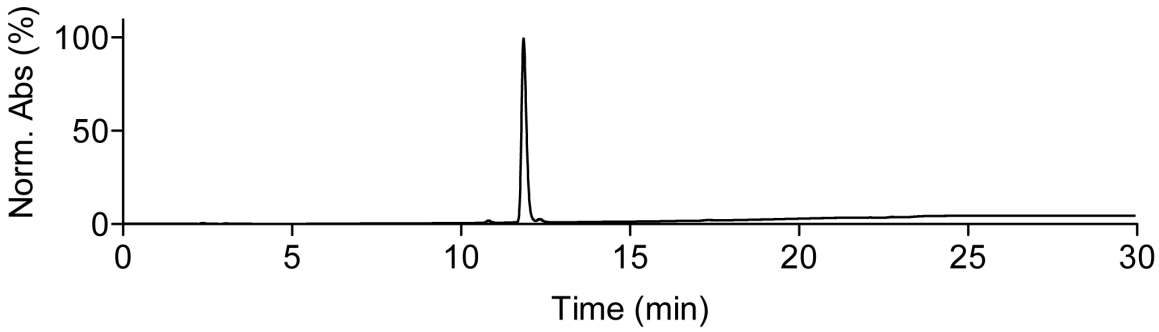

Figure 4.15. Analytical HPLC trace of **95** following purification by preparative HPLC. Purity >95% by integration of chromatogram. Monitored by UV absorbance at 254 nm.

4.7.3 Biological Assays and Protocols

General. Reagents were purchased from Sigma-Aldrich, Fisher Scientific, and Acros Organics. Cell culture reagents were from Sigma-Aldrich. Herceptin (*trastuzumab*) was kindly provided by Prof. Liang Xu (KU Molecular Biosciences). UV/Vis absorbance measurements to determine antibody concentration and degree of labeling employed a NanoDrop 6000 spectrophotometer. The HER2-CFP expression plasmid was purchased from AddGene (Plasmid #40268). Transfection of plasmids employed the XTremeGene HP reagent (Roche) according to the commercial protocol.

Cell culture. Jurkat lymphocytes (human acute leukemia, ATCC #TIB-152) were cultivated in Roswell Park Memorial Institute (RPMI) 1640 media. SKBr3 cells

(ATCC #HTB-30) were cultivated in DMEM/F12K media. HEK-293T cells were cultivated in DMEM media. All media were supplemented with Fetal Bovine Serum (FBS, 10%), penicillin (100 units/mL), and streptomycin (100 µg/mL) and cell lines were incubated in a humidified 5% CO_2 incubator at 37 °C. Media used for cell culture and all wash steps contained antibiotics and 10% FBS unless otherwise noted.

Microscopy. An inverted Leica TCS SPE confocal laser-scanning microscope fitted with a Leica 63X oil-immersion objective was employed for imaging. Fluorescent probes were excited with either a 405 nm (CFP) or 488 nm (fluorescein) solid-state laser and emitted photons were collected from 410-470 nm or 495-600 nm, respectively. HEK-293T or SKBr3 cells were imaged using 8-well cover glass plates (Ibidi). To allow accurate comparisons of differences in cellular fluorescence, laser power and PMT gain settings were identical for all samples shown in a given figure.

Analysis by Flow Cytometry of Cytotoxicity from Release of Disulfide-Linked Colchinol. Jurkat lymphocytes were suspended at 350,000 cells per mL in media and aliquoted into a 48-well plate at 500 µL per well. SKBr3 cells were plated at 50,000 cells per well in 500 µL into 48-well plates. For wells treated with endosome disruptor, either **80** or **84** were added at 1 µM (diluted from a 10 mM DMSO stock) prior to aliquoting. N-Acetyl Colchinol methyl ether (NACME, **90**), the disulfide-linked colchinol probe **91**, the amide control **92**, or the CME-

Herceptin conjugate **96** were added at various concentrations from 1 nM to 10 μM (diluted from a 500x DMSO stock) in duplicate. The samples were incubated at 37 °C for 48 or 72 h as indicated for each graph. For SKBr3 cells, each well was treated with 75 μL of 0.05% trypsin and incubated for 8 minutes at 37 °C. The trypsin was then neutralized with 150 μL of complete DMEM/F12K media. Cells were then analyzed by flow cytometry using an Accuri C6 flow cytometer. Forward scatter (FSC) and side scatter (SSC) were used to gate live cells and each well was sampled for exactly 10 seconds. Cell viability was determined based on the total live cell count normalized to vehicle controls (as 100%). The normalized percent viability was plotted versus concentration and analyzed by non-linear regression in GraphPad Prism 5 to provide an IC_{50} value.

Procedure for Labeling Herceptin with compounds 94 or 96. Lyophilized Herceptin was reconstituted in sterile water and the protein concentration was determined by absorbance at 280 nm (ε E1% = 13.7 L g^{-1} cm^{-1}). To remove stabilizing agents and salts, Sephadex G-25 resin (Superfine, Sigma) was suspended in PBS (pH 7.0). The resulting slurry (900 μL) was added to a mini-spin column (USA Scientific) and centrifuged at 16,000 x G to remove the buffer and pack the resin. The solution containing Herceptin was loaded onto the packed resin of the spin column (50-70 μL per column) and centrifuged at 16,000 x G for 1 min to separate the protein from the small molecules retained by the resin. The absorbance at 280 nm was used to determine the resulting concentration.

Either the fluorescent disulfide **93** or the CME disulfide **95** were dissolved in DMSO to give 10 mM stocks. Aqueous sodium bicarbonate (final concentration = 50 mM, pH 8) was added to the Herceptin solution, followed by either **93** or **95** (10 eq. from DMSO stock). Reaction of the NHS ester was allowed to proceed at 37 °C for 20 min. To purify the conjugate, a Sephadex G-25 resin mini-column was used as described above (50 – 70 µL per column). The absorbance at 280 nm and 495 nm (5-carboxyfluorescein, ε = 70,000 M^{-1} cm^{-1})[38] of the eluent was used to determine the concentration and degree of protein labeling of **94**. This protocol typically afforded 3-4 molecules of **93** per IgG molecule. It was assumed that this procedure also produced 3-4 molecules of **95** per IgG molecule since the ADC **96** contains no other distinguishable chromophore.

Analysis by Confocal Microscopy of Release of Fluorophore from 94 by Endosome Disruption. HEK-293T or SKBr3 cells were plated at 25,000 cells per well in 300 µL into an 8-well cover glass. Cells were allowed to adhere for 24 h at 37 °C.

For transfection of HEK-293T cells. The HER2-CFP plasmid was co-treated with the XTremeGene HP reagent according to the manufacturers protocol at a ratio of 2 µL reagent per 1 µg of plasmid DNA. The transfection was allowed to proceed for 48 h at 37 °C.

Cells were treated with the fluorescent Herceptin conjugate **94** (1 µM) in the absence and presence endsome disruptors **61** (1 µM, in HEK cells) or **78** (1 µM, in SKBr3 cells). Treatments were allowed to incubate at 37 °C for 24 h. Following

treatment, the wells were washed 3x with complete media and analyzed for fluorescence localization by confocal microscopy.

4.8 References

1. Bhattacharyya, B.; Panda, D.; Gupta, S.; Banerjee, M., Anti-mitotic activity of colchicine and the structural basis for its interaction with tubulin. *Med. Res. Rev.* **2008,** *28*, 155-183.

2. Cook, J. W.; Loudon, J. D., Colchicine. *Alkaloids* **1952,** *2*, 261-329.

3. Sun, Q.; Cai, S.; Peterson, B. R., Selective disruption of early/recycling endosomes: Release of disulfide-linked cargo mediated by a *N*-alkyl-3β-cholesterylamine-capped peptide. *J. Am. Chem. Soc.* **2008,** *130*, 10064-10065.

4. Brossi, A.; Yeh, H. J. C.; Chrzanowska, M.; Wolff, J.; Hamel, E.; Lin, C. M.; Quin, F.; Suffness, M.; Silverton, J., Colchicine and its analogs - recent findings. *Med. Res. Rev.* **1988,** *8*, 77-94.

5. Kang, G. J.; Getahun, Z.; Muzaffar, A.; Brossi, A.; Hamel, E., N-Acetylcolchinol O-methyl ether and thiocolchicine, potent analogs of colchicine modified in the C-ring - evaluation of the mechanistic basis of their enhanced biological properties. *J. Biol. Chem.* **1990,** *265*, 10255-10259.

6. Ritchie, M.; Tchistiakova, L.; Scott, N., Implications of receptor-mediated endocytosis and intracellular trafficking dynamics in the development of antibody drug conjugates. *mAbs* **2013,** *5*, 13-21.

7. Lambert, J. M., Drug-conjugated antibodies for the treatment of cancer. *Br. J. Clin. Pharmacol.* **2013,** *76*, 248-262.

8. Scott, A. M.; Wolchok, J. D.; Old, L. J., Antibody therapy of cancer. *Nat. Rev. Cancer* **2012,** *12*, 278-287.

9. Alley, S. C.; Okeley, N. M.; Senter, P. D., Antibody-drug conjugates: targeted drug delivery for cancer. *Curr. Opin. Chem. Biol.* **2010,** *14*, 529-537.

10. Roopenian, D. C.; Akilesh, S., FcRn: the neonatal Fc receptor comes of age. *Nat. Rev. Immunol.* **2007,** *7*, 715-725.

11. Ober, R. J.; Martinez, C.; Lai, X. M.; Zhou, A. C.; Ward, E. S., Exocytosis of IgG as mediated by the receptor, FcRn: An analysis at the single-molecule level. *Proc. Natl. Acad. Sci. U. S. A.* **2004,** *101*, 11076-11081.

12. Vincent, K. J.; Zurini, M., Current strategies in antibody engineering: Fc engineering and pH-dependent antigen binding, bispecific antibodies and antibody drug conjugates. *Biotechnol. J.* **2012,** *7*, 1444-1450.

13. Ducry, L.; Stump, B., Antibody-Drug Conjugates: Linking Cytotoxic Payloads to Monoclonal Antibodies. *Bioconjugate Chem.* **2010,** *21*, 5-13.

14. Johnston, J. B.; Navaratnam, S.; Pitz, M. W.; Maniate, J. M.; Wiechec, E.; Baust, H.; Gingerich, J.; Skliris, G. P.; Murphy, L. C.; Los, M., Targeting the EGFR pathway for cancer therapy. *Curr. Med. Chem.* **2006,** *13*, 3483-3492.

15. Jonker, D. J.; O'Callaghan, C. J.; Karapetis, C. S.; Zalcberg, J. R.; Tu, D. S.; Au, H. J.; Berry, S. R.; Krahn, M.; Price, T.; Simes, R. J.; Tebbutt, N. C.; van Hazel, G.; Wierzbicki, R.; Langer, C.; Moore, M. J., Cetuximab for the treatment of colorectal cancer. *N. Engl. J. Med.* **2007,** *357*, 2040-2048.

16. Willett, C. G.; Boucher, Y.; di Tomaso, E.; Duda, D. G.; Munn, L. L.; Tong, R. T.; Chung, D. C.; Sahani, D. V.; Kalva, S. P.; Kozin, S. V.; Mino, M.; Cohen, K. S.; Scadden, D. T.; Hartford, A. C.; Fischman, A. J.; Clark, J. W.; Ryan, D. P.; Zhu, A. X.; Blaszkowsky, L. S.; Chen, H. X.; Shellito, P. C.; Lauwers, G. Y.; Jain, R. K., Direct evidence that the VEGF-specific antibody bevacizumab has antivascular effects in human rectal cancer. *Nat. Med.* **2004,** *10*, 145-147.

17. Ferrara, N.; Hillan, K. J.; Gerber, H. P.; Novotny, W., Discovery and development of bevacizumab, an anti-VEGF antibody for treating cancer. *Nat. Rev. Drug Discov.* **2004,** *3*, 391-400.

18. Burris, H. A.; Tibbitts, J.; Holden, S. N.; Sliwkowski, M. X.; Phillips, G. D. L., Trastuzumab Emtansine (T-DM1): A Novel Agent for Targeting HER2(+) Breast Cancer. *Clin. Breast Cancer* **2011,** *11*, 275-282.

19. Slamon, D. J.; Leyland-Jones, B.; Shak, S.; Fuchs, H.; Paton, V.; Bajamonde, A.; Fleming, T.; Eiermann, W.; Wolter, J.; Pegram, M.; Baselga, J.; Norton, L., Use of chemotherapy plus a monoclonal antibody against HER2 for metastatic breast cancer that overexpresses HER2. *N. Engl. J. Med.* **2001,** *344*, 783-792.

20. Jain, P.; O'Brien, S., Anti-CD20 monoclonal antibodies in chronic lymphocytic leukemia. *Expert Opin. Biol. Ther.* **2013,** *13*, 169-182.

21. Younes, A.; Bartlett, N. L.; Leonard, J. P.; Kennedy, D. A.; Lynch, C. M.; Sievers, E. L.; Forero-Torres, A., Brentuximab Vedotin (SGN-35) for Relapsed CD30-Positive Lymphomas. *N. Engl. J. Med.* **2010,** *363*, 1812-1821.

22. Hamann, P. R.; Hinman, L. M.; Hollander, I.; Beyer, C. F.; Lindh, D.; Holcomb, R.; Hallett, W.; Tsou, H. R.; Upeslacis, J.; Shochat, D.; Mountain, A.; Flowers, D. A.; Bernstein, I., Gemtuzumab ozogamicin, a potent and selective anti-CD33 antibody-calicheamicin conjugate for treatment of acute myeloid leukemia. *Bioconjugate Chem.* **2002,** *13*, 47-58.

23. Erickson, H. K.; Park, P. U.; Widdison, W. C.; Kovtun, Y. V.; Garrett, L. M.; Hoffman, K.; Lutz, R. J.; Goldmacher, V. S.; Blattler, W. A., Antibody-maytansinoid conjugates are activated in targeted cancer cells by lysosomal degradation and linker-dependent intracellular processing. *Cancer Res.* **2006,** *66*, 4426-4433.

24. Doronina, S. O.; Mendelsohn, B. A.; Bovee, T. D.; Cerveny, C. G.; Alley, S. C.; Meyer, D. L.; Oflazoglu, E.; Toki, B. E.; Sanderson, R. J.; Zabinski, R. F.; Wahl, A. F.; Senter, P. D., Enhanced activity of monomethylauristatin F through monoclonal antibody delivery: Effects of linker technology on efficacy and toxicity. *Bioconjugate Chem.* **2006,** *17*, 114-124.

25. Austin, C. D.; Wen, X. H.; Gazzard, L.; Nelson, C.; Scheller, R. H.; Scales, S. J., Oxidizing potential of endosomes and lysosomes limits intracellular cleavage of disulfide-based antibody-drug conjugates. *Proc. Natl. Acad. Sci. U. S. A.* **2005,** *102*, 17987-17992.

26. Younes, A.; Yasothan, U.; Kirkpatrick, P., Brentuximab vedotin. *Nat. Rev. Drug Discov.* **2012,** *11*, 19-20.

27. Senter, P. D.; Sievers, E. L., The discovery and development of brentuximab vedotin for use in relapsed Hodgkin lymphoma and systemic anaplastic large cell lymphoma. *Nat. Biotechnol.* **2012,** *30*, 631-637.

28. Hamblett, K. J.; Senter, P. D.; Chace, D. F.; Sun, M. M. C.; Lenox, J.; Cerveny, C. G.; Kissler, K. M.; Bernhardt, S. X.; Kopcha, A. K.; Zabinski, R. F.; Meyer, D. L.; Francisco, J. A., Effects of drug loading on the antitumor activity of a monoclonal antibody drug conjugate. *Clin. Cancer Res.* **2004,** *10*, 7063-7070.

29. Linenberger, M. L., CD33-directed therapy with gemtuzumab ozogamicin in acute myeloid leukemia: progress in understanding cytotoxicity and potential mechanisms of drug resistance. *Leukemia* **2005,** *19*, 176-182.

30. Verma, S.; Miles, D.; Gianni, L.; Krop, I. E.; Welslau, M.; Baselga, J.; Pegram, M.; Oh, D. Y.; Dieras, V.; Guardino, E.; Fang, L.; Lu, M. W.; Olsen, S.; Blackwell, K.; Grp, E. S., Trastuzumab Emtansine for HER2-Positive Advanced Breast Cancer. *N. Engl. J. Med.* **2012,** *367*, 1783-1791.

31. LoRusso, P. M.; Weiss, D.; Guardino, E.; Girish, S.; Sliwkowski, M. X., Trastuzumab Emtansine: A Unique Antibody-Drug Conjugate in Development for Human Epidermal Growth Factor Receptor 2-Positive Cancer. *Clin. Cancer Res.* **2011,** *17*, 6437-6447.

32. Waksal, H. W., Role of an anti-epidermal growth factor receptor in treating cancer. *Cancer Metastasis Rev.* **1999,** *18*, 427-436.

33. Baselga, J., The EGFR as a target for anticancer therapy - focus on cetuximab. *Eur. J. Cancer* **2001,** *37*, S16-S22.

34. Ross, J. S.; Schenkein, D. P.; Pietrusko, R.; Rolfe, M.; Linette, G. P.; Stec, J.; Stagliano, N. E.; Ginsburg, G. S.; Symmans, W. F.; Pusztai, L.; Hortobagyi, G. N., Targeted therapies for cancer 2004. *Am. J. Clin. Pathol.* **2004,** *122*, 598-609.

35. Hynes, N. E.; Lane, H. A., ERBB receptors and cancer: The complexity of targeted inhibitors. *Nat. Rev. Cancer* **2005,** *5*, 341-354.

36. Besong, G.; Billen, D.; Dager, I.; Kocienski, P.; Sliwinski, E.; Tai, L. R.; Boyle, F. T., A synthesis of (aR,7S)-(-)-N-acetylcolchinol and its conjugate with a cyclic RGD peptide. *Tetrahedron* **2008,** *64*, 4700-4710.

37. Bergemann, S.; Brecht, R.; Buttner, F.; Guenard, D.; Gust, R.; Seitz, G.; Stubbs, M. T.; Thoret, S., Novel B-ring modified allocolchicinoids of the NCME series: Design, synthesis, antimicrotubule activity and cytotoxicity. *Bioorg. Med. Chem.* **2003,** *11*, 1269-1281.

38. Ueno, Y.; Jiao, G. S.; Burgess, K., Preparation of 5-and 6-carboxyfluorescein. *Synthesis-Stuttgart* **2004**, 2591-2593.

Chapter 5

Detection of Protein-Protein Interactions by Proximity-Driven S_NAr Reactions of a Lysine-Linked Fluorophore

5.1 Introduction

Protein-protein interactions are involved in virtually every biochemical process that occurs in cell biology, from replication and growth signaling to apoptosis. Consequently, the identification and analysis of these interactions is of critical importance to a variety of scientific disciplines. Numerous methods have been developed to detect and characterize protein-protein interactions, from classical methods such as affinity blotting and immunoprecipitation to more modern techniques such as yeast two-hybrid assays, phage display, quantitative mass spectrometry, and NMR spectroscopy.[1-5] Several fluorescence-based techniques have also been developed, including fluorescence polarization and fluorescence resonance energy transfer (FRET).[6-8] These experiments typically involve a fluorescently labeled protein that undergoes a change in fluorescence intensity, wavelength, or polarization upon binding an interacting protein.

Fluorescence-based methods generally provide a simple way to measure protein-protein interactions, however they are also subject to a variety of limitations. The protein under investigation typically requires labeling with a single fluorophore at a specific residue to produce a proper signal. Extensive labeling can dramatically decrease the signal-to-noise for the spectroscopic changes

observed in a protein complex. Moreover, fluorescence methods generally require purified and/or engineered protein(s) and can seldom be utilized in complex biological systems to identify unknown protein interactions.

In this chapter, we report a new fluorescence-based method for the detection of protein-protein interactions. This method utilizes fluorinated pyronin fluorophores that readily react with lysine residues to form stable protein conjugates. However, when a labeled protein is in complex with an interacting partner, the high effective concentration of proximal lysine residues at the protein-protein interface provides a driving force for the reversible exchange of these fluorophores. The exchange of this label produces a fluorescent binding partner that can be easily detected by gel electrophoresis and/or proteomics methods (Figure 5.1).

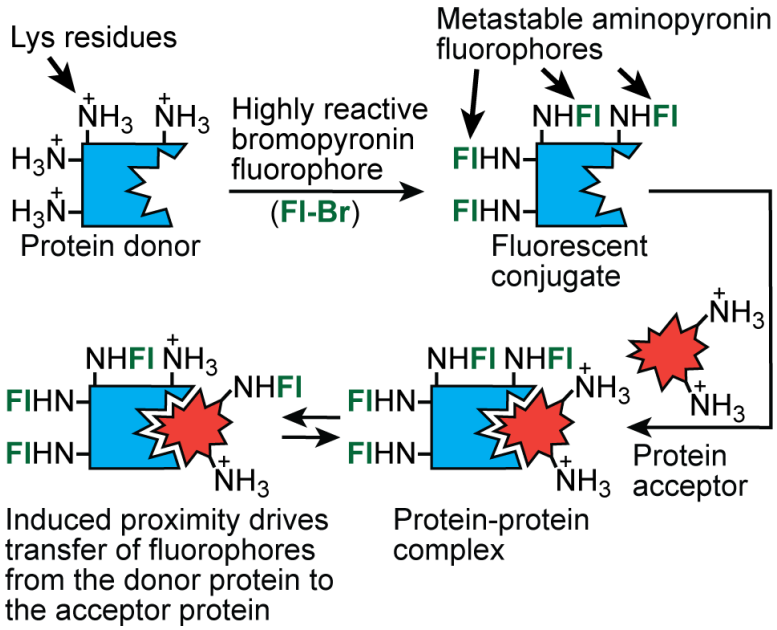

Figure 5.1. Proximity-driven transfer of fluorinated pyronin fluorophores between lysine residues for detection of protein-protein interactions.

Several analogous methods of studying ligand-protein and protein-protein interactions have been developed utilizing proximity-driven reactivity of cysteine residues,[9-11] lysine residues,[12-15] label-transfer reagents,[16-18] and other reactions.[19, 20] However, proximity-driven exchange of a fluorophore between lysine residues at protein-protein interfaces has not been previously reported.

5.2 Synthesis, Photochemical Properties, and Reactivity of Novel Fluorinated Pyronins

The Peterson lab recently published the synthesis of fluorinated xanthones such as compounds **101** – **103** (Figure 5.2).[21] Treatment of these xanthones with triflic anhydride followed by tetrabutylammonium bromide (TBABr) produces the fluorinated bromopyronins **104** – **106**. These compounds are stable solids, but react quickly with amine nucleophiles to produce aminopyronins such as the ethylamine derivatives **107** – **109**.

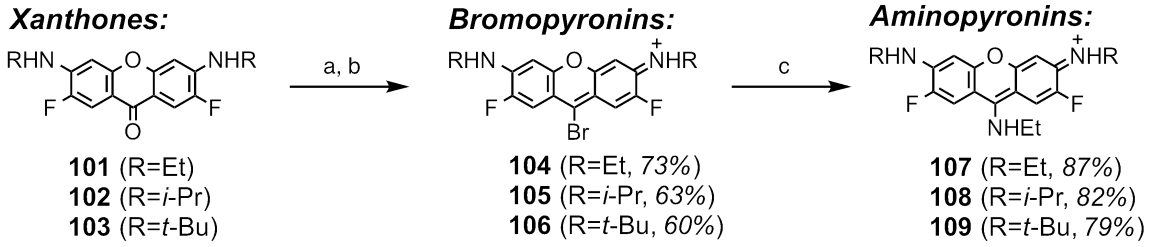

Figure 5.2. Synthesis of bromopyronins (**104** – **106**) and aminopyronins (**107** – **109**). Reagents and conditions: a) triflic anhydride, DCM, 5 min, 22 °C; b) TBABr, 30 min, 22 °C; c) bubbling ethylamine, DCM, 1 min, 22 °C.

The photophysical properties of compounds **104** – **109** are listed in Table 5.1. The aminopyronins **107** - **109** possess photophysical properties similar to other published pyronin molecules.[22, 23] The ethyl (**107**) and *iso*-propyl (**108**)

substituted molecules are excellent fluorophores (QY ~0.8) with large Stokes shifts of ~100 nm (Figure 5.3). The quantum yield of the *tert*-butyl substituted **109** is significantly decreased, likely due to steric bulk causing a decrease in conjugation of the nitrogen lone pair electrons. To ensure that the fluorescence quantum yield of the aminopyronins would not be affected near neutral pH, the pKa of compounds **107** – **109** was determined using UV/Vis spectroscopy in phosphate-buffered saline (PBS). The absorbance spectra of these compounds were unaffected in buffer ranging from pH 4 – 9, however deprotonation was observed at higher pH and provided the pKa values listed in Table 5.1.

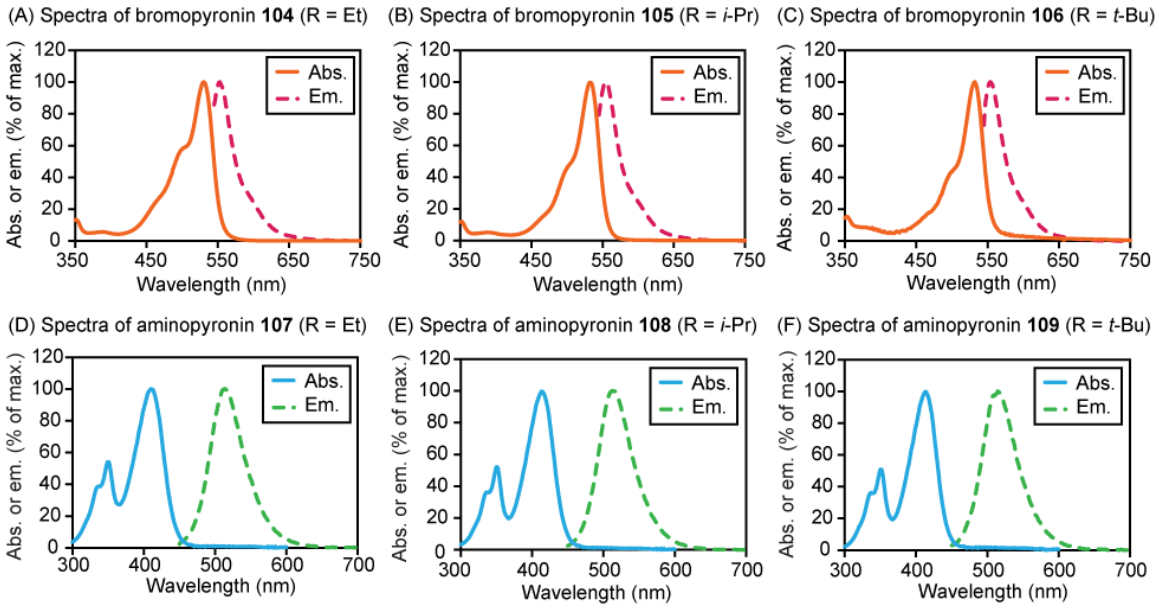

Figure 5.3. Absorbance and fluorescence emission spectra for bromo- and aminopyronins **104** – **109** in PBS (pH 7.0).

	R =	ε (λ_{max}) (M^{-1} cm^{-1})	Abs. (λ_{max}, nm)	Em. (λ_{max}, nm)	Φ	pKa
104	Et	77,300	530	552	0.72	-
105	*i*-Pr	76,000	532	554	0.74	-
106	*t*-Bu	62,100	532	554	0.50	-
107	Et	40,600	410	515	0.78	11.2
108	*i*-Pr	40,600	414	512	0.83	10.8
109	*t*-Bu	34,500	414	515	0.45	9.9

Table 5.1. Photochemical properties of bromo- and aminopyronins **104** – **109** in PBS. pKa measured by change in absorbance at λ_{max} as a function of pH and fit to a non-linear regression. Φ = Quantum Yield

To determine whether fluorinated aminopyronins could undergo nucleophilic aromatic substitution (S_NAr) with amines, we followed the reactivity of compounds **107** – **109** in the presence of excess methylamine by low-resolution mass spectrometry. As shown in Figure 5.4, aminopyronins **107** – **109** are highly stable under physiological conditions in buffered aqueous solutions. Treatment of these compounds with a large excess of methylamine (10 mM) resulted in <1% reaction after 96 h. However, under the same conditions in non-buffered methanol:water (9:1), the addition of methylamine (10 mM) resulted in the clean conversion to the substituted aminopyronins **110** – **112** in less than 24 h. The reaction profiles were fit using pseudo first order kinetics to provide half-times for the reaction of each compound. The reactivity of the tert-butyl substituted **109** was ~2-fold higher than that of **107** and **108**. This result correlated with the lower quantum yield and decreased pKa of **109** resulting from decreased conjugation of the nitrogen lone pair electrons.

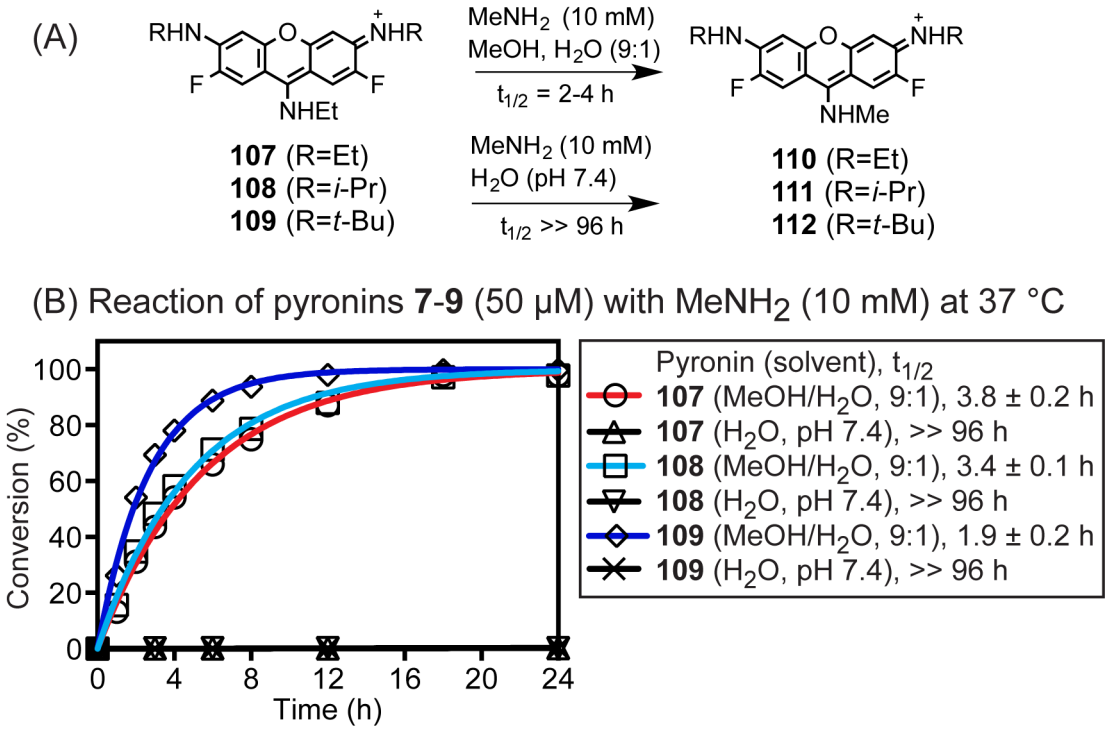

Figure 5.4. S_NAr exchange of amine substituent of aminopyronins. (A) Reaction scheme of ethylaminopyronins **107** – **109** in buffered aqueous or organic solutions. (B) Reaction kinetics of conversion of **107** – **109** (50 μM) to **110** – **112** by reaction with methylamine (10 mM) at 37 °C.

5.3 S_NAr Exchange of Aminopyronins between Lysine Residues at the Interface of a Model Protein-Protein Interaction

We hypothesized that the unique reactivity of fluorinated aminopyronins may be useful for the detection of protein-protein interactions. Using the ethylamine-substituted compounds **107** – **109** as model substrates, we found that these molecules are highly stable under physiological conditions in a buffered aqueous environment. However under more basic conditions, these molecules readily react to exchange their amine substituents through S_NAr. The high effective concentration of proximal lysine residues at the interface of a protein-protein interaction could provide a driving force for the exchange of these

fluorophores from donor to acceptor lysines. As a result, protein partners could be revealed by simple SDS-PAGE analysis with fluorescence detection.

We chose to evaluate this hypothesis by studying the well-known interaction between the constant region (Fc) of human immunoglobulin-G (IgG, 150 kDa) and Protein A from *Staphylococcus aureus* (SpA, 42 kDa).[24, 25] SpA binds the Fc region of IgG with a K_d of approximately 20 – 150 nM.[24] We used the bromopyronins **104** – **106** to label lysine residues of human IgG to produce the aminopyronin conjugates **113** – **115**. The reaction mixtures were purified by size exclusion chromatography and typically provided IgG conjugates with a fluorophore:antibody ratio of 3 – 4. Conjugates **113** – **115** were then added to aqueous buffer (pH 7.4) containing both SpA and bovine serum albumin (BSA, 66 kDa) as a non-binding control. As shown in Figure 5.5, transfer of the fluorophore was observed from IgG to SpA, but not to BSA, following analysis by SDS-PAGE with fluorescence imaging. Each of the conjugates showed a significant amount of transfer after 16 h, but conjugate **114** demonstrated the best properties upon quantification of the fluorescent SpA bands. The *iso*-propyl aminopyronin benefits from intermediate reactivity and the highest quantum yield compared to the ethyl or *tert*-butyl substituted molecules.

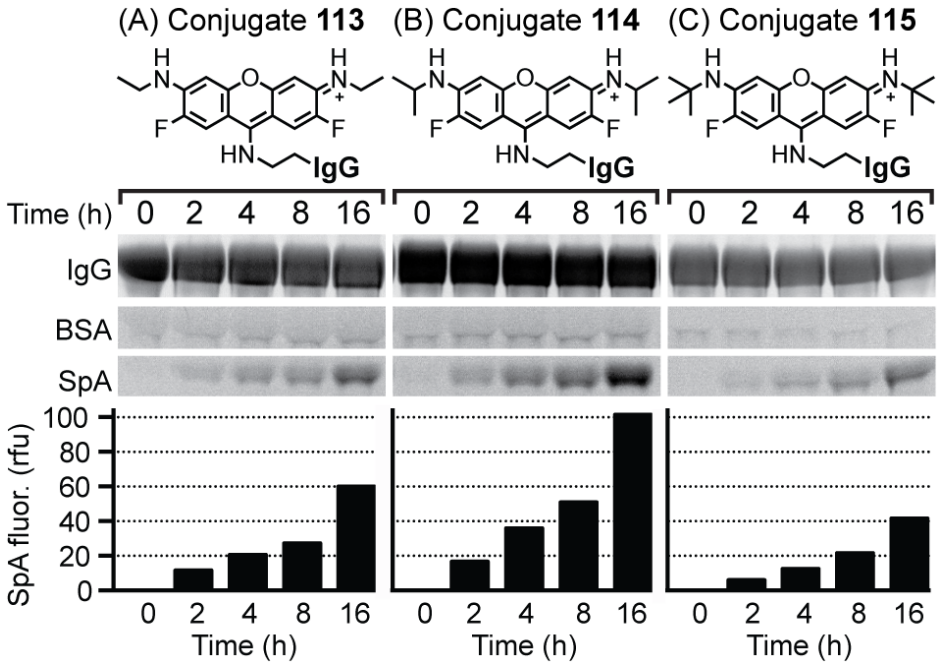

Figure 5.5. Analysis of transfer of pyronins between proteins. Human IgG was conjugated to pyronins **104** (A), **105** (B), and **106** (C), added at 5 μM to PBS (pH 7.4) containing unlabeled SpA (5 μM) or BSA (5 μM), allowed to react at 37 °C, and analyzed by SDS-PAGE with fluorescence detection. Quantification of the fluorescence of SpA bands is shown on the bottom.

SpA consists of five homologous binding domains that each have high binding affinity for the Fc region.[26] This protein has also been shown to bind the variable Fab fragments of some IgG subclasses.[27] To ensure that the Fc region of human IgG was responsible for the observed transfer, we labeled the lysine residues of purified human Fc region and Fab fragments using the *iso*-propyl bromopyronin **105** to produce conjugates **116** and **117**. These conjugates, along with the IgG conjugate **114**, were added to aqueous buffer containing SpA. The labeled Fc conjugate **116** demonstrated robust transfer of the aminopyronin to SpA, whereas the Fab conjugate **117** showed little to no transfer (Figure 5.6).

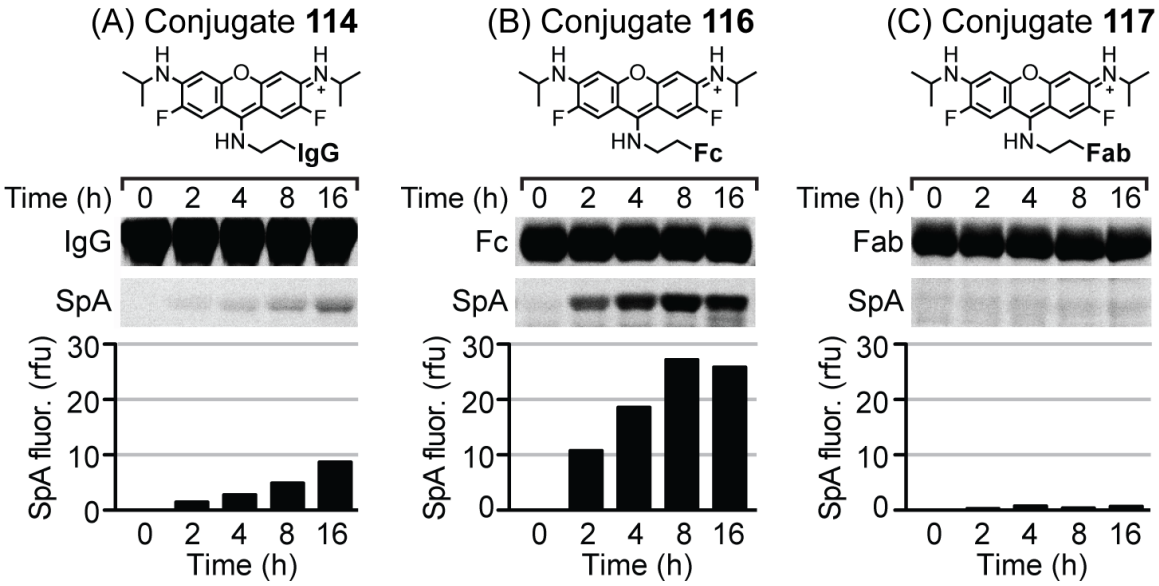

Figure 5.6. Analysis of transfer of pyronin from full-length human IgG (A), the IgG Fc region (B), and the IgG Fab fragment (C) to SpA. The IgG proteins were conjugated to pyronin **105**, added at 5 μM to PBS (pH 7.4) containing unlabeled SpA (5 μM), allowed to react at 37 °C, and analyzed by SDS-PAGE with fluorescence detection. The bands shown are from a single gel where the proteins were analyzed in parallel. Quantification of background-subtracted total fluorescence of each SpA band is shown on the bottom.

A second control experiment was done using human IgG conjugated to 5-carboxyfluorescein (via an NHS ester, **118**) or fluorescein isothiocyanate (FITC, **119**) through much more stable amide or thiourea linkages. These two amine-reactive fluorophores are commercially available and commonly used to label proteins of interest. Using similar conditions, these two conjugates showed no transfer of fluorophore to SpA (Figure 5.7), confirming that the unique reactivity of fluorinated aminopyronins is critical for the detection of protein-protein interactions.

(A) Pyronin conjugate **114** (B) 5-Carboxyfluorescein conjugate **118** (C) FITC conjugate **119**

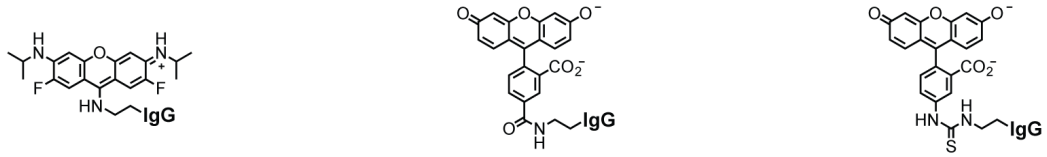

(D) Transfer of fluorophores from IgG conjugates to SpA after 16 h

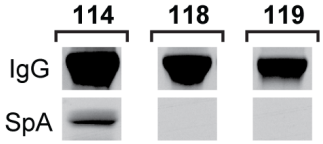

Figure 5.7. Examination of the extent of transfer of other fluorophores from IgG to SpA. Panels A-C: Comparison of the structures of the fluorophores of IgG conjugates. Panel D: Transfer of fluorophores from full-length human IgG to SpA as analyzed by SDS-PAGE with fluorescence detection. Human IgG was conjugated to pyronin **105**, 5-carboxyfluorescein, or FITC. These conjugates were purified, added to PBS at 5 μM (pH 7.4) containing unlabeled SpA (5 μM), and allowed to react at 37 °C for 16 h. The bands shown in Panel D are from a single gel where the proteins were analyzed in parallel. In contrast to the pyronin conjugate **114**, no transfer of fluorophore was observed with the amide-linked or thiourea-linked conjugates **118** or **119**.

We further investigated the mechanism of pyronin transfer using proteomics methods to identify which lysine residues of SpA were labeled following transfer from IgG. Conjugate **114** was incubated with SpA for 18 h at 37 °C to allow for pyronin transfer. Following incubation, **114** was removed from the protein mixture using a large excess of resin-bound SpA and the supernatant containing label-transferred SpA was analyzed by trypsin digestion and peptide sequencing by mass spectrometry. Remarkably, among the 118 total lysine residues of mature SpA, only four homologous residues, Lys-69, Lys-130, Lys-188, and Lys-246, were found to exchange with the pyronins of IgG (Figure 5.8).

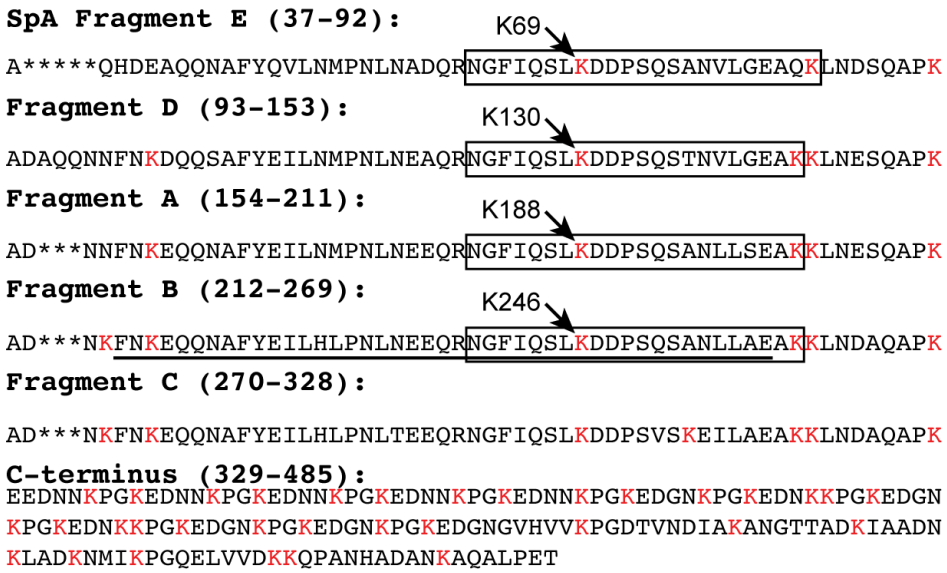

Figure 5.8. Analysis of fluorophore transfer from IgG conjugate **114** to SpA by trypsin digestion and MS/MS seqeuencing. The amino acid sequence of mature SpA (UniProt ID P02976) is shown with Fragments A – E aligned by homology. Lysine residues are colored red. Four dominant pyronin-modified tryptic peptides, identified with >99% probability, are shown boxed, with arrows illustrating sites of lysine modification. The underlined residues in Fragment B represent the residues visible in the X-ray crystal structure of IgG Fc-SpA (Figure 5.9).

To investigate the molecular basis for this specific reactivity, we examined the X-ray crystal structure of the Fc region of human IgG bound to Fragment B of SpA (Figure 5.9).[28] This structure illustrates that the ε-amino groups of Lys-246 of SpA and Lys-288 of IgG reside within 5 – 9 Å of each other and represent the most proximal lysine residues in the protein complex. The proximity of these residues explains the highly selective reactivity of Lys-246 in Fragment B and the homologous residues Lys-69, Lys-130, and Lys-188 in Fragments E, D, and A, respectively.

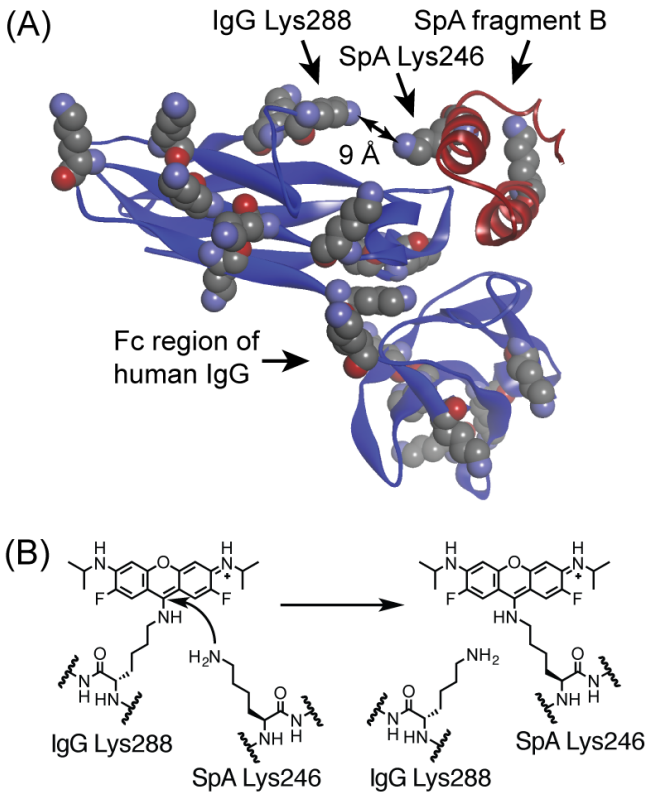

Figure 5.9. Panel A: X-ray structure of the Fc region of human IgG (blue) bound to Fragment B of SpA (red, PDB ID 1FC2). Carbohydrates of the IgG were omitted for clarity. Lysine residues are shown as CPK models. Panel B: Mechanism of molecular transfer of pyronin between lysine residues of SpA and IgG.

5.4 Detection of a Protein-Protein Interaction in a Complex Biological System

Based on the ability to detect a model protein-protein interaction, we hypothesized that this approach could be used to detect protein-protein interactions in complex biological systems, such a cell extract. To evaluate this, we examined another well-known protein-protein interaction between ribonuclease A (Rnase A, 14 kDa) and ribonuclease inhibitor (50 kDa).[29, 30] Rnase inhibitor is a constitutively expressed cytosolic protein comprising

approximately 0.1% of total cellular protein. Its abundance provides an excellent starting point for validation of this method in a complex biological matrix.[31] Moreover, a crystal structure of the interaction between bovine Rnase A and porcine Rnase inhibitor illustrates several lysine residues in close proximity that may undergo fluorophore transfer (Figure 5.10, Panel A).[30, 32]

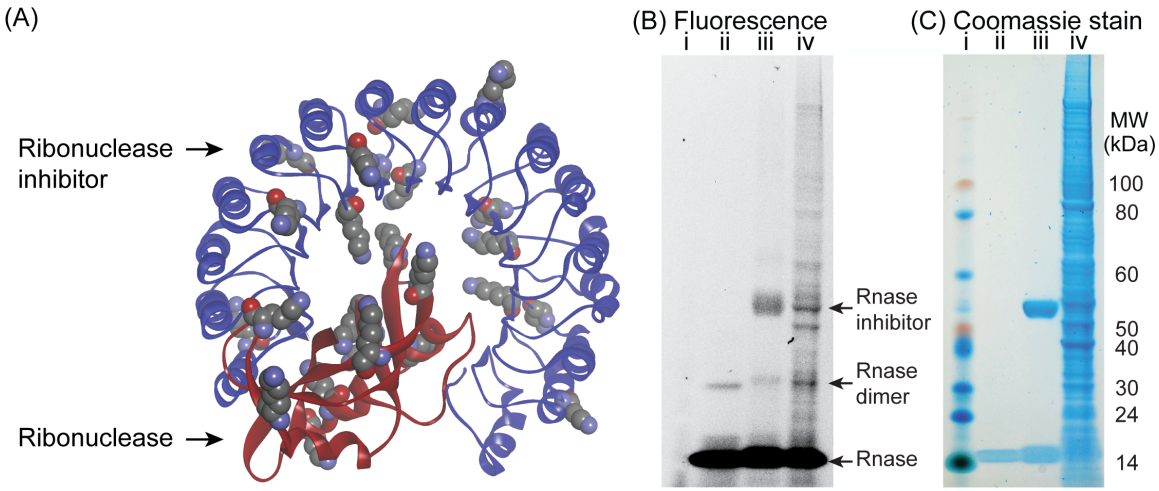

Figure 5.10. Panel A: X-ray structure of bovine Rnase A (red) bound to porcine Rnase inhibitor (blue, PDB ID 1DFJ) illustrating the proximity of lysine residues (CPK models) in the complex. Panels B – C: SDS-PAGE gel imaged by fluorescence (B) followed by staining of the same gel with coomassie (C). Lane i: protein MW marker; ii: Pyronin-conjugated Rnase A alone; iii: Reaction of pyronin-conjugated bovine Rnase A (20 μM) with recombinant human Rnase inhibitor (20 μM) for 18 h at 37 °C; iv: Reaction of pyronin-conjugated bovine Rnase A (20 μM) with a crude HeLa cell extract for 18 h at 37 °C. The arrows show specific proteins identified by comparison with authentic standards.

We conjugated bovine Rnase A to bromopyronin **105** using a procedure similar to the conjugation of human IgG. The solubility of pyronin-labeled bovine Rnase A was significantly reduced, allowing for only 0.3 – 0.6 fluorophores per protein molecule. Nevertheless, this conjugate was added to both purified recombinant human Rnase inhibitor and a crude protein extract of HeLa cells. Following incubation at 37 °C, SDS-PAGE analysis revealed the transfer of

fluorophore to both recombinant Rnase inhibitor and endogenous Rnase inhibitor in a HeLa extract (Figure 5.10, Panel B). These proteins, along with fluorescent Rnase A and its oligomers[33], were identified by co-migration with authentic standards. Following fluorescence imaging, the gel was then stained using coomassie blue to reveal total cellular protein (Figure 5.10, Panel C). A comparison of the limited number of fluorescent bands with the abundance of total protein present demonstrated the remarkable selectivity of this method for detecting interacting proteins.

5.5 Conclusions

We demonstrated that fluorinated pyronin fluorophores are unique tools for the detection of protein-protein interactions. These molecules form highly stable protein conjugates under physiological conditions (pH 7.4), even in the presence of high concentrations of other soluble amines. However, the high effective concentration of amines between lysine residues at a protein-protein interface can produce a proximity-driven S_NAr reaction to transfer these fluorescent labels and enable detection of interacting partners. Given that lysine is one of the most common amino acids on protein surfaces[34], and these residues are often in close proximity at the interface of a protein complex, this method may be useful for the discovery of novel protein-protein interactions and/or small molecule inhibitors[35, 36] of these interactions.

5.6 Experimental Section

5.6.1 General

Reagents were purchased from Sigma Aldrich, Fisher Scientific, Acros, or Aapptec. ^{1}H (500 MHz) and ^{13}C (125 MHz) NMR spectra were acquired on Bruker DRX-500 or Bruker Avance AV-III 500 instruments. Chemical shifts are reported in ppm and are referenced to CD_3CN (1.94 ppm for ^{1}H and 118.3 ppm for ^{13}C) or CD_3OD (3.31 ppm for ^{1}H and 49.0 ppm for ^{13}C). ^{1}H and ^{13}C NMR spectra of compounds 7-9 were acquired at 65 °C. Coupling constants J_{HH} are in hertz and are reported as follows: chemical shift, multiplicity (app = apparent, s = singlet, d = doublet, t = triplet, q = quartet, dd = doublet of doublets), coupling constant, and integration. Melting points were acquired using a Thomas Hoover Capillary Melting Point Apparatus and are uncorrected. Infrared spectra (IR) were recorded with a Perkin-Elmer Spectrum 100 FT-IR spectrophotometer. UV/Vis measurements employed an Aligent 8452A diode array spectrophotometer. Fluorescence measurements used a Perkin-Elmer LS55 spectrometer. High-resolution mass spectra were obtained at the Mass Spectrometry Laboratory at the University of Kansas. Low-resolution mass spectra were acquired on a Waters Micromass ZQ instrument with electrospray ionization (ESI+). Thin layer chromatography (TLC) used EMD aluminum-backed silica plates (0.20 mm, 60 F-254), and flash chromatography used ICN silica gel (200-400 mesh). Plates were visualized by UV or staining with ceric sulfate/molybdic acid. Preparative HPLC was performed with an Agilent 1200 instrument equipped with a Hamilton PRP-1 reverse phase column (250 mm length, 21 mm ID, 12-20 μm particle size)

with detection by absorbance at 215, 254, and 350 nm. All non-aqueous reactions were carried out using flame- or oven-dried glassware under an atmosphere of dry argon or nitrogen. Dichloromethane used as reaction solvent was purified via filtration through two columns of activated basic alumina under an atmosphere of Ar using a solvent purification system from Glass Contour. Other commercial reagents were used as received unless otherwise noted. Yields are reported based on isolated material.

5.6.2 Synthetic Procedures and Characterization Data

General procedure A: Synthesis of bromopyronins (**104** – **106**) from xanthones (**101** – **103**). Xanthones, prepared as previously reported,[21] were added to round-bottom flasks containing dry DCM (2 – 3 mL). Trifluoromethanesulfonic anhydride (1 M in DCM, 1.5 eq.) was added dropwise with stirring, and the reaction mixture transitioned from pale yellow to bright red. The reaction was stirred at room temperature (22 °C) for 5 min. After this period, tetrabutylammonium bromide (3 eq.) was added, and the reaction was stirred at room temperature for an additional 30 min. The reaction mixture was loaded onto silica gel and subjected to flash chromatography (eluent: DCM:CH_3CN, 20:1 to 3:1). Eluted fractions containing pure material were combined and concentrated by rotary evaporation. The resulting residue was dissolved in a minimal amount of DCM and precipitated with excess diethyl ether. The resulting red solid was filtered, washed extensively with diethyl ether, and dried under high vacuum to yield pure products as trifluoromethanesulfonate salts.

General procedure B. Synthesis of ethylaminopyronins (**107** – **109**) from bromopyronins (**104** – **106**). The bromopyronin starting material was added to a round-bottom flask containing dry CH_2Cl_2 (1 – 2 mL). Gaseous ethylamine was bubbled through the solvent with stirring for 1 min or until the bright red color was eliminated and the solution became yellow. The solvent was removed under vacuum, the residue was dissolved in DMSO, and the product purified by preparative RP-HPLC (Gradient: H_2O:CH_3CN (9:1) to (0:100) with added TFA (0.1%) over 20 min; elution time = 11 – 13 min). Pure fractions were collected, combined, and dried under high vacuum.

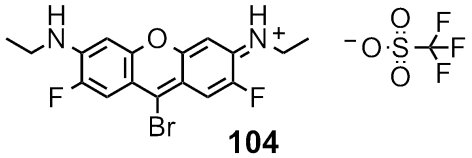

104

N-(9-bromo-6-(ethylamino)-2,7-difluoro-3H-xanthen-3-ylidene)ethanaminium trifluoromethanesulfonate (104). Following general procedure A, 3,6-bis(ethylamino)-2,7-difluoro-9*H*-xanthen-9-one (**101**, 104 mg, 0.327 mmol) yielded compound **104** (128 mg, 0.241 mmol, 73%), a red solid, as the trifluoromethanesulfonate salt. mp 222-226 °C; ^{1}H NMR (500 MHz, CD_3CN) δ 7.81 (d, *J* = 11.7 Hz, 2H), 7.15 (s, 2H), 6.87 (d, *J* = 6.8 Hz, 2H), 3.51 (qd, *J* = 7.2, 5.7 Hz, 4H), 1.36 (t, *J* = 7.2 Hz, 3H); ^{13}C NMR (126 MHz, CD_3CN) δ 155.77, 151.81 (d, *J* = 251.6 Hz), 149.37 (d, *J* = 15.6 Hz), 148.10 (t, *J* = 5.6 Hz), 122.05 (q, *J* = 320.8 Hz), 115.24 (d, *J* = 9.5 Hz), 113.73 (d, *J* = 23.4 Hz), 96.33 (d, *J* = 4.2 Hz), 39.39, 13.72; IR (film) n_{max} 3272, 2978, 1621, 1582, 1524, 1480, 1321,

1253, 1139, 1032, 856 cm^{-1}; HRMS (ESI) *m/z* 381.0419 (M^+, $C_{17}H_{16}BrF_2N_2O^+$ requires 381.0409).

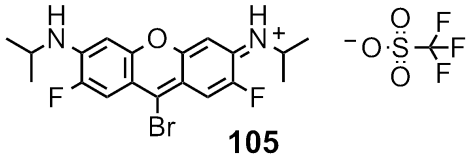

105

N-(9-bromo-6-(isopropylamino)-2,7-difluoro-3H-xanthen-3-ylidene)propan-2-aminium trifluoromethanesulfonate (105). Following general procedure A, 2,7-difluoro-3,6-bis(isopropylamino)-9H-xanthen-9-one (**102**, 90 mg, 0.268 mmol) yielded compound **105** (95 mg, 0.170 mmol, 63%), a red solid, as the trifluoromethanesulfonate salt. mp 214-218 °C; ^1H NMR (500 MHz, CD_3CN) δ 7.78 (d, *J* = 11.7 Hz, 2H), 6.93 (s, 2H), 6.89 (d, *J* = 6.8 Hz, 2H), 4.01 (dq, *J* = 13.0, 6.5 Hz, 2H), 1.36 (d, *J* = 6.4 Hz, 12H); ^{13}C NMR (126 MHz, CD_3CN) δ 155.82, 151.78 (d, *J* = 251.8 Hz), 148.53 (d, *J* = 15.6 Hz), 147.91 (t, *J* = 5.6 Hz), 122.05 (q, *J* = 320.9 Hz), 115.18 (d, *J* = 9.5 Hz), 113.83 (d, *J* = 23.6 Hz), 96.58 (d, *J* = 4.1 Hz), 46.92, 21.83; IR (film) n_{max} 3255, 2980, 1655, 1624, 1580, 1537, 1523, 1487, 1426, 1360, 1324, 1271, 1203, 1151, 1034, 871 cm^{-1}; HRMS (ESI) m/z 409.0714 (M^+, $C_{19}H_{20}BrF_2N_2O^+$ requires 409.0722).

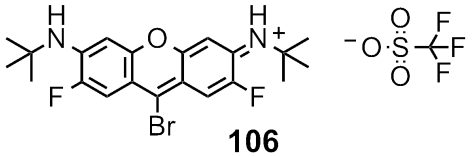

106

N-(9-bromo-6-(ethylamino)-2,7-difluoro-3H-xanthen-3-ylidene)-2-methylpropan-2-aminium trifluoromethanesulfonate (106). Following general

procedure A, 3,6-bis(tert-butylamino)-2,7-difluoro-9H-xanthen-9-one (**103**, 84 mg, 0.231 mmol) yielded compound **106** (82 mg, 0.139 mmol, 60%), a red solid, as the trifluoromethanesulfonate salt. mp 194-199 °C; ^{1}H NMR (500 MHz, CD_3CN) δ 7.84 (d, *J* = 12.0 Hz, 2H), 7.12 (d, *J* = 6.9 Hz, 2H), 6.58 (s, 2H), 1.56 (s, 18H); ^{13}C NMR (126 MHz, CD_3CN) δ 155.27, 152.33 (d, *J* = 251.9 Hz), 148.70 (t, *J* = 5.6 Hz), 147.94 (d, *J* = 14.2 Hz), 122.07 (q, *J* = 320.9 Hz), 115.40 (d, *J* = 9.8 Hz), 113.46 (d, *J* = 24.6 Hz), 98.16 (d, *J* = 3.3 Hz), 54.92, 28.71; IR (film) n_{max} 2964, 2877, 1620, 1520, 1471, 1344, 1260, 1147, 1030, 868 cm^{-1}; HRMS (ESI) m/z 437.1019 (M^+, $C_{21}H_{24}BrF_2N_2O^+$ requires 437.1035).

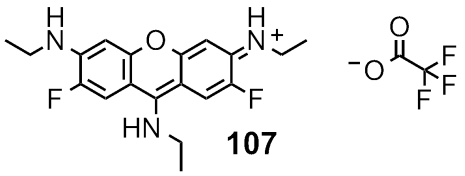

107

***N*-(6,9-bis(ethylamino)-2,7-difluoro-3*H*-xanthen-3-ylidene)ethanaminium 2,2,2-trifluoroacetate (107).** Following general procedure B, compound **104** (53 mg, 0.100 mmol) yielded compound **107** (40 mg, 0.087 mmol, 87%), a yellow solid, as the TFA salt. mp 136-140 °C; ^{1}H NMR (500 MHz, CD_3OD) δ 7.86 (d, *J* = 13.3 Hz, 2H), 6.68 (d, *J* = 7.4 Hz, 2H), 4.00 (q, *J* = 7.2 Hz, 2H), 3.35 (q, *J* = 7.2 Hz, 4H), 1.52 (t, *J* = 7.2 Hz, 3H), 1.33 (t, *J* = 7.2 Hz, 6H); ^{13}C NMR (126 MHz, CD_3OD) δ 162.93 (q, *J* = 34.5 Hz), 155.94, 155.45, 150.01 (d, *J* = 243.0 Hz), 146.36 (d, *J* = 14.8 Hz), 118.41 (q, *J* = 293.8 Hz), 110.19, 101.60, 97.64 (d, *J* = 4.5 Hz), 44.17, 38.68, 14.83, 13.98; IR (film) n_{max} 3441, 3264, 2985, 1686, 1650,

1624, 1512, 1471, 1314, 1197, 1174, 1124, 797, 718 cm^{-1}; HRMS (ESI) *m/z* 346.1698 (M^+, $C_{19}H_{22}F_2N_3O^+$ requires 346.1725).

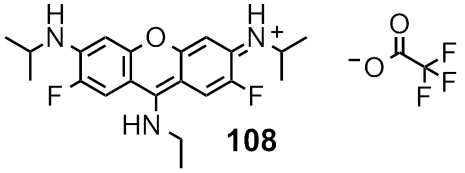

108

***N*-(9-(ethylamino)-2,7-difluoro-6-(isopropylamino)-3*H*-xanthen-3-ylidene)propan-2-aminium 2,2,2-trifluoroacetate (108).** Following general procedure B, compound **105** (34 mg, 0.061 mmol) yielded compound **108** (24 mg, 0.050 mmol, 82%), a yellow solid, as the TFA salt. mp 174-178 °C; ^1H NMR (500 MHz, CD_3OD) δ 7.90 (d, *J* = 13.2 Hz, 2H), 6.77 (d, *J* = 7.4 Hz, 2H), 4.03 (q, *J* = 7.2 Hz, 2H), 3.85 (hept, *J* = 6.4 Hz, 2H), 1.52 (t, *J* = 7.2 Hz, 3H), 1.34 (d, *J* = 6.4 Hz, 12H); ^{13}C NMR (126 MHz, CD_3OD) δ 162.94 (q, *J* = 25.4 Hz), 156.11, 155.58, 150.02 (d, *J* = 243.1 Hz), 145.62 (d, *J* = 14.6 Hz), 118.46 (q, *J* = 306.2 Hz), 110.37, 101.68, 98.15 (d, *J* = 4.3 Hz), 45.80, 44.16, 22.14, 14.81; IR (film) n_{max} 3265, 2923, 2852, 1650, 1623, 1589, 1518, 1479, 1324, 1168, 1142, 875, 816, 760 cm^{-1}; HRMS (ESI) *m/z* 374.2060 (M^+, $C_{21}H_{26}F_2N_3O^+$ requires 374.2038).

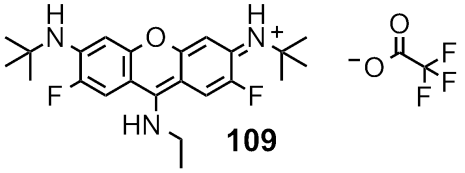

109

***N*-(6-(*tert*-butylamino)-9-(ethylamino)-2,7-difluoro-3*H*-xanthen-3-ylidene)-2-methylpropan-2-aminium 2,2,2-trifluoroacetate (109).** Following general procedure B, compound **106** (46 mg, 0.078 mmol) yielded compound **109** (32

mg, 0.061 mmol, 79%), a yellow solid, as the TFA salt. mp 166-170 °C; ^{1}H NMR (500 MHz, CD_3OD) δ 7.95 (d, *J* = 13.5 Hz, 2H), 7.04 (d, *J* = 7.6 Hz, 2H), 4.05 (q, *J* = 7.2 Hz, 2H), 1.54 – 1-50 (m, 21H); ^{13}C NMR (126 MHz, CD_3OD) δ 162.98 (q, *J* = 31.4 Hz), 156.34, 154.89, 150.53 (d, *J* = 242.8 Hz), 144.76 (d, *J* = 13.4 Hz), 118.74 (d, *J* = 294.3 Hz), 110.16, 101.88, 100.18 (d, *J* = 3.5 Hz), 53.26, 44.16, 29.13, 14.75; IR (film) n_{max} 3435, 3260, 2922, 2851, 1677, 1648, 1622, 1514, 1470, 1320, 1199, 1170, 1132, 827, 798, 718 cm^{-1}; HRMS (ESI) *m/z* 402.2336 (M^+, $C_{23}H_{30}F_2N_3O^+$ requires 402.2351).

Measurement of extinction coefficients (ε). Beer's Law plots of absorbance versus concentration were measured in aqueous PBS (pH 7.0) with increasing concentrations of sample (Figure 5.11). Values for absorbance λ_{max} were determined for all samples. Linear least squares fitting of the data (including a zero intercept) was used to determine the slope, which corresponds to the extinction coefficient. Molar absorptivity (M^{-1} cm^{-1}) was calculated using the following equation (b = path length = 1 cm): Absorbance = [ε] [b] [concentration (M)]

Measurement of quantum yields (Φ). Samples were excited at absorbance λ_{max} and the integrated fluorescence emission was quantified (a 1 cm path length quartz cuvette was used). Fluorescein (Φ = 0.92 in 0.1 M NaOH) and carboxyfluorescein (Φ = 0.925 in 0.1 M NaOH) provided standards. The integrated fluorescence emission at a given concentration was plotted against

the maximum absorbance of the sample at that concentration determined by extrapolation based on absorbance measurements at higher concentrations (Figure 5.12). Linear least squares fitting of the data (including a zero intercept) was used to calculate the slope, which is proportional to the quantum yield. Quantum yields were calculated with the following equation using the average of the values measured for fluorescein and carboxyfluorescein as standards: $\Phi_x = \Phi_{st}(Grad_x/Grad_{st})$, where Φ_{st} represents the quantum yield of the standard, Φ_x represents the quantum yield of the unknown, and *Grad* is the slope of the best linear fit.

Measurement of pKa values. Absorbance spectra for pyronins **107** – **109** (10 μM in PBS) were obtained between pH 4 – 12. Samples were analyzed immediately upon adjustment to final pH values with aqueous HCl or NaOH to avoid potential hydrolysis. The absence of hydrolysis under these conditions was confirmed by analysis of absorbance spectra upon re-acidification of aliquots subjected to basic pH. The absorbance spectra of **107** – **109** did not change appreciably in the range of pH 4 – 9 (data not shown), but substantial changes in absorbance were observed at more basic pH values (Figure 5.13). Values for pKa were calculated using non-linear regression of pH-dependent changes in absorbance at 415 nm.

Analysis of the kinetics of reaction of pyronins 107 – 109 with methylamine. To ethylaminopyronins **107** – **109** (50 μM) at 37 °C in either MeOH/H_2O (9:1), or

H_2O, was added aqueous methylamine (final [$MeNH_2$]=10 mM). The pH of the reaction in pure H_2O was adjusted to 7.4 by addition of conc. aq. HCl. Low-resolution mass spectra were collected from three independent reactions of each pyronin over time. The integrated peak intensities of the ethyl-substituted starting materials and methyl-substituted products were summed and normalized to 100% to quantify changes in starting material and product over time. The resulting curves, corresponding to pseudo first order kinetic profiles, were analyzed with an exponential one-phase association model (Prism 6 software) to calculate half-time values.

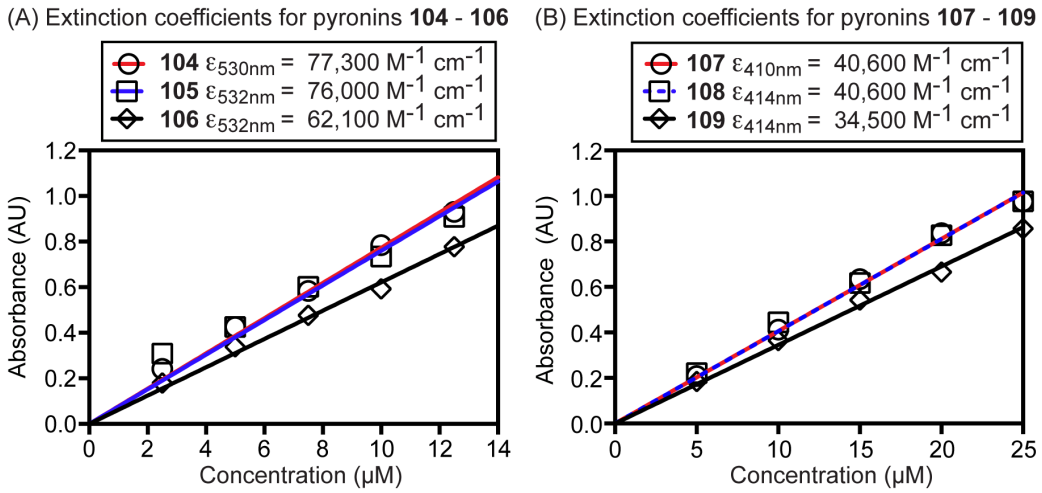

Figure 5.11. Determination of extinction coefficients (ε) in PBS (pH 7.0).

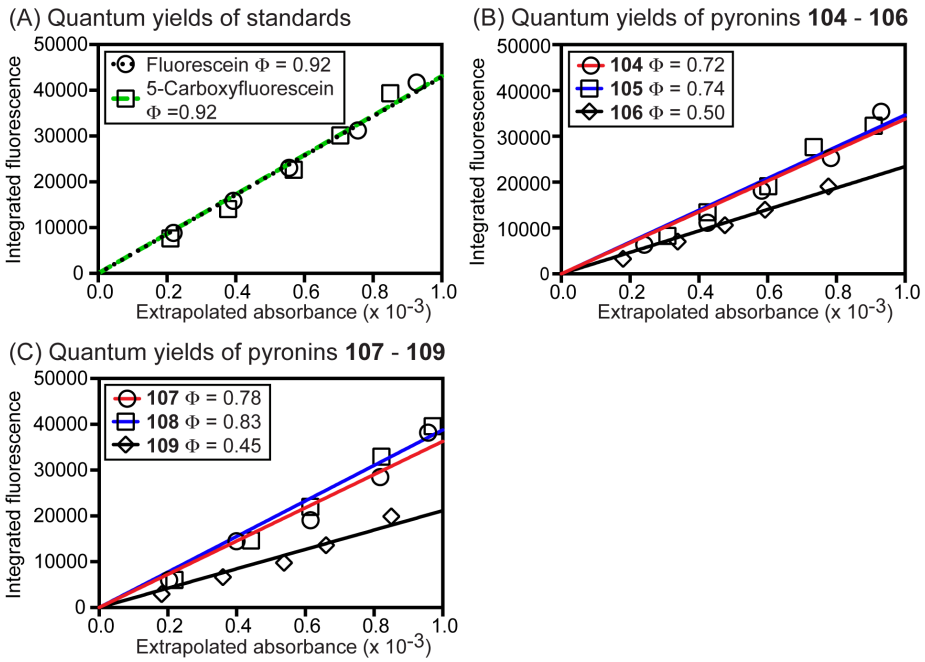

Figure 5.12. Determination of quantum yields (Φ) for pyronins **104** - **109**. Fluorescein and 5-carboxyfluorescein in aqueous NaOH (0.1 M, Φ = 0.92) provided standards. Values for **104** – **109** were obtained in PBS (pH 7.0).

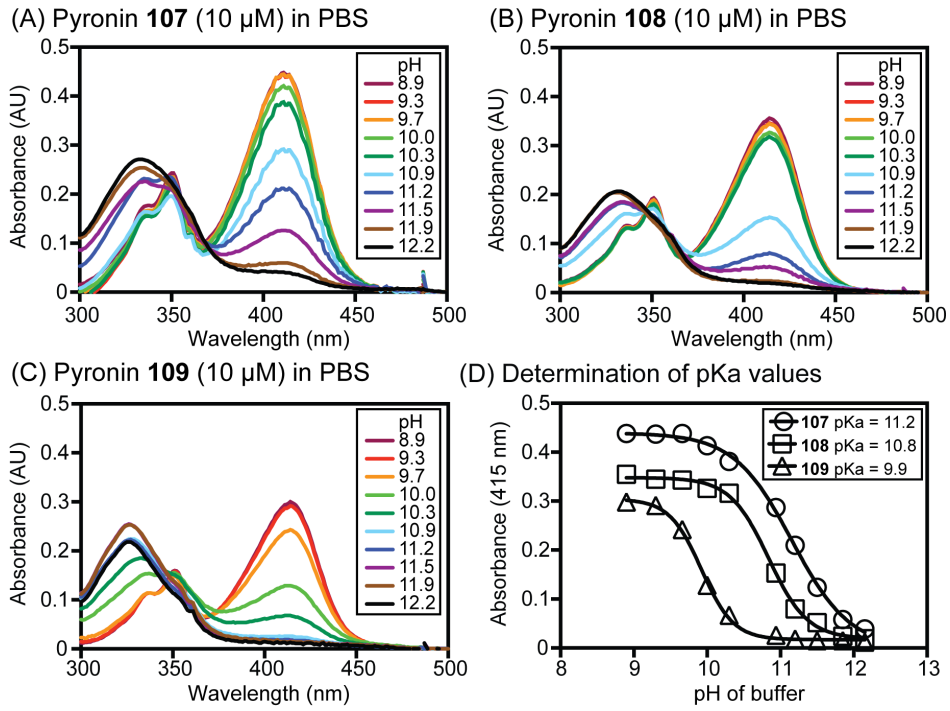

Figure 5.13. Determination of pKa values of aminopyronins **107** - **109**. Absorbance at 415 nm was plotted as a function of pH and analyzed by non-linear regression (Prism 6 software). Samples were analyzed immediately upon adjustment to final pH values with aqueous HCl or NaOH to avoid any potential hydrolysis.

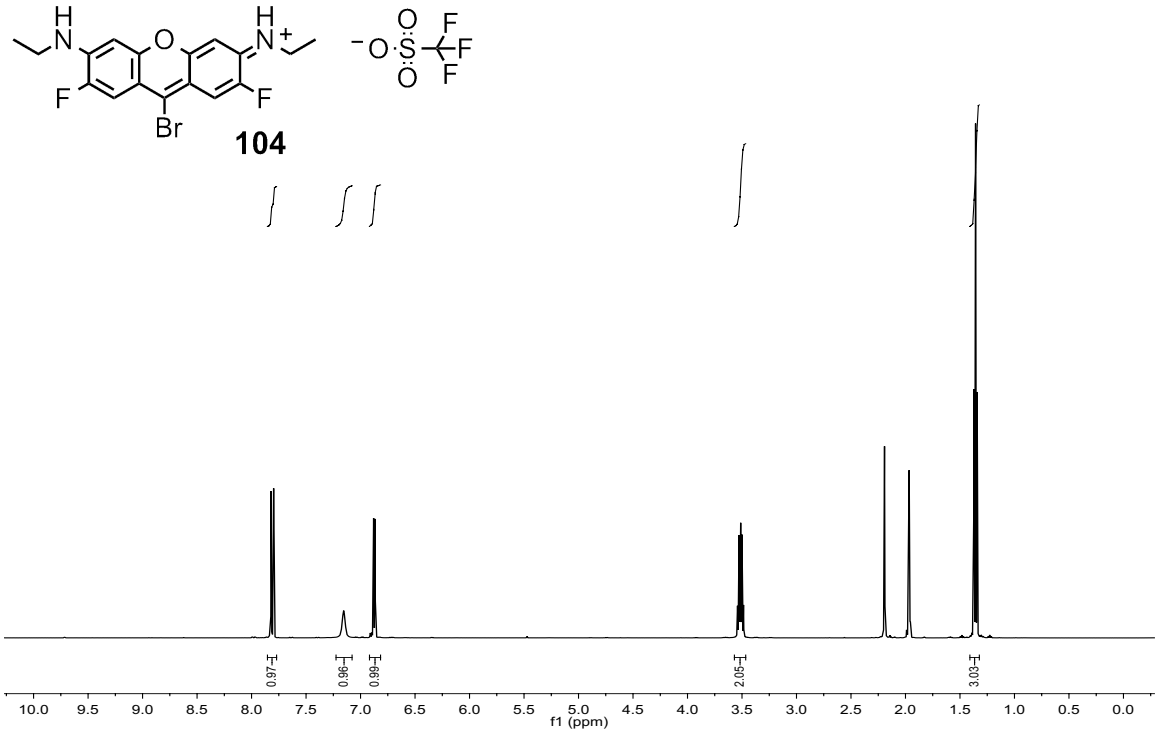

Figure 5.14. ^{1}H NMR (500 MHz) of **104** in CD_3CN.

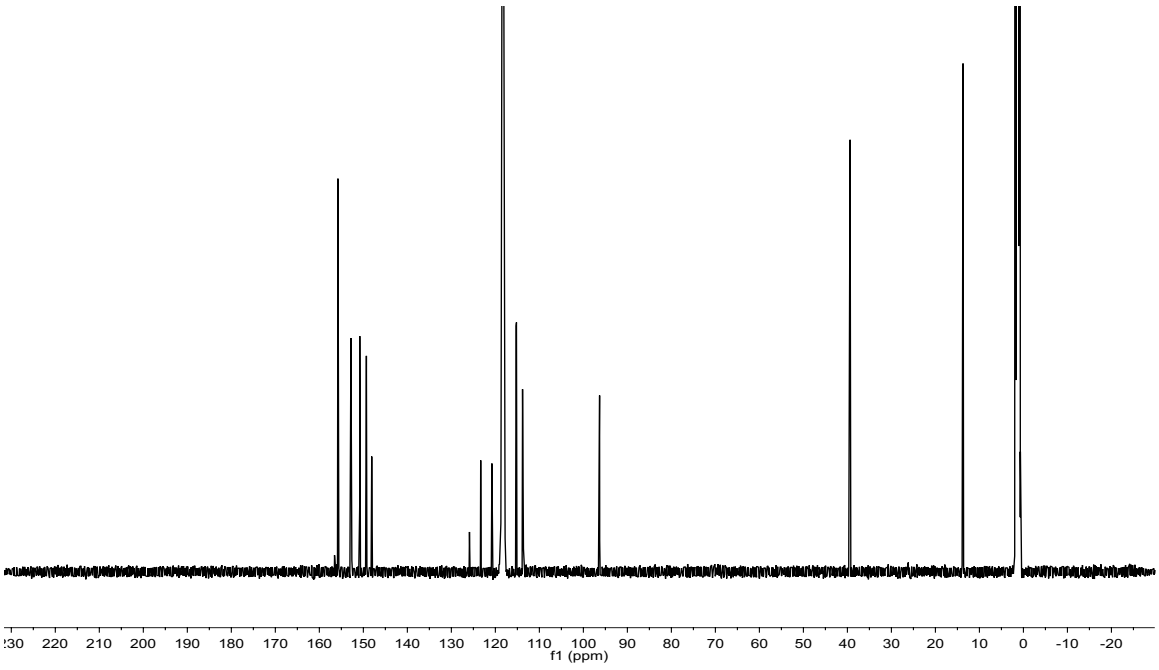

Figure 5.15. ^{13}C NMR (125 MHz) of **104** in CD_3CN.

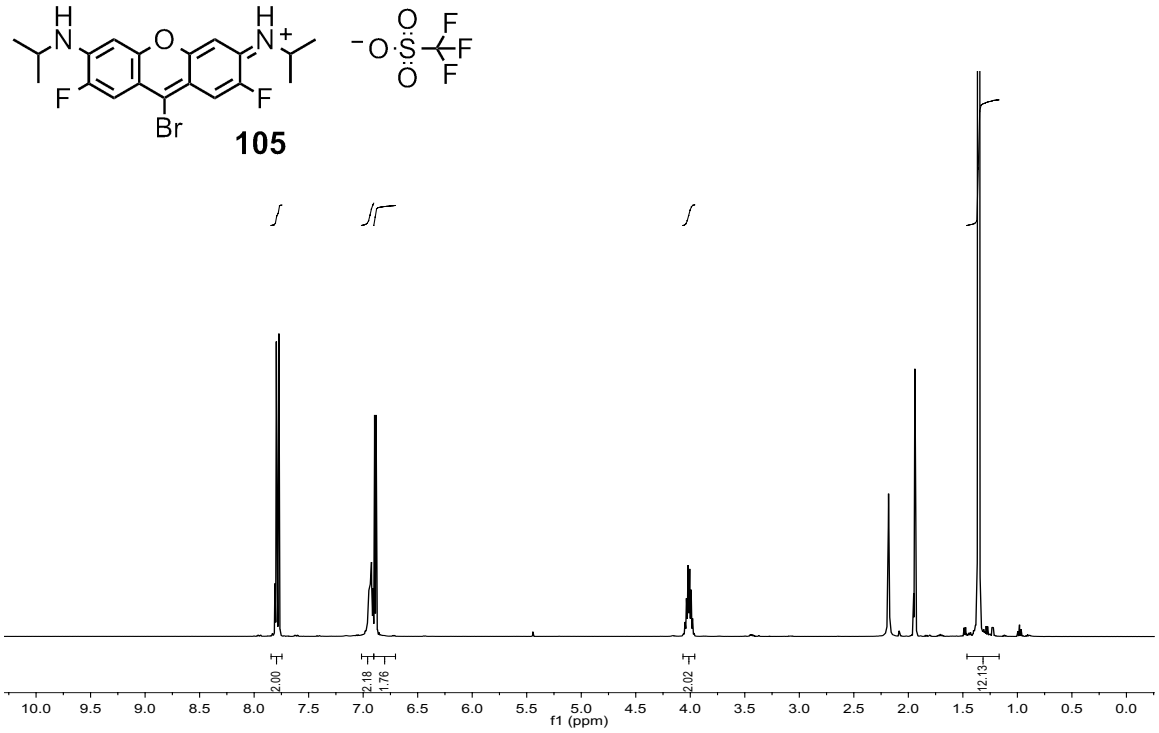

Figure 5.16. ^{1}H NMR (500 MHz) of **105** in CD_3CN.

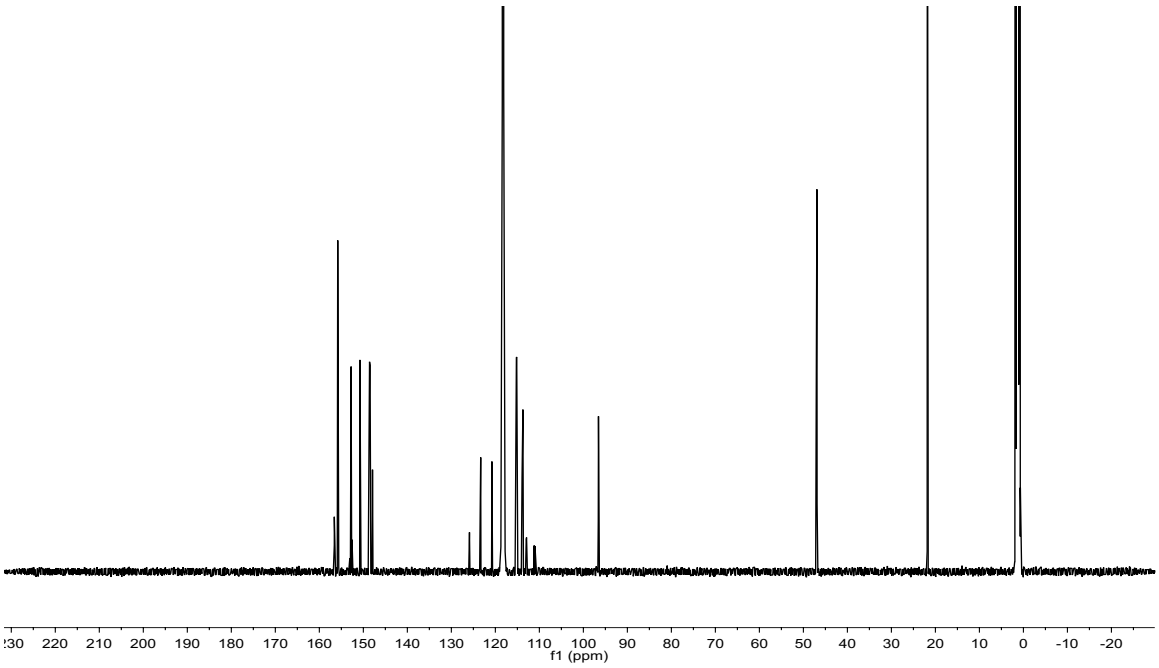

Figure 5.17. ^{13}C NMR (125 MHz) of **105** in CD_3CN.

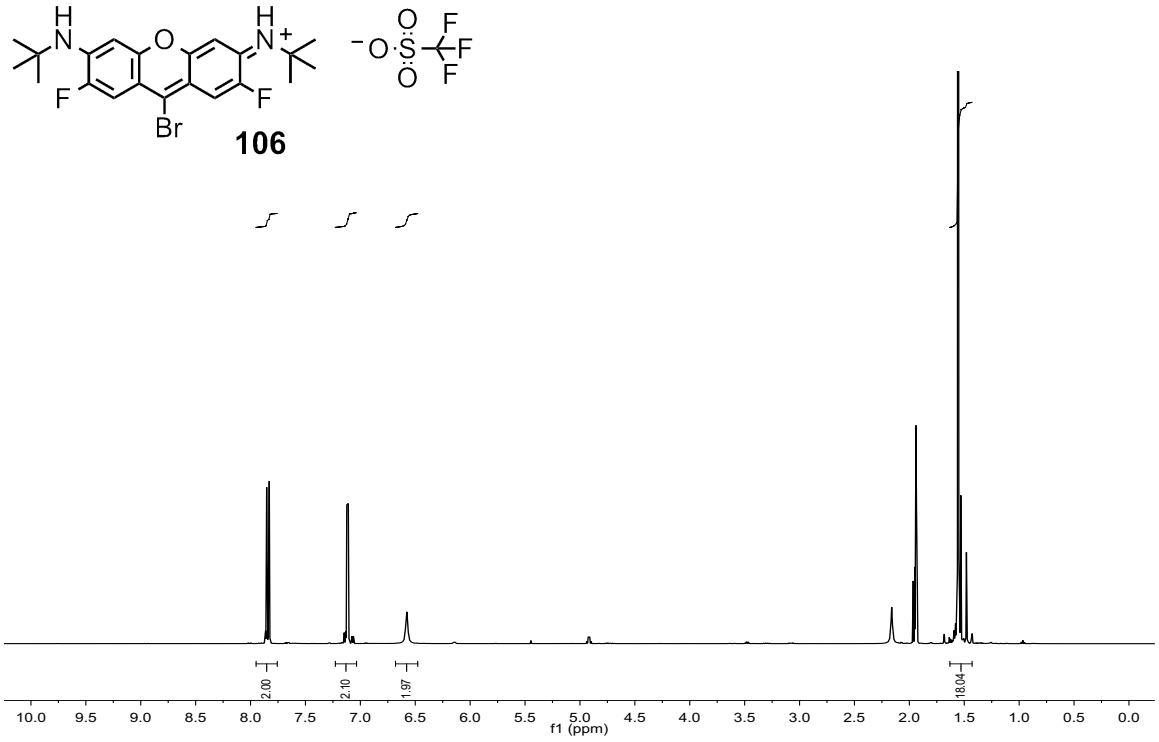

Figure 5.18. ^{1}H NMR (500 MHz) of **106** in CD_3CN.

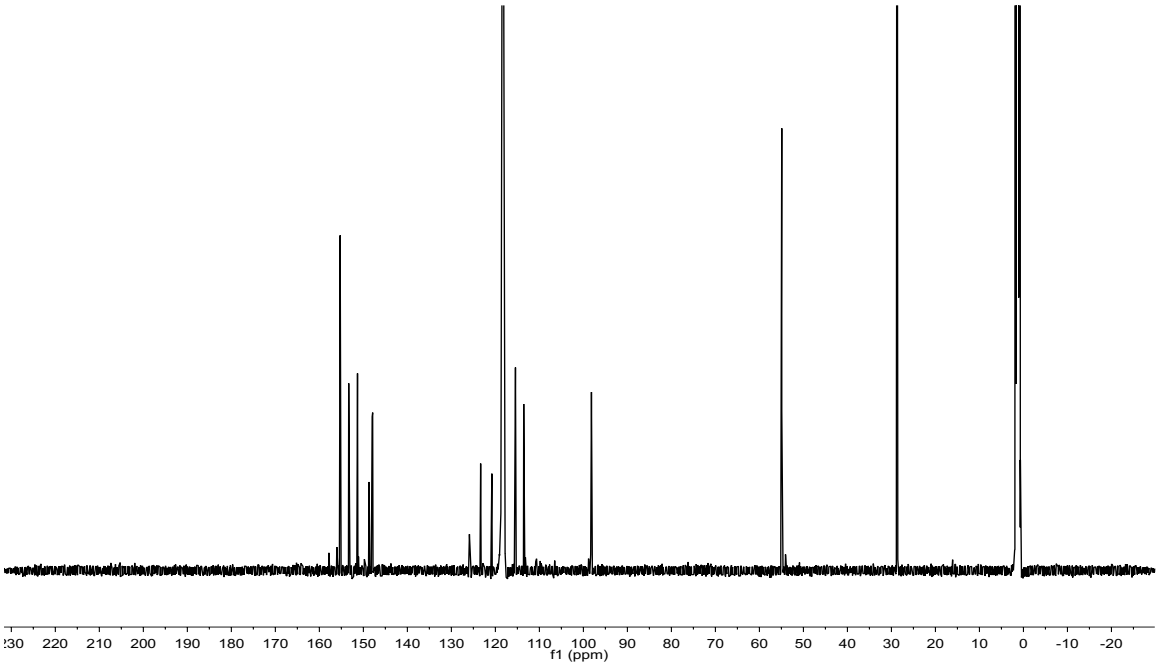

Figure 5.19. ^{13}C NMR (125 MHz) of **106** in CD_3CN.

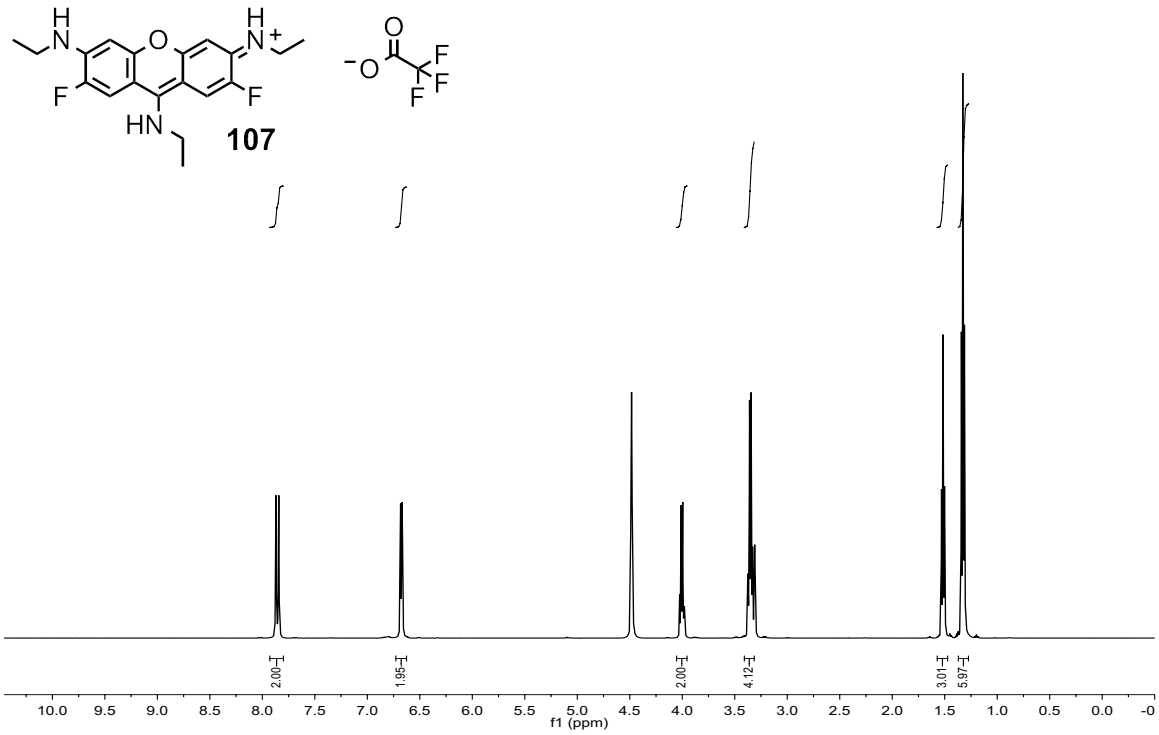

Figure 5.20. ^{1}H NMR (500 MHz) of **107** in CD_3OD at 65 °C.

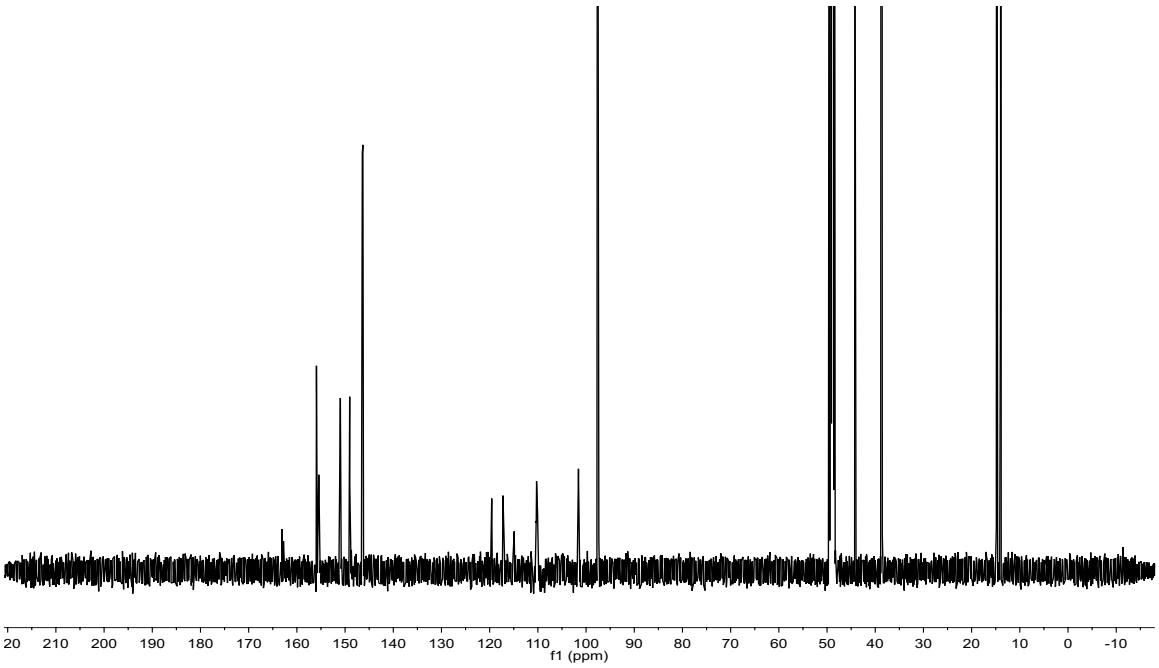

Figure 5.21. ^{13}C NMR (125 MHz) of **107** in CD_3OD at 65 °C.

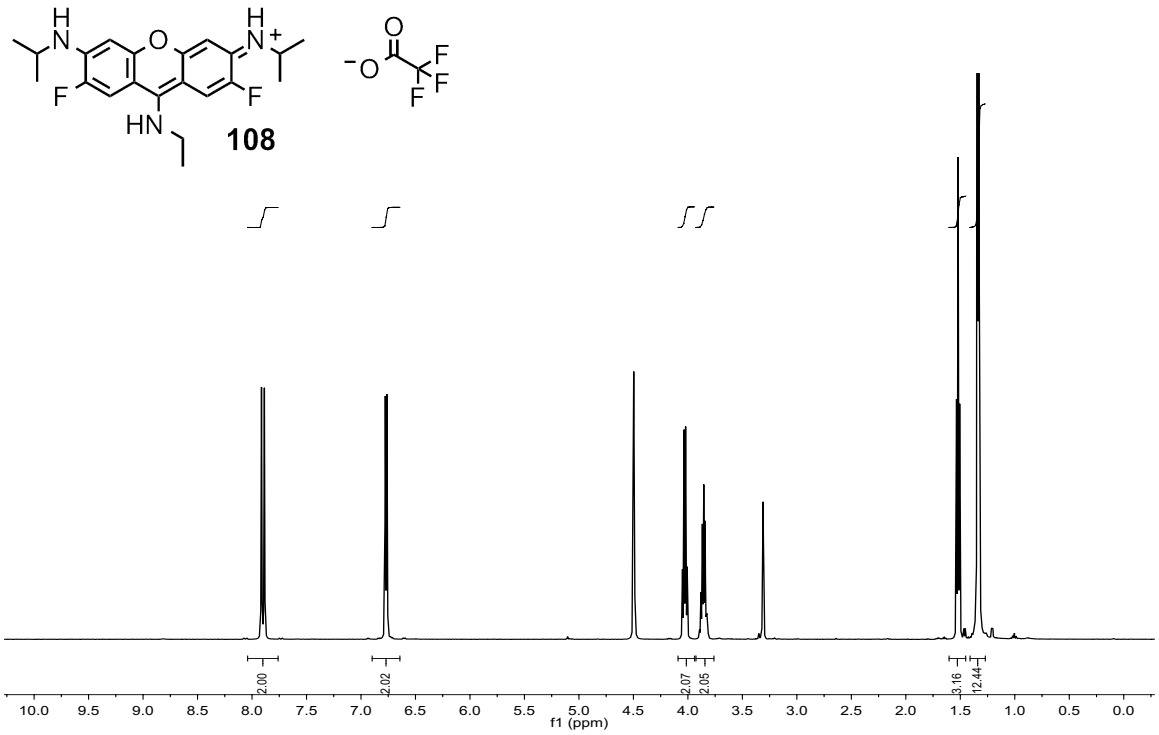

Figure 5.22. ^{1}H NMR (500 MHz) of **108** in CD_3OD at 65 °C.

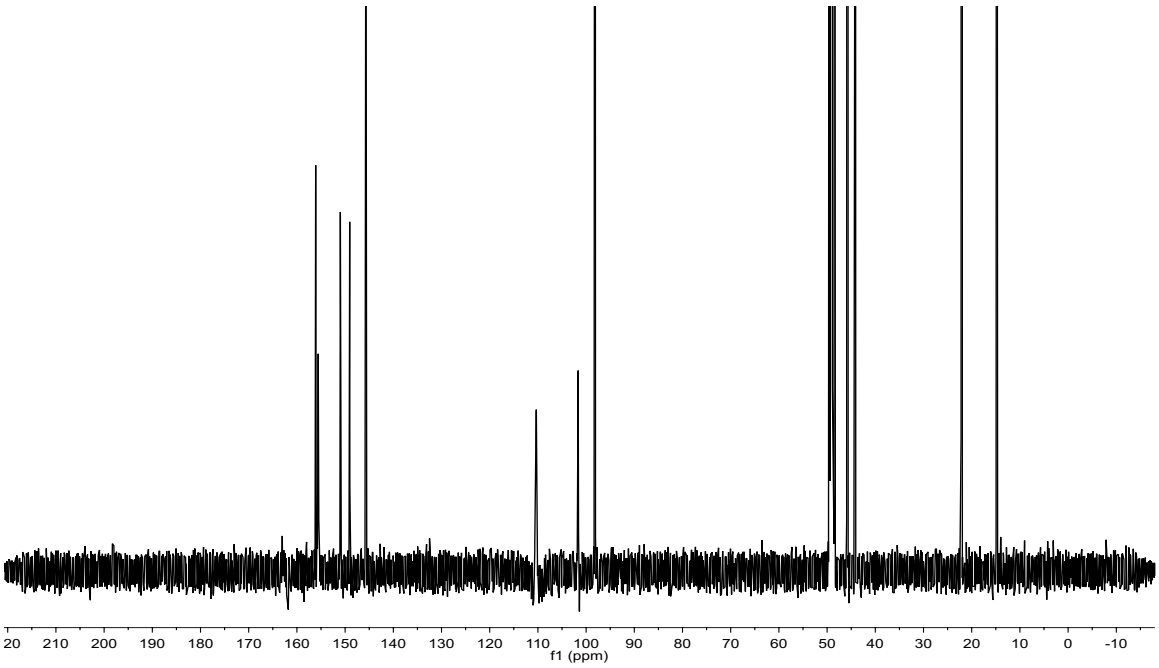

Figure 5.23. ^{13}C NMR (125 MHz) of **108** in CD_3OD at 65 °C.

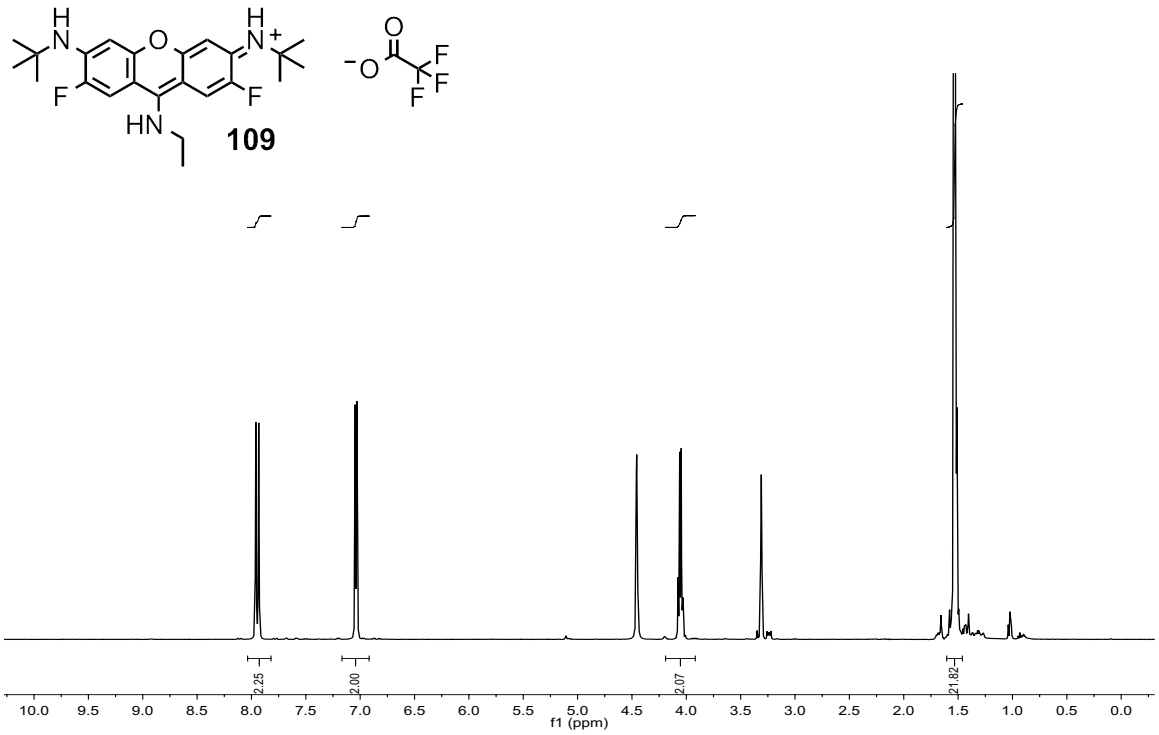

Figure 5.24. ^{1}H NMR (500 MHz) of **109** in CD_3OD at 65 °C.

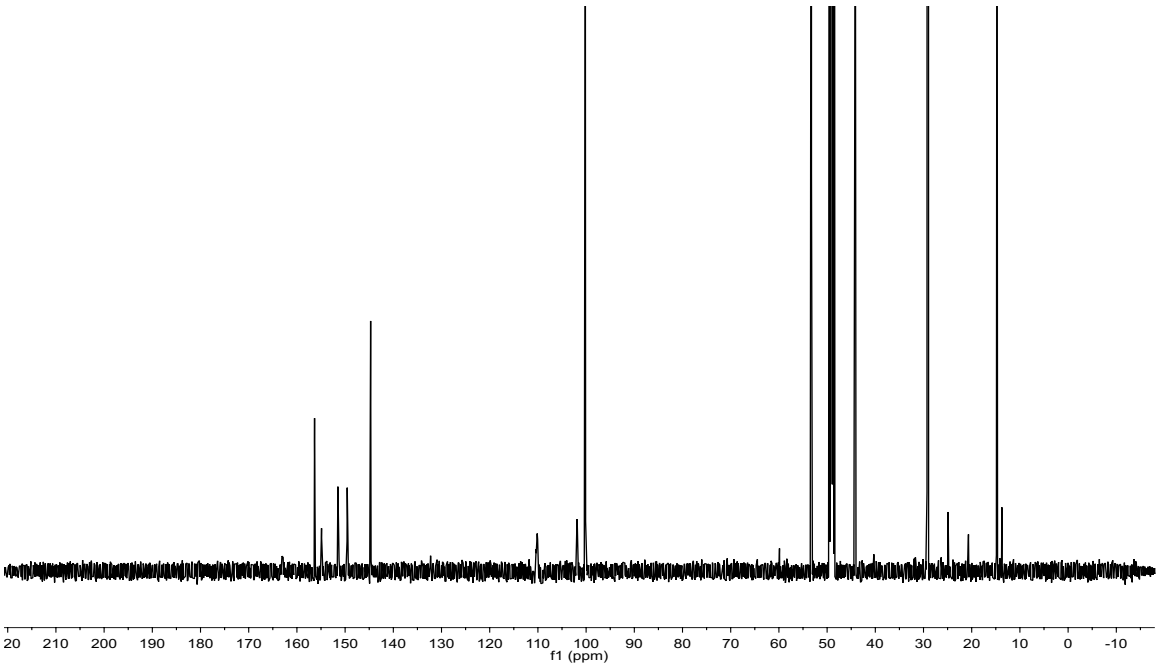

Figure 5.25. ^{13}C NMR (125 MHz) of **109** in CD_3OD at 65 °C.

5.6.3 Biological assays and Protocols

General. Reagents were purchased from Sigma-Aldrich, Fisher Scientific, and Acros Organics. Cell culture reagents were from Sigma-Aldrich. Staphylococcyl Protein A (SpA, recombinant) was obtained from GenScript. Human immunoglobulin-G and bovine ribonuclease A (from bovine pancreas) were from Sigma-Aldrich. Human IgG Fc region and human IgG Fab fragment were purchased from Athens Research and Technology. Ribonuclease inhibitor (recombinant, human placental) was from New England BioLabs. Absorbance data for protein quantification were collected on a Thermo Scientific NanoDrop 1000 spectrophotometer. Analysis by SDS-PAGE employed an XCell II module with Bis-Tris 4-12% polyacrylamide gradient gels (1.5 mm, Life Technologies) and MOPS-SDS running buffer (Life Technologies). An Alpha Imager MultiImage II Light Cabinet (DE-500) with UV excitation (365 nm) and a 560 ± 40 nm emission filter was used for fluorescence imaging of gels. Sequencing of tryptic peptides by mass spectrometry was performed by the KU Analytical Proteomics Laboratory (APL) with a Thermo Finnigan LTQ-FTICR hybrid mass spectrometer.

Cell Culture. HeLa cells (ATCC #CCL-2) were cultivated in DMEM containing fetal bovine serum (FBS, 10%), penicillin (100 units/mL), and streptomycin (100 µg/mL). Cells were grown in a humidified incubator (5% CO_2) at 37 °C.

Procedure for labeling of human IgG with pyronins. Lyophilized human IgG was reconstituted in sterile water and the protein concentration was determined by absorbance at 280 nm (ε E1% = 13.7 L g^{-1} cm^{-1}).[37] The corresponding bromopyronin (**104** – **106**) was dissolved in ethanol at 10 mM. Aqueous sodium bicarbonate (final concentration = 50 mM, pH 8) was added to the protein solution, followed by the bromopyronin (10 equiv.) in ethanol. This reaction was allowed to proceed at 37 °C for 20 min. To purify the conjugate, Sephadex G-25 resin (Superfine, Sigma) was suspended in PBS (pH 7.0). The resulting slurry (900 µL) was added to a mini-spin column (USA Scientific) and centrifuged at 16,000 x G to remove the buffer and pack the resin. After the 20 min conjugation reaction, the solution containing the bromopyronin and IgG was loaded onto the packed resin of the spin column (50 – 70 µL per column) and centrifuged at 16,000 x G for 1 min to separate the labeled protein from the small molecule retained by the resin. The absorbance at 280 nm and 425 nm of the eluent was determined to quantify the degree of protein labeling. This protocol typically afforded 3 – 4 molecules of pyronin per IgG molecule.

Procedure for labeling of human IgG with commercial amine-reactive fluorophores. Lyophilized human IgG was reconstituted in sterile water and the protein concentration was determined by absorbance at 280 nm (ε E1% = 13.7 L g^{-1} cm^{-1}).[37] Aqueous sodium bicarbonate (final concentration = 50 mM, pH 8) was added to the protein solution. The commercially available fluorophores 5-carboxyfluorescein NHS-ester (10 equiv. from 10 mM DMSO stock solution) or

fluorescein isothiocyanate (G-isomer, 10 equiv. from 10 mM DMSO stock solution) were added and the reaction was incubated at 37 °C for 20 min. Purification of the conjugate protein was performed using Sephadex G-25 loaded spin columns as described above. Typical labeling was 5 molecules of 5-carboxyfluorescein per molecule protein and 4 molecules FITC per molecule protein.

Procedure for labeling of human Fc and Fab regions with pyronins. Human Fc and Fab regions were obtained as aqueous solutions ([Fc] = 1.5 mg/mL, [Fab] = 5 mg/mL). Aqueous sodium bicarbonate (final concentration = 50 mM, pH 8) was added to this protein solution, followed by bromopyronin **105** in ethanol (10 equiv., from a 10 mM stock solution). The reaction was allowed to proceed for 20 min at room temperature (21-23 °C), and the labeled protein was purified using Sephadex G-25 and the spin column protocol described for purification of full-length human IgG conjugates. The final protein concentration was determined by absorbance at 280 nm (ε E1% = 13.5 L g^{-1} cm^{-1} used for both proteins; provided by product data sheet). Both the Fc and Fab regions were typically labeled at 1.5 to 2 molecules of pyronin per molecule of protein.

Procedure for labeling of ribonuclease A with pyronin. Bovine ribonuclease A was reconstituted in sterile water and the protein concentration determined from absorbance at 280 nm (ε = 8,640 M^{-1} cm^{-1}, calculated with the peptide property calculator: http://www.basic.northwestern.edu/biotools/proteincalc.html

based on the sequence for bovine ribonuclease A (UniProt: P61823). Aqueous sodium bicarbonate (final concentration = 50 mM, pH 8) was added to this protein solution, followed by bromopyronin **105** in ethanol (2 equiv., from a 10 mM stock solution). NOTE: Unlike the more soluble IgG, extensive labeling of ribonuclease A was found to cause this protein to precipitate from solution, greatly reducing the yield. The reaction was allowed to proceed for 20 min at room temperature (21 – 23 °C), and the labeled protein was subsequently separated from excess fluorophore using the spin column protocol described for purification of human IgG conjugates. Ribonuclease A was typically labeled at 0.3 – 0.6 molecules of pyronin per molecule of ribonuclease A.

Analysis of transfer of pyronin from human IgG to SpA. Human IgG was labeled with bromopyronins **104** – **106** as previously described. These IgGs were combined with bovine serum albumin (BSA) and *Staphylococcal* protein A (at a final concentration of 5 μM for each protein) in phosphate-buffered saline (PBS) at pH 7.4. These protein mixtures were incubated at 37 °C for 0 – 16 h and analyzed by SDS-PAGE with fluorescence imaging. Quantitative analysis of SpA fluorescence was performed using Adobe Photoshop (CS6). Fluorescence intensity was measured using average pixel density of a fixed region of interest (ROI) encompassing each SpA band. Background fluorescence was adjusted for by measuring fluorescence intensity at t = 0 and subtracting this value from subsequent time points.

Analysis of transfer of pyronin from human Fc and Fab regions to SpA. The full-length human IgG, Fc region, and Fab fragment were labeled with bromopyronin **105** as previously described. These proteins were combined with *Staphylococcal* protein A (at a final concentration of 5 μM for each protein) in phosphate-buffered saline (PBS) at pH 7.4. These protein mixtures were incubated at 37 °C for 0-16 h and analyzed by SDS-PAGE with fluorescence imaging. Quantitative analysis of SpA fluorescence was performed as described above for pyronin transfer between human IgG and SpA.

Analysis of transfer of commercially available fluorophores from human IgG to SpA. Human IgG was labeled with bromopyronin **105**, 5-carboxyfluorescein NHS-ester, or FITC as previously described. These IgGs were combined with *Staphylococcal* protein A (at a final concentration of 5 μM for each protein) in phosphate-buffered saline (PBS) at pH 7.4. These protein mixtures were incubated at 37 °C for 16 h and analyzed by SDS-PAGE with fluorescence imaging.

Analysis of lysine residues on SpA that accept pyronins from IgG. Human IgG was conjugated with bromopyronin **105** as previously described. This labeled IgG (25 μM) was allowed to react with SpA (10 μM) in PBS (pH 7.4) at 37 °C for 18 h. Following this incubation period, excess Protein A agarose (Pierce Biotechnology) was added to immobilize the IgG. The resulting slurry was

centrifuged at 2,000 rpm for 5 min, and the supernatant containing enriched SpA was removed for analysis by sequencing of tryptic peptides. Protein samples were diluted with ammonium bicarbonate (0.2 M), and treated with DTT (10 mM) at 37 °C for 30 min. Iodoacetamide was added (final concentration = 20 mM) and samples were further incubated at room temperature for 30 minutes to alkylate cysteine residues. Following this incubation period, sequencing-grade Trypsin (0.5 µg, Promega) was added and the samples incubated at 37 °C overnight. Trifluoroacetic acid (0.1% final concentration) was added to neutralize the trypsin, and samples were stored at 4 °C prior to analysis by MS/MS sequencing. Tandem mass spectra were extracted using Xcalibur version 2.1. All MS/MS samples were analyzed using Mascot software (Matrix Science, London, UK; version 2.3.02). Mascot was used to search the uniprot_sprot database (538010 entries) assuming digestion by trypsin. Mascot was searched with a fragment ion mass tolerance of 0.50 Da and a parent ion tolerance of 20 PPM. Carbamidomethyl cysteine was specified in Mascot as a fixed modification. Modification of lysine by the pyronin was specified in Mascot as a variable modification. Scaffold (version 4.0.4, Proteome Software Inc., Portland, OR) was used to validate MS/MS based peptide and protein identifications. Peptide identifications were accepted if they could be established at greater than 95.0% probability by the Peptide Prophet algorithm with Scaffold delta-mass correction.[38, 39] Protein identifications were accepted if they could be established at greater than 99.0% probability and contained at least 2 identified peptides. Protein probabilities were assigned by the Protein Prophet algorithm.[38, 39]

Proteins that contained similar peptides and could not be differentiated based on MS/MS analysis alone were grouped to satisfy the principles of parsimony.

Transfer of pyronin from ribonuclease A to endogenous ribonuclease inhibitor present in a lysate of HeLa cells. Ribonuclease A was labeled with bromopyronin **105** as previously described. HeLa cells (~10^7) in a T75 culture flask were trypsinized, centrifuged at 2,000 rpm for 2 min, and washed with PBS (pH 7.4). The cell pellet was re-suspended in PBS (200 µL) containing 10 mM DTT, 1 mM EDTA, and 1 mM PMSF. The cell suspension was cooled to 4 °C and homogenizied by brief ultrasonication (one 3 sec. pulse). The resulting lysate was centrifuged (18,000 x G, 10 min, 4 °C). The supernatant containing the cytosolic fraction was removed and the total protein concentration was determined with a Pierce BCA Protein Assay Kit. An aliquot containing 50 µg of total protein was added to PBS (pH 7.4) containing pyronin-labeled ribonuclease A (20 µM) and incubated at 37 °C for 18 h. As a positive control, labeled ribonuclease A (20 µM) was co-incubated with purified human recombinant ribonuclease inhibitor (200 units) at 37 °C for 18 h. Following incubation, the protein mixtures were subjected to SDS-PAGE with fluorescence imaging. The gel was subsequently stained using Coomassie blue to reveal all proteins and allow examination of the specificity of fluorophore transfer.

5.7 References

1. Phizicky, E. M.; Fields, S., Protein-Protein Interactions - Methods for Detection and Analysis. *Microbiol. Rev.* **1995,** *59*, 94-123.

2. Berggard, T.; Linse, S.; James, P., Methods for the detection and analysis of protein-protein interactions. *Proteomics* **2007,** *7*, 2833-2842.

3. Jones, S.; Thornton, J. M., Principles of protein-protein interactions. *Proc. Natl. Acad. Sci. U. S. A.* **1996,** *93*, 13-20.

4. Ito, T.; Tashiro, K.; Muta, S.; Ozawa, R.; Chiba, T.; Nishizawa, M.; Yamamoto, K.; Kuhara, S.; Sakaki, Y., Toward a protein-protein interaction map of the budding yeast: A comprehensive system to examine two-hybrid interactions in all possible combinations between the yeast proteins. *Proc. Natl. Acad. Sci. U. S. A.* **2000,** *97*, 1143-1147.

5. Schwikowski, B.; Uetz, P.; Fields, S., A network of protein-protein interactions in yeast. *Nat. Biotechnol.* **2000,** *18*, 1257-1261.

6. Truong, K.; Ikura, M., The use of FRET imaging microscopy to detect protein-protein interactions and protein conformational changes in vivo. *Curr. Opin. Struct. Biol.* **2001,** *11*, 573-578.

7. Kenworthy, A. K., Imaging protein-protein interactions using fluorescence resonance energy transfer microscopy. *Methods* **2001,** *24*, 289-296.

8. Lavis, L. D.; Raines, R. T., Bright ideas for chemical biology. *ACS Chem. Biol.* **2008,** *3*, 142-155.

9. Levitsky, K.; Ciolli, C. J.; Belshaw, P. J., Selective inhibition of enqineered receptors via proximity-accelerated alkylation. *Org. Lett.* **2003,** *5*, 693-696.

10. Chen, Z. X.; Jing, C. R.; Gallagher, S. S.; Sheetz, M. P.; Cornish, V. W., Second-Generation Covalent TMP-Tag for Live Cell Imaging. *J. Am. Chem. Soc.* **2012,** *134*, 13692-13699.

11. Xiang, Z.; Ren, H. Y.; Hu, Y. S.; Coin, I.; Wei, J.; Cang, H.; Wang, L., Adding an unnatural covalent bond to proteins through proximity-enhanced bioreactivity. *Nat. Methods* **2013,** *10*, 885-888.

12. Tsukiji, S.; Miyagawa, M.; Takaoka, Y.; Tamura, T.; Hamachi, I., Ligand-directed tosyl chemistry for protein labeling in vivo. *Nat. Chem. Biol.* **2009,** *5*, 341-343.

13. Hughes, C. C.; Yang, Y. L.; Liu, W. T.; Dorrestein, P. C.; La Clair, J. J.; Fenical, W., Marinopyrrole A Target Elucidation by Acyl Dye Transfer. *J. Am. Chem. Soc.* **2009,** *131*, 12094-12096.

14. Fernandez-Suarez, M.; Chen, T. S.; Ting, A. Y., Protein-protein interaction detection in vitro and in cells by proximity biotinylation. *J. Am. Chem. Soc.* **2008,** *130*, 9251-9253.

15. Slavoff, S. A.; Liu, D. S.; Cohen, J. D.; Ting, A. Y., Imaging Protein-Protein Interactions inside Living Cells via Interaction-Dependent Fluorophore Ligation. *J. Am. Chem. Soc.* **2011,** *133*, 19769-19776.

16. Liu, B.; Archer, C. T.; Burdine, L.; Gillette, T. G.; Kodadek, T., Label transfer chemistry for the characterization of protein-protein interactions. *J. Am. Chem. Soc.* **2007,** *129*, 12348-12350.

17. Andrews, S. S.; Hill, Z. B.; Perera, B. G. K.; Maly, D. J., Label Transfer Reagents to Probe p38 MAPK Binding Partners. *ChemBioChem* **2013,** *14*, 209-216.

18. Fancy, D. A., Elucidation of protein-protein interactions using chemical cross-linking or label transfer techniques. *Curr. Opin. Chem. Biol.* **2000,** *4*, 28-33.

19. Amini, F.; Kodadek, T.; Brown, K. C., Protein affinity Labeling mediated by genetically encoded peptide tags. *Angew. Chem.-Int. Edit.* **2002,** *41*, 356-359.

20. Takaoka, Y.; Ojida, A.; Hamachi, I., Protein Organic Chemistry and Applications for Labeling and Engineering in Live-Cell Systems. *Angew. Chem.-Int. Edit.* **2013,** *52*, 4088-4106.

21. Woydziak, Z. R.; Fu, L. Q.; Peterson, B. R., Synthesis of Fluorinated Benzophenones, Xanthones, Acridones, and Thioxanthones by Iterative Nucleophilic Aromatic Substitution. *J. Org. Chem.* **2012,** *77*, 473-481.

22. Wu, L. X.; Burgess, K., Fluorescent amino- and thiopyronin dyes. *Org. Lett.* **2008,** *10*, 1779-1782.

23. Stacko, P.; Sebej, P.; Veetil, A. T.; Klan, P., Carbon-Carbon Bond Cleavage in Fluorescent Pyronin Analogues Induced by Yellow Light. *Org. Lett.* **2012,** *14*, 4918-4921.

24. Langone, J. J., Protein-A of Staphylococcus-aureus and Related Immunoglobulin Receptors Produced by Streptococci and Pneumococci. *Adv.Immunol.* **1982,** *32*, 157-252.

25. Gouda, H.; Shiraishi, M.; Takahashi, H.; Kato, K.; Torigoe, H.; Arata, Y.; Shimada, I., NMR study of the interaction between the B domain of

staphylococcal protein A and the Fc portion of immunoglobulin G. *Biochemistry* **1998,** *37*, 129-136.

26. Moks, T.; Abrahmsen, L.; Nilsson, B.; Hellman, U.; Sjoquist, J.; Uhlen, M., Staphylococcal Protein-A Consists of 5 IgG-Binding Domains. *Eur. J. Biochem.* **1986,** *156*, 637-643.

27. Graille, M.; Stura, E. A.; Corper, A. L.; Sutton, B. J.; Taussig, M. J.; Charbonnier, J. B.; Silverman, G. J., Crystal structure of a Staphylococcus aureus protein A domain complexed with the Fab fragment of a human IgM antibody: Structural basis for recognition of B-cell receptors and superantigen activity. *Proc. Natl. Acad. Sci. U. S. A.* **2000,** *97*, 5399-5404.

28. Deisenhofer, J., Crystallographic Refinement and Atomic Models of a Human Fc Fragment and its Complex with Fragment-B of Protein-A from Staphylococcus-aureus at 2.9-A and 2.8-A Resolution. *Biochemistry* **1981,** *20*, 2361-2370.

29. Dickson, K. A.; Haigis, M. C.; Raines, R. T., Ribonuclease inhibitor: Structure and function. In *Progress in Nucleic Acid Research and Molecular Biology, Vol 80*, Moldave, K., Ed. Elsevier Academic Press Inc: San Diego, 2005; Vol. 80, pp 349-+.

30. Kobe, B.; Deisenhofer, J., A Structural basis of the interactions between leucine-rich repeats and protein ligands. *Nature* **1995,** *374*, 183-186.

31. Kobe, B.; Deisenhofer, J., Mechanism of ribonuclease inhibition by ribonuclease inhibitor protein based on the crystal structure of its complex with ribonuclease A. *J. Mol. Biol.* **1996,** *264*, 1028-1043.

32. Blackburn, P.; Gavilanes, J. G., Identificaiton of lysine residues in the binding domain of ribonuclease-A for the rnase inhibitor from human placenta. *J. Biol. Chem.* **1982,** *257*, 316-321.

33. Libonati, M.; Gotte, G., Oligomerization of bovine ribonuclease A: structural and functional features of its multimers. *Biochem. J.* **2004,** *380*, 311-327.

34. Fukuchi, S.; Nishikawa, K., Protein surface amino acid compositions distinctively differ between thermophilic and mesophilic bacteria. *J. Mol. Biol.* **2001,** *309*, 835-843.

35. Arkin, M. R.; Wells, J. A., Small-molecule inhibitors of protein-protein interactions: Progressing towards the dream. *Nat. Rev. Drug Discov.* **2004,** *3*, 301-317.

36. Yin, H.; Hamilton, A. D., Strategies for targeting protein-protein interactions with synthetic agents. *Angew. Chem.-Int. Edit.* **2005,** *44*, 4130-4163.

37. Johnstone, A.; Thorpe, R., Immunochemistry in Practice, 2nd edition. *Trends in Biochemical Sciences* **1988,** *13*, 73.

38. Keller, A.; Nesvizhskii, A. I.; Kolker, E.; Aebersold, R., Empirical statistical model to estimate the accuracy of peptide identifications made by MS/MS and database search. *Anal. Chem.* **2002,** *74*, 5383-5392.

39. Nesvizhskii, A. I.; Keller, A.; Kolker, E.; Aebersold, R., A statistical model for identifying proteins by tandem mass spectrometry. *Anal. Chem.* **2003,** *75*, 4646-4658.

APPENDIX A

List of cell lines used in the research

Cell Line	Media	Growth	Organism	Tissue Type	Source	Notes
BxPc-3	DMEM + 10% FBS + Pen/Strep	Adherent	Human	Pancreas	Liang Xu_KU (via ATCC)	ATCC #CRL-1687
CHO-K1	F12K + 10% FBS + Pen/Strep	Adherent	Chinese Hamster	Ovary	ATCC	ATCC #CCL-61
CHO-ldlA	DMEM/F12K Mix + 10% FBS + Pen/Strep	Adherent	Chinese Hamster	Ovary	Monty Krieger MIT	Stable knockdown of LDLR
CHO-ldlA_mSR-B1	DMEM/F12K Mix + 10% FBS + Pen/Strep + 200 µg/mL G418	Adherent	Chinese Hamster	Ovary	Monty Krieger MIT	Stable knockdown of LDLR + Stable expression of mouse SR-B1
HEK-293T	DMEM + 10% FBS + Pen/Strep	Adherent	Human	Kidney	ATCC	ATCC #CRL-11268
HeLa	DMEM + 10% FBS + Pen/Strep	Adherent	Human	Cervical	ATCC	ATCC #CCL-2
HeLa_GFP	DMEM + 10% FBS + Pen/Strep + 200 µg/mL G418	Adherent	Human	Cervical	Matt Levy Einstein University	Stable expression of GFP
HeLa_pGE-NEG	DMEM + 10% FBS + Pen/Strep + 200 µg/mL G418	Adherent	Human	Cervical	Peterson Lab (dh)	Stable expression of empty vector
HeLa_pGE-POS	DMEM + 10% FBS + Pen/Strep + 200 µg/mL G418	Adherent	Human	Cervical	Peterson Lab (dh)	Stable expression of shRNA against human Rnase inhibitor
Jurkat	RPMI-1640 + 10% FBS + Pen/Strep	Suspension	Human	T-cell Lymphocyte	ATCC	ATCC #TIB-152
KBM-7	Iscove's MEM + 10% FBS + Pen/Strep	Suspension	Human	T-cell Lymphocyte	Haplogen	Haploid for all chromosomes except chr8
NPC1 (-/-) Fibroblast	Earle's MEM + 15% FBS + Pen/Strep	Adherent	Human	Fibroblast	Coriell Cell Repository	Non-functional NPC1 GM-03123
NPC2 (-/-) Fibroblast	Earle's MEM + 15% FBS + Pen/Strep	Adherent	Human	Fibroblast	Coriell Cell Repository	Non-functional NPC2 GM-18455
SKBr-3	DMEM/F12K Mix + 10% FBS + Pen/Strep	Adherent	Human	Breast	ATCC	ATCC #HTB-30
THP-1	RPMI-1640 + 10% FBS + Pen/Strep + 50 µM 2-ME	Suspension	Human	Macrophage	ATCC	ATCC #TIB-202
wt Fibroblast	Earle's MEM + 10% FBS + Pen/Strep	Adherent	Human	Skin	ATCC	ATCC #CRL-2076 Control line for NPC1/2(-/-)

APPENDIX B

List of plasmids

Name	Gene Product	Gene Species	Vector	Type	Source	Notes
pCMV-XL5_NPC2	NPC2	Human	pCMV6-XL5	Mammalian Expression Vector	Origene	Origene Cat.# SC116115
pcDNA3_NPC2	NPC2	Human	pcDNA3	Mammalian Expression Vector	P. Gao (KU PPG)	
pcDNA3_NPC2_F85A	NPC2 Mutant	Human	pcDNA3	Mammalian Expression Vector	P. Gao (KU PPG)	Expresses NPC2 with diminished activity
pcDNA3_NPC2_V115F	NPC2 Mutant	Human	pcDNA3	Mammalian Expression Vector	P. Gao (KU PPG)	Expresses NPC2 with diminished activity
pcDNA3_NPC2_W128A	NPC2 Mutant	Human	pcDNA3	Mammalian Expression Vector	P. Gao (KU PPG)	Expresses NPC2 with diminished activity
pcDNA3_NPC2_W128F	NPC2 Mutant	Human	pcDNA3	Mammalian Expression Vector	P. Gao (KU PPG)	Expresses NPC2 with diminished activity
pcDNA3_NPC2_W128V	NPC2 Mutant	Human	pcDNA3	Mammalian Expression Vector	P. Gao (KU PPG)	Expresses NPC2 with diminished activity
NPC2_mCherry	NPC2-mCherry fusion	Human	pCMV6-XL5	Mammalian Expression Vector	P. Gao (KU PPG)	C-terminal mCherry fusion
NPC2_shRNA_pSil 6-1	shRNA targeting NPC2	Human	pSilencer	Mammalian Expression Vector	F. Moatamed (UCLA)	
NPC2_shRNA_pSil 3-3	shRNA targeting NPC2	Human	pSilencer	Mammalian Expression Vector	F. Moatamed (UCLA)	
pSil_ΔshRNA	Empty Vector	Human	pSilencer	Mammalian Expression Vector	F. Moatamed (UCLA)	
N-term HA tag_NPC2	NPC2-HA fusion	Human	pCMV6-XL5	Mammalian Expression Vector	P. Gao (KU PPG)	N-terminal hemagglutinin tag
C-term HA tag_NPC2	NPC2-HA fusion	Human	pCMV6-XL5	Mammalian Expression Vector	P. Gao (KU PPG)	C-terminal hemagglutinin tag
Myc-DDK-TSPAN2	Tetraspanin 2	Human	pCMV6	Mammalian Expression Vector	Origene	Origene Cat.# RC204809
HSH000133-1-mU6	shRNA targeting TSPAN2	Human	n/a	shRNA	Genecopoeia	Product ID# HSH000133
HSH000133-2-mU6	shRNA targeting TSPAN2	Human	n/a	shRNA	Genecopoeia	Product ID# HSH000134
HSH000133-3-mU6	shRNA targeting TSPAN2	Human	n/a	shRNA	Genecopoeia	Product ID# HSH000135
HSH000133-4-mU6	shRNA targeting TSPAN2	Human	n/a	shRNA	Genecopoeia	Product ID# HSH000136
CSHCTR001-mU6	Scrambled shRNA	n/a	n/a	Scrambled shRNA	Genecopoeia	
pGFP-UV	GFP-UV	n/a		Bacterial Expression Vector	Clonetech	
pEGFP-C1	EGFP	n/a		Mammalian Expression Vector	Clonetech	
pmCherry-N1	mCherry	n/a		Mammalian Expression Vector	Clonetech	

Name	Gene Product	Gene Species	Vector	Type	Source	Notes
pGE-NEG	Empty Vector	n/a	pGE-1	Mammalian Expression Vector	K. Dickson (Lawrence U.)	
pGE-POS	shRNA targeting Rnase Inhibitor	Human	pGE-1	Mammalian Expression Vector	K. Dickson (Lawrence U.)	
EGFR-wt	EGFR	Human	pBABE puro	Mammalian Expression Vector	Addgene	Addgene Plasmid #11011
HER2-wt	HER2	Human	pcDNA3	Mammalian Expression Vector	Addgene	Addgene Plasmid #16257
pErbB1-Citrine	EGFR-YFP fusion	Human	pEYFP-N1	Mammalian Expression Vector	Addgene	Addgene Plasmid #40266
pErbB2-CFP	HER2-CFP fusion	Human	pcDNA3	Mammalian Expression Vector	Addgene	Addgene Plasmid #40268
pcDNA3	Empty Vector	n/a	pcDNA3	Mammalian Expression Vector	D. Sahoo (Med. Coll. of Wisc.)	
pClaI	SR-B1	Human	pcDNA3	Mammalian Expression Vector	D. Sahoo (Med. Coll. of Wisc.)	
pClaI_S112F	SR-B1 Mutant	Human	pcDNA3	Mammalian Expression Vector	D. Sahoo (Med. Coll. of Wisc.)	Expresses SR-B1 with diminished activity
pClaI_T175A	SR-B1 Mutant	Human	pcDNA3	Mammalian Expression Vector	D. Sahoo (Med. Coll. of Wisc.)	Expresses SR-B1 with diminished activity
pCS2+_DISP wt_5myc	Dispatched 1_C-term 5 myc tag	Mouse	pCS2+	Vertebrate Expression Vector	A. Salic (Harvard Univ)	
pCS2+_DISP delta loop1_5myc	Dispatched 1_C-term 5 myc tag	Mouse	pCS2+	Vertebrate Expression Vector	A. Salic (Harvard Univ)	
pCS2+_DISP wt_mCherry	Dispatched 1_mCherry fusion	Mouse	pCS2+	Vertebrate Expression Vector	A. Salic (Harvard Univ)	
pCS2+_DISP delta loop1_mCherry	Dispatched 1_mCherry fusion	Mouse	pCS2+	Vertebrate Expression Vector	A. Salic (Harvard Univ)	